Titre: Title:	Attachment of Therapeutic and Imaging Agents to Magnetotactic Bacteria Acting as Self-Propelled Bio-Carriers for Cancer Treatment
Auteur: Author:	Samira Taherkhani
Date:	2015
Type:	Mémoire ou thèse / Dissertation or Thesis
Référence: Citation:	Taherkhani, S. (2015). Attachment of Therapeutic and Imaging Agents to Magnetotactic Bacteria Acting as Self-Propelled Bio-Carriers for Cancer Treatment [Thèse de doctorat, École Polytechnique de Montréal]. PolyPublie. https://publications.polymtl.ca/2005/

URL de PolyPublie: PolyPublie URL:	https://publications.polymtl.ca/2005/
Directeurs de recherche: Advisors:	Sylvain Martel, & Maryam Tabrizian
Programme: Program:	Génie biomédical

UNIVERSITÉ DE MONTRÉAL

ATTACHMENT OF THERAPEUTIC AND IMAGING AGENTS TO MAGNETOTACTIC BACTERIA ACTING AS SELF-PROPELLED BIO-CARRIERS FOR CANCER TREATMENT

SAMIRA TAHERKHANI

INSTITUT DE GÉNIE BIOMÉDICAL

ÉCOLE POLYTECHNIQUE DE MONTRÉAL

THÈSE PRÉSENTÉE EN VUE DE L'OBTENTION

DU DIPLÔME DE PHILOSOPHIAE DOCTOR

(GÉNIE BIOMÉDICAL)

DÉCEMBRE 2015

UNIVERSITÉ DE MONTRÉAL

ÉCOLE POLYTECHNIQUE DE MONTRÉAL

Cette thèse intitulée :

ATTACHMENT OF THERAPEUTIC AND IMAGING AGENTS TO MAGNETOTACTIC BACTERIA ACTING AS SELF-PROPELLED BIO-CARRIERS FOR CANCER TREATMENT

présentée par : TAHERKHANI Samira

en vue de l'obtention du diplôme de : Philosophiae Doctor

a été dûment acceptée par le jury d'examen constitué de :

Mme HOEMANN Caroline, Ph. D., président

M. MARTEL Sylvain, Ph. D., membre et directeur de recherche

Mme TABRIZIAN Maryam, Ph. D., membre et codirectrice de recherche

Mme LEBLOND-CHAIN Jeanne, Ph. D., membre

M. SYLVESTRE Michel, Ph. D., membre

DEDICATION

To my beloved husband, Farshad

&

To my parents, Fatemeh and Hossein

ACKNOWLEDGEMENTS

First and foremost, I would like to express my deepest gratitude to my research supervisors: Professor Sylvain Martel, director of the "Nanorobotics Laboratory" and Professor Maryam Tabrizian, director of the "Biomat'X Research Laboratories" for giving me the opportunity to work on this project, and for strategic vision, unwavering patience, mental support and trust all these years from the initial to the final level enabled me to develop an understanding of the subject. I am truly honored to have had the privilege to work under the supervision of such outstanding scholars as Prof. Martel and Prof. Tabrizian. I am also grateful to them for careful reading and minute criticism of this thesis.

My most sincere thanks go to Prof. Martel, not only as my thesis supervisor, but also as a teacher with whom I am always impressed by his moral and ethical attitude toward the people in general and students especially. I learned from him about how to look at research as a tool that should or possibly could have applications in our real lives and resolve industrial issues. I would like to thank him for his strong belief and trust, continuous guidance, encouragement and enthusiasm to assist me in conducting a successful research. I should say that during this research, there was no barrier in terms of facilities and tools, and the project was financially well supported by him for which I am grateful. Prof. Martel is stunningly passionate about Nanorobotics and his hard work always inspires me during my Ph.D. That is a great endowment that I had during this period, thanks to his dedication to students and research. While he has vast knowledge on the field, he is very humble and has the sense of humor which makes the students feel comfortable with him.

I would like to gratefully thank Prof. Tabrizian for her supervisory role, enthusiasm, immense knowledge, and vision. It was a privilege to work under her supervision on this pioneering project in the field of drug delivery. One of the most amazing things about Prof. Tabrizian is her availability to students and helping concerns. Without her precious support, it would not be possible to conduct this research. My deepest thanks go to her for having allowed me to be a part of her group. Besides learning about research from Prof. Tabrizian, I have learned much more from her about a good work ethic.

I would like to sincerely thank my examination committee members, Dr. Hoemann, Dr. Leblond-Chain, Dr. Sylvestre, and Dr. Gourdeau that have agreed to evaluate this thesis. You honor me by evaluating this work.

I am thankful Dr. Mahmood Mohammadi for his guidance and comments that were essential to the accomplishment of this work.

I would like to gratefully acknowledge Prof. Danuta Radzioch for her guidance and collaboration in using the animal facility at General Hospital, which was complemented by her insightful comments. Despite her demanding clinical duties, Dr. Danuta was always available to reach. I would also like to acknowledge the members of her team who welcomed me into their group.

A very special thanks go to Daniel Houle, whose his support and encouragement enabled the implementation of *in vivo* tests that were a revolving point in my work. It was a pleasure to work with you.

Thanks to Dr. Louis Gaboury (IRIC, UdeM) for the many tips during the analysis of histological sections, and the UdeM histology team, Mirela Birlea and Julie Hinsinger, for the tissues preparation and their attention to this project.

My deepest gratitude goes to all from the Nanorobotics laboratory, for their professional and technical supports. Also, I wish to thank all friends, in particular, Dr. Nina Olamaei (for her valuable contribution in MR imaging), Dr. Nasr Tabatabaei, and Dr. Fatemeh Afkhamizarreh for their supportive friendship and help over the years. I thank Dr. Ouajdi Felfoul, Dominic de Lanauze, and Dumitru Loghin from the Nanorobotics laboratory for their contributions to the project in the design and development of the magnetotaxis platform.

I thank Dr. Neila Kaou and Mr. Michael Atkin, whose presence in the laboratory provided support and organization. It was a great pleasure to have attended over the years.

Special thanks go to Eunice You, who was always willing to help, for her friendship and time dedicated to reviewing my thesis.

I would also like to show my appreciation to all the members of the Biomat'X lab– Tohid, Amir, Mina, Lamees, Saber, Andrew, Steve, Christina, Kaushar, and Ryan for their friendship and continuous support. Special thanks in particular to Dr. Kristen Bowey for her friendship, willingness to discuss, and her time dedicated to helping and sharing her findings and experience.

I would also like to thank Dr. Jamal Daoud for his collaboration on the cell-culture project, his enthusiasm for research was a great inspiration to me. I would like to extend my appreciation to Mr. Timothy Jones and Dr. Sherief Essa without whom the liposome preparation for *in vivo* aspects of this project would not have been possible. As well, special thanks to Ms. Line Mongeon, Ms. Jeannie Mui, and Dr. Kelly Sears for their technical expertise towards the microscopy studies.

I would also like to gratefully acknowledge Quebec Consortium for Drug Discovery (CQDM), Canada Research Chair (CRC) in Medical Nanorobotics, Research Chair of École Polytechnique in nanorobotics, National Sciences and Engineering Research Council of Canada (NSERC) and Mathematics of Information Technology and Complex Systems (MITACS) for funding my research.

I would like to thank my parents, Fatemeh and Hossein, to whom I am greatly indebted for their moral support and unwavering love throughout my life. Thanks for giving me the strength to reach my dreams. Without you, I would not have had the ability to tackle challenges head on.

Most importantly, I wish to give a special heartfelt thanks to my spouse, Farshad, who has been very supportive and understanding, and for his unconditional love and always being a continuous source of inspiration. Thanks for not leaving me alone as I faced different obstacles, and for supporting me as I solved various challenges during this journey. Thank you for always being with me in the difficult situations. I would like to say “thank you, for everything!”

Last but not least, I want to offer my regards and blessings to all of those who supported me in any way during the completion of the project. I will forever be appreciative.

RÉSUMÉ

Malgré les progrès de la médecine moderne, les traitements anticancéreux actuels n'arrivent toujours pas à vaincre le cancer. Seulement une fraction des doses de médicaments administrées parvient à la tumeur en raison d'un ciblage non spécifique, de barrières physiologiques au niveau du système vasculaire ainsi que de l'élimination immédiate de médicaments par le système immunitaire. Des dosages fréquents de médicaments deviennent nécessaires afin de surmonter ces obstacles, entraînant une toxicité systémique, des effets secondaires et un échec thérapeutique. De plus, les systèmes actuels d'imagerie médicale sont incapables de produire des images de haute qualité des structures tumorales pour les diagnostiques et les traitements. Ceci est dû aux restrictions de la résolution spatiale et de l'incapacité des agents de contraste à pénétrer dans les zones tumorales afin de générer un signal suffisamment intense. Le développement de nouveaux agents thérapeutiques ainsi que de nouvelles techniques de ciblage thérapeutique sont donc requis afin d'améliorer l'efficacité des traitements actuels.

Pour ce projet de recherche doctorale, l'attachement de charges utiles à la surface de bactéries magnétotactiques flagellées *Magnetococcus Marinus* MC-1 (BMT) a été mise en place pour transporter de façon ciblée une quantité optimale de médicaments profondément dans les zones tumorales. Ces bio-robots autopropulsés de dimensions adéquates sont équipés d'un système de propulsion dirigeable, d'un système de navigation, et de capacités sensorielles. Divers types de complexes BMT ont été fabriquées en attachant aux BMT (i) des liposomes vides (BMT-LP), (ii) des liposomes contenant un agent anticancéreux SN38 (BMT-LSC), et (iii) des nanoparticules superparamagnétiques de magnétite (BMT-S200). L'efficacité de l'attachement des charges et du comportement des bactéries soumises à un champ magnétique directionnel ont été étudiés. Par la suite, la capacité des complexes BMT à naviguer le long d'une trajectoire prédéterminée, à infiltrer profondément l'espace interstitiel, et à cibler des zones tumorales inaccessibles, ont été étudiés dans un modèle animal soumis à un champ magnétique externe. Pour parvenir à des complexes BMT aptes à transporter suffisamment de produits pharmaceutiques et de s'accumuler préférentiellement dans les régions affectées, il faut assurer un attachement solide et stable qui ne compromet pas la motilité des BMT.

Les BMT-LP ont été préparés par réaction carbodiimide (EDC/NHS) en formant des liaisons covalentes directes entre des liposomes fonctionnalisés et les groupes aminés présents à la surface des BMT. Cette technique permet à environ 70 liposomes (diamètre ~170 nm) d'être attachés à la surface de chaque cellule MC-1. Ceci a réduit de 60% la vitesse de nage, passant de 200 à 80 μm s^{-1}. L'absorption cellulaire des BMT-LP a été testée sur différentes lignées cellulaires: cellules fibroblastes (NIH/3T3), macrophages (J774), et cellules d'adénocarcinome colorectal humain (Colo205). Les résultats *in vitro* démontrent que l'attachement ne perturbe en aucun cas la capture liposomique de ces lignées cellulaires.

Les expériences de navigation *in vivo* ont été effectuées à l'aide des vecteurs optimisés BMT-LP, BMT-LSC et BMT-S200, injectés péritumoralement dans des tumeurs xénogreffées colorectales humaines HCT116, implantées dans le flanc de souris immunodéficientes (SCID)-beige. La livraison de BMT chargées ciblant les zones tumorales, tout en franchissant la limite de diffusion de molécules médicamenteuses, a été obtenue en exploitant le comportement magnéto-aérotaxique. Lorsque les bactéries s'approchent de la zone tumorale ciblée par magnétotaxie, l'intensité du champ magnétique est réduite, permettant ainsi à la bactérie d'exploiter son comportement aérotaxique et de migrer en fonction de la concentration préférentielle en oxygène (< 0.7%) vers la zone de transition oxique/anoxique. Dans le contexte de cette thèse, la présence et répartition des BMT dans les tumeurs par coloration immunofluorescence (IF) à l'aide d'un anticorps anti-BMT ont démontré que la méthode d'attachement proposée n'a pas enlever la capacité de diriger les complexes BMT chargées sous l'influence d'un champ magnétique, et de les accumuler dans la zone nécrotique des tumeurs solides. L'analyse histologique et la quantification des BMT ont démontré que plus de 50% des bactéries (~20 μl de 2.92×10^7 MTB ml^{-1} dans du PBS) sont parvenues à s'infiltrer et s'accumuler en plus grande concentration dans les régions hypoxiques et nécrotiques des tumeurs. L'efficacité du traitement a été évaluée en injectant des BMT-LSC péritumoralement avec une dose cumulative moyenne de 6.4 μg SN38. Les résultats ont montré une réduction statistiquement significative de la tumeur colorectale à la suite du traitement.

Le BMT-S200 a été développé comme un agent de contraste d'imagerie par résonance magnétique (IRM) afin de visualiser les régions hypoxiques dans les xénogreffes HCT116. Pour la préparation des BMT-S200, les nanoparticules magnétiques ont d'abord été fonctionnalisées avec les anticorps contre une protéine de surface de la BMT par réaction carbodiimide. Ensuite,

la nanoparticule munie de l'anticorps a été conjuguée à la BMT. Les résultats *in vitro* démontrent que la décroissance de signal des images de relaxation longitudinale et transversale change de manière proportionnelle à la concentration des BMT. Les résultats *in vivo* indiquent que l'injection BMT-S200 (~200 μl de 5×10^9 MTB ml^{-1}, 3.6×10^{-6} de S200 (μg)/BMT) de façon péritumorale permet d'augmenter la diffusion des agents de contraste traditionnels et génère un artéfact en augmentant les distorsions du champ magnétique homogène de l'appareil de résonnance magnétique, causant une diminution du signal beaucoup plus important comparativement à leur taille réelle. En effet, les complexes BMT-S200 peuvent générer des images à haut contraste dans les relaxations T_1- and T_2/T_2*, ce qui reflète l'emplacement de l'artéfact, corroborant ainsi la livraison à la tumeur, et permettant de visualiser le modèle de distribution dans les régions hypoxiques. Les données IF correspondantes et la coloration hémalun-phloxine-safran (HPS) ont corroboré les résultats d'IRM. Les résultats démontrent que le BMT-S200 a la capacité de suivre la structure de la tumeur et ces régions hypoxiques ainsi que d'exercer un contrôle de rétroaction dans la navigation du BMT.

Dans l'ensemble, cette thèse propose méthodes d'attachement à des BMT chargées pour des fins de thérapie et d'imagerie dans le but d'atténuer la croissance tumorale ou de détecter et visualiser les régions hypoxiques, respectivement.

ABSTRACT

Despite the substantial achievements of modern medicine, current medical therapies cannot eradicate cancer. Due to nonspecific targeting, the multiple physiological barriers that blood-borne agents must encounter, and the rapid sequestration of drugs by the immune system, a suboptimal fraction of the total injected dose reaches the intended target. These obstacles necessitate frequent dosing to compensate therapeutic effects, resulting in systemic toxicity, undesirable side effects, and treatment failure. In addition, existing medical imaging modalities struggle to provide high quality clinical images of tumor structures for treatment purposes due to limitations in spatial resolution and lack of penetration of contrast agents into tumoral regions to induce sufficient signal intensity. To address these issues, the development of new therapeutic agents alongside improved strategies for targeting therapy with the ability to control their fate is required.

The attachment of payloads to the flagellated *Magnetococcus Marinus* MC-1 magnetotactic bacteria (MTB) to directly transport optimal quantities of pharmaceutical agents to regions located deep in tumors is what has been proposed during the accomplishment of this PhD project. These engineered self-propelled bio-robots with an appropriate dimension are equipped with steerable propulsion, navigation system, and onboard sensory capabilities. MTB complexes were fabricated by attaching the MTB to (i) empty liposomes (MTB-LP), (ii) SN38 anticancer drug encapsulated in liposomes (MTB-LSC), and (iii) 200 nm superparamagnetic magnetite nanoparticles (MTB-S200). The attachment efficacy and magnetic response behavior from the influence of a directional magnetic field of loaded bacteria with therapeutic or imaging agents were studied. Subsequently, results showed that the attachment method was suitable to allow MC-1 MTB to transport therapeutic and imaging agents along a planned trajectory prior to penetrate deep through the interstitial space in order to reach the hypoxic regions of a tumor in an animal model. To achieve MTB complexes capable of carrying sufficient pharmaceutical agents and accumulating preferentially at disease sites, the attachment must be strong and stable without compromising the natural motility of MTB.

The MTB-LP were prepared by direct covalent attachment of functionalized liposomes to the amine groups naturally presented on the surface of MTB using carbodiimide (EDC/NHS)

chemistry. Such a technique allows approximately 70 liposomes (~170 nm in diam.) to be attached on the surface of each MC-1 cells. The attachment resulted in ~60% reduction in swimming velocity from 200 to 80 μm s^{-1}. Cellular uptake of MTB-LP was examined in different cell lines including fibroblast (NIH/3T3), macrophage (J774), and human colorectal adenocarcinoma (Colo205). The results demonstrated that the attachment does not interfere with liposomal uptake *in vitro*.

The *in vivo* navigation experiments were conducted on the optimized MTB-LP, MTB-LSC and MTB-S200 injected peritumorally into the HCT116 human colorectal mouse tumor xenograft implanted in the flank of the severe combined immunodeficiency (SCID)-beige mice. Delivery of loaded MTB toward tumor-targeted regions while passing the diffusion limit of conventional drug molecules was achieved by exploiting natural magneto-aerotaxis behavior. As the bacteria approach the tumor targeted zone by magnetotaxis-based directional control, the intensity of the magnetic field is decreased, which allows bacteria to migrate toward preferred oxygen concentration (< 0.7%) at the oxic-anoxic transition zone (OATZ) in hypoxic regions by their natural aerotaxis behavior. In the context of this thesis, the presence and distribution pattern of the MTB inside the tumor by immunofluorescence (IF) staining using an antibody against MTB demonstrated that the attachment method was suitable to navigate the loaded MTB complexes using magnetic field and to accumulate them in the targeted necrotic zone of solid tumors. The analysis of histology slides and quantification of MTB showed that more than 50% of the injected bacteria (~20 μl of 2.92×10^7 MTB ml^{-1} in PBS) were able to penetrate and accumulate with greater concentration in the hypoxic and necrotic areas of the tumor tissue. To study the treatment efficacy, MTB-LSC were peritumorally injected with a mean cumulative dose of 6.4 μg SN38. The results showed statistically significant shrinkage of colorectal tumor xenograft upon treatment.

The MTB-S200 was developed as a magnetic resonance imaging (MRI) contrast agent to visualize hypoxic areas in HCT116 xenografts. To prepare MTB-S200, the magnetic nanoparticles were first functionalized with an antibody against the MTB protein surface using carbodiimide chemistry. The antibody-grafted particles were then conjugated to the MTB. The *in vitro* results demonstrated that the signal decay in the T_1- and T_2-weighted images were changed proportionally to the concentration of MTB complexes. The *in vivo* studies indicated that peritumorally injected MTB-S200 (~200 μl of 5×10^9 MTB ml^{-1}, 3.6×10^{-6} of S200 (μg)/MTB)

enable the diffusion limits of conventional contrast agents to be bypassed and generates susceptibility artifact by local distortions of the homogeneous magnetic field of MR scanner, which caused the signal loss in a much larger scale than their actual size. Indeed, the MTB-S200 complexes can generate a high contrast in both T_1- and T_2/T_2*-weighted images, which reflecting the position of the artifact, confirming the delivery into the cancer tissue, and allowing visualization of the distribution pattern in well-penetrated tumor hypoxic regions. Corresponding IF and hematoxylin-phloxine-saffron (HPS) histology results confirmed the MRI data. The results demonstrated that the MTB-S200 agent provides the opportunity for monitoring of tumor structure and hypoxic regions as well as feedback control in MTB navigation operations.

Overall, this thesis proposes attachment methods to load therapeutic and imaging agents on the MTB with the aims of attenuating tumor growth or visualization of tumor hypoxic regions, respectively.

TABLE OF CONTENTS

LIST OF TABLES

LIST OF FIGURES

LIST OF SYMBOLS AND ABBREVIATIONS

2D	Two-dimensional
3D	Three-dimensional
AB	Antibody
ABF	Artificial bacterial flagellum
BCS	Bovine calf serum
BMT	Bactérie magnétotactique
BOLD-MRI	Blood-oxygen-level-dependent MRI
CH	Cholesterol
CLSM	Confocal laser scanning microscopy
COBALT	Combination bacteriolytic therapy
CT	Computed tomography
DCE	Dynamic contrast-enhanced
DLS	Dynamic light scattering
DMEM	Dulbecco's modified eagle's medium
DSPC	Distearoylphosphatidylcholine
DSPE-PEG(2000)-COOH	1,2-distearoyl-sn-glycero-3-phosphoethanolamine-N-[carboxy(polyethylene glycol)2000]
ECM	Extracellular matrix
EDC	1-Ethyl-3-(3-dimethylaminopropyl)carbodiimide
ELISA	Enzyme linked immunosorbent assay
EPR	Enhanced permeability and retention effect
FACS	Fluorescence-activated cell sorting
FBS	Fetal bovine serum
FE-STEM	Field-emission scanning transmission electron microscopy
FISH	Fluorescence *in situ* hybridization
FITC	Fluorescein isothiocyanate
FSC	Forward scatter
FTIR	Fourier transform infrared spectroscopy
Gd-DTPA	Gadolinium-diethylenetriamine pentaacetic acid
GRE	Gradient recalled echo
H&E	Hematoxylin and eosin
HPLC	High performance liquid chromatography
HPS	Hematoxylin phloxine saffron
i.p.	Intraperitoneal
i.t.	Intratumoral
i.v.	Intravenous

IF	Immunofluorescence
IgG	Immunoglobulin G
LP	Liposome
LPS	Lipopolysaccharide
LP-SN38	Liposome-SN38
MBC	Magnetotactic bacterial count
MC-1 MTB	Magnetotactic Coccus 1 strain of magnetotactic bacterium
MDT	Magnetic drug targeting
MES	2-(N-morpholino)-ethanesulfonic acid
MNP	Magnetic nanoparticle
MP	Magnetic particles
MP-AB	Magnetic particle-antibody
MRI	Magnetic resonance imaging
MRN	Magnetic resonance navigation
Ms	Saturation magnetization
MTB	Magnetotactic bacteria
MTB-F200	MTB- Ferromagnetic particle, 200 nm
MTB-F500	MTB- Ferromagnetic particle, 500 nm
MTB-LP	MTB-Liposome
MTB-LSC	MTB-Liposome-SN38 complex
MTB-MP	MTB-Magnetic particle
MTB-S200	MTB- Superparamagnetic particle, 200 nm
MTB-S500	MTB- Superparamagnetic particle, 500 nm
NHS	N-hydroxysuccinimide
OATZ	Oxic-anoxic transition zone
OE-MRI	Oxygen-enhanced MRI
p.t.	Peritumoral
PBS	Phosphate buffered saline
PCS	Photon correlation spectroscopy
PDI	Polydispersity index
PEG	Polyethylene glycol
PET	Positron emission tomography
pN	PicoNewtons
RF	Radio frequency
Rhodamine DHPE	Lissamine Rhodamine B 1, 2-dihexadecanoylsn-glycero-3-phosphoethanolamine, triethylammonium salt
rpm	Revolutions per minute
RPMI-1640	Roswell park memorial institute 1640
SCID	Severe combined immunodeficiency
SD	Standard deviation

SE	Spin echo
SEM	Scanning electron microscopy
SN38	7-Ethyl-10-hydroxycamptothecin
SPION	Superparamagnetic iron oxide nanoparticle
Sulfo-NHS	Sulfo-N-hydroxysulfosuccinimide
TE	Echo time
TEM	Transmission electron microscopy
TIFP	Tumor interstitial fluid pressure
TOLD-MRI	Tissue oxygen level-dependent MRI
TR	Repetition time
TRITC-DHPE	N-(6-Tetramethylrhodaminethiocarbamoyl)-1, 2-dihexadecanoyl-sn-glycero-3-phosphoethanolamine, triethylammonium salt
VSM	Vibrating sample magnetometer
WST-1	4-[3-(4-Iodophenyl)-2-(4-nitrophenyl)-2H-5-tetrazolio]-1,3-benzene disulfonate

LIST OF SYMBOLS

cm	Centimeter
emu	Electromagnetic unit
G	Gauss
g	Gram
H	Applied magnetic field
h	Hour
k	Kilo
L	Liter
m	Magnetic moment of the sample
M	Magnetization (magnetic moment per unit volume)
min	Minute
mm	Millimeter
s	Second
T	Tesla
T_1	Longitudinal relaxation time
T_2	Transverse relaxation time
σ_M	Mass magnetization of the sample

LIST OF APPENDICES

CHAPTER 1 INTRODUCTION

Cancer is recognized as one of the major chronic diseases and a leading cause of death worldwide. Despite recent reductions in morbidity and mortality associated with cancer, it still accounts for roughly 30% of deaths and imposes a significant economic burden, with over $2.5 trillion attributed to health care costs per year. In 2015, it is estimated that 196,900 Canadians will be diagnosed with cancer and 78,000 will die of cancer [1]. The clinical therapeutic strategies employed depend on the location, type, size, stage and cancer's specific characteristics. Among the most common treatments available (surgery, radiation therapy, and *etc.*) for this disease, chemotherapy remains one of the widely used forms of treatment against advanced tumors and metastases.

Upon systemic administration, pharmaceutical agents with short biological half-lives and relatively low therapeutic index lead to an increase in acute and cumulative toxicities (such as myelosuppression and cardiac toxicity). Frequently, dose-limiting toxicity for both chemotherapy and radiation therapy can directly impact survival. Moreover, physiological barriers exist at every level of drug targeting at the tumor site, which typically render most efficient theranostic agents clinically ineffective. For instance, systemic administration of agents causes rapid clearance by immune cells such as reticuloendothelial system of the liver and spleen [2]. The presence of intracellular tight junctions [3] and high cellular packing density (composed of collagen, glycosaminoglycans, and proteoglycans) [4, 5] are another impermeable barrier that impede cellular permeability and penetration of macromolecules or particles into tumor tissues [6, 7]. Drug encapsulation in PEGylated nanocarriers (*e.g.* liposomes, polymers, micelles) as long-circulating pharmaceutical agents can improve targeting through enhanced permeation and retention (EPR) effect [8, 9] but still only a small fraction of nanocarriers enter tumors (~2% after 4 h circulation) [10] with limited intratumoral penetration through the tumor extracellular matrix [6, 11, 12].

The hypoxic region as a tumoral barrier is often associated with an aggressive tumor behavior and driven malignant progression [13]. The tumor microenvironment is characterized by heterogeneous oxygen concentrations (approximately < 0.7% O_2; < 10 mmHg partial pressure of oxygen) and is known to be resistant to both radiotherapy and chemotherapy due to

characteristics such as malformed angiogenesis capillaries, distance from blood vessels, and heterogeneous blood flow [14]. Moreover, the high tumor interstitial fluid pressure (TIFP) with an outward convective gradient (due to lack of lymphatic drainage and abnormal angiogenesis) as well as densely packed extracellular matrix creates obstacles to transcapillary transports the conventional pharmaceutical agents towards the hypoxic regions [12, 13]. There are some strategies to target hypoxic cells, improve uptake and result in homogenous distribution of active agents in the tumor tissue. Examples are targeting associated endogenous markers [15], modifying the extracellular matrix to increase drug penetration [12], using the bio-reductive prodrugs [16, 17], reducing tumor pressure [18], and using a multistage nanoparticle delivery system [19]. However, systemic administration of these agents leads to low passive targeting efficacy.

Direct transportation of therapeutic agents to the tumor site with high efficacy is still an unmet goal since the current strategies lack the important feature such as targeting and tracking. Magnetic targeting offers one the most plausible solution. However, the magnetic drug targeting (MDT) and magnetic resonance navigation (MRN) methods cannot be effectively applied in the tumoral microenvironments [20-22]. In depth-dependent MDT, the magnetic field rapidly decreases from the magnetic source, and very often is limited to treat cancers near the skin. In the case of depth-independent MRN, insufficient magnetic induction volume of the magnetic material at the capillary level prevents efficient direct delivery. Currently artificial bacteria are under investigation for delivering therapeutics [23, 24]. However, despite their enormous potential, the technology is not mature enough to be used in the context of targeted drug delivery due to their constraints such as non-autonomous characteristics and lack of precise navigation. Conversely natural aerotaxis or chemotaxis bacteria such as *Clostridia* [25, 26], *Salmonella* [27-29], *Bifidobacterium* [30], and *Escherichia coli* [31] showed promising therapeutic potential due to the fact that they can preferentially accumulate in tumor tissues. However, their main limitation remains their incapacity to be navigated using computer-assisted magnetotaxis-based directional control *in vivo*.

To address this issue, the MC-1 MTB [32, 33] was proposed for drug delivery applications. An external directional magnetic field causes magnetotaxis behavior of the bacteria by inducing a torque on the chain of membrane-based single-domain iron oxide magnetic nanoparticles that are naturally synthesized in the cells during cultivation, known as magnetosomes [34, 35]. Like a

compass needle, the swimming direction of the MTB is aligned along a small magnetic field (0.5-100 Gauss), causing magnetotaxis behavior. Their ideal size of 1-2 μm (half of the diameter of the smallest human blood vessels) enables the MTB to navigate and pass through the smallest blood vessels, endothelial fenestrations and cellular interstitial spaces. The MTB cells possess two bundles of flagella at a single pole (they are said to be bilophotrichous), which generate a significant propulsive force of ~4.0-4.7 piconewtons (pN) (roughly a tenfold increase in power compared to the other well-known flagellated bacteria species) allowing them to penetrate deeply in tumors and pass the diffusion limit of typical large drug molecules. The flagella also enable the bacteria to reach an average swimming velocity of approximately 200 and up to 300 μm s^{-1} (100 to 150 body (cell) lengths per second). In addition, these microaerophilic MTB with their embedded oxygen sensor are capable of detecting oxygen gradient for directional migration towards their preferred ~0.5% oxygen level, which generally corresponds to the oxygen level expected at the targeted hypoxic tumor regions.

Improved intratumoral drug distribution within the tumor mass can be achieved by attaching pharmaceutical agents encapsulated within nanoscale particles to the surface of the self-propelled MTB [36]. Self-actuation, navigation and sensory capability of MC-1 MTB provide a sufficient propelling force to penetrate hypoxic regions leading to superior delivery ratios of active agents with minimized systemic circulation compared to all other known targeting modalities, such as drug-encapsulated micro/nanoparticles [37, 38], magnetic drug targeting [20-22], receptor–ligand targeting [39, 40], and previous bacterial therapies.

Targeted delivery of therapeutic or imaging cargos to desired anatomical compartments using an external control system and flagellated propulsion of MTB exhibit many unique capabilities that are unattainable with existing clinical methods such as control over location, active penetration into inaccessible tissue, the bypass of the cellular barrier, controlled release of encapsulated substances proximal to the target, facilitated spatial distribution and cellular internalization, and non-invasive imaging and monitoring of treatment efficacy. Moreover, the maximum-tolerated doses to elicit the desired therapeutic response and counter the progression of the tumor can be improved and thereby to minimize adverse side effects [13]. Many different medical applications can be driven from this controllable MTB, such as delivering hydrophilic/hydrophobic anti-cancer drugs, tumor markers, imaging agents, gene, vaccines, to name a few.

Therefore, for the first part of this project, we engineered the liposomal loaded MTB as a targeted delivery vehicle for anticancer drugs. In parallel, the ability to remotely navigate the loaded MTB in a three-dimensional manner and control their biodistribution in colorectal tumor model was studied *in vivo*. Finally, to provide the MTB complex system with the ability of the tracking, we were successful in developing MRI contrast agents loaded MTB to visualize the tumor structure in an *in vivo* animal model using a 3 Tesla MRI scanner.

1.1 Contribution of Authors

This thesis presents the data collected by the candidate throughout the document. It should be noted that this PhD work performed in the framework of a major research project funded by the Quebec Consortium for Drug Development (CQDM) and led by Dr. Sylvain Martel, where the aim was to develop a novel approach for cancer treatment using MTBs. To elucidate the work performed by the candidate within this collaborative effort, a description of the original contribution of the candidate is presented below:

Chapter 3 gathers results of the work performed by the candidate on the development of the MTB liposomal-based delivery system. As part of this project, the candidate was mainly responsible for the design, preparation, characterization, and analysis of an innovative attachment technique to magnetotactic bacteria for carrying therapeutic and imaging agents for cancer therapy. The candidate wrote the published manuscript.

Chapter 4 presents results on the attachment of a payload that led to the development of MTB-magnetic particles complexes as navigable MRI contrast agents. The candidate performed the preparation, evaluation of the attachment efficacy, and characterization of magnetic properties of the complexes. More specifically, the candidate assessed if the motion behavior of the MTB based on magnetotaxis would be influenced by the attachment of a superparamagnetic nanoparticles in sufficiently large quantity to enable MRI contrast effect and as such could have a negative impact on the magnetotaxis directional control of the MTB. The candidate wrote the protocols and analyzed the *in vivo* data. Histology and animal studies were performed in collaboration with Dr. Louis Gaboury and Dr. Danuta Radzioch from the Histology and Molecular Pathology Research Unit of the Institute for Research in Immunology and Cancer

(IRIC) and also the animal facilities at McGill Centre for the Study of Host Resistance, respectively. Dr. Mahmood Mohammadi provided the bacteria. Dr. Nina Olamaei from NanoRobotics Laboratory provided the expertise for MR imaging.

Chapter 5, Appendixes A and B gather results of a multidisciplinary work encompassing diverse disciplines (clinical oncologists, chemists, physicians, pathologists, and immunologists) along with using various research platforms (McGill University, Jewish General Hospital, IRIC, and University of Montreal) for *in vivo* experiments. In this collaborative effort, the candidate designed and performed the attachment of SN38-loaded liposomes to the MTB cells. In addition, the candidate was also involved in the *in vivo* experiments, including taking part in the writing of the related *in vivo* protocols, the daily batch preparation of MTB complexes for the injection, and the post-evaluation of the complexes using electron microscopy. The candidate also assisted in data analyses and evaluating the targeting capability of the complexes in tumor tissue through their counting and biodistribution visualization performed by fluorescence microscopic imaging of immunostained histological slides and tumor homogenization followed by optical microscopy. Dr. Ouajdi Felfoul designed the three-dimensional navigation magnetic platforms and the software control system and initially performed the magnetic navigation of the MTB. Mr. Dominic De Lanauze tested the magnetotactic control sequences and performed the magnetic navigation, which were executed by Mr. Dumitru Loghin. Dr. Mahmood Mohammadi provided the bacteria and acted as project manager. Dr. Louis Gaboury performed histopathological analyses. Liposome-SN38 was prepared by Dr. Sherief Essa working under supervision of Dr. Michel Lafleur and Dr. Maryam Tabrizian. Dr. Danuta Radzioch and Dr. Nicole Beauchemin were responsible for the implantations of tumor xenografts and performed animal studies. Mr. Daniel Houle performed the peritumoral injections in animals. Dr. Yong Zhong Xu implanted the xenografts and performed tumor measurements. All authors assisted in data analysis.

Dr. Sylvain Martel as primary supervisor and Dr. Maryam Tabrizian as co-supervisor appear on the published and unpublished works to reflect their supervisory role throughout the execution of this thesis.

1.2 Thesis outline

This thesis is organized into seven chapters.

In Chapter 1, a general introduction and motivation behind this PhD thesis, specifically the requirement for developing a liposome-based system to encapsulate therapeutic agents, and the imaging application of MTB-magnetic particles in MRI to treat cancer are presented. This chapter also provides the contribution of the authors and the originality of this work. The research hypothesis and objectives of the thesis are also outlined in this chapter.

Chapter 2 presents the background information and a comprehensive literature review required for the completion of this project. This chapter highlights current therapeutic technologies and tumor imaging modality approaches for cancer therapy. A primer on the role of bacterial-based system as a bio-carrier as well as their various pharmacological applications to treat cancer disease is also included in this chapter. An exhaustive review is dedicated to liposome technology as a drug carrier as well as the use of superparamagnetic nanoparticles in imaging applications. The knowledge gained from the literature review was crucial for establishing the research hypothesis and objectives of this PhD thesis towards the design of the bacteria-based targeted drug delivery systems.

Chapter 3 contains the published article in *American Chemical Society (ACS) Nano* entitled "Covalent Binding of Nanoliposomes to the Surface of Magnetotactic Bacteria for the Synthesis of Self-Propelled Therapeutic Agents" where the development of MTB-LP complex and its characterization in terms of the attachment efficacy, swimming behavior, response to magnetic field, cytotoxicity and cellular uptake are presented.

Chapter 4 presents the attachment of magnetic iron oxide nanoparticles to the MTB to form a navigable and trackable MRI contrast agent for tracking the loaded bacteria and visualization of tumor hypoxic regions in the colorectal mouse tumor xenograft.

Chapter 5 highlights only the candidate contribution within a collaborative effort for the evaluation of *in vivo* tumor transportation and the attachment efficiency of MTB-LSC complex. The complete version of data produced for *in vivo* targeting evaluation is presented in Appendix A as a manuscript under revision by *Nature Nanotechnology* entitled "Non-Systemic Magneto-

Aerotactic Bacteria-Mediated Delivery of Drug-Loaded Nanoliposomes in Tumor Hypoxic Regions", where the candidate appears as co-first author.

Chapter 6 presents the general discussion and highlights the main finding on this PhD project.

Chapter 7 provides the general conclusion and overall outcomes of this PhD thesis followed by new avenues of research and recommendations for future works.

1.3 Justification of originality

The originality of this thesis lies in the development of bacteria-based complexes as a "living and self-propelled drugs" for transportation of therapeutic and imaging agents inside unattainable tumor regions with the aim of improving treatment of cancer diseases while reducing secondary toxicity. There are no reports on producing stable and straightforward bioconjugation of pharmaceutical agents including liposome-loaded anti-cancer drug (SN38 as a model) and contrast imaging agent (superparamagnetic iron oxide nanoparticles) to a micro-biorobot, and the assessment and validation of such an attachment approach during the targeting phase of solid tumors in animal models. The chemical coupling of liposomal nanoparticles to the MTB, by taking advantage of biologically inherent moieties presented on MTB cell membrane, is another novel aspect of this work. In the development of such MTB complexes, optimizing the number of liposomes or magnetic particles per MTB was a technological challenge in order to carry a sufficient concentration of pharmaceutical agents to induce therapeutic effects without affecting the natural motility or magnetic response of the loaded MTB. Such studies on the attachment of payload to the surface of the MC-1 cells enable targeted delivery using MTB as untethered microcarriers that can be employed in many areas such as drug delivery, gene, vaccine delivery, and real-time imaging, to name but a few examples.

1.4 Thesis hypothesis and objectives

1.4.1 Thesis hypothesis

Attachment of particles to the surface of the self-propelled MTB can be prepared without compromising their magnetic response, motility, swimming behavior or cellular uptake. These

MTB-based complexes can be magnetically navigated to pass the cellular obstacle, target and accumulate in the hypoxic and necrotic regions and deliver an effective dose of pharmaceutical agents to the tumor. Integrating the superparamagnetic iron oxide nanoparticles as a navigable and trackable contrast agent with MTB will allow MRI visualization of the tumor microenvironment.

1.4.2 Thesis objectives

To confirm the aforementioned thesis hypothesis, the overall goal of this PhD work was to study and assess the attachment of therapeutic and imaging agents on the surface of the self-propelled MTB as a delivery vehicle to propel and transport such payloads directly to regions being located deep in solid tumors. To meet this goal the objectives of this thesis were set as follows:

Objective 1:

Develop methods and protocols for stable covalent bonding of liposome-based drug delivery system to the MTB and investigate the effect of the liposome attachment on viability, speed and sensitivity to the magnetic field, cytotoxicity, and *in vitro* cellular uptake of the MTB-LP complex (Chapter 3 (ACS paper)).

Objective 2:

Develop MTB-magnetic iron oxide nanoparticles complexes as navigable and trackable MRI-contrast agents to visualize hypoxic regions of tumor xenograft model (Chapter 4).

Objective 3:

Within such multidisciplinary and collaborative project for the evaluation of *in vivo* targeting capabilities of the MTB complexes developed in objective 1, objective 3 consists of adopting the protocol developed during objective 1 for the attachment of SN38 encapsulated in liposomes on the MTB (MTB-LSC), preparations of the MTB-LSC for *in vivo* injection and investigate the attachment stability during navigation and distribution of MTB-LSC in tumor tissue (Chapter 5, an article under revision in Appendix A, and Appendix B).

CHAPTER 2 LITERATURE REVIEW AND BACKGROUND

The following chapter provides the comprehensive literature review and the fundamental contextual knowledge required to appropriately select materials and methods for this project. The first part of this literature review covers the current cancer therapy and characteristic of cancer microenvironment, as well as the physiological barriers that influence targeting efficacy. The second part discusses drug delivery approaches, namely magnetic drug targeting and magnetic resonance navigation using different nano/micro particles carriers. The third part presents the clinical applications of bacteria-based therapy and addresses the use of MC-1 magnetotactic bacteria as a new strategy to overcome the limitations of other types of bacteria in cancer treatment. The fourth part tackles SN38 as an anti-cancer drug and liposomes as a drug carrier. The fifth part describes the common bioconjugation techniques employed to attach nanoparticles to the surface of the MTB cells, in particular carbodiimide chemistry. Finally, the last part of this literature review discusses current clinical imaging modalities in resolving the tumor structure and the limitations of cancer visualization. The current contrast agents to improve the imaging outcomes and their drawbacks are introduced and also the motivation behind the use of superparamagnetic iron oxide nanoparticles in tumor imaging is highlighted.

2.1 Therapeutic approaches for cancer therapy

Despite the big strides in defeating many diseases, cancer is still the major cause of mortality worldwide [1]. Colorectal cancer that was our target disease in this study is the 3rd most prevalent diagnosed cancer and the 2nd leading cause of cancer-related mortality in Canada. An estimated incidence will be 25,100 (13% of all other cancer cases), and estimated deaths from colorectal cancer will be 9,300 (12% of all other cancer deaths) in 2015 [1].

Current cancer treatments can be categorized into main strategies including surgery, radiation therapy, and chemotherapy. Surgery is an invasive curative treatment option that removes the tumor completely with part of the healthy tissue around it [41]. Complications are arising from the location or the size of the tumor, the potential risk of host-pathogen interactions, metastasis, and damage to the healthy tissue. Radiation therapy uses high dose of ionizing radiation and radioactive substances that can travel all over the body and cause severe side effects. Radiation

beam lacks specificity and damaging all the normal and cancerous cells in its path. Moreover, cancer cells placed in hypoxic oxygen-deficient regions of a tumor are known to be resistant to both chemotherapy and radiotherapy [14, 42]. Chemotherapy suffers from non-specific distributions, unfavorable pharmacokinetic, and the systemic side effects that often narrows therapeutic indices. To reach an effective anti-cancer drug dose often requires dangerously high concentrations, which can lead to adverse side effects, organ failure, developed drug resistance, and unsustainable drug levels. Moreover, after extravasation from leaky tumor vessels, the drugs often get stuck to the cellular barriers and are unable to reach the inaccessible side of tumors. Therefore, quiescent cells in hypoxic regions located distantly far from the vasculature are hardly affected by chemotherapy [13]. In some cases, effective treatment requires integration of different methods to improve the therapeutic indices [43, 44]. Thus, the use of an active transport carrier to improve therapeutic benefits by delivering therapeutic agents directly to the tumor site, protecting the healthy cells from systemic drug exposure, as well as optimizing the required dose of therapeutic agents is beneficial.

2.2 Tumor microenvironment and physiological barriers

In order to provide a feel about the need for a sufficiently high binding force for the attachment approach being proposed and the obstacles that may put additional stress on the attachment method, knowledge about the physiological barriers that agents encounter as well as the microenvironment in which the carrier must operate is required. Several key differences exist between the microenvironment of tumors and that of normal tissues. The microenvironment in solid tumors is characterized by a highly defective leaky vascularized surface, hypoxic intermediate regions, and a necrotic core (Figure 2.1). Other characteristics include inadequate and heterogeneous perfusion, hyper-permeable and irregularly shaped angiogenesis capillaries, inhomogeneous and inefficient blood supply, acidic extracellular pH, increased interstitial pressure, and nutrient deprivation. Tumors are also notorious for their ability to evade immune system surveillance and destruction [45]. These sets of parameters affect the delivery and distribution of drugs inside the tumors, which serve as a backdrop for the various cancer treatment approaches.

2.2.1 Tumor angiogenesis

The uncontrolled and inconsistent tumor angiogenesis are abnormal in form and architecture, lacking smooth muscle layer, possessing poorly-aligned defective endothelial cells with wide fenestrations, and produce an inefficient blood flow pattern (Figure 2.1). Thereby, tumor angiogenesis cannot prevent large particles in the blood from leaking out of the vessel. The pore cutoff size is observed to range from 0.38 to 2 μm in chaotic tumor vessel walls [46]. Accordingly, intravenously administered particles and macromolecules of certain sizes with molecular mass < 160,000 kDa [47] tend to extravasate the tumor vasculature and accumulate in tumor sites through the enhanced permeability and retention (EPR) effect [48]. Yuan *et al.* demonstrated the transvascular transport of fluorescent liposomes resulted in heterogeneous accumulation in the tumor regions [49]. Conventional chemotherapeutics affects only the cells in well-oxygenated regions (normoxia) near the blood vasculature while the effectiveness of conventional cancer therapies in hard-to-treat hypoxic regions is consequently limited [7, 12].

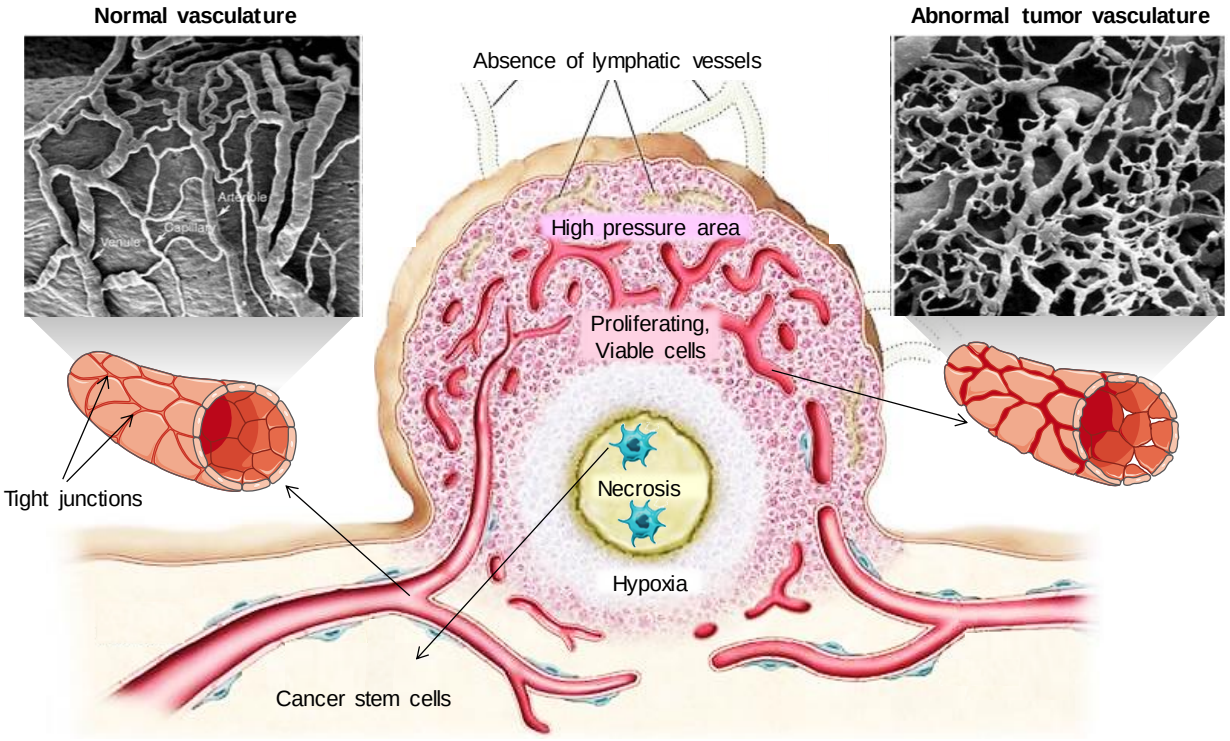

Figure 2.1: Cross-section of a solid tumor including the outer proliferating zone with the well-developed vascular network and high oxygen level, the hypoxic area, and the necrotic region. Adapted from [50]. SEM images compare the regulated and homogenous normal vasculature (top left) with the irregular angiogenic tumor blood vessels (top right). Adapted from [51].

2.2.2 Intratumoral transportation in tumor

The main physiological barriers that block the intratumoral diffusion of macromolecules after extravasation cross the vasculature and before reaching tumor cells are as below:

2.2.2.1 Tumor extracellular matrix (ECM)

The ECM in tumor tissue functions as a sink that decreases anti-cancer drug penetration and creates concentration gradients. This matrix contains a dense and thick network of collagen fibers (Figure 2.2), which imparts it more rigidity in comparison with normal loose connective tissue. Moreover, tumors exert greater tension between fibers due to an increased number of fibroblasts that connect to the collagen fibers in an integrin-dependent manner [12]. The tumor microenvironment is typically composed of vasculature, ECM, matrix-associated cells, signaling molecules, and tumor-infiltrating stromal cells (*e.g.* macrophages, cancer-associated fibroblasts, monocytes, neutrophils, dendritic cells, endothelial cells, platelets) [3, 44].

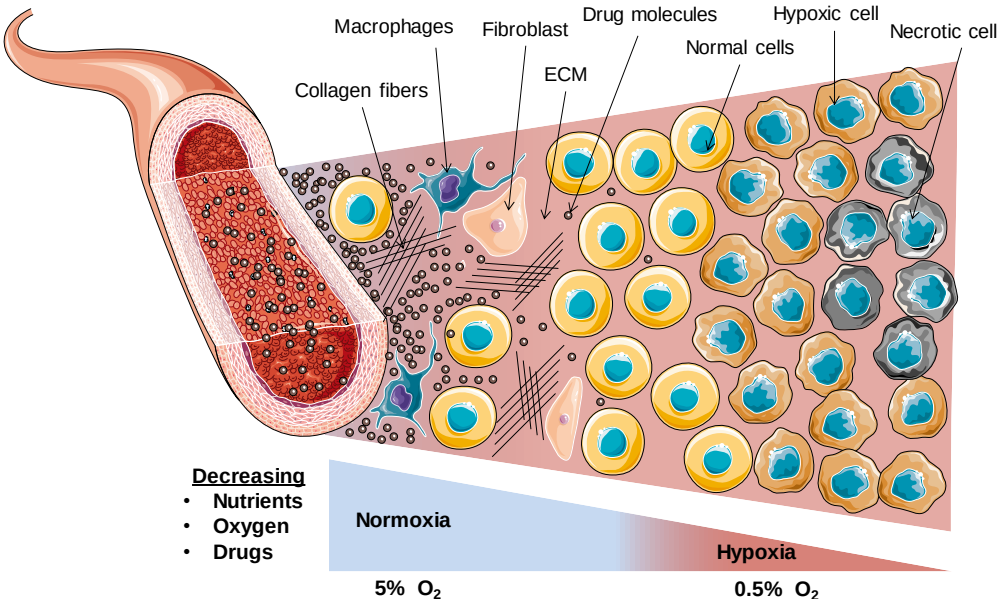

Figure 2.2: Schematic presenting the main microenvironments of a tumor. Diagram is showing the drug, oxygen, nutrients and energy concentration gradient in tumor.

2.2.2.2 Tumor cell junctions

Around 90% of solid tumors have an epithelial origin with characteristics of intercellular junctions including tight junctions, desmosomes and adherens junctions (zonula adherens) [52,

53]. These junctions act as a barrier that restricts ions, particles and macromolecules with a molecular weight of > 400 Da from passing through the paracellular space [3, 52, 53]. Knowing that the most conventional chemotherapy drugs have a molecular weight of greater than 400 Da (*e.g.* Irinotecan and Paclitaxel have a molecular weight of 586.7 and 856.9 Da, respectively), it is not surprising to see the moderate outcomes of this treatment. Similarly, the commonly used nanoparticle-based chemotherapy drugs have a size of approximately larger than 100 nm, which hinder them to penetrate into tumor and accumulate around the leaky vessels [19]. For instance, albumin-paclitaxel (Abraxane) and liposome-doxorubicin (Doxil) as FDA-approved nanoparticle-based drug delivery systems have an average diameter of 130 and 90 nm, respectively, which preferentially accumulate in solid tumors by the EPR effect without deep penetration [19].

2.2.2.3 Tumor interstitial fluid pressure (TIFP)

Rapid tumor cell proliferation, lack of lymphatic drainage, abnormal capillaries, and increased number of inflammatory cells that enhances the release of cytokines and growth factors, cause inefficient removal of interstitial fluid and soluble proteins. This generates an increase in outward fluid pressure, resulting in TIFP enhancement [54]. Due to the high interstitial fluid gradient from the center of the tumor to the periphery, passive molecules and particles usually sit at the rim of the tumor without penetrating. Therefore, hypoxic and necrotic tissues are located in high-pressure regions, which greatly minimizes chemotherapy and radiotherapy effects in those regions [42]. Jain *et al*. assessed the outward fluid velocity to be 0.1-0.2 μm s^{-1} at the periphery of 1 cm of tissue-isolated tumor [55] in which the molecules need to overcome this outward fluid motion to be able to reach the tumor interior.

2.2.3 Tumor hypoxia

An important instigator of hypoxia is unregulated and leaky angiogenesis coupled with the ineffective delivery of oxygen and other nutrients to rapidly proliferating cells. Oxygen concentration which is maximal at the angiogenic zone decreases to less than 0.7% at the angiogenic-hypoxic transition zone, and declines gradually to around zero at the anoxic area beyond hypoxic-necrotic boundaries. The hypoxic-angiogenic transition zone shows low blood flow toward the center of the tumor caused by the TIFP. As presented in Figure 2.3, the hypoxic microenvironment of tumors is often associated with an aggressive tumor behavior and increased

resistance to radiotherapy and chemotherapy compared to well-vascularized oxygenated regions [7, 13]. Main strategies to target and treat tumor hypoxia are including targeting endogenous associated hypoxia-related molecular markers (*e.g.* Hypoxia-inducible Factor 1 (HIF-1), Carbonic anhydrase IX, and osteopontin) [15, 56], modifying the extracellular matrix to increase drug penetration [12], reducing tumor pressure [18], increase drug penetration using a multistage nanoparticle delivery system [19], using the bio-reductive prodrugs [16, 17].

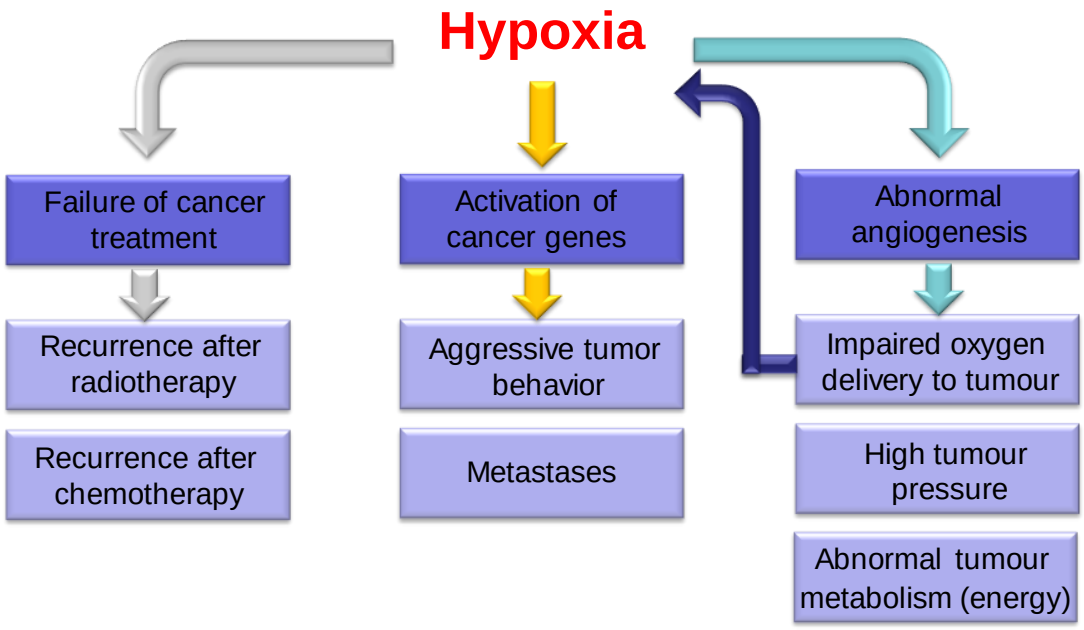

Figure 2.3: Diagram depiction of hypoxic tumor microenvironment linked to failure of cancer treatment and aggressive tumor behavior.

2.3 Targeted cancer therapy strategies

The efficiency of systemic therapies relies on transporting pharmaceutical agents to the tumor in sufficient quantity. For this purpose, the active agent has to reach the main blood vessels that feed the tumor, extravagate in the interstitial space, and then migrate into the tumor tissue in order to be in direct contact with the targeted cells [11]. Development of passive or active tumor targeting systems helps to enhance the efficacy of therapeutic or diagnostic agent's delivery to cancer cells that can be achieved by particulate-based drug formulation (*e.g.* liposome, polymers, and dendrimer) [37, 38], by chemoembolization [57], or by magnetic navigation [58, 59].

2.3.1 Passive targeting

Many tumors have hyper permeable vasculature (pores size of 0.38 to 2 μm) [46, 60] that provides an effective means for passive targeting of particles or macromolecules to extravasate at tumor sites due to the EPR effect (Figure 2.4a). The drug could be released in the extracellular matrix and diffuse throughout the tissue [11, 49, 61]. The particle size, charge, and surface coating alter the passive targeting efficacy and also dictate their clearance rates [62]. For instance, particles larger than 2 μm are more likely to be phagocytosed by macrophages, while particles smaller than 6 nm are readily cleared by renal filtration [63].

2.3.2 Active targeting

An interesting feature of the drug-loaded particles is the ability to decorate their surface with high affinity targeting moieties (such as peptides, antibodies, proteins) that selectively recognize and bind to the specific overexpressed receptor in cancer cells that are lacking in normal tissues [39, 40]. As such, active targeting contributes to cellular internalization through receptor-mediated endocytosis, thereby can improve delivery efficiency of the agents to a specific location and achieve the desired therapeutic effects (Figure 2.4b). A major concern of active targeted therapy is that, upon arrival at tumor sites, the ligand conjugated particles tightly attach to the tumor cells receptors proximal to vessels, thus preventing drug penetration deep into the tissue, which is referred to as the binding-site barriers effect.

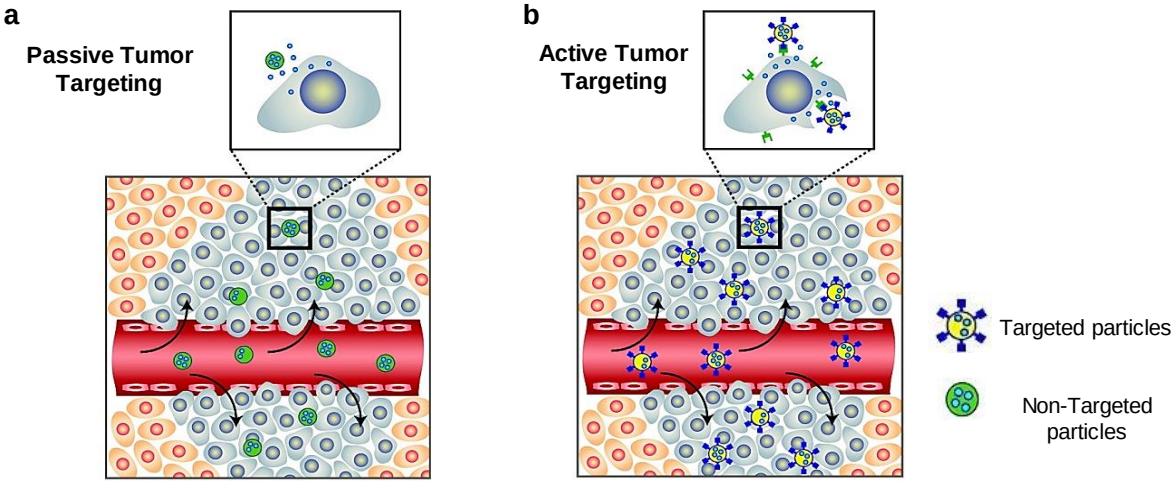

Figure 2.4: Accumulation of nanocarriers in solid tumor by (**a**) passive and (**b**) active targeting. Both types of targeted and non-targeted particles reach cancer cell through the broken vessel, and preferentially extravasated through the EPR effect. Adapted from [39].

2.3.3 Magnetic targeting

To transport therapeutic agents to a target site, appropriate steering delivery systems is required that could be achieved with magnetic targeting methods including MDT and MRN [59, 64]. Current magnetic targeting consists of encapsulating therapeutic agents inside liposomes or polymeric-magnetic particles hybrids and guiding them to concentrate drugs at the tumor site using an external magnet [58, 59] or using the gradient coils of an MRI system [20, 65]. Implementation of MDT depends on external electro- or permanent magnets placed near the disease site, while a catheter is typically used to release the agents closer to the target (Figure 2.5). By using an external magnet, the magnetic field strength decays extensively with distance, yielding suboptimal performance when the tumor is located deeper in the body. Due to the higher magnetic gradient intensity towards the external magnet, targeting efficacy is higher for tumors within the vicinity of the magnet [32].

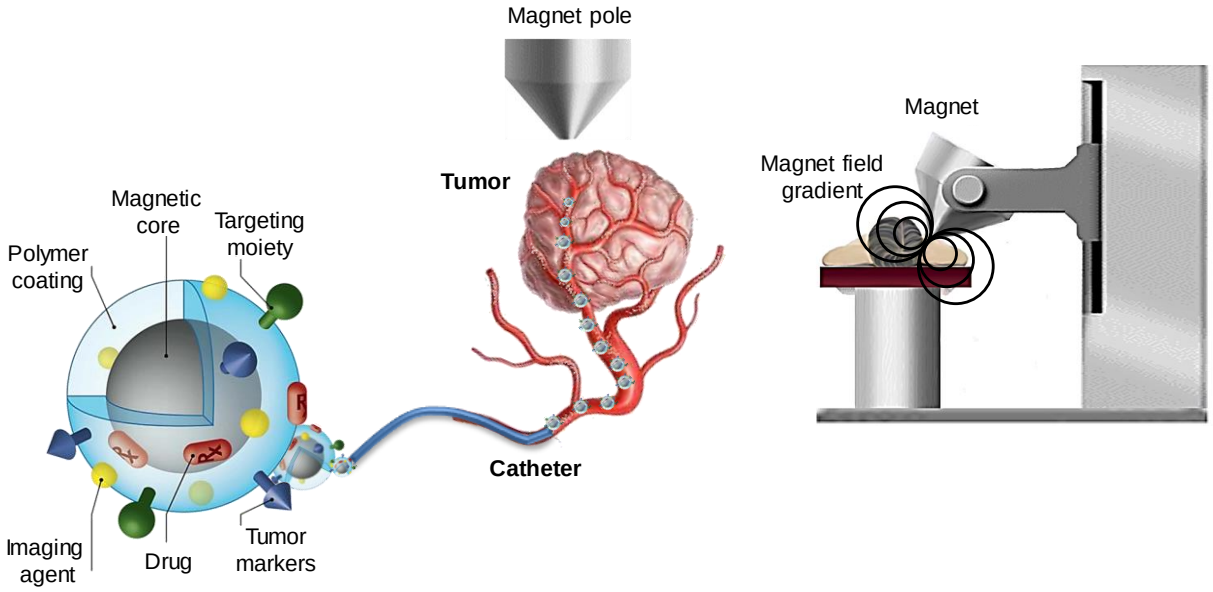

Figure 2.5: Schematic illustration of the principle of magnetic drug targeting. Magnetic nanoparticles loaded with pharmaceutical agents are delivered intra-arterially via a catheter into the arterial supply of the tumor. Applied external magnetic field accumulates and retains the particles at the targeted site.

The depth independent MRN technique has been developed for navigation of an untethered device in tumors located deep in the body using an MRI for improving the targeting efficacy

therapeutics [66]. The MRN relies on an induced 3D directional magnetic propulsion force on a magnetic carrier, generated by three orthogonal gradient coils placed inside a conventional MRI scanner [67, 68]. The efficiency of magnetic targeting toward the tumor is limited due to the lack of navigational control over the pre-planned trajectory combined with architecture microvascular networks in the tumor, as well as the limitations that inducing sufficient force on smaller magnetic carriers capable of transiting past the arterioles to reach capillary level [20, 32]. Tamaz *et al*. (2008) showed the feasibility of the magnetic targeting technique in a living swine by releasing microparticles and applying steering gradients to navigate the carriers towards a certain capillary where the tumor was located [69]. Martel *et al*. (2009) reported on the use of MRN system for applying a magnetic force on magnetized magnetic microparticles in the presence of a magnetic gradient, and directed them in the main vascular system of a live pig [70]. MRN combined with chemoembolization represents a significant advance in MRI-based navigation of untethered micro devices to a targeted area [65]. Pouponneau *et al.* (2014) showed the simultaneous steering and real-time tracking of the doxorubicin and magnetic FeCo nanoparticle both embedded in polymeric microparticle of 50 μm through a single bifurcation of the hepatic artery to the pre-determined liver lobe in a rabbit model using a clinical MR scanner equipped with upgraded gradient coils of 400 mT m^{-1} [65, 71].

However, most of the magnetic targeting techniques can only be advanced to the arterial level, while the tumor is located at the capillary level, which causes a significant portion of the injected drug to be released into the systemic circulation. The minimum diameter to induce a propelling force on magnetic therapeutic microcarriers using magnetic gradients for efficient navigation in the vascular network is limited technologically to 40 μm. The smaller particle size requires a higher gradient field. Therefore, the specifications of current MDT and MRN strategies are well beyond today's technological limits.

2.4 Microrobotics

Micro-robotics has found application in surgery, detection of cancer, and targeted drug delivery [36, 72]. Among them, self-propelled robotic devices that enable to penetrate into the tumor tissue are particularly of interest, since they can improve many medical tasks such as on-site delivery of imaging contrast agents [36, 73], highly localized drug delivery [74], or thermal treatment of the diseased tissues at selected sites. The major technological constraints for transportation and navigation of untethered carriers bearing therapeutic agents to reach the desired target at the capillary level and to penetrate inside tumors include a proper propulsion force and a steering system, a remotely directional control system, the miniaturization of robotic systems to the appropriate microscale size, an energy source, and their insertion in and removal from the human body [23, 24, 36]. Various ongoing research studies related to the development and application of microrobots are categorized into artificial or natural type.

2.4.1 Artificial microrobots

Kodati *et al*. (2007) attempted to reproduce the propulsion mechanism similar to aquatic species, called fish box, but the relatively large size (a few centimeters) of the device was the drawback of this approach [75]. Further, the administration of the microrobot into the body, recovery of device, the immune system response, and degradation of the robot were also the critical tasks that needed to be addressed. Moreover, a synthetic robot should not rely on an external power source to induce autonomy and propulsion force for *in vivo* applications. The approaches to compensate for their energy requirement consist of (i) miniaturizing the energy source in the form of an electric battery, (ii) incorporating the transducers for extracting energy from the environment (*e.g.* chemical energy, temperature differences, and vibrations) and then converting into electrical energy [76], and (iii) using an external energy source such as gradient magnetic fields to provide required power by magnetic induction [70] or optical source such as laser to control the direction of the device, which is depth-dependent with limited penetration into biological tissues [77]. However, these techniques are presently beyond the limit of current engineering knowledge and face many technological challenges, such as large size and/or non-autonomous characteristics that remain elusive.

2.4.2 Natural and artificial bacterial-based microrobots

Over the last few years, microorganisms such as motile bacteria have been considered as micro-actuators in engineered microdevices to overcome the scaling limitation and miniature source of power. Most biological microorganisms moving by the organelle called flagella that act as a nanomotor, have inspired many researchers to artificially design the propulsion mechanism and fabricate an artificial microrobot. Figure 2.6a shows an artificial bacterial flagellum (ABF) microrobot similar to the natural magnetic bacteria, which is composed of a helical tail (resembling a natural flagellum) responsible for the bacterial motion through its spinning and a soft-magnetic metal head [23]. The direction of helical motion and the velocity of the ABFs are controlled wirelessly using an external low-strength alternating magnetic field that induce a magnetic moment on a magnetized body and generates a torque on their magnetic head [23, 24]. Despite the enormous potential and development, the use of ABF devices for targeting and delivery applications is still at the theoretical stage and the technology is not mature enough due to their constraints such as non-autonomous characteristics and a lack of precise navigation.

Several research groups have exploited naturally available bacteria to be used as a prefabricated microrobot. These investigations demonstrated that many types of bacteria have similar characteristics as a desirable microrobot in terms of appropriate size, self-propulsion (using flagella), self-powering, and ability to remotely control their directional movement due to their chemotaxis, magnetotaxis, aerotaxis, and phototaxis behavior [33, 36, 78]. The bacteria have been used for various applications such as magnetic separation of material in liquid environments [79], for cancer therapy application [27, 80], engineered micro-systems such as in micro-rotary motors [81], and propel or transport micro-objects (Figure 2.6b) [82, 83].

Figure 2.6c shows the microstructure of the flagella motor, which is driven by a rotary engine and powered by flow of hydrogen ions (protons) across the bacteria cell membrane. This self-powered rotary engine is notably attractive in those applications where the availability of electrical power is restricted, as it is often the case for miniature untethered artificial robots. The molecular rotor embedded in flagella alone can operate at 6,000 to 17,000 rpm by crossing less than 300 hydrogen atoms. However, with the flagellar filament as a propeller attached to the rotor, the rotation usually reaches only 200 to 1000 rpm based on the type of the bacteria.

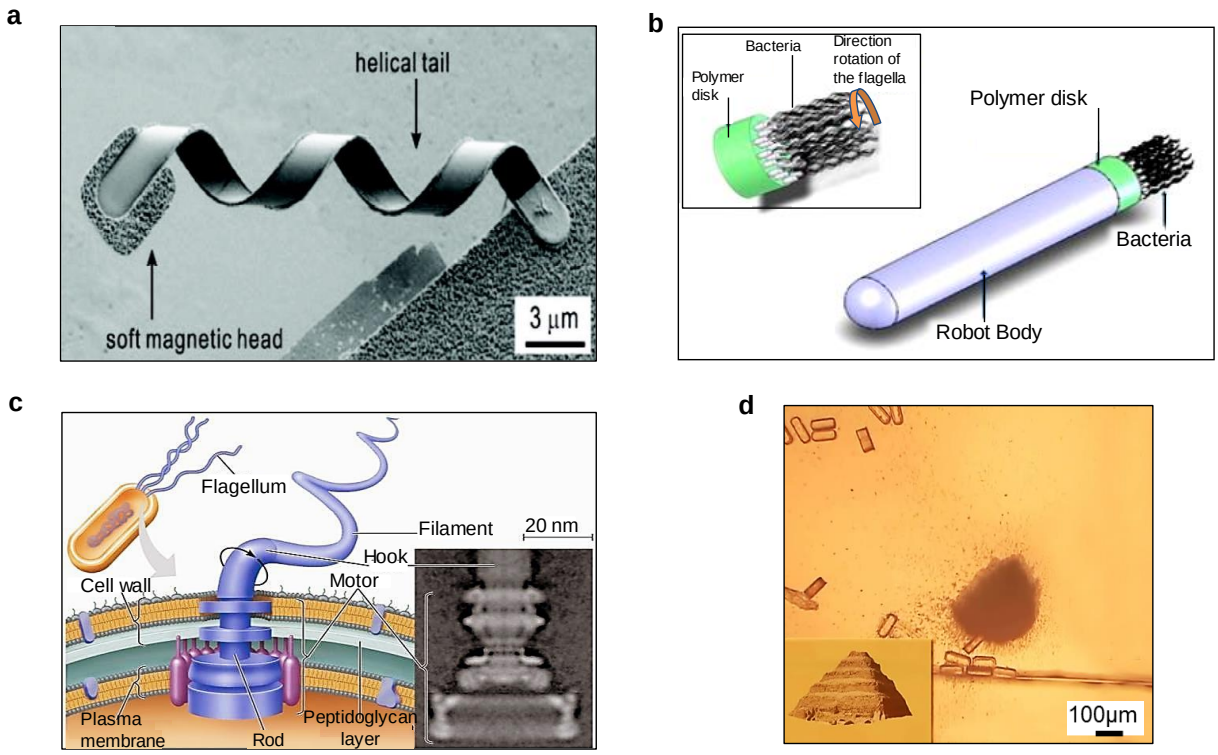

Figure 2.6: (**a**) SEM micrograph of artificial bacteria with a diameter of 2.8 μm composed of a helical tail and the soft-magnetic head [23]. (**b**) A scheme of a hybrid system made of several bacteria using their flagella motors as actuators to propel synthetic materials [83]. (**c**) Structure and composition of flagellar motor. (**d**) Assembly of a microscopic pyramid using a swarm of magnetotactic bacteria working in union to transport microscopic bricks [84].

Even though natural organisms can react to different stimuli by chemotaxis, phototaxis, and aerotaxis, for precision applications such as targeting solid tumors, directional magnetotaxis control can be more advantageous [36]. Steager *et al*. (2007) proved that several flagellated bacteria can be used to move a larger microstructure using phototaxis [85]. However, the disadvantages of phototaxis for *in vivo* applications include limited penetration depth of light into the body and lack of formation and displacement control of an aggregate of bacteria within a 3D volume, which is critical in enhancing targeted drug delivery. On the other hand, chemotaxis as the most common directional system in microorganisms is not an appropriate steering control system for *in vivo* application either due to incompatibility of the technique with electronic

computers, as well as the instability of chemical environment variables, such as concentration of substances, pH, salt level, and *etc.* [78].

Flagellated magnetotactic bacteria with magnetotaxis system that can be controlled using external magnetic field are more efficient for computer-based navigation to operate in the angiogenesis networks and the tumor interstitial microenvironment [33, 36, 86]. Lee *et al*. (2004) demonstrated the controlled assembly of magnetic nanoparticles taken from magnetotactic bacteria in fluid using microelectromagnets. They showed that after lysis of the magnetically oriented bacteria, the chain of the aligned magnetic particles remained on the substrate [87]. Martel *et al*. (2006) reported the first bacterial transport application under magnetotaxis directional control along a planned trajectory [82, 88]. They also experimentally validated the ability to two-dimensionally control the *Magnetococcus Marinus* MC-1 magnetotactic bacteria. They used a single electromagnet positioned close to the bacterial solution to magnetically control a swarm of approximately 5000 MC-1 cells to assemble micro-bricks as a miniature replica of an Egyptian pyramid in less than 15 minutes (Figure 2.6d) [84, 89].

2.4.3 Bacteria in cancer therapy

Coley in 1891 accidentally discovered bacterial cancer therapy [90] that inspired many researchers to investigate various strategies to improve treatments [27, 31, 91-94]. The key characteristics of bacteria to be used for cancer therapy include: (i) the ability to swim in low Reynolds number hydrodynamics as encountered in the tumor microenvironments and human capillaries, (ii) having self-propulsion and self-powered properties, (iii) specifically target, accumulate, and proliferate inside solid tumor regions, (iv) having sensory apparatus allowing them to respond to external signals and/or internal stimuli in the tumor microenvironment, (v) producing toxins that can lyse and destruct tumor tissue, and (vi) generating externally detectable signals [26, 27, 31, 92].

The *Clostridia* [25, 26], *Salmonella* [27-29] and *Bifidobacterium* [30] strains are the most commonly used bacteria that are considered as potential candidates to naturally penetrate deep region and accumulate preferentially in the hypoxic regions. Investigations on animal models showed that following intravenous administration, *Salmonella* can enter the tumor via broken vessels. Subsequently, due to an appropriate environment for their proliferation in the tumor transition zone, the *Salmonella* can colonize and induce apoptosis [27, 29]. The bacteria can be

used as carriers for gene therapy or genetically be modified to express certain genes that induce antitumor effects [25, 91, 94]. They can also act as a carrier to deliver therapeutic agents [26]. Figure 2.7 illustrates some strategies for fighting cancer using bacteria-based technology [95].

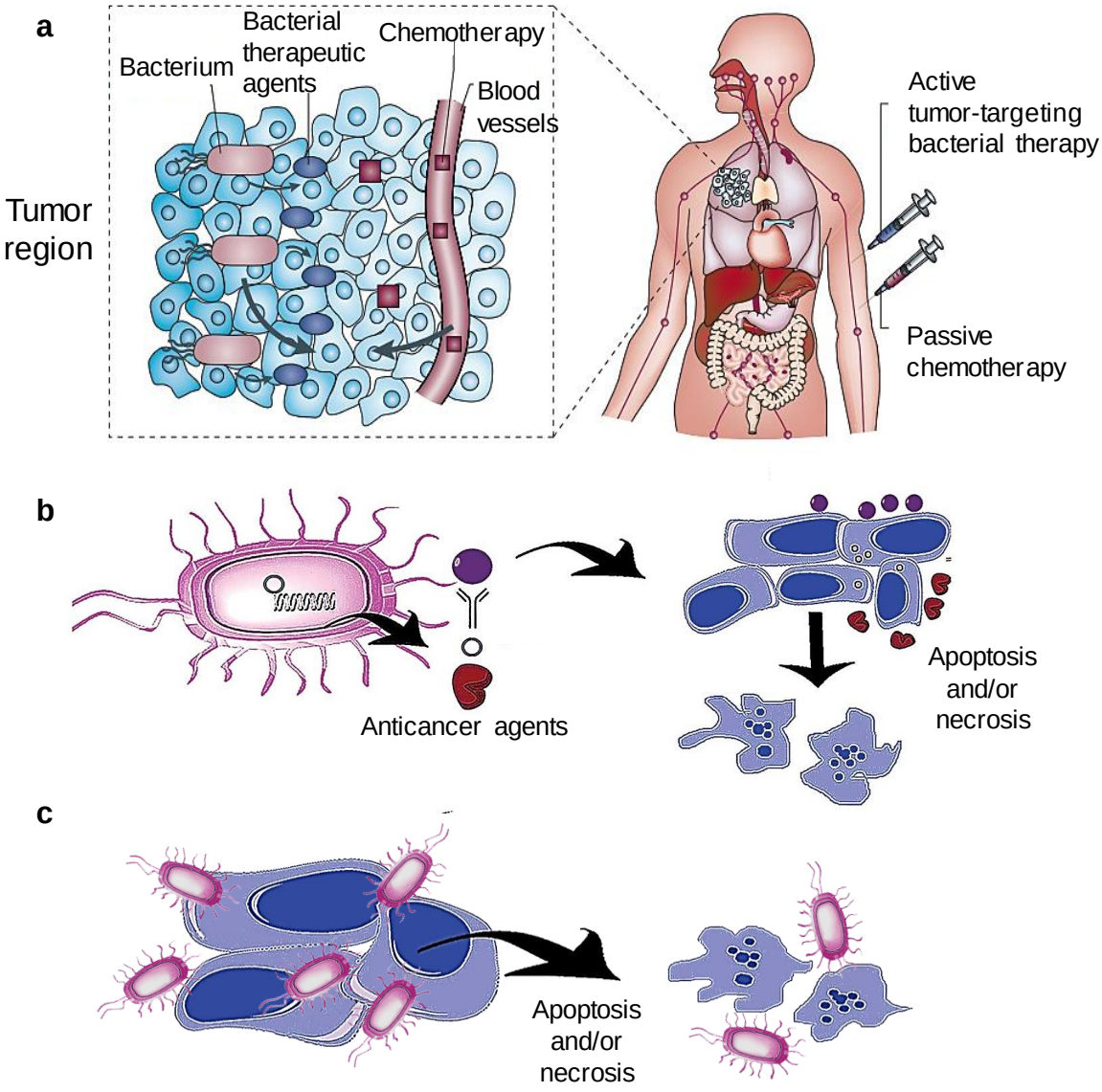

Figure 2.7: Schematic illustrating the strategies for bacterial-cancer therapy. (**a**) The aerotactic bacteria extravasate through leaky vessels, accumulate into the hypoxic/necrotic regions, and proliferate to kill the cancer cells. (**b**) The bacteria can be engineered as carrier for anti-cancer agents such as cytotoxic drugs, anti-angiogenic agents, cytokines, antibodies, enzymes. (**c**) After accumulation in hypoxic regions, the bacteria can multiply and act as oncolytic agents to cause rupture of cancer cells. Reproduced from [95].

2.4.3.1 Bacteria in combination with conventional cancer therapy techniques

Despite the tremendous research on the bacteria in cancer therapy, the technique still faces many drawbacks and unexplored challenges before it becomes clinically effective. For instance, a high dose is required to induce a significant therapeutic effect, which is often associated with the severe toxic side effects of bacteria. Moreover, the absence of hypoxic regions at an early tumor stage can significantly reduce the efficacy of intravenously injected anaerobic bacteria to target, colonize, and produce toxins in the central regions of solid tumors [94, 95]. For instance, phase I clinical trials using a genetically modified anaerobe *Salmonella typhimurium* (VNP20009) for targeting small tumors that lacked a necrotic zone, indicated that tumor colonization of bacteria can be achieved at very high dose but without providing any antitumor effects [96].

Anaerobic bacteria mostly accumulate and affect the hypoxic and necrotic cells while the living cancerous cells remain intact. On the other hand, chemotherapy and radiation therapy are limited to destroy the cells within hypoxic and necrotic regions. To improve the outcomes of such a treatment, a combination of bacterial therapy and conventional cancer treatment such as chemotherapy and radiotherapy, so-called “combination bacteriolytic therapy” (COBALT) was suggested [97]. For instance, *C. novyi* bacteria have been investigated in combination with radiotherapy agents [92]. Cheong *et al.* (2006) showed that the bacteria enhance the release of drugs-encapsulated liposome into the necrotic region of the tumor by cell membrane-disrupting properties of bacteria protein [98]. However, these types of bacteria can reach and accumulate in tumor lesions by means of chemotaxis or aerotaxis [27, 28] that are not compatible with computer-assisted navigation. Therefore, magnetotactic bacteria are proposed as potential remotely computer-controllable living microorganisms to transport drugs to solid tumors.

2.4.4 Proper characteristics of magnetotactic bacteria for *in vivo* applications

Since discovery of magnetotactic bacteria by Blackmore in 1975 [99], their utilization is continually increasing in numerous applications, such as MRI contrast agents [80] and drug-targeting vehicles for cancer treatment [100]. The use of live magnetotactic bacteria as a controllable microdevice compared to isolated magnetosomes, self-propelled micro-jets and synthetic nanoparticles presents some important advantages [32, 101, 102]. Magnetotactic bacteria are flagellated microorganisms that optimizing their movements in their natural environment using the Earth's magnetic field due to the presence of an embedded chain of

magnetic nanoparticles, called magnetosomes, which are composed of iron oxide (Fe_3O_4) or iron sulfide (Fe_3S_4). Their swimming direction can be controlled through a computer interface using magnetic coils or magnets that forces the chain of magnetosomes to align along with applied external magnetic field. Despite the existence of various types of magnetotactic bacteria [33, 86], only a few of them are suitable for *in vivo* drug delivery application. Table 2.1 summarizes the characteristic of several morphotypes of magnetotactic bacteria with various dimensions, morphology, and swimming velocities [32]. High swimming velocity and small size are the key features of the appropriate magnetic bacteria for *in vivo* applications. The smaller size enable the bacteria to more easily navigate in the narrowest blood vessels and also penetrate deep in the tissue, but it may cost slower swimming speeds (*e.g.* MV-4, ~0.5 μm, ~30-80 μm s^{-1}). Most of the magnetotactic spirilla show the slowest velocity of < 100 μm s^{-1}. In general, a speed of > 100 μm s^{-1} (most of magnetotactic cocci) with a size of < 2 μm is preferred. Therefore, the polar MC-1 MTB with the average size of 1-2 μm and the velocity of 200-300 μm s^{-1} appears to be a potential candidate for drug targeting applications to invade and access the tumor regions [32, 36, 103].

Table 2.1: Features of some of the magnetotactic bacteria. Reproduced from [32].

MTB Name	**Cell morphology**	**Mean speed (μm s^{-1})**	**Width (or diameter) (μm)**	**Length (μm)**
MC-1	Spherical (Coccoid)	200	2	2
MMP(many called magnetotactic bacteria)	Sphere (a cluster of 10-30 coccoid cells	105	3-12	-
Magnetospirillum gryphiswaldense	Spirillum (Helical)	50	0.2-0.7	1-20
AMB-1	Spirillum (Helical)	49	0.5	3-10
Magnetobacterium bavaricum	Rod-shaped	40	1-1.5	6-9
Magnetospirillum magnetotacticum (MS-1)	Spirillum (Helical)	40	0.5	5

2.4.5 *Magnetococcus Marinus* MC-1 magnetotactic bacteria

As proposed by Martel *et al*. (2009), flagellated *Magnetococcus Marinus* MC-1 magnetotactic bacterium can provide the main characteristics required for delivery of therapeutic agents into inaccessible tumor regions [36]. As can be observed in Figure 2.8, the MC-1 MTB cells have a spherical shape 1-2 μm in diameter, which gives them the ability to extravasate through the leaky tumor blood vessels with pores size of 0.38 to 2 μm [46, 60]. Moreover, the appropriate size of the cells provides a maximum surface area with which to attach nanoscale components. The MC-1 MTB cells can act as microrobots with a directional autonomous propulsion system which is produced by two bundles of nine flagella on one side (polar bacteria). The flagella provide a propelling force of ~4 pN that can be very effective when operating in low Reynolds number hydrodynamic conditions, such as in the smallest blood vessels and tumor microenvironment [104]. This value is relatively greater than most of the other flagellated bacteria with a typical thrust force in the range of 0.3-0.5 pN. The flagella provide the average swimming speed of 200 μm s^{-1} at room temperature.

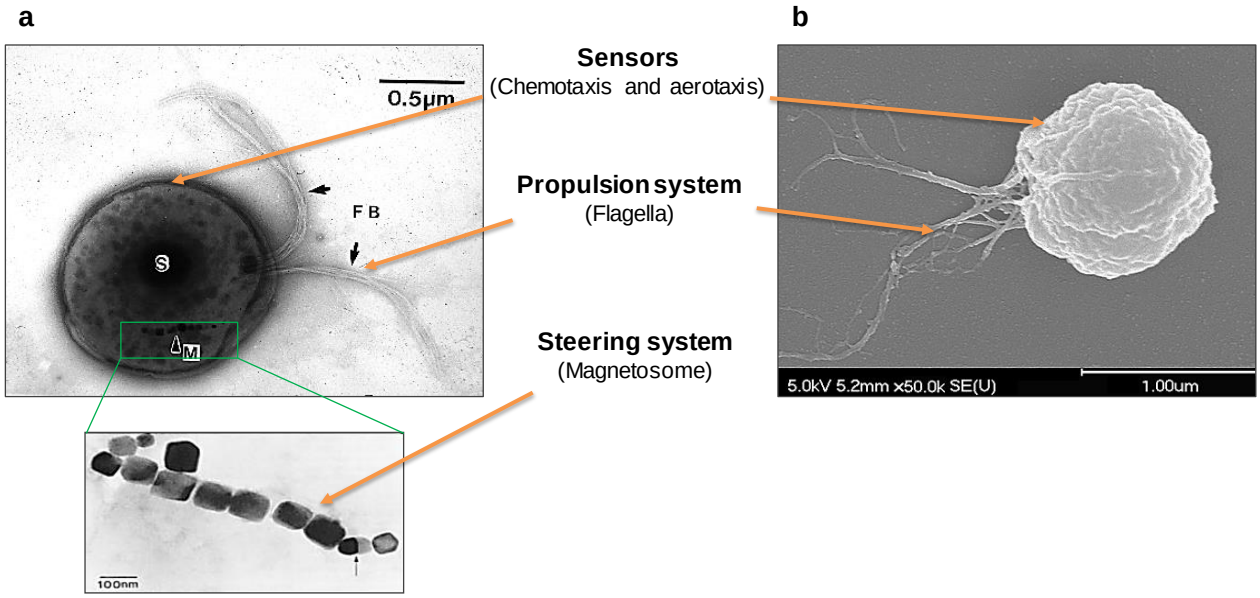

Figure 2.8: (**a**) TEM [33] and (**b**) SEM photographs of a MC-1 MTB cell as a microrobot with the main sensor and actuator components required for carrying therapeutics deep inside solid tumors. The images show the two bundles of flagella as propulsion system (a, b) and the single chain of magnetosomes with the size ranging from 30 to 80 nm as steering system.

As shown in Figure 2.8a, the single magnetosome chain of MC-1 MTB cell is composed of 10-15 membrane-based single domain magnetite (Fe_3O_4) nanoparticles ranging from 30 to 80 nm. From an engineering perspective, the MC-1 MTB cell can be considered as a microrobot due to the fact that it possesses an embedded remote control interface, an efficient molecular motor as well as, and sensory and actuation capabilities.

As shown in Figure 2.9, once the MC-1 MTB cell is exposed to an external directional magnetic field slightly higher than the Earth's geomagnetic field, the magnetized chain provides the magnetic dipole moment (m). The MC-1 MTB cells have the magnetic moment of approximately 10^{-15} Am^2 (or J T^{-1}), which enables them to react to magnetic fields as low as 50 μT (5×10^{-20} J) [86]. The magnetic torque is exerted on the chain when there is an angle (θ) between the magnetic dipole of the chain and the applied magnetic field (B) [103, 105, 106]. The induced torque can result in the chain acting like a compass and aligns the MTB cells along the magnetic field through magnetotaxis [73, 88]. This magnetotaxis phenomenon allows the MTB cells to navigate efficiently while locating and maintaining an optimal position in chemical gradients (*e.g.*, oxygen and nutrition) in its natural environment using the Earth's geomagnetic field lines [33, 86].

The sensitivity of a MTB cells to the applied magnetic field is influenced by their magnetic moment, which is in turn given by the properties of its magnetosomes chain, and more specifically, the number of nanoparticles and their size. The Fe_3O_4 nanoparticles inside the MTB are arranged in chain form in order to maximize the magnetic moment of the bacteria. Naturally, the MC-1 MTB move in response to the earth's magnetic field toward oxic-anoxic transition zone (OATZ) where oxygen concentrations is preferred by the MC-1 cells (~1-2% O_2), which is called magneto-aerotaxis behavior [33]. These characteristics become very important for using MTB for control purposes for *in vivo* drug delivery into tumor microenvironments and hypoxic regions in which the overall swimming direction of the polar MC-1 MTB is influenced by magnetotaxis in conjunction with aerotaxis, and causes the bacteria react according to a balance of these stimuli.

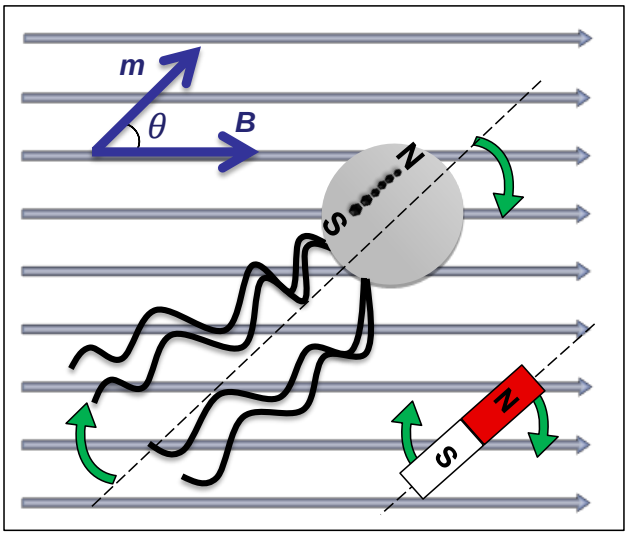

Figure 2.9: Schematic illustration of the induced magnetic moment on magnetosome chain of the polar MC-1 MTB in a homogenous magnetic field. *m* represents the magnetic moment of a MTB, *B* represents the external field, and θ is the angle between them [106].

2.4.5.1 MC-1 MTB *versus* magnetic particle

From the microrobotic point-of-view, appropriate size, high velocity, and self-propulsion force are important factors for targeted delivery to tumor regions. In comparison with the small magnetic bacteria with high swimming velocity (*e.g.* MC-1, MV-1, MV-2 and MS-1), magnetite particles with the same size require a much higher magnetic field to reach the same magnetophoretic velocity. Directional control of the magnetic bacteria is possible using a weak directional magnetic field (slightly higher than the earth's geomagnetic field) instead of tens to hundreds of thousands times higher field required for any other magnetic targeting methods. In addition, in MTBs, the propulsion force is provided by two bundles of flagella instead of an induced force generated from an external source. For instance, to make a comparison between the magnetic microcarriers and MC-1 MTB with the same size (2 μm) at the same velocity (200 μm s^{-1}), bacteria are indeed subjected to a much weaker magnetic field (< 10 Gauss) than the magnetic carrier (7.6×10^3 mT m^{-1}) [32], which is well above the threshold for clinical practices [68].

Even though live MTB looks promising as a mean of enhancing tumor targeting efficacy and possibility to penetrate deep as compared to magnetic particles targeting using MDT and MRN

techniques [20-22], but it still faces certain limitations when traveling through the blood stream. The maximum diameter of carrier should be approximately half of the diameter of the smallest capillaries (~4 μm, velocity of < 300 μm s^{-1}) and reach a propelling force of at around 4 pN [32, 36, 100]. Moreover, since the size of the openings in the leaky tumor vessels are typically < 2 μm [46, 60], it emphasizes the need to maintain the maximum diameter of navigable agent below 2 μm. Although the molecular motor of MC-1 MTB is much more effective when operating in the microvasculature and in the tumors environment than any other known technologies [36, 107], they are far less efficient in larger blood vessels due to high blood flows. They cannot theoretically be controlled at turbulent motion of fluidic and become disoriented by flow.

Therefore, an intravenous or intra-arterial administration as typically performed in chemotherapy is definitively not the best option for the MTB-based therapeutic interventions. For the flagellated bacteria using techniques such as embolization or balloon catheter to temporarily reduce the blood flow supplying the tumor may allow the navigation of the bacteria in larger blood vessels [32]. In contrast, magnetic microparticles with high saturation magnetization are more effective in larger vessels. In the case of larger magnetic particles, they must be submitted to a much lower magnetic gradient than a smaller particle (due to the volume of magnetic material) to reach the same magnetophoretic velocity. For instance, the particle with a size of 50 μm or higher needs only < 500 mT m^{-1} magnetic gradients, which is in acceptable range for targeting but not suitable for operating at the capillary level.

2.4.5.2 Magneto-aerotaxis system to navigate MC-1 MTB

Targeting the MTBs to a tumoral site to reach the dose of therapeutic agents as well as directional control of their movement requires forming a swarm aggregation of MTB within a three-dimensional volume. Felfoul and De Lanauze designed three-dimensional magnetic navigation platforms, magnetic sequences, software control systems, and physic theories for MC-1 MTB accumulation in a specific region (Figure 2.10) [103, 105, 108]. Briefly, a magnetotaxis platform containing six electromagnets is constructed with a configuration of three-axis orthogonal pairs of independent magnetic gradient coils and special time-varying sequences capable of generating a 3D magnetic field. Electric coils positioned in a Maxwell configuration and carrying equal but opposite currents. Therefore, by independently current ratio variations between the electric coils of each pair in the magnetotaxis platform, it is possible to generate a MTB aggregation and

control its position at the center of the coils. Because the field used to generate magnetic field is DC, thus it does not cause overheat, nor radiation or any known side effects on the animals. Moreover, the magnetic fields for navigation of MTB is very weak at around 10-100 Gauss (0.001-0.1 Tesla). In general, when MTB cells are subjected to a magnetic field slightly higher than 0.5 Gauss (the earth's magnetic field), the oxygen concentration appears to have no more influence on the swimming direction, and MTB direction is exclusively dependent on magnetotaxis, which is completely controllable by electronics and computers [36, 82]. 3D field can induce a torque and directional movement on the MTB to form an aggregate within a certain volume (referred to as the aggregation zone), and also to control its position and movement in a 3D space using computer software [108, 109].

The basic operation of the magnetotaxis platform is depicted in Figure 2.10. The directional magnetic field strength decreases as the distance from the coils increases (blue arrows). The magnitudes of the electrical currents circulating in the coils are adjusted to reach the region that is the outer boundary of the aggregation zone. This location corresponds to the field intensity where insufficient directional torque is induced on the chain of magnetosomes and swimming direction of MTB is not affected by field any further. An aggregation of therapeutic agent-loaded MTB occurs since any MTB exiting this 3D volumetric aggregation zone is forced to come back within the zone. This is due to a sufficient directional torque that is being induced on the chain of magnetosomes outside this zone. Inside the aggregation zone, magnetotaxis directional control is no longer possible due to a very weak directional torque being induced on the magnetosomes. Indeed, when gathered in the aggregation zone the MTB follow a continuous free circular motion. In the tumor regions, subsequently aerotaxis takes an effect with displacements of the MTB being guided by their microaerophilic behavior seeking hard-to-treat hypoxic regions of solid tumors.

It should be emphasized that for *in vivo* operations, unlike the artificial implementation or standard bacterial therapy approaches explained earlier, MC-1 MTB cannot survive or proliferate in the tumor. Their propelling force and swimming velocity decrease gradually when entering the physiological environment and they become non-motile after ~40 minutes due to the changes in their growth culture environment and higher temperature [36].Therefore, the entire *in vivo* procedure for targeting and navigation using MC-1 MTB is restricted to the short time frame in which the MTB remain active and alive.

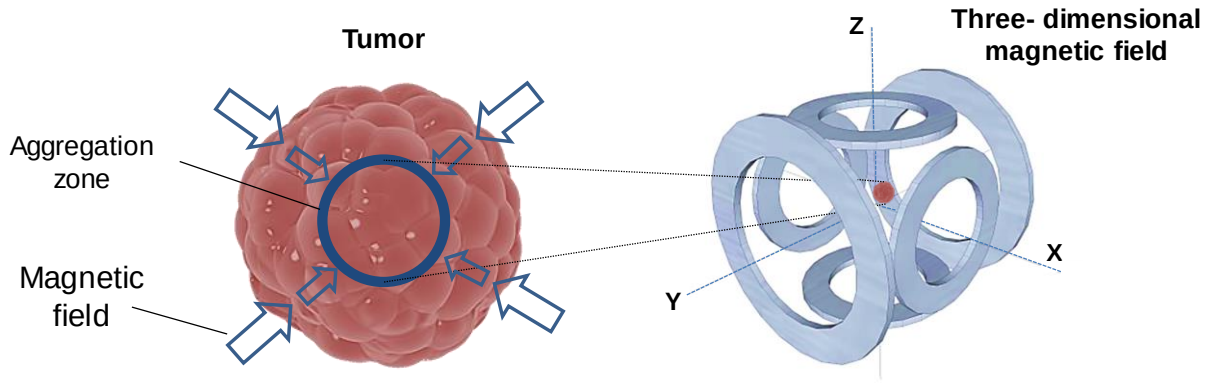

Figure 2.10: Schematic illustrating basic operational principle of the magnetotaxis system composed of three independent magnetic gradient coils aimed at exploiting the capability of the MTB micro-actuator at delivering therapeutics in the hypoxic regions of tumors [109].

2.5 SN38 as an anticancer drugs

A great numbers of efficacious drug such as cetuximab, bevacizumab, oxaliplatin, capecitabine, leucovorin, 5-fluorouracil (5-FU), and camptothecin (CPT) are available for treating colorectal cancer. A combination of 5-FU, family of irinotecan, and oxaliplatin [110] are more effective, since these drugs attack the different parts of cancer cells. Particularly, hydrophobic camptothecins such as irinotecan (CPT-11) and its active metabolite SN38 (7-Ethyl-10-hydroxycamptothecin) have been widely used for treating various types of cancer such as lung, leukemia, pancreatic, ovarian, cervix, breast, lymphoma, stomach, and the treatment of colorectal cancer [111].

2.5.1 Mechanism of CPT-11 and SN38

CPT-11 as a prodrug needs to be enzymatically hydrolyzed by hepatic and intestinal carboxylesterase to form the biologically active metabolite SN38 (Figure 2.11a). The transformation of CPT-11 yields less than 10% SN38, and extremely depends on the genetic inter-individual variability of carboxylesterase activity [112]. Variability and unpredictability metabolic conversion rates of the CPT-11 to SN38 pose significant life-threatening toxicity risks, limit the therapeutic potential of the drug, and complicate clinical management of patients. Also, SN38 in turn can be detoxified and inactivated primarily through hepatic UDP-

glucuronosyltransferase 1A1 (UGT1A1)-catalyzed glucuronidation to form SN38-G [113, 114]. SN38-G can be converted to the active form of SN38 by intestinal bacterial β-glucoronidases, which induces sever intestinal toxicity [114]. SN38-G can also be easily excreted from the body, which may lead to poorly predicted toxicity from CPT-11.

Studies demonstrated that the antitumor drug CPT and its analogues act as DNA Topoisomerase I Inhibitors [115]. This enzyme binds to DNA and relieves the torsional stress of supercoiled DNA by inducing single-strand breaks, thereby permitting cleaving and unwinding of DNA necessary for DNA replication, RNA transcription and DNA repair. Typically, in dividing tumor cells, CPT antitumor drugs and its analogues inhibit topoisomerase I activity by binding to the topoisomerase I-DNA complex (forming ternary complex) during DNA synthesis. In fact, the drug prevents topoisomerase I-mediated religation of the DNA strand and blocking the movement of the DNA polymerase along the DNA, which consequently result in double-strand DNA breakage causing in DNA damage (Figure 2.11b). Mammalian cells cannot efficiently repair these double-strand breaks, which lead to cell apoptosis [115, 116]. In non-dividing cells (such as kidney cells), the drug causes single-strand breaks in DNA, which are not lethal to the cell but lead to side effects and diseases such as systemic autoimmune [116].

2.5.2 Limitation of direct use of SN38

Direct use of SN38 has the advantage of being active metabolite and up to 1000-fold more cytotoxic than the CPT-11 parent drug. Nonetheless, SN38 suffers from the limited direct clinical application due to the insolubility and shorter biological half-life compared to CPT-11 or Topotecan [117]. In fact, the SN38 is poorly soluble in aqueous solutions (solubility in water < 5 μg ml^{-1}) and it is practically insoluble in most pharmaceutically acceptable and physiologically compatible solvents such as ethanol, polysorbate, and cremophor [118]. For its clinical use, it is therefore essential to develop a soluble form of water-insoluble SN38. Furthermore, it is a pH-sensitive drug that is rapidly converted from its active form (hydroxy lactone, closed-ring structure) to an inactive form (carboxylate, open-ring structure) at pH 7.4 and 37 °C [119].

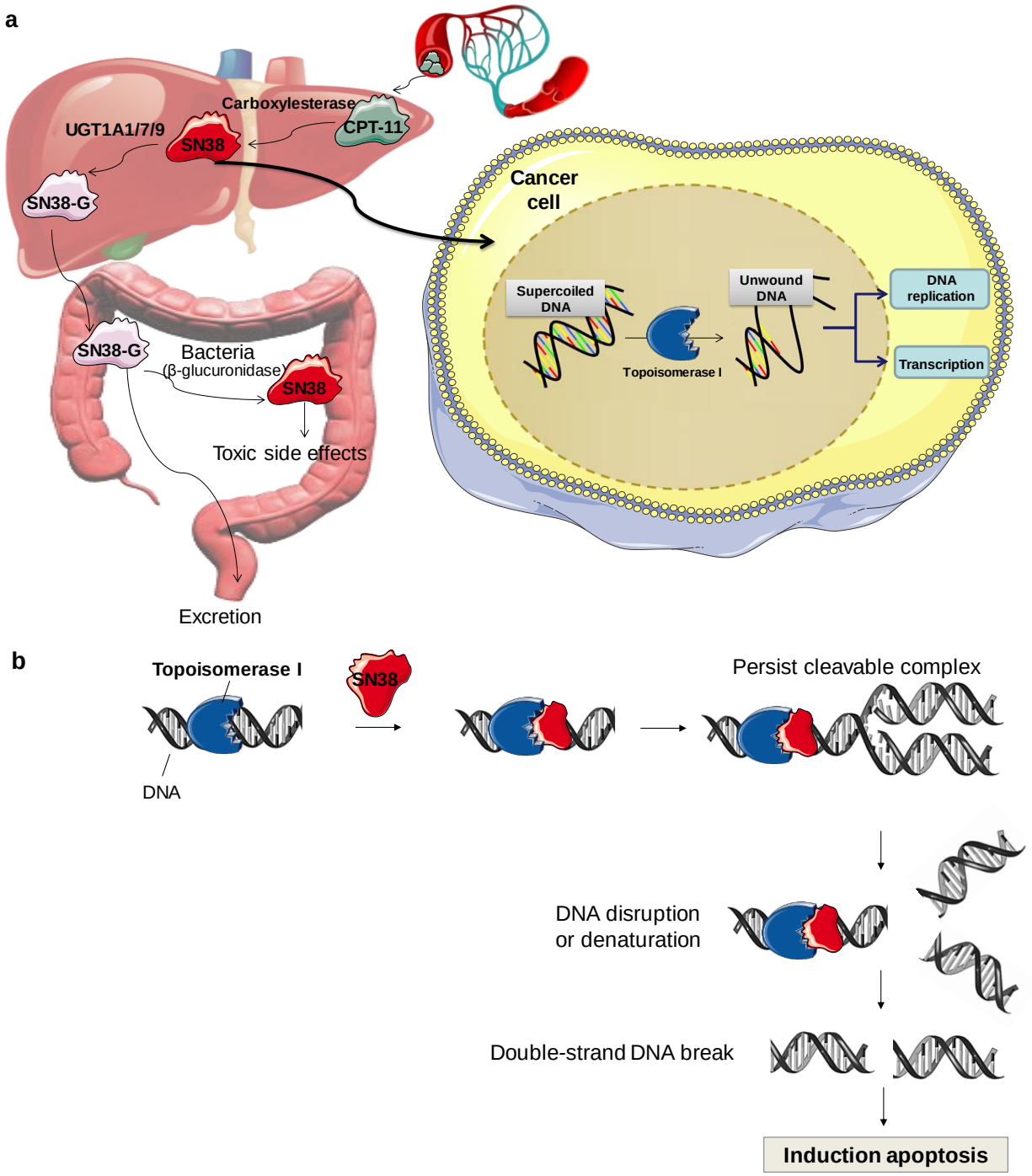

Figure 2.11: CPT-11 and SN38 activity and metabolic pathway. (**a**) CPT-11 is metabolized to the active SN38 compound by carboxylesterase in liver. UGT1A1 in the liver is associated with metabolic clearance and causes inactivation of SN38 by forming the SN38 glucuronide (SN38G). Intestinal bacteria transform SN38-G to SN38 and cause toxicity. (**b**) SN38 prevents DNA synthesis by inhibition of topoisomerase I activity and formation of double-strand DNA break, which induce DNA damage and apoptosis [116].

An acidic pH promotes the formation of the lactone ring while in basic pH lactone ring hydrolyzes rapidly and opens to the inactive carboxylate form, which results in the complete loss of biological activity. The pH-dependent equilibrium of SN38 is shown in Figure 2.12. The lactone form is an essential structural requirement for successful drug interface with the Topoisomerase I target [120]. The half-life of this conversion is about 12 min, and within 2 h, 99% of the active drug is converted to the inactive carboxylate form [121].

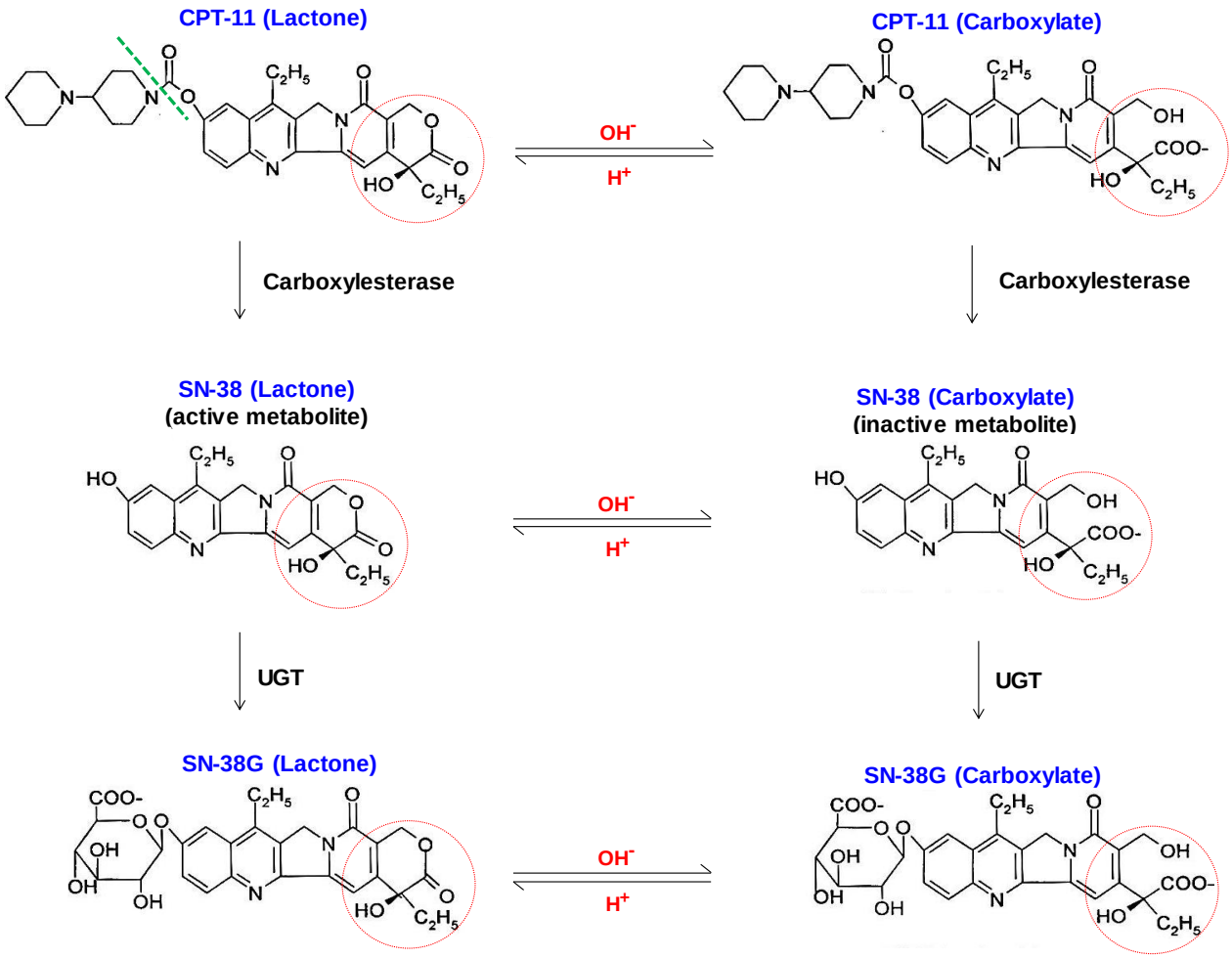

Figure 2.12: pH-dependent equilibrium of CPT-11 and SN38. An acidic pH promotes the active lactone ring while a more basic pH favors the inactive carboxylate formation [111].

To overcome the delivery concerns of SN38, two main approaches can be employed. The first method consists of a chemical modification of the SN38 structure by conjugating a cationic peptide [122] or hydrophilic functional group (*e.g.* polyethylene glycol) [123] to the drug. The second approach is to develop drug delivery vehicles that can carry SN38 either by chemical

conjugation or physical entrapment. Polymeric micelles [124], dendrimers [125], magnetic nanoparticles [126], liposomes [111, 127], and polymeric particles [128] have been used as carriers for delivery of SN38 into cancer cells and showed promising results in enhancing the solubility, protecting from rapid drug degradation, and increasing cytotoxicity against various tumor cells as compared to free SN38 [111]. Liposome holds notable promise for the delivery of active metabolite form of SN38.

2.6 Liposomal-based formulation for drug delivery applications

2.6.1 Liposome structure

Liposomes are made out of phospholipids bilayer, which own the similarity to cell membrane with the advantage of being biodegradable, biocompatible, and flexible, thus being able to pass along the smallest vessels without causing clotting [129]. These artificial vesicles discovered by Bangham *et al*. in 1965 [130], are composed of an aqueous core surrounded by the lipid bilayer and are evaluated as drug nanocarriers for decades [131]. As shown in Figure 2.13, phospholipids are amphiphilic molecules that have a hydrophilic head (polar phosphate group) and a hydrophobic tail (non-polar glycerol bonded to two fatty acid chains) [131].

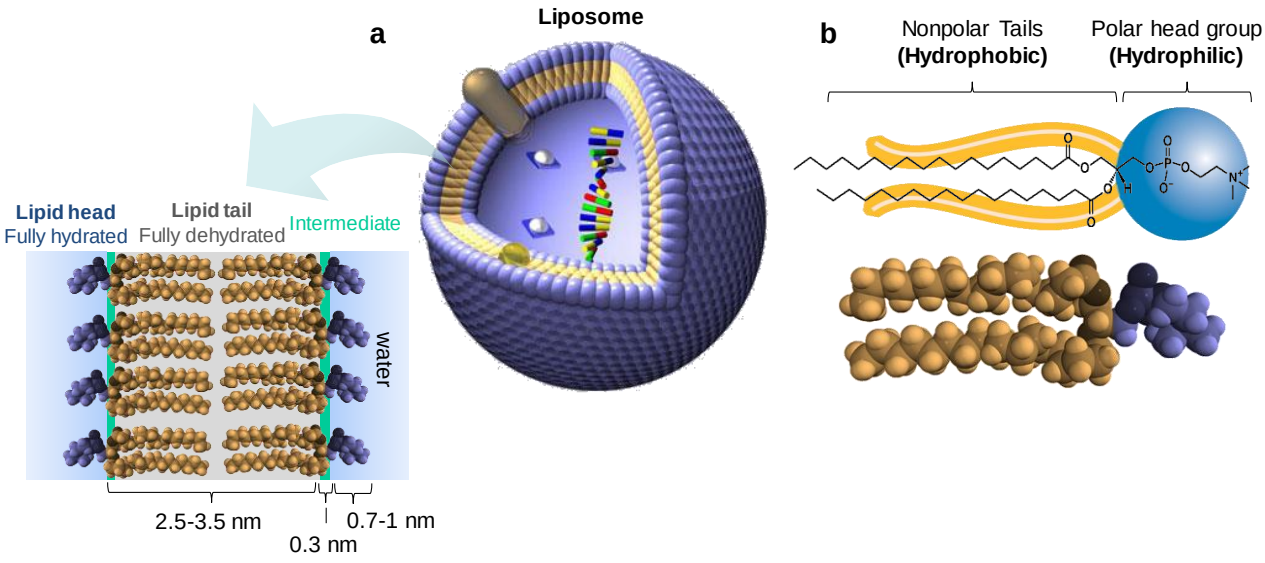

Figure 2.13: Schematic presents the structure of a liposomal lipid bilayer. (**a**) Liposome structure contains three distinct regions including the fully hydrated head groups, partial hydrated intermediate region, and the fully dehydrated alkane core. (**b**) Individual phospholipid (DSPC) molecules showing the hydrophobic nonpolar tail region and hydrophilic polar head group.

In the presence of water environment, the tails are repelled, and the heads are attracted to water to combine structure and form a membrane bilayer. According to their lipid composition, size, and lamellarity, liposome configurations can be classified as nanoscale small unilamellar vesicles (SUVs; below 400 nm), microscale large unilamellar vesicles (LUVs; 400 nm to several microns), giant unilamellar vesicles (GUV; 200 μm) and multilamellar vesicles (MLVs) consisting of a few concentric layers.

2.6.2 Liposomes as drug delivery carriers

Liposomes of various configuration and size were investigated extensively as versatile carriers for multitude application such as encapsulate cosmetics [132], imaging contrast agents [133, 134], genetic material [135], enzyme [136], vaccine [137], and proteins to cellular sites [131] as well as for targeting anticancer drugs [131, 138-141]. Liposomes can house more than one active agent and simultaneously loaded both hydrophilic chemicals (in the aqueous core) and lipophilic molecules (into the lipid bilayer domain) [40]. The possibility of modifying them physically or chemically confer liposomes with the ability to target the drug, alter the drug biodistribution [142], improve residence time, control drug release kinetic [143], enhance cellular uptake [144], shield the body from toxic side effects [145], and to have a control over pharmacokinetics [8]. Also, they can protect the active metabolite form of pH-sensitive drugs such as SN38 and improve drug solubility in acidic core under physiological conditions. However, like other delivery systems, liposomes are unable to pass through tissue destinations and mostly accumulate around broken vessels [12, 49].

2.6.3 Liposomes stability

The physical, chemical, and biological stability of liposomes are the concerns for biological applications [146]. Physical stability of liposome can be influenced by size, coating, composition, surface charge, and the ratio of the lipid to the active substances. Induced charges on the surface of liposomes prevent aggregation through like charge repulsion. An alternative method of creating water-dispersible particles is to form a hydrophilic coating using hydroxylic polymers or polyethylene glycol (PEG).

Chemical stability of liposomes is altered due to oxidation and hydrolysis of the lipids. This is affected by size distribution, pH and ionic strength of the solution, and the presence of

unsaturated lipid chains. To improve the stability and reduce the risk of hydrolysis, the use of lipids with high molecular weight, stable saturated bond, hydrophobic of ester bond, addition of antioxidants (*e.g.* butylated hydroxytoluene) and chelating agents to the liposome formulation are recommended. Sterols such as cholesterol are component that can affect membrane permeability and stability of liposome [147, 148].

Similarly, biological stability and circulation half-lives of liposomes also depend on their size, composition, and surface properties. Cationic liposomes aggregate in biological condition. Prior to the uptake of liposomes with circulating phagocytic cells, high-density lipoproteins (HDLs) in plasma are responsible for their destabilization of liposomes due to the lipid exchange between the liposomes and HDLs. Nanoliposomes with a size ranging from 10 to 100 nm are not immediately recognized by the immune system, and also they are big enough to evade renal filtration [149]. Common strategies for stabilizing, inhibit nonspecific adsorption of serum proteins and prolong retention time of the liposomes include surface ionization (*e.g.* citrate acid), grafting small molecules (*e.g.* alkanethiol), hydrophilic polymers (*e.g.* PEG derivates, co-block polymer) [140, 150, 151], and biomolecules (*e.g.* DNA, polypeptide) [152, 153]. For instance, many studies demonstrated an increased circulation lifespan and improved accumulation of drugs encapsulated within the PEGylated liposomes at the disease site, which result in effective tumor targeting and therapeutic efficacy [8, 151, 154].

2.6.4 Liposome manufacturing and synthesis techniques

Bangham method [130], detergent-depletion [155], direct (ethanol/ether) injection [156], heating [157], reverse-phase evaporation/thin film hydration technique [158], electroformation [159], supercritical fluid techniques [160], high-pressure homogenization [161], dual asymmetric centrifugation [162], freeze drying [163], freeze-thawing [164], microfluidic method [165] are the techniques used for the preparation of liposomes. The general conventional procedure is first to dissolve the phospholipid in an organic solvent, dispersion of lipid mixture in an aqueous phase, and then the post-processing filtration of the liposomes (such as membrane extrusion, sonication, or freeze-thawing) to achieve desired sizes and configurations [166]. The proper choice of liposome preparation method relies on the physicochemical characteristics of the liposome compositions and those of the substance to be entrapped along with the nature of the medium in which the lipids are dispersed, the effective concentration of the entrapped

pharmaceutical agents and its potential toxicity, additional steps (*e.g.* functionalization) involved during preparation, reproducibility, and scaling up.

Reverse-phase evaporation/thin film hydration method was employed in the current study (Figure 2.14). In this technique, the lipids are initially dissolved in an organic solvent such as chloroform–methanol mixture. Then, the solvent is evaporated using a rotary evaporator to form a thin film of phospholipids. The resulting dry lipid film is re-hydrated at a temperature above the transition temperature of the lipid with an appropriate buffer. The individual phospholipid molecules are aligned tail to tail (*i.e.* hydrophobic-end-to-hydrophobic-end) and formed phospholipid bilayer sheets. These bilayer conformations are highly unstable, and when reach a certain length by vigorous shaking, the sheets fold upon themselves and form the liquid-filled large multilamellar vesicles with various sizes [167]. To obtain SUVs, extrusion through polycarbonate membranes can be performed at around transition temperature of lipids to downsize the particles and yields homogeneous unilamellar vesicles [166].

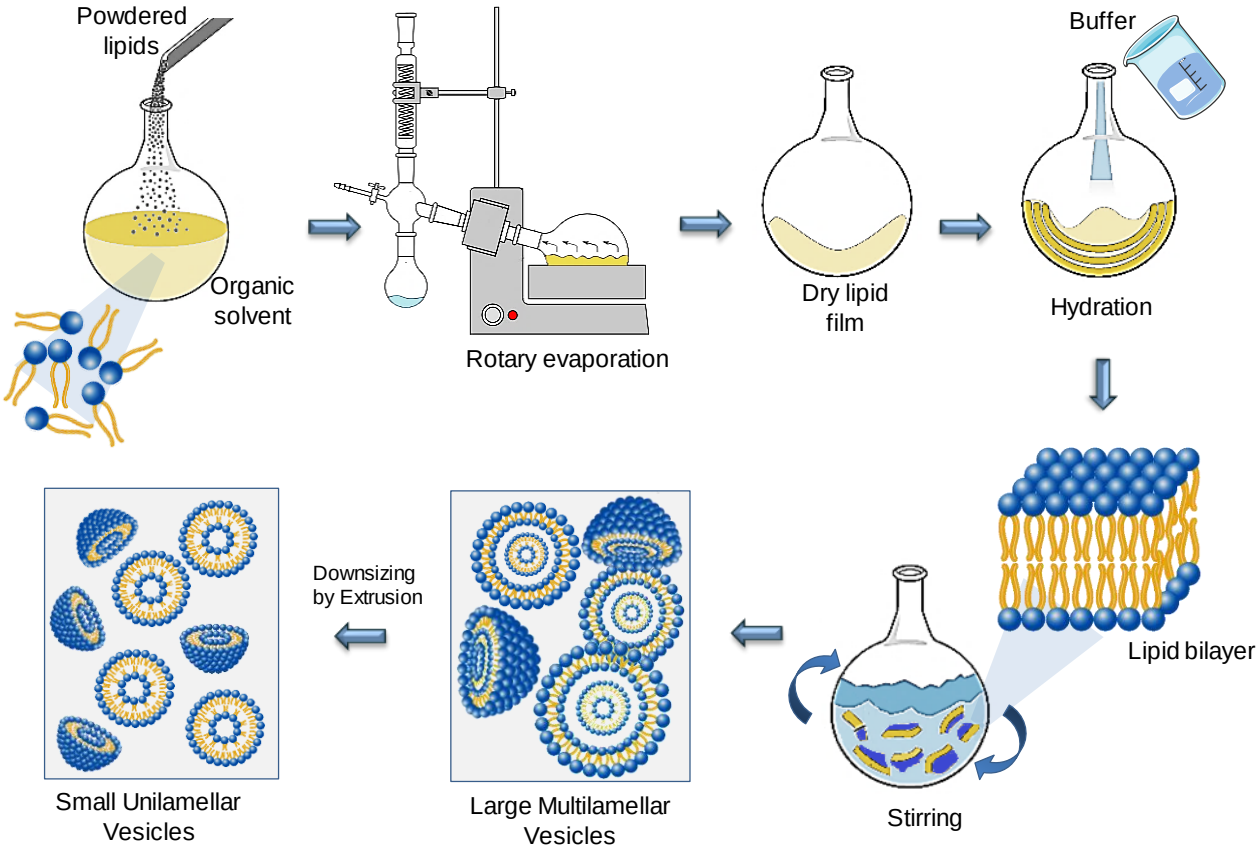

Figure 2.14: Schematic illustrating the reverse-phase evaporation/thin film hydration technique for liposome manufacturing. Reproduced from [168].

2.6.5 Liposome drug loading strategies

Depending on the physico-chemical properties of the therapeutic agents such as solubility, stability, biocompatibility, and therapeutic application of the final product different encapsulation strategies can be employed [169].

2.6.5.1 Passive encapsulation

In passive encapsulation method, the bioactive molecule is loaded into the internal aqueous core of liposome during the stages of vesicle formation without any external force. The most common method is the thin film hydration, in which the desired biomolecule is added during rehydration process. Highly water soluble hydrophilic drugs with small molecular weight can be encapsulated passively because they are not amenable to gradient-based drug loading methods due to their minimal membrane permeability [170]. Although this encapsulation method is simple, the encapsulation efficacy is quite low (drug-to-lipid molar ratio of 1:20–1:100) [170, 171]. For lipophilic drugs, both drug and lipid are co-dispersed in buffer resulting in entrapment of drug inside the bilayer of liposomes. Polyions substances (*e.g.* nucleic acid-based therapeutics and doxorubicin) can be complexed with oppositely charged lipids to improve trapping efficiencies and drug-to-lipid ratio [140, 170].

2.6.5.2 Active encapsulation

The active encapsulation methods employ transmembrane gradient strategy to efficiently trap and stabilize the weakly basic and acidic amphipathic drugs into the pre-formed liposomal lumen [29]. These methods usually facilitate the drug permeation by the formation of a pre-established transmembrane gradient between the aqueous core and the external environment. This gradient can be generated either by (i) translocation of K^+ ions, (ii) buffers exhibit substantial difference in pH (citrate buffer (pH = 4) inside and HBS buffer (pH = 7.5) outside), (iii) ($(NH_4)_2SO_4$) and ($(NH_4)_2HPO_4$)-gradient, whereby one NH_3 molecule moves out of core and leaves one H^+ behind, thus creating pH gradient [172, 173], and (iv) the ethylenediaminetetraacetic acid (EDTA) ion gradient method [174]. Briefly, prior to encapsulation, the drug molecule is uncharged and permeated across the lipid bilayer. Upon reaching low pH inside the intravesicular space, the drug undergoes a chemical transformation and becomes protonated. Since, charged molecules are less permeable, the encapsulated compound is effectively trapped inside the aqueous core of

liposomes [148]. Doxorubicin that contains ionizable amine group is an example of successfully formulated drug from this loading method [175].

2.6.6 Liposomal SN38 formulation

Research studies demonstrated that incorporating water insoluble hydrophobic camptothecins such as CPT-11 and SN38 into a pharmaceutical formulation like liposomes can improve their solubility, stability, and activity profiles [111, 112, 127]. These drugs have a low affinity to lipid membranes and tend to precipitate into aqueous phase. Besides, the neutral form (lactone, the loadable form) has limited solubility in most of the compatible organic solvents. One of the current methods uses the high solubility of SN38 in dimethylsulfoxide (DMSO) to prepare SN38 loaded liposomes [158]. However, one of the concerns is the DMSO toxicity to cells.

Therefore, loading strategy and formulation of SN38 in pharmaceutical delivery systems for parenteral administration is very challenging to ensure the availability of the more-loadable lactone form during the encapsulation process with reduce toxic effects. Another solution is to dissolve the SN38 in an alkaline condition (*e.g.* pH = 11) in a buffer such as PBS, which is more compatible with cells and bacteria. Figure 2.15 shows a pH gradient strategy (pH inside = 4 and pH outside = 8) for the encapsulation of SN38 into liposome. The external pH is a compromise between a pH providing a reasonable solubility of the drug and a considerable proportion of its neutral form which resulting greater precipitation of SN38 into the liposome core. The inside pH can be generated by encapsulating a buffer such as ammonium sulfate ($(NH_4)_2SO_4$) with an acidic pH in the liposome [111]. The water-soluble inactive carboxylate form of SN38 is transformed to the neutral active lactone form by reducing pH during transportation across the liposome wall [111]. At interior acidic pH, the SN38 is trapped in its active neutral lactone ring, likely forms insoluble crystals with ammonium sulfate and becomes almost impermeable, which allow it to remain inside the liposome until reaching the delivery site.

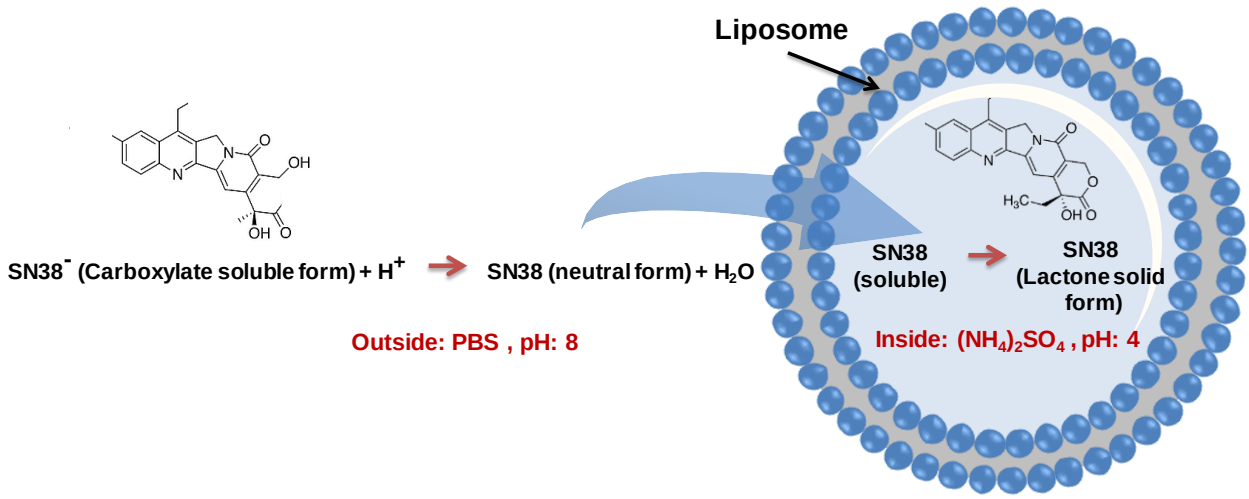

Figure 2.15: pH gradient method to accommodate SN38 within the aqueous core of the liposome. At alkaline condition, SN38 exists as inactive hydrophilic charged carboxylate forms outside of the liposomes. In the acidic liposome interior, SN38 converts to the hydrophobic active closed lactone forms.

2.6.7 Mechanism of drug release from liposome

One of the critical challenges for drug delivery is to control spatially and temporally drug release after the localization at the target tissue. Extensive works with liposomal formulation of vincristine and doxorubicin as cell cycle-specific drugs [176, 177] with high drug-to-lipid ratios showed long-term drug release rates which could potentially affect many tumor cells at their vulnerable part of the cell cycle [176]. The physico-chemical characteristic of liposomes can be engineered and designed differently relative to the application, tissue environment, and specific drug release mechanism including temperature sensitive liposomes [139, 170], pH sensitive [139, 170], enzymatic release [141, 178, 179], ultrasound sensitive [180], and photosensitive [170].

The lipid composition consisted of saturated long-chain lipid with incorporated cholesterol provide high retention, while using shorter and unsaturated acyl chains resulting in more leaky systems. For instance, the factors that influence the magnitude of drug release from the sonosensitive liposomes include lipid composition (*e.g.* grafted PEG group, unsaturation of acyl chain), amplitude of ultrasound, pulse or continuous irradiation, and exposure time [180]. Cavity formation and subsequently drug leakage can be induced by short-term exposure to low-

frequency ultrasonic irradiation (~20 kHz, < 3 min) [181]. However, this method may not be possible for solid tumors located deep in the body.

Enzyme-activated liposome for drug release in the solid tumor is a promising method in which the tumor microenvironment contributes to locally degrade the liposomal carrier through the release of enzymes (lipases) and oxidizing agents. Moreover, mildly acidic pH of the tumor can be used for the degradation of pH-sensitive liposomes without any external stimulation. Secretory phospholipase A2 (sPLA2) enzymes play a fundamental role in destabilization and cleavage of the lipid molecules leading to the generation of lysolipids and fatty acids [141, 178, 179]. The factors that influence the PLA2 activity include size, charge, lipid composition (*e.g.* acyl-chain length, polymer coverage, and length), and structural defects such as at domain boundaries. Incorporation of anionic PEGylated lipids such as DPPG can promote the PLA2-catalyzed degradation of the phospholipids membrane. However, the activity is diminished significantly in the presence of cholesterol, potentially limiting the range of drugs that can be delivered using this approach [179]. Elevated expression of PLA2 was shown in several human tumor types including breast, gastric, pancreatic, venom, prostate, small bowel, and colon. PLA2 is overexpressed in 65 colon carcinomas (50% of colon cancers) and eight colorectal cancer cell lines [178].

2.6.8 Cellular uptake mechanism

Successful drug targeting and delivery approaches rely on understanding of the cellular processes and underlying pathways that occur during delivery. Drugs and nanoparticles must be adequately taken up by target cells to exert their therapeutic effects. It is well known that cellular incorporation and clearance of particles are highly related to their physico-chemical properties such as the size, shape, charge, composition, coating, surface chemistry, and cell type [182, 183]. Figure 2.16 shows the effect of particle size in cellular uptake mechanisms and accumulation. The cell's semi-permeable plasma membrane allows free diffusion of small and non-polar molecules. However, bigger substances are unable of crossing the membrane and require uptake mechanisms. The cellular uptake of the drug-delivering carriers can occur with an adsorption process on the negatively charged cell membrane followed by the internalization of nanoparticles by the specific pathways. Phagocyte cells could take up large particles, aggregates, opsonized particles, and ligand modified particles through phagocytosis. Nonphagocytic cells can uptake the

nanoparticle mainly through direct penetration or pinocytosis (*e.g.* nonspecific endocytosis, receptor-mediated endocytosis) (Figure 2.16b) [40, 183].

In the case of liposomes, the structures and many physicochemical properties of lipid bilayers are similar to cell membranes. This similarity may increase the permeability and fusion of liposomes with cell membrane to deliver their contents into the cytosol. This method is mostly used for the DNA or drugs that would normally be unable to diffuse through the cell membrane and fusogenic liposome help to indiscriminately delivered past the lipid bilayer [184].

According to literature, the kinetic of uptake is size dependent and takes several hours to reach saturation (or equilibrium) [185]. For instance, the particles with the size of 50–100 nm, the saturation time is ~30 min while it is increased to several hours for 200 nm particles. It was established that particles carrying an overall positive charge can improve cellular uptake, most likely due to the electrostatic interaction with the net negative surface charge on the cells membrane [186]. For instance, to target phagocytic cells, particles can be made in a particular size range, positively charged, and decorated with opsonins that make them viable targets for natural macrophage phagocytosis. These particles may be digested in the macrophage's phagosome and releasing drug contents [182]. Many studies showed that the outer membrane of tumor cells typically carry a net negative surface charge due to an overexpression of sialic acid-rich glycoproteins, phosphatidylserine (PS) residues, *O*-sialoglycoproteins, and heparan sulfate proteoglycans [187, 188]. In comparison, normal mammalian cell membranes have zwitterionic phospholipids (*e.g.* phosphatidylethanolamine (PE), phosphatidylcholine (PC), or sphingomyelin (SM)) in their membranes. As such, their membranes are less negative in net charge.

The micron-size bacteria can be internalized by macropinocytosis and phagocytosis process in non-phagocytic and phagocytic cells, respectively. For macropinocytosis, the external stimulation is required to activate a signaling cascade to induce changes in the dynamics of the actin-mediated membrane and triggering plasma membrane ruffling [189, 190]. The bacteria that die quickly in physiological condition such as MC-1 magnetotactic bacteria (40 minutes) [36] cannot take advantage of macropinocytosis.

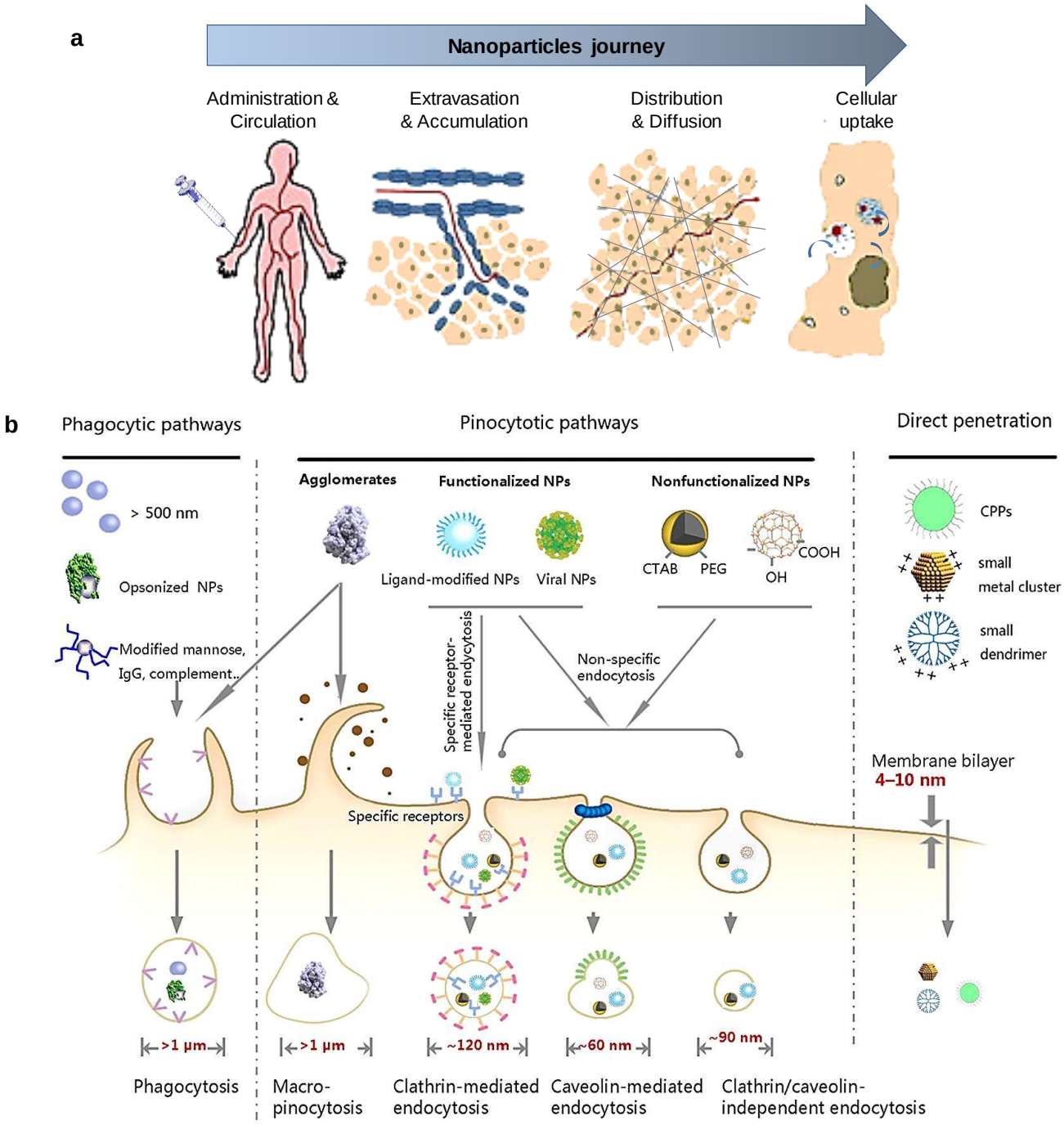

Figure 2.16: (**a**) The journey of nanoparticle carrying the drug from the injection site into the action site. (**b**) The various cellular uptake mechanisms of macromolecules and nanoparticles across the cellular membrane into the cells are indicated according to their size. Reprinted with permission from [183]. Copyright 2012, American Chemical Society.

2.7 Bioconjugation techniques

Conjugation of biomolecules such as peptides and antibodies, nucleic acids, oligonucleotides, fluorescent dyes, polymers, drugs, markers, and various enzymes to nanoparticles creates hybrid materials that can alter their functionality, effectiveness, water-solubility, and stability in the physiological environment and allowing the nanoparticles interact specifically with biological systems. The strategies commonly used for bioconjugation consist of (i) non-covalent binding including physical adsorption (physisorption) and biological affinity-binding, (ii) covalent attachments (chemisorption) [152, 153]. Figure 2.17 presents some of the main chemistry available for coupling of biomolecules to the particles. The non-covalent interactions can be classified as electrostatic interactions (*e.g.* ionic, hydrogen, and halogen binding), Van der Waals forces (*e.g.* dipole-dipole and London), and hydrophobic interactions. Each technique has its benefits and drawbacks and is used in the context of specific application, reagent requirements, and timetable.

2.7.1 Non-covalent binding

2.7.1.1 Physical adsorption

One of the simplest and straightforward noncovalent attachment methods is through the passive adsorption of molecules to particles without additional functionalization. The adsorption mechanism mostly occurs by electrostatic interaction between oppositely charged compounds. For instance, adsorption of negatively charged DNA onto non-functionalized positively charged gold nanoparticle [191] or adsorption of avidin to negatively charged nanoparticles [192]. Proteins, as zwitterionic molecules, are positively charged at pH values below their isoelectric point (pI) and negatively charged above it. Therefore, proteins can have different charges (natural, positive or negative) under physiochemical environment. The hydrophobic ligands (*e.g.* immunoglobulins) can be adsorbed onto the surface of the particles through the hydrophobic attraction. In the case of less hydrophobic ligands (*e.g.* human serum albumin and hemoglobin) and more hydrophilic particles (bearing -COOH groups), the attachment can take place via both hydrophobic and ionic interactions. For hydrophobic antibodies, their Fc portion is more hydrophobic than the Fab region, and therefore, the antibodies are more likely adsorbed in their most biologically active orientation by hydrophobic attraction [193]. The major drawbacks of the

physical adsorption method are the lacks of stability and specificity [194, 195]. The strength of the hydrophobic interaction is also sensitive to the environment properties such as ionic strength and pH changes. To overcome this problem, the pH of the adsorption buffer needs to be kept at or near the isoelectric point of the protein.

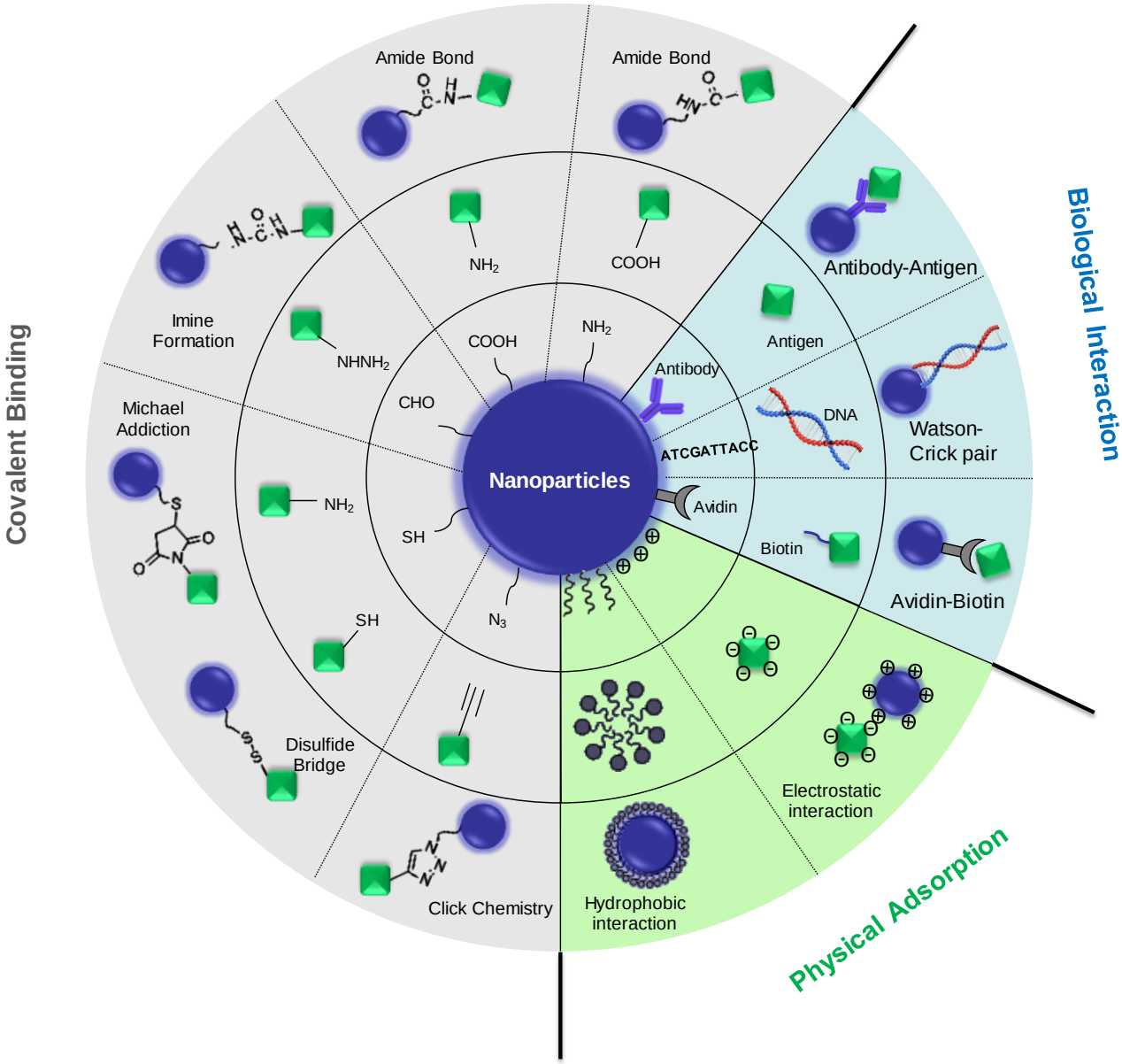

Figure 2.17: Schematic illustrating of bioconjugation techniques based on the functional groups involved. Reproduced from [196].

2.7.1.2 Biological affinity-based binding

The application of non-covalent affinity-based receptor-ligand systems has been well-established for different biomolecules such as antibody-antigen interaction, receptor-target binding, and enzyme-substrate interaction. It is possible to use these high specific interactions for bioconjugation of biomolecules to micro/nanoparticles. For instance, oligo DNA-functionalized particles were used to target genetic materials, which is often a complementary base pair of nucleic acid [197]. Moreover, the immobilization of IgG antibody on the protein G functionalized particles for capturing staphylococcus bacteria [198].

One of the most well-known affinity bindings is the (strept)avidin–biotin system in which both particles and molecules are pre-coated with a generic binding proteins [199]. The dissociation constant of this noncovalent affinity bind is relatively high ($K_{diss} > 1.3 \times 10^{15}$ M), which lead to an extremely robust bond, resistant to high temperature and harsh chemical conditions. Due to the strong bond and specificity of the biotin–avidin system, the method has been employed in a large number of biotechnology applications. Particles can be functionalized with (strept)avidin by either covalent coupling or electrostatic adsorption and then used to label biotinylated antibody, DNA oligomers, antibodies, peptides, and fluorescent dyes. Another well-known class of affinity-based system is polyhistidine tagged (His-tag) proteins or peptides that allow strong but reversible binding to the metal-ion-chelating particles such as Ni-nitrilotriacetic acid (Ni-NTA)-coated magnetic nanoparticles [200]. The disadvantage of the technique is the need to modify both particles and biomolecules with an affinity pair. Moreover, the conjugation interference by other chemical groups available for adsorption within the biomolecule.

2.7.2 Covalent coupling

Among the various coupling strategies, covalent coupling is often employed for the immobilization of biomolecules when a specific and stable cross-linkage is required. Particle-biomolecule conjugates prepared with this method are effectively bound, and do not desorb/leach for a long period of time if desired. Moreover, the ligands and binding moieties are favorably presented on the surface of the particle and are available for interaction with target [195].

Covalent binding by conjugation chemistry exploit functional groups on both biomolecules and particles such as carboxylic, amine, and thiol group (Figure 2.17). For instance, the preparation of

immunoliposomes, lipid derivatives incorporated into the bilayer construction must contain functional groups available for cross-linking. The PEGylated distearoyl phosphatidyl ethanol-amine with a terminal carboxyl group (DSPE-PEG-COOH) [151, 195] or PEGylated dipalmitoyl phosphatidyl ethanol-amine with a terminal maleimide group (DPPE-PEG-Mal) [150] provide an ideal functional group for activation and subsequent bioconjugation.

As shown in Figure 2.17, the thiol group (R–SH) can selectively react and couple with maleimides preferentially under pH 6.5-7.5 [195]. The amine-functionalized particles can be conjugated with various thiolated biomolecules such as thiol-peptide, residue thiol-DNA, and proteins and peptides with free or reduced cysteine, or vice versa. Disulfide bridges can be also used for reversible coupling of particles [201]. One-step click chemistry is another common approach for covalent bioconjugation, which involves coupling of alkyne to an azide (N_3^-) group and results in 1, 2, 3-triazole ring in presence of Cu (I) catalyst. However, the azide or alkyne-functional bioactive species requires special preparations that decreases the products yield [202].

Covalent coupling via amine and/or carboxyl functional groups is one of the most commonly used conjugation strategy. Primary amine exists in various proteins (*e. g*. enzyme and antibodies) [203, 204] or amine-terminated nucleic acid [205] can react with carboxylic acid-functionalized particles to form a covalent amide bonds [206]. The linkage is usually mediated by zero-length carbodiimide agents. Moreover, due to the active nucleophilicity of amine group, they can react with other functional amine-containing groups, such as aldehydes, thiols, isocyanates, and epoxides. For instance, glutaraldehyde agents by bridging two amines from each species allow to conjugate enzymes to nanoparticle surface with a small space of the linkage (~0.7 nm) [207].

2.7.2.1 Carbodiimide-mediated chemistry

There are currently several zero-length bioconjugation techniques including carbodiimide, Woodward's Reagent K, N, N-carbonyldiimidazole, and Schiff base formation and reductive amination [195]. Carbodiimide dehydrated agents are the most prevalent type of smallest zero-length crosslinker that often mediates the activation of carboxylic acid groups toward the formation of amide or ester linkage without introducing a spacer arm. One of the advantages of the technique is several types of amine-containing molecules such as antibodies, peptides, enzymes, and DNA that can be immobilized to the functionalized surface of the substrate without prior modification. Moreover, most of the biomolecules are soluble in aqueous buffer solutions.

The widely used carbodiimides activation agents include 1-ethyl-3-(3-dimethylaminopropyl) carbodiimide hydrochloride (EDC, EDAC or EDCI), 1-cyclohexyl-3-(2-morpholinoethyl)carbodiimide (CMC), dicyclohexylcarbodiimide (DCC), diisopropyl carbodiimide (DIC)), Woodward's reagent K (N-ethyl-3-phenylisoxazolium-3′-sulfonate), and N,N′-carbonyldiimidazole (CDI) [195]. These carbodiimides catalysts can be categorized into water-soluble and water-insoluble (soluble in organic solvents) types. The water-soluble agents are preferred for biochemical conjugations, which allows for direct reaction in physiologic solutions without prior organic solvent dissolution [203, 206].

The water-soluble EDC carbodiimide along with water-soluble N–hydroxysuccinimide (NHS) or its analog (sulfo-NHS) are successful way of creating zero-length crosslink [195, 208]. By far, the most common coupling strategy for direct coupling of negatively charged carboxylates (–COOH) to primary amines ($–NH_2$) containing molecules is through EDC-mediated process to mediate the formation of amide linkages without becoming part of the final crosslink between target molecules [151, 195, 203]. The method is highly efficient for crosslinking biological substances such as proteins or immobilizing proteins, forming amide bonds in peptide synthesis, attaching haptens to carrier proteins to form immunogens, and labeling nucleic acids.

Figure 2.18 presents a generalized description of conjugation of an amine-containing molecule to a carboxylate molecule using carbodiimide coupling method. The technique usually involves a single step or two-step process. In a simple one-step procedure, the carboxyl-containing molecule is activated with EDC to form an active ester (*O*-acylisourea) intermediates. This active species can react with a nucleophile such as a primary amine to form an amide bond (Figure 2.18a). In aqueous solutions, the generated reactive ester complex is labile, gradually loss activity, and has slow reaction rate with amines. Hydrolysis is the major competing reaction cleaving off the activated ester intermediate, forming an isourea, and regenerating the carboxylate group (Figure 2.18b). To reach the desired coupling efficacy, the reaction needs to be carried out promptly to prevent hydrolysis of reactive ester before meeting the target amine.

A two-step procedure (Figure 2.18c) results in better control of the reaction and the higher yield of amide bond formation. First, the carboxylate-containing compound can form an *O*-acylisourea intermediate reactive ester. To increase the stability of this active ester, NHS or sulfo-NHS can be used by forming a considerably more stable sulfo-NHS ester intermediate from the reaction of the

hydroxyl group of sulfo-NHS with the EDC active-ester complex. Sulfo-NHS esters are hydrophilic reactive groups that couple rapidly with amines nucleophiles on target molecules, which dramatically increase the resultant amide bond formation. An effective separation steps (*e.g.* gel filtration or dialysis) in a reasonable time frame are required to remove excess reactants and by-products of the reaction such as the water-soluble isourea.

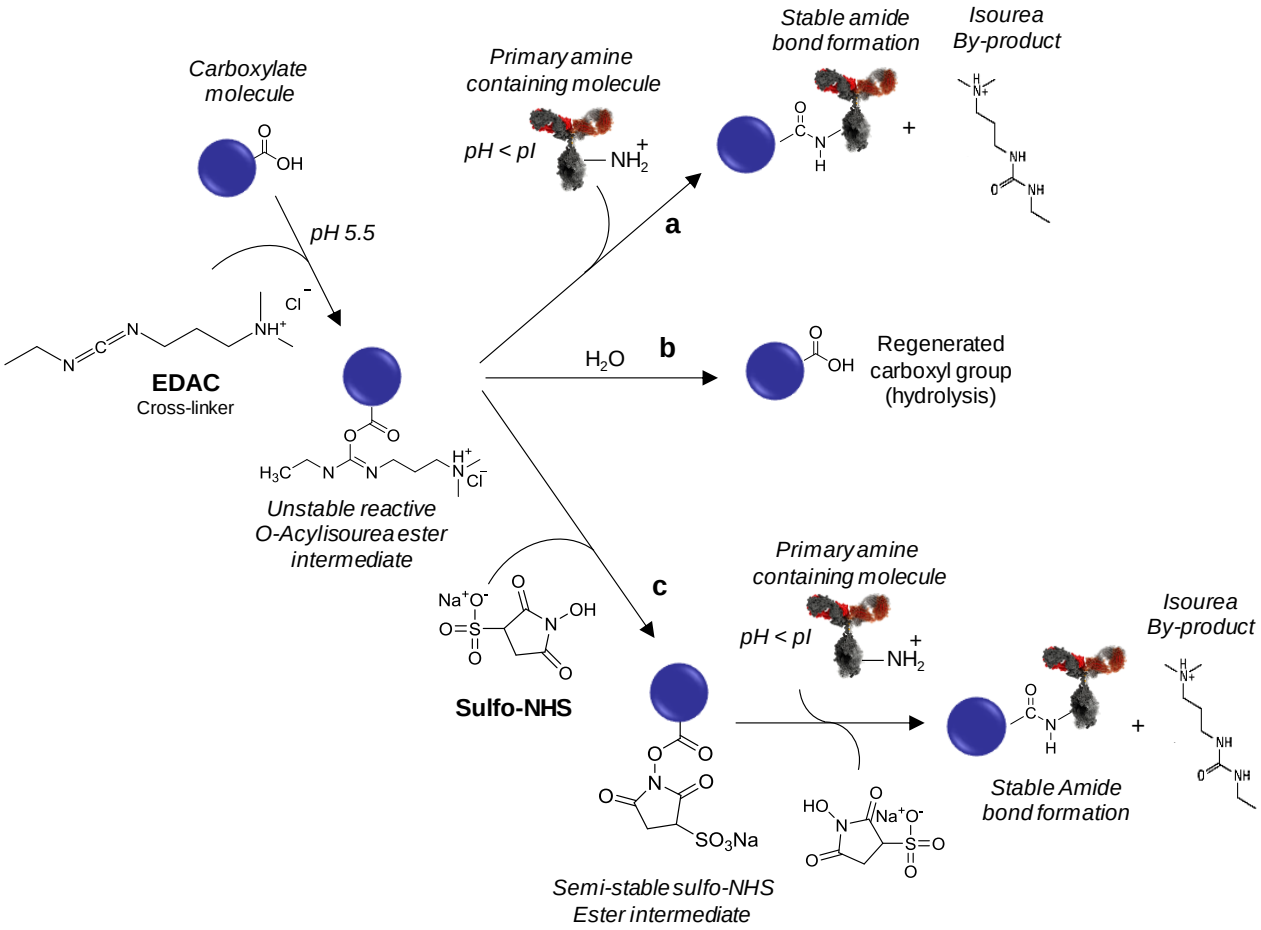

Figure 2.18: Reaction scheme describes the carbodiimide EDC/NHS crosslinking procedures. Molecules containing carboxylate groups can be activated by EDC and sulfo-NHS to create an active ester intermediate. By nucleophilic displacement, the activated particle can couple with amine-containing compounds to form amide bond linkages. Adapted from [195].

Although NHS or Sulfo-NHS are not necessary for carbodiimide reactions, their presence can greatly improve the solubility, stability, and coupling efficiency by enhancing yield of EDC-active intermediate significantly through the formation of more stable amine-reactive

intermediate [209]. For example, an addition of 5 mM sulfo-NHS to the EDC for coupling of glycine to keyhole limpet hemocyanin increased the yield of derivatization about 20-fold as compared to using EDC alone [209]. Sulfo-NHS is more effective due to preserving or increasing water-solubility of the activated carboxylate molecule, longer-lived, and slow hydrolysis of formed ester intermediates. Moreover, the sulfo-NHS ester intermediate is negatively charged aiding to maintain the stability of particles due to repulsion between like-charged particles.

Working with carbodiimide needs to balance out between activation efficiency, hydrolysis rates, and stability of the components involved in the reaction. Intermediates can be hydrolyzed within hours or minutes depending on water content and pH of the reaction solution. EDC hydrolysis occurs maximally at acidic pH with enhancing the stability of the carbodiimide in solution at or above pH 6.5 while the hydrolysis rate of the esters is greatly slower at slightly acid pH. As the pH becomes basic the hydrolysis kinetics of the Sulfo-NHS activated -COOH group increases. In general, NHS-esters have a half-life of 4-5 hours at pH 7, 1 hour at pH 8 and just 10 minutes at pH 8.6 [210]. On the other hand, the carboxylate activation occurs most efficiently with EDC at pH 3.5-4.5 while the highest yield of the amide bond formation is in the range of pH 4-6. When working with proteins and peptides, the amide bond formation effectively occurs between pH 4.5-7.5. Beyond this range, the coupling reaction occurs with lower yields. Since the pI of IgG is in the range of 6.4 to 9.0, at pH less than pI, the amines on the protein will be protonated and thus be more reactive toward the sulfo-NHS esters.

The activation rate and attachment efficiency are pH, particle size, incubation time, and concentration dependent. Overall, for best efficacy in two-step crosslinking reactions, it is recommended to perform the EDC and Sulfo-NHS activation in 0.1 M MES [2-(N-morpholino) ethane sulfonic acid] buffer for 30 min incubation time at room temperature at pH 4.5-6.0, which cause the most activation of EDC and less hydrolysis of intermediates. Then, raising the pH to neutral immediately prior to reaction to the biomolecule using suitable buffers devoid of extraneous amine- or carboxylate-containing molecules (*e.g.* phosphate buffers) will maximize the reaction of Sulfo-NHS activated molecules with primary amines [195].

The EDC-mediated crosslinking reaction may promote unwanted self-polymerization. For instance, the IgG antibody usually contains both accessible amine and carboxylate groups, which results in antibody polymerization among themselves and severe precipitation. The following

procedure could be performed to minimize the polymerization of proteins including (i) titration and scaling back the amount of EDC/NHS, (ii) performing reaction under mildly alkaline conditions, (iii) chemically quenching the unreacted EDC with 2-mercaptoethanol (2-ME) to form a stable complex with the remaining carbodiimide, (iv) removing the excess agents and terminating the activation (*e.g.* by dialysis, desalting using gel filtration or centrifugal spin columns), and (v) adjusting the reaction pH by buffer exchange with a desalting column. These operations should be done rapidly to minimize hydrolysis and undesirable crosslinking, and recover as much active ester functionality as possible [195, 208].

This chemistry has been used in various applications. Biosensor transducer surfaces have been functionalized with EDC chemistry for the detection of pathogenic bacteria [211]. Signal amplification of captured bacteria has also been performed using quantum dot nanoparticle bioconjugation based on carbodiimide chemistry [212]. Bacterial morphology has also been assessed through coupling substrates for microscopy to cell membranes through EDC/NHS interactions [213]. Furthermore, the detailed study of outer lipoproteins membrane has been investigated for their capacity to behave as cell surface receptors for cationic antimicrobial peptides through EDC/NHS bioconjugation [214]. In terms of biomolecule conjugation for targeted delivery applications, this chemistry has also been applied for the functionalization of a wide range of nanoparticles [215], superparamagnetic iron oxide nanoparticles [216], gold [217], and paramagnetic microparticles [218].

2.7.2.2 Antibody immobilization on particles

Various direct and indirect techniques have been developed for the conjugation of antibodies to the surface of particles [195]. Functional groups available on the surface of an antibody include primary amines (-NH_2), carboxyls (–COOH), sulfhydryl groups (–SH), and carbonyls (–CHO) (Figure 2.19) [219, 220]. Amine groups occur at the N-terminus of each polypeptide chain and in the side chain of lysine residues that are distributed over the entire antibody. Due to the positive charge of primary amines at physiologic conditions, they are usually outward-facing of proteins; therefore, they are typically accessible for the conjugation without denaturing protein structure. Carboxyls occur at the C-terminus of each polypeptide chain and in the side chains of aspartic acid and glutamic acid. Sulfhydryls appear in the side chain of cysteine residues that are joined via disulfide bonds (–S–S–) to stabilize the whole molecule structure. However, the sulfhydryls

must be reduced to become available for crosslinking. Carbohydrate (sugars) in the polysaccharide moieties can be oxidized with sodium metaperiodate to generate active ketone or aldehydes in glycoproteins for coupling.

In the case of direct antibody conjugation, the activated particles with appropriate functional groups (such as carboxyl, azide, maleimide, thiol, aldehyde, and amine) specifically react with inherent reactive groups of antibodies (*e.g.* lysine, tyrosine, glutamate, aspartate, methionine, serine, histidine, and arginine) using appropriate crosslinker chelates (*e.g.* EDC, DIC, CMC, and DDC) [195, 219]. For the biological activation of biomolecules, antigen binding domain needs to be accessible and exposed with the appropriate orientation to maximize antibody functionality. For instance, lysine residues are relatively abundant on protein structure and can be considered as primary target sites for EDC conjugation. Bovine serum albumin (BSA) has 30 to 35 lysine groups available on its surface and IgG antibody molecule usually has about 90 lysine residues, of which 30 are potentially suitable for conjugation with particles. In the indirect bioconjugation technique, modified antibody with functional group (*e.g.* avidin, biotin, thiol, maleimide, aldehyde, and hydrazide) can attach to the functionalized particles (*e.g.* Biotin, avidin, PDP, maleimide, MBP, MCC, PDP, hydrazide, and aldehyde).

2.7.2.3 Quantification of antibody–particle coupling efficiency

One of the challenging issues of assessing antibody–particle coupling efficiency is the selection of an assay compatible with the final products. For instance, in the immunoliposomes samples, lipids strongly interfere with direct protein assays such as, bicinchoninic acid (BCA) or Lowry assay [203]. The most common techniques include centrifugation, magnetic separation, dialysis, column separations (*e.g.* size exclusion chromatography), and gel filtration separation. These techniques typically need to be combined with the protein assays such as Lowry, Bradford, or BCA assay, protein absorbance (at 280 nm), fluorescent assays, enzyme-linked immunosorbent assay (ELISA), and sodium dodecyl sulfate-polyacrylamide gel electrophoresis (SDS-PAGE) [203, 221]. Also, microscopic methods such as atomic force microscopy (AFM) [222] and transmission electron microscopy (TEM) can be employed to obtain additional information on the conjugation of antibody to particles.

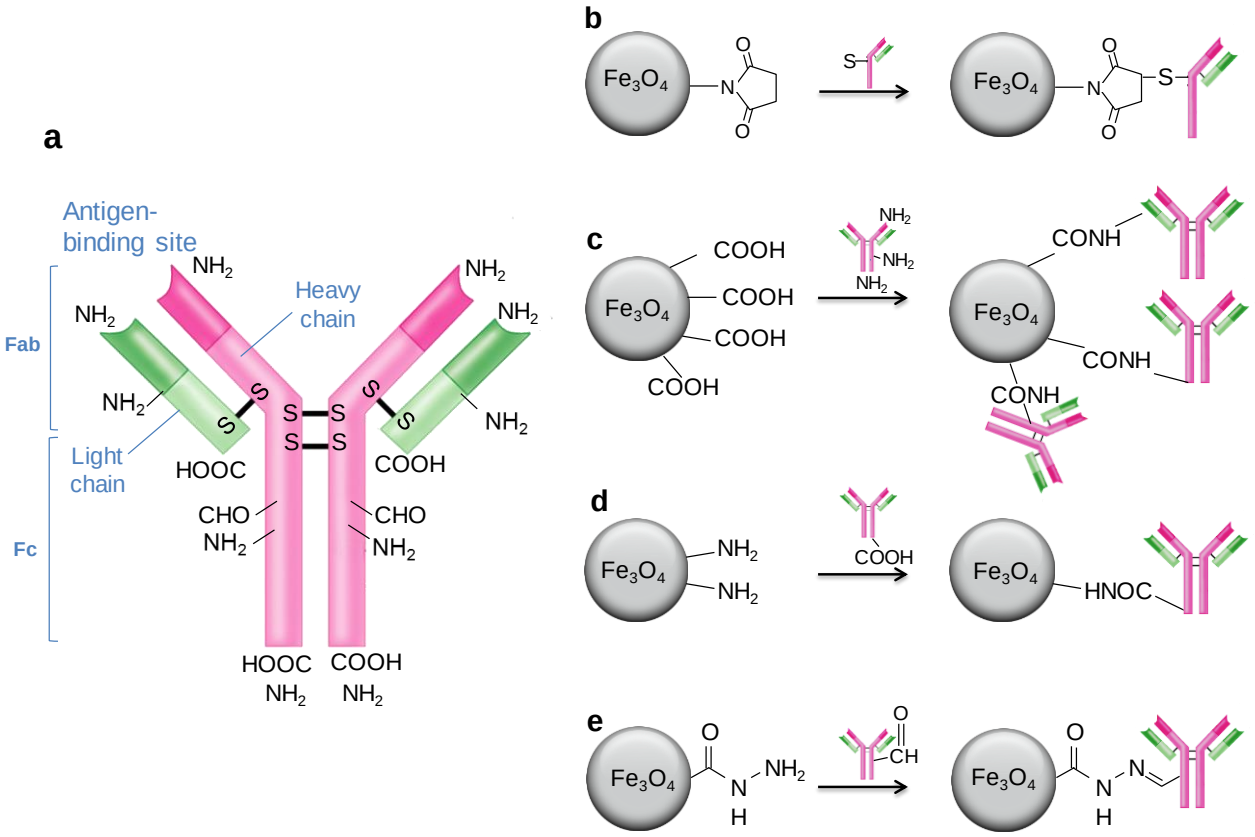

Figure 2.19: Some strategies for attachment of an antibody onto functionalized magnetite nanoparticles. (**a**) A typical structure of an IgG antibody and its labeling sites. (**b**) Maleimide-particle covalently linked with thiol (sulfhydryl) group of antibody and form thioether bond. (**c, d**) Carbodiimide chemistry that forms amide bond, (**e**) Hydrazide-particle attached to aldehyde group of antibody and form hydrazone linkage [195].

2.8 Characterization of the tumor: tools and technologies

The need to understand the tumor structure and microenvironment has led to the development of different imaging techniques to non-invasively visualize the three-dimensional tumor features as well as to quantify biological processes taking place within intact living subjects. Visualization of tumor microstructures including hypoxia and necrotic regions remain beyond the resolution capabilities of the current clinical imaging modalities and become an important issue to advance state-of-the-art medical imaging, diagnostics, and therapeutic interventions. Detailed knowledge of individual tumor microstructure and biologic characteristics are clinically crucial in oncology for tumor characterization, treatment planning, and evaluation of tumor response to a treatment. Various visualization technologies such as conventional X-ray computed tomography (CT) [223], positron emission tomography (PET) [224], ultrasonography [225], optical microscopy [226, 227], and MRI [228, 229] have been developed to produce images of tumor microenvironment. Table 2.2 and Table 2.3 present some of imaging modalities with associated advantages and disadvantages in terms of methods for image generation, spatial resolution, depth penetration, acquisition time, and detection thresholds. The main limitation of these techniques is however poor spatial resolution and low penetration depth which are required to acquire accurate information regarding the tumor microstructures.

2.8.1 Magnetic resonance imaging

MRI as a non-invasive imaging technique is an essential part of modern clinical diagnostics. It offers many advantages over other imaging techniques such as lack of ionizing radiation exposure, relatively high spatial resolution, excellent soft tissue contrast, and nearly unlimited tissue penetration. These profits have turned the MRI to one of the most accessible modalities clinically compared to the other conventional clinical imaging techniques. MRI has a wide range of applications such as molecular and cellular imaging [230, 231], angiography using contrast agents [228, 232, 233], and real-time drug delivery to the tumor sites [65], and *etc.*

MRI uses a strong magnetic field (B_0) and radio frequency (*RF*) pulses to generate detailed cross sectional pictures of internal body structures. Upon exposure to magnetic field in the MRI tunnel, most abundant ^{1}H proton atoms that naturally exist within the body (or other paramagnetic molecules ^{13}C, ^{17}O, ^{19}F, ^{23}Na, and ^{31}P) are aligned with the direction of the field without causing

any chemical fluctuations in the tissues. Applied tuned radio frequency waves redirect alignment of hydrogen atoms. Upon removal of the radio wave, the protons return to their thermodynamic equilibrium alignment in a process called relaxation which is detected as a change in electromagnetic flux. The deterioration of signal is described in terms of two relaxation constants including the longitudinal (or spin-lattice) relaxation time T_1 or the transverse (or spin-spin) relaxation time T_2. The relaxations emit the energy according to the differences in proton content in body tissue. The changes in the induced electrical current in the receiver coil of MR scanner creates a picture of the tissues scanned. The spins reorientation which is the source of contrast in MRI mostly depend on the tissue type, density of proton spins, the magnetic environment of the tissues, the relaxation times of the nuclear magnetization, and the blood flow to the tissues.

Table 2.2: Features of currently employed clinical imaging modalities. Adapted from [234].

Imaging Modality	**Image generation**	**Spatial resolution**	**Time scale**	**Depth penetration**	**Primary contrast**
X-ray computed tomography (CT)	Ionizing radiation (X-ray)	50-200 μm	Millisec to sec (X-ray ~10 ms, CT ~0.5 s)	No limit	X-ray absorption by tissues
Magnetic resonance imaging (MRI)	Radiowaves	~25-500 μm	Sec (~0.5 sec)	No limit	Tissues proton density
Positron emission tomography (PET)	Ionizing radiation (High energy γ-rays)	1.5-4 mm	Min (~5 min)	No limit	Radiolabel atoms decay in tissues
Single-photon emission computed tomography (SPECT)	Ionizing radiation (Lower energy γ-rays)	1-4 mm	Min (~10 min)	No limit	Radiolabel atoms decay in tissues
Ultrasound (US)	Acoustic waves	~50 μm	Millisec (~40 ms)	mm-cm	Tissues impedance difference
Optical coherence tomography (OCT)	Long wavelength light (near-infrared)	~10 μm	sec to min	~1-3 mm	Tissue's characteristic in optical scattering light
Optical	Visible light	2-5 mm	sec to min	1-2 cm	Excitation and emission light

Table 2.3: Advantages and disadvantages of different imaging modalities. Reproduced from [234].

Imaging modalities	Advantages	Disadvantages
CT	- Unlimited penetration depth - High spatial resolution - Whole body imaging - Short acquisition times (min) - Anatomical imaging - Differentiates osseous from soft tissue - Clinical translation	- Poor soft tissue contrast - Contrast dye injection - Radiation exposure - Limited sensitivity - No quantification - Moderately expensive
MRI	- Unlimited penetration depth - High spatial resolution - Whole body imaging - Excellent soft tissue resolution - Anatomical imaging - Differentiate osseous from soft tissue - Non-ionizing radiation burden - Clinical translation	- High cost - No quantification - Long acquisition times (min to h) - Limited sensitivity
PET	- Unlimited penetration depth - High sensitivity - Whole body imaging - Soft tissue imaging - Can be combined with CT - Clinical translation	- Radiation exposure - Limited spatial resolution - Long acquisition times (min to h) - High cost - need cyclotron or generator
SPECT	- Unlimited penetration depth (< PET) - High sensitivity - Whole body imaging - Combined with CT for anatomical imaging - Distinguish between radionuclides, (simultaneously imaging of multiple processes) - Clinical translation	- Radiation exposure - Limited spatial resolution - Long acquisition times (min to h) - High cost
Ultrasound	- Non-radiation - Non invasive - Inexpensive and available - Soft tissue imaging - Short acquisition times	- Operator dependency - Low spatial resolution - limited in some parts of body - No morphological information
Optical	- Short acquisition times - Highly sensitive and quantitative - Whole body imaging of animal - Can be combined with CT for anatomical imaging of animals - Inexpensive	- Limited depth penetration - Whole body imaging of humans not possible

The current clinical MR scanners are categorized into conventional (1-1.5 T), high-field (3-4 T) and ultra high-field (7-8 T), which depends on the intensity of the magnetic field. Conventional MR scanners provide a spatial resolution of ~0.8 mm which can be improved further to ~0.5 mm and ~0.1 mm for high field and ultra high-field scanners, respectively [235]. Higher field systems provide a higher signal to noise ratio and improve the imaging quality. However, availability of such high-field scanners for clinical applications is limited.

2.8.1.1 Magnetic particles as MRI contrast agents

MRI provides an excellent soft tissue contrast whereas its characteristic such as low sensitivity and limited resolution does not allow the visualization of the microstructures. To provide detailed physiological information and overcome insufficient contrast between certain diseased or abnormalities and normal tissues, the use of specific contrast agents is required. Contrast agents can improve the sensitivity and signal by accelerating proton relaxation and shortening the T_1, T_2 and T_2* relaxation times of the surrounding nuclei, producing increased signal intensity on T_1-weighted images or decreased signal intensity on T_2-weighted images, or both. The T_2* is the spin–spin relaxation time composed of differences from molecular interactions and intrinsic magnetic heterogeneities of tissues in the magnetic field. All the contrast agents produce changes in magnetic susceptibility by enhancing local magnetic field perturbation. This phenomenon enhances image resolution, reduces artifacts, and decreases scan time [45, 236]. The efficiency of a contrast agent is evaluated by the relaxivity including $r_1 = 1/T_1$, $r_2 = 1/T_2$, and $r_2* = 1/T_2*$ (mM^{-1} s^{-1}).

Most commonly used components for contrast enhancement can be classified based on their magnetic properties as paramagnetic (*e.g.* gadolinium-based agents (Gd^{3+}) and manganese (Mn^{2+})) or superparamagnetic (*e.g.* iron oxide nanoparticles). Paramagnetic gadolinium ions produce positive contrast (brighter) and accelerating spin-lattice (T_1) relaxation, while superparamagnetic iron oxide formulations lead negative contrast (darker) images by decreasing signal and affecting spin-spin (T_2) relaxation.

Susceptibility-based contrast in MRI provides a mean to amplify and visualize the effect of a magnetic particle, while its volume is greatly inferior to the spatial resolution of the system. In the presence of the MRI's homogeneous high strength magnetic field, magnetic materials with high magnetic susceptibility become magnetized. As a result, the agents induce inhomogeneities

in the local magnetic field (B_0) of the MRI to enlarge the effect of particles which is much larger than their actual size. If the degree of the distortion reaches the size of a typical MRI pixel (~0.5 mm^2), the inhomogeneity appears in the form of a signal loss artifact (hypo-intense signal) in the T_2^*-weighed gradient recalled echo (GRE) images. The susceptibility artifacts can serve as a source of contrast by showing the presence and the location of magnetic particles and cause the visualization of structures of tumor. The size, degree of the distortion, and intensity of the signal loss are directly proportional to the susceptibility of material, saturation magnetization, the total magnetic volume, the scan parameters (*e.g.* echo time (TE) and repetition time (TR)), and the scan sequence type (gradient-echo (GE) and spin-echo (SE) sequences) [237, 238].

2.8.1.2 Magnetic properties of magnetic particles

Magnetic nanoparticles have been widely used for biomedicine-based applications such as contrast agents in MRI and multimodality imaging, hyperthermia, targeted gene and drug delivery [231, 239-241]. In terms of magnetic susceptibility, most materials can be categorized as diamagnetic (non-magnetic materials), paramagnetic, ferromagnetic, and superparamagnetic.

Paramagnetism is the characteristic of the materials that become magnetized in the presence of a magnetic field but their magnetism disappears when the field is removed. Atoms or ions of these materials have unpaired number of electrons in their outer shell. The individual atoms with random orientation have intrinsic magnetic dipole moments which make them as a permanent magnet even in the absence of an applied field. Upon removal of the externally applied magnetic field, the material does not retain any magnetization and all the individual atoms return to their original state. Even at the presence of magnetic field only a small fraction of the spins will be oriented by the field and induces small magnetization. This is due to the thermal motion that randomizes the spin orientation and causes the small fraction of unpaired atoms to be aligned with the magnetic field unless they are exposed to absolute zero temperatures (-273˚C).

Ferromagnetic materials, as opposed to paramagnetic materials, exhibit a long-range ordering phenomenon at the atomic level which causes the unpaired electron spins to line up parallel with each other in a region called domain. Ferromagnetic materials are usually unmagnetized due to the multiple domains with random orientations with respect to one another. Once these materials subjected to an external magnetic field, all the individual magnetic domains are aligned with each other and orient parallel to the direction of the magnetic field. As a result, the material becomes

fully magnetized. Upon removal of the driving magnetic field, the individual domains keep their orientation parallel to the magnetic field and materials tend to retain the fraction of the saturation magnetization, this is called remanence magnetization (M_r) (Figure 2.20). The reason for this phenomenon is that parallel spin alignment is a preferred lowest-energy state and therefore some energy is required to demagnetize them. The tendency of ferromagnetic materials to remember their magnetic history is called hysteresis. The high magnetic susceptibility of these materials generates a high inhomogeneity in the magnetic field, and subsequently, they become suitably traceable in MR images. Adversely, the clinical applications of ferromagnetic materials with high magnetizations are limited due to their tendency to maintain a high M_r value.

Superparamagnetism occurs when the size of the multi-domain particles decreases to a nanometer sized single magnetic domain particle. The magnetization (M) initially increases sharply when it is exposed to a magnetic field until it reaches the maximum value known as the saturation magnetization (M_S). These materials will not retain any net magnetization property in the absence of an external magnetic field. The size of the individual magnetic domain is in the range of tens of nanometers and depends on the magnetic anisotropy.

2.8.1.3 Superparamagnetic iron oxide nanoparticles in MRI

Superparamagnetic iron oxide (SPIOs) nanoparticles contrast agents have been vastly investigated as MRI negative contrast agents for various biomedical applications such as angiogenesis imaging in tumors [242, 243] and molecular-cellular imaging and tracking [231, 239, 244]. The parameters that affect the relaxometric behavior of these magnetic particles include size, structure, coating, and concentration of the particles within an imaging voxel. Figure 2.20a, b depicts the magnetization curve of iron oxide (Fe_3O_4) particles that are widely used as MRI contrast agents [245]. A transition from ferromagnetic multi-domain structure to superparamagnetic single-domain structure occurs with the reduction of the particles size to approximately 30 nm, which is accompanied by a decrease in the saturation magnetization (Figure 2.20a). Even though the superparamagnetic particles have smaller magnetization than ferromagnetic materials, lower aggregation formation in the absence of the magnetic field make them suitable options to be used as contrast agents in MRI for *in vivo* applications.

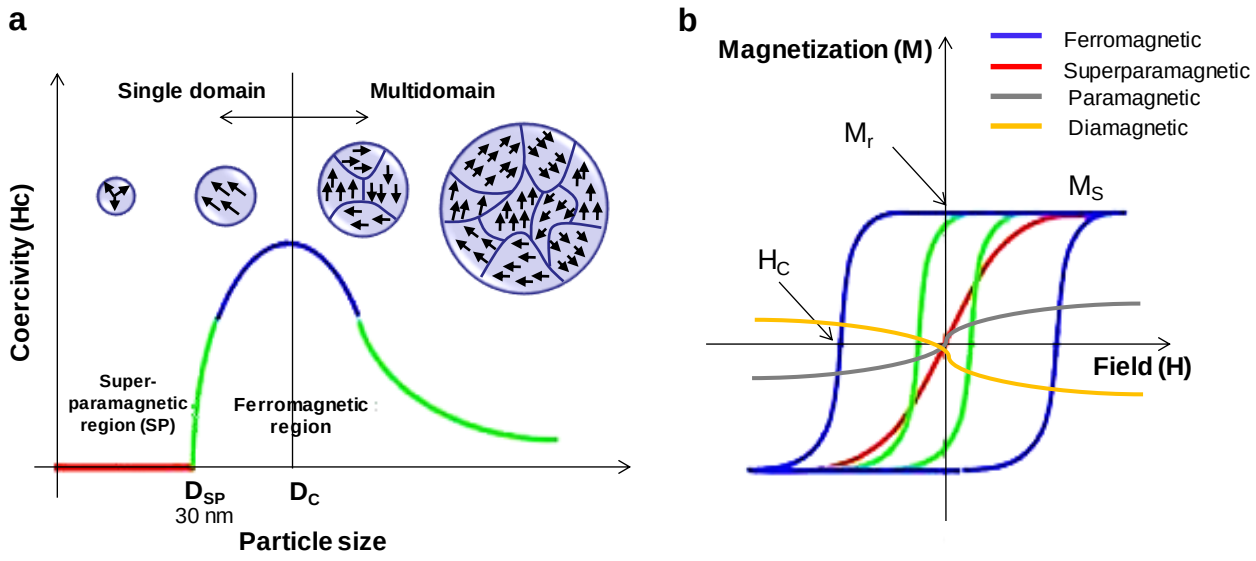

Figure 2.20: (**a**) Typical magnetization hysteresis loop of magnetic materials. (**b**) Transition from multi-domain to single-domain to superparamagnetic regimes of Fe_3O_4 and also their magnetic domain morphology [245].

SPIOs contrast agents are mostly in two main forms of magnetite (Fe_3O_4) and its oxidized form maghemite (γ-Fe_2O_3) [246] with a core diameter in the range of 4-12 nm. Both are water insoluble iron oxide crystals and require modifications, for instance, polymer coating [65] or encapsulation in liposomes [134]. Modified SPIOs have shown higher physico-chemical stability, lower aggregation, greater circulating half-life and biocompatibility [9, 247] compared to the Gd [231, 248-250]. For instance, conventional intravenously administration of Gd-chelates has a toxic effect that can be nephritic [248, 249]. To target a specific site in the body and induce a hyperintense signal in the vicinity of the targeted regions, ligands such as antibodies, peptides and aptamers could also be grafted onto the surface of the MRI contrast agents [251, 252].

Even though the SPIOs show higher saturation magnetization than Gd-based contrast agents, causing a higher sensitivity and enhancing proton relaxation in the field of MRI [243], SPIOs do not own the highest saturation magnetization among the magnetic materials. Iron-cobalt nanocrystals coated with graphitic carbon, as an alternative to SPIOs, have the highest magnetization among all magnetic materials and can lead to the visualization of smallest vessels in MR images [2]. However, drawbacks of using such a material are the easy oxidation and the

potential toxicity. These characteristics make the SPIOs as a promising contrast agent. Two example of SPIO-based contrast agents that are clinically approved include ferucarbotran (Resovist; 60 nm) [253] and ferumoxides (Feridex or Endorem; 120 to 180 nm) [254].

The MR imaging of SPIOs formulations is usually achieved by the T_2/T_2*-weighted imaging sequences and SPIOs are mostly effect on the shortening T_2* relaxation time. The tissue signal loss (void) induced by magnetic field inhomogeneity is due to the susceptibility effects of the iron oxide core and is considered as an indication of the presence of the particles in the tissue [255]. The signal voids can also be caused by the presence of different sources of negative contrast. For instance, tissues with a low proton density result in an undesirable negative contrast and encumber the distinction of the negative contrast associated with the magnetic particles. Consequently, the magnetic particles cannot be distinguished from a void in the image. To overcome the problem, positive contrast images can be acquired through modifying sequences and employing T_2-weighting for the tissues containing SPIOs [256, 257]. The T_1-weighted images are not as sensitive as the T_2-weighted counterparts in detecting SPIO nanoparticles, but still affected by such particles providing the T_1-weighted imaging with a less pronounced positive T_1-contrast effect [242, 258].

2.8.1.4 Magnetic resonance imaging of MTB

The embedded magnetosomes inside the MTB are single domain superparamagnetic iron oxide nanoparticles (SPIONs). Similar to MRI contrast agent, when the MTB is exposed to the MR magnetic field, the magnetosomes become magnetized and cause a local distortion of the homogenous magnetic field inside the bore of a MRI scanner [36, 73, 80, 259]. The magnetosome chain in MC-1 MTB is consisted of 11 magnetosomes (~70 nm) aligned in chain and 20 nm distance between each of them.

In the present of MTB, the T_1 and T_2 relaxation times are affected by the magnetic field perturbations. The relaxivities of contrast agents in MRI can be calculated by:

$$r_{1,2} = \frac{1}{T_{1,2}} = r_{1,2}^{0} + \alpha_{1,2} C \tag{2.1}$$

where $r_{1,2}^{0}$ (r_1, r_2) are the relaxation rates without the presence of the contrast agent (medium), C is the concentration of the contrast agent ([MTB] ml^{-1}), and $\alpha_{1,2}$ are the relaxivity constants (T_1-

and T_2-relaxivity) of the agent expressed in unit of mM^{-1} s^{-1}. $\alpha_{1,2}$ is a property specific to the effect of MTB on the NMR signal [259]. Relaxation values are then estimated by fitting the data to a monoexponential decay curve.

Felfoul *et al*. (2007) demonstrated that the presence of magnetosomes caused a local distortion of the homogenous magnetic field of MRI *in vitro*. The T_1 and T_2 relaxivities for different concentration of MTB ((6.7, 6.2, 4.8, 3.5, 2.2, and 0) × 10^7 MTB ml^{-1}) using 1.5 T MRI scanners was calculated [73, 259]. As shown in Figure 2.21a, MTB show slightly higher signal compared to the medium in T_1-weighted images in which the signal intensity improvement is not significantly concentration-dependent. However, as shown in Figure 2.21b, T_2-weighted images are more affected by MTB concentration. As the concentration of MTB enhances, the signal decay becomes more significant. In general, both T_1 and T_2 value decrease by presence of MTB in a manner inversely proportional to the concentration. However, due to the inherent characteristic of superparamagnetic MRI contrast agents the effect of magnetosome chain on T_2 is found to be more significant than on the T_1. They also showed that the MTB at a concentration of 2.2 × 10^7 MTB ml^{-1} can be detected *in vitro* using a clinical 1.5 T MRI scanner. For the concentration of < 10^6 MTB no contrast was observed compared to the background and for the concentration more than 5 × 10^9 signal was completely disappeared [259].

Benoit *et al*. (2009) demonstrated the visualization of the magnetotactic bacteria (*AMB-1* strain) in mice tumor xenograft using MRI equipped with customized coils. They reported the possibility to generate either positive (T_1-weighted) or negative (T_2-weighted) MR contrast *in vitro* [80]. Moreover, positive contrast was obtained in mice tumor xenografts after direct intratumoral (*i.t.*) injection of approximately 5 × 10^8 low-Fe *AMB-1* cell (in 25 μl Magnetospirillum medium) containing 6.0 ultra-small superparamagnetic iron oxide particles with an average size of 25.3 nm (Figure 2.21c). Moreover, they examined the systemic injection of 1 × 10^9 *AMB-1* suspended in 100 μl media via tail-vein (Figure 2.21d). Overall, their results demonstrated that the *AMB-1* cells can produce positive contrast in tumor xenografts following *i.t.* and intravenous (*i.v.*) injection.

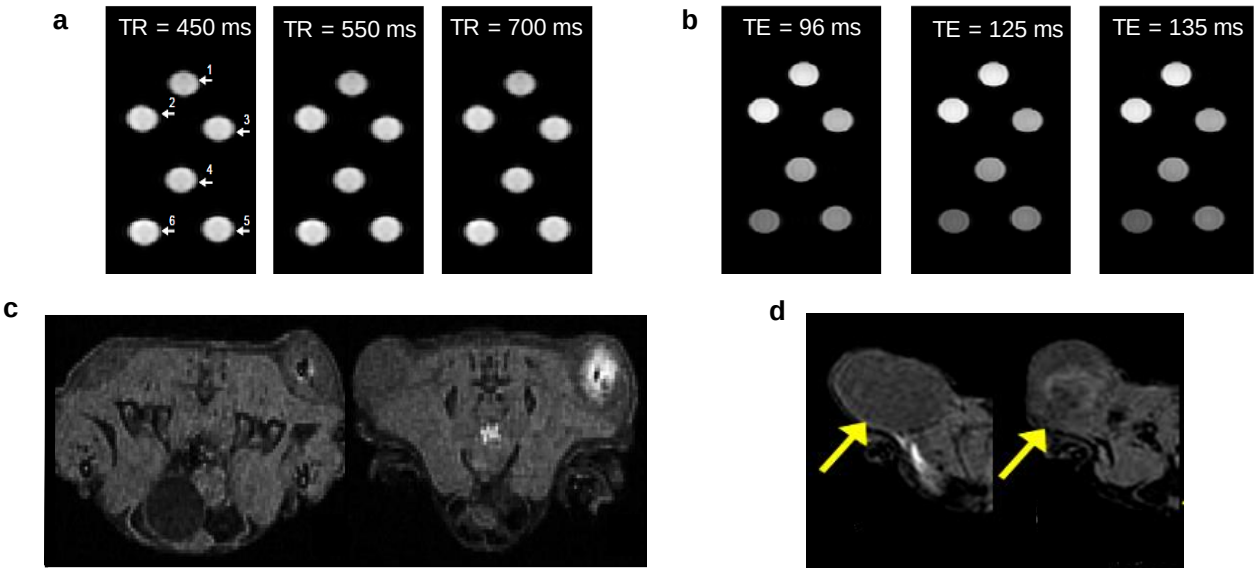

Figure 2.21: (**a**) T_1-weighted images of MC-1 MTB at different concentration using SE sequence with TE = 11 ms, TR = 450/550/700 ms, slice thickness of 20 mm, and pixel spacing of 0.586 mm. Insert numbers from 1 to 6 indicate increasing in the concentration. (**b**) T_2-weighted images of several MC-1 MTB concentrations using fast spin echo sequence with TE = 96/125/135 ms, TR = 5096 ms, slice thickness of 20 mm, and pixel spacing of 0.293 mm. a and b reproduced form [259]. (**c**) T_1-weighted MR images of *AMB-1* cells show enhanced signal (positive contrast) in mouse tumors 1 day after *i.t.* injection (right) but not in the control tumor (injected with media) immediately post-injection (left). (**d**) T_1-weighted images of tumor prior to *i.v.* injection of media (left) and 2 days post-injection of *AMB-1* (right). c and d adapted from [80].

2.9 Tumor imaging modalities

The structural and functional differences between normal tissues and tumors in overexpression of biomarkers (*e.g.* HIF-1) and enzymes (*e.g.* proteases), leaky angiogenesis, and acidic environment can be used for tumor diagnosis and therapeutic approaches. Currently, standard methods for tumor assessment are serial invasive biopsy sampling, monitoring the changes in tumor size by physical examinations, or biological- and anatomical-based imaging techniques. However, the reduction in tumor size is a relatively late consequence of effective therapy, which is the main drawback by physical examination.

Biopsy sampling followed by histological analysis is a precise technique to assess the degree of response to treatment. The technique provides detailed information on cellular proliferation, tumor products, and expression of receptors. However, biopsy as an invasive technique has inadequate spatial sampling, needs multiple time point biopsies, and contains significant sampling error.

The anatomically-based imaging methods for the characterization of tumors and their environment include MRI [228, 229], X-ray/CT scan [260], ultrasound [225], and optical imaging [226, 227]. These techniques offer regional information and can determine the extent of tumor and differentiate tumors from normal tissue based on tumor size, shape, density, vascularity, and relative fat/water content but provide limited information regarding the tumor biological/metabolic activities.

The tumor biological/metabolism-based imaging technique can be beneficial to assess regional tumor biochemistry and for planning biologically directed treatments. This biological imaging technique may overcome the inherent limitations of serial biopsy and able to evaluate response to treatment at a much earlier time than anatomical-based methods. This can be performed by PET scan that employs different tracers to target the various areas of tumor and provides substantial information on regional biological properties such as hyper-glucose metabolism [261], tumor hypoxia [262], cellular proliferation [263], expression of particular tumor receptor, protein, and gene products. Limitations of PET arise from the short half-life radionuclides tracer, the risk of pharmacologic toxicity and radiation burden for the patient [264]. Although PET has a relatively high spatial resolution (1.5-4 mm), it provides limited anatomical information on the tumor, therefore requiring added-on physical imaging tools such as X-rays/CT scans and MRI.

2.9.1 Tumor angiography imaging

From the therapeutic perspective, visualization of angiogenesis network provides important information on the tumor microenvironment. It allows evaluating of the functional changes and the efficiency of applied treatments such as chemotherapy, radiotherapy or targeted therapy. Further, it provides information about blood vessel growth, blood flow and vascular permeability, cellular and molecular abnormalities in the blood vessel and vascular heterogeneity. Advanced imaging modalities for tumor angiogenesis are classified into (i) invasive microscopic optical imaging (fluorescence, bioluminescence) methods [61, 265] and (ii) clinical noninvasive imaging

(MRI, CT, PET, ultrasound color flow Doppler imaging [266], and digital subtraction angiography (DSA)) techniques. Microscopic techniques provide high-resolution images (confocal microscopy (~100 nm), and electron microscopy (few nanometers)) while the clinical imaging methods provide the ability to visualize deep living tissues and larger arteries and veins. However, these techniques are unable to image the microvasculature due to low resolution (MRI and CT (100 to 500 μm), PET (1.5-4 mm), ultrasonography and optical imaging (few millimeters)), Doppler color flow (~200 μm), and DSA (~180-200 μm). These approaches are promising but rely on a systemic injection and sub-optimal transportation of the agents through the blood flow.

2.9.1.1 PET imaging of angiogenesis

Various PET contrast agents provide different functional information about the tumor [265, 267]. For instance, [^{18}F]-2-fluoro-deoxy-D-glucose (^{18}F-FDG), which mainly reflects tumor metabolism, can be used to localize primary tumors and metastases (Figure 2.22a, left). ^{11}C-carbon monoxide (CO) agent reflects blood volume within tumors. After inhalation, labeled CO irreversibly binds to erythrocytes and is distributed in accordance with vascular volume (Figure 2.22a, right) [265].

2.9.1.2 MRI of angiogenesis

MR imaging of tumor angiogenesis can perform through accumulation of the contrast agents in any area that has increased blood flow and provide positive or negative contrast. The contrast agents with a longer half-life in the circulation, such as modified SPIONs and Gd protected with albumin, dendrimers, graft copolymer, and liposomes can improve visualization of angiogenesis architecture [228, 268]. Kobayashi *et al*. (2001) showed the tumor vascularity using Gd-dendrimer. High molecular weight Gd-dendrimer (400 kDa) cannot extravasate the tumor vessels and remains intravascular, which changed local relaxivity and displayed larger tumor blood vessels (Figure 2.22b, bottom). They also showed that the lower molecular weight Gadolinium-diethylenetriamine pentaacetic acid (Gd-DTPA) (547 Da) extravasated rapidly and created a uniform positive contrast in the tumor (Figure 2.22b, top) [268]. However, detailed 3D map of the microvessels is not possible using this technique.

2.9.1.3 X-ray/CT imaging of angiogenesis

Figure 2.22c shows an example of the X-ray images after rapid intra-arterial infusion of an iodinated contrast agent [265]. The drawbacks of the technique consist of an insufficient resolution to resolve the microvasculature, exposure to ionizing radiation, and potential nephrotoxic of iodinated agents. Figure 2.22c (inset) shows the CT angiography with an intravascular latex contrast agent. Preclinical techniques suitable for scanning of small animals such as microMRI and microCT provide much high spatial resolution (~10-20 μm) but have poor temporal resolution [269, 270]. They have the high signal-to-noise ratio using a surface coil but a partial penetration depth and limited sensitive area. However, long scanning time in the microCT involves large radiation exposures that can reach the lethal dose limit in the small animals.

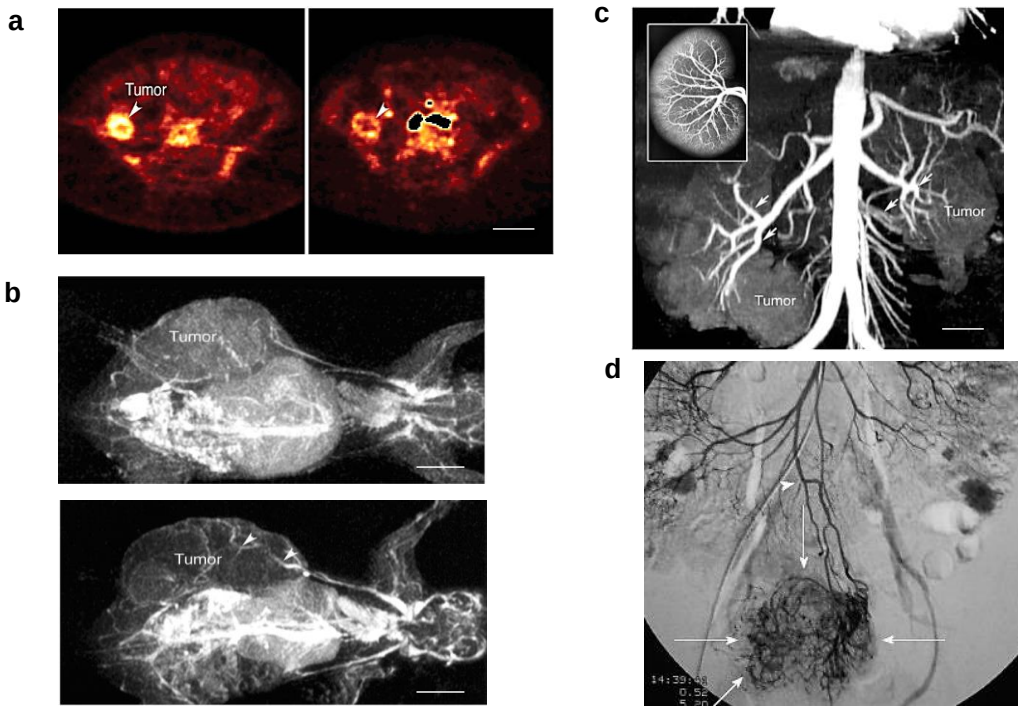

Figure 2.22: *In vivo* angiography imaging of tumors. (**a**) PET images of a renal tumor showing a metastatic tumor (arrowheads) in the pelvis using ^{18}F-FDG (left); ^{11}C-CO reflects tumor blood volume (right). Adapted from [267]. (**b**) The MRI of the tumor of rapidly extravasated 547 Da Gd-DTPA (top) and 400 kDa Gd-dendrimer agent (bottom), which remains intravascular (arrowheads). Adapted from [268]. (**c**) CT angiogram of artery branches (arrows) in renal tumors. The incorporated image shows the angiographic image of renal vasculature after *i.v.* injection of latex. Adapted from [265]. (**d**) DSA images acquired from gastrointestinal stromal tumors. Adapted from [271]. Scale bar is 5 cm in a; 5 mm in b; 3 cm (inset 4 cm) in c.

2.9.1.4 DSA imaging of angiogenesis

DSA considered as the reference imaging modality in the determination of the tumor location, identification of the bleeding, and visualization of vascular structure [272]. Figure 2.22d shows the DSA images from gastrointestinal stromal tumors [271]. The DSA images can be produced by exposing the region with time-controlled X-rays while injecting contrast medium into the blood vessels. The method is useful for the visualization of large arteries and veins but the visualization of microvasculatures less than 200 μm remains an issue. Other limitations involve invasive intra-arterial catheterization and using an iodinated contrast agent with potential nephrotoxic. Also, a rapid drop in the contrast level of *i.v.* injected iodine caused limited imaging time frame with the resultant 2D images [273].

2.9.2 Tumor hypoxia imaging

The assessment of tumor hypoxia can provide information regarding the impact of treatment strategies, follow-up the response to a therapy after the onset of treatment, or predict the tumor resistance to chemotherapy or radiotherapy. Various invasive and noninvasive techniques are available to evaluate tumor hypoxia and its metabolism [13, 274]. According to their principles and ability to quantify tissue oxygenation, current clinical and preclinical techniques to assess hypoxia are categorized into (i) indirect measurements (*e.g.* histological staining) and (ii) direct measurements which consist of oxygen tension (pO_2) polarographic needle electrode, optical imaging, radionuclide PET, SPECT, and MRI methods.

2.9.2.1 *In vitro* histological staining of tumor hypoxia

The histology staining can quantitatively assess the parameters associated with tumor oxygenation and its metabolism using exogenous hypoxia markers (*e.g.* nitroimidazole derivates such as misonidazole, pimonidazole, EF3, and EF5) and endogenous hypoxia-related proteins (*e.g.* HIF-1α, carbonic anhydrase IX, and osteopontin) on tumor biopsy samples [275, 276]. The exogenous markers typically form stable adducts with intracellular macromolecules when the oxygen pressure is less than 10 mmHg [276]. For IF staining, several antibodies have been developed against nitroimidazole, EF3, EF5, and pimonidazole biomarkers. Meijer *et al.* (2012) demonstrated the targeting of HIF-1 hypoxia biomarker by pimonidazole staining in head and neck tumor xenograft (Figure 2.23a). However, the technique suffers from relatively inadequate

sampling of the tumor, lack of spatial coverage, and the necessity of frequent sampling for the evaluation of treatment response.

2.9.2.2 Polarographic needle electrode

The direct measurement of oxygen tension (pO_2) in hypoxic regions using invasive polarographic needle electrodes can predict treatment response and the metastatic potential of tumors but it is limited to easily accessible tumors such as head and neck cancer, cervical, lung, and prostate [277]. Indeed, insertion of an electrode into the tumor requires a great expertise, disrupts tissues, and has difficulty to distinguish necrotic areas to differentiate the patterns of hypoxia. The studies confirmed that polarographic needle electrode is less sensitive than exogenous markers [278].

2.9.2.3 Optical imaging of tumor hypoxia

The optical imaging of tumor microenvironment using bioluminescence, fluorescent, near-infrared (NIR) [279], and phosphorescence probes plays a significant role in assessing the tumor hypoxia. The techniques are constructed based on the characteristic feature of hypoxia such as pH differences, overexpressed molecular markers (*e.g.* HIF-1), and enzymes (*e.g.* proteases) in the tumor microenvironment [226, 227] and are designed based on the shift of excitation and emission spectra of the probes when they are exposed to the tumor milieu. Bioluminescence imaging techniques are capable of measuring the products of tumor metabolism by highlighting the spatial distribution of high energy areas, high glucose and the waste products such as lactate generated by glycolysis [280]. Saha *et al*. (2011) showed the HIF-1α bioluminescence imaging of tumor hypoxia dynamic in the brain over the six weeks *in vivo* (Figure 2.23b) [280]. Due to the biological complication of tumor hypoxia, typically combinations of various markers have been used to create a hypoxia-prognostic profile [56]. One of the limitations of the techniques is the very low value expression of HIF-1α or other markers. In NIR spectroscopy spectral changes of excited light (650-900 nm) with transmitted or reflected light through tissue are recorded for the quantification of oxygen concentration in the tumor vasculature. The pO_2 of the tumor vascular can also be evaluated by phosphorescence imaging following the injection of an albumin loaded with a metal porphyrin complex (Oxyphor) into the vasculature. The level of oxygen can be measured by oxygen-dependent quenching of phosphorescence [281]. However, clinical translation of optical imaging is limited due to the low spatial resolution, low sensitivity, limited path length, light scattering, and being affected by the environment.

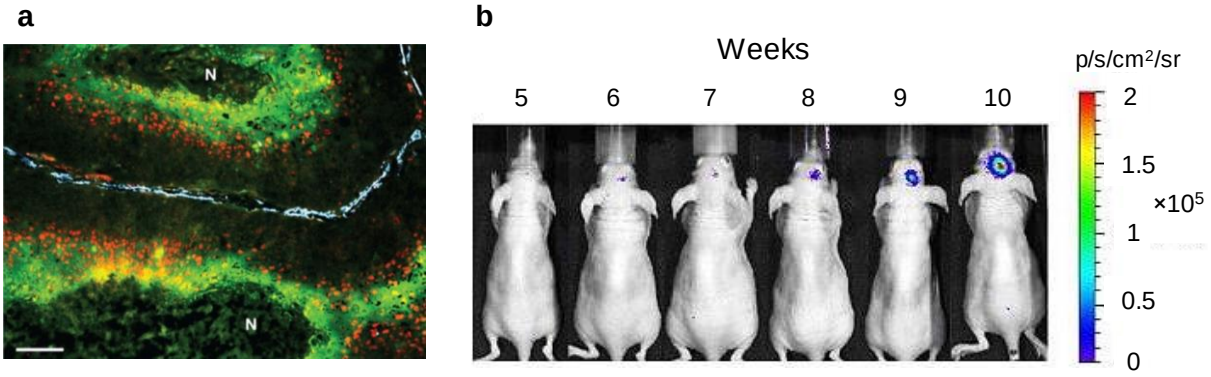

Figure 2.23: Optical imaging of tumor hypoxia. (**a**) Immunofluorescence image of a human head and neck carcinoma xenograft displays expression of HIF-1α (red) in hypoxic regions as evaluated by pimonidazole staining (green). The white color indicates a blood vessel and N indicates necrotic cells. Scale bar represents 100 μm. Magnification 100×. Adapted from [282]. (**b**) *In vivo* HIF-1α bioluminescence assay showing a dynamic tumor hypoxia over the period of 6 weeks in a breast cancer brain metastasis implanted in a nude mouse. Adapted from [280].

2.9.2.4 MR imaging of tumor hypoxia

The MRI techniques to investigate tumor hypoxia and oxygenation of its environment include dynamic contrast-enhanced (DCE), blood oxygen level-dependent (BOLD)-MRI, tissue oxygen level-dependent (TOLD)-MRI, ^{19}F MRI, and oxygen-enhanced MRI (OE-MRI). Jordan *et al.* (2013) developed MRI sequences that are sensitive to tumor oxygenation, which is called mapping of oxygen by imaging lipids relaxation enhancement (MOBILE) technique [283]. In this method, oxygen serves as paramagnetic endogenous contrast probes that by changing the relaxation time and susceptibility can help to distinguish diseased tissue from normal tissue. Crayton *et al.* (2011) showed that the metabolically directed pH-titratable SPIONs or glycol chitosan-SPIONs can penetrate and accumulate in acidic tumor environment following *i.v.* administration. They demonstrated that the presence of the probes in the tumor hypoxia can generate a signal loss in T_2*-weighted images and reveal a hypointense heterogeneous region in the tumor [284].

DCE-MRI. This modality enables to analyze oxygen tension, tumor angiogenesis and their permeability, and decipher tumor heterogeneity. After *i.v.* injection of contrast agents, well-vascularized/perfused regions are visualized by rapid contrast extravasation from the blood

vessels to the extracellular matrix followed by quick washout. Reduced vascularized hypoxic regions are recognized by delayed contrast signal buildup and the agents remain much longer in the tissue causing a decrease in relaxation time and higher contrast compared to normal tissue [285]. The necrotic areas exhibit quiet slow or no discernible contrast uptake. Stoyanova *et al.* (2012) studied the DCE-MRI using the Gd-DTPA *in vivo* to identify pattern of tumor microenvironment by measuring the signal buildup within the hypoxia [45].

BOLD and TOLD MRI. BOLD- and TOLD-MRI, as tumor vascular and tissue oxygenation, respectively, are involved in oxygen-induced MR effects in tumor hypoxia, [286]. The TOLD is associated with T_1 relaxation time changes affected molecular O_2 in tissues. The BOLD is developed to exploit the differences in T_2 relaxation induced by regional changes in deoxygenated hemoglobin levels. In oxygen-deficient states, intravascular oxyhemoglobin (diamagnetic) is presented as deoxyhemoglobin (paramagnetic), which acts as image contrast that induces a reduction in MR signal and affect the T_2/T_2*relaxation rates [287]. These qualitative techniques have disadvantages of being easily affected by environment factors such as hematocrit concentration, flow effects, pH, and temperature [288]. Simultaneous use of TOLD and BOLD during a single dynamic MRI may provide complementary information [289].

^{19}F MRI. Fluorine (^{19}F) MRI uses two types of markers as contrast agents including fluorinated nitroimidazoles and perfluorocarbons (PFCs). The ^{19}F T_1 relaxation rate of hydrophobic PFCs with high oxygen solubility varies linearly with the dissolved oxygen concentration, which allows to quantify the oxygenation levels *in vivo* [290]. However, the measurements are easily affected by the blood flow artifacts, dilution, pH, rapid clearance [291]. Fluorinated nitroimidazole have also shown good results in detecting hypoxia while the toxicity profile such as neuropathy and acute central nervous system (CNS) remain as a major drawback [279].

OE-MRI. OE-MRI is based on the effect of dissolved paramagnetic dioxygen (O_2) molecules in blood and tissue interstitial fluid on the MRI signal that result in enhancing the T_1 relaxation rate [292]. Linnik *et al.* (2014) employed the OE-MRI to evaluate the tumor vasculature, perfusion, and tumor oxygenation compared with DCE-MRI data and IF biomarkers in murine U87 glioma xenografts as well as in patients with glioblastoma [292].

2.9.2.5 PET imaging of hypoxia

Using noninvasive PET for assessing tumor hypoxia *in vivo* requires the administration of an positron-emitting radioisotope including ^{124}I, ^{18}F and $^{60/64}$Cu labeled with the hypoxia molecular biomarkers such as 2-nitroimidazoles derivates (*e.g.* fluoromisonidazole (FMISO) [293], EF5 [294], and fluoroetanidazole (FETA) [295]), nucleoside conjugates (*e.g.* iodoazomycin arabinoside (IAZA)) [293], and Cu (II)-diacetyl-bis (N4-methylthiosemicarbazone) (Cu-ATSM) [296]. The significant hypoxia imaging agent uptake requires a hypoxic level of typically less than 10 mmHg [276, 297]. After uptake and retention of markers, the stable adducts formation between markers and hypoxic cells can be detected by exposing the patients to the ionizing radiation of PET scanner. The compound can be rapidly reoxidized and removed from the normoxic cells, and thus providing good differentiation between hypoxic and normal cells.

2.9.2.6 Combination of existing imaging methods

Co-injection of multiple tracers and the combination of different imaging techniques resulted in improvement of measurements. For instance, the coinjection of ^{18}F-FAZA (hypoxia marker) and ^{18}F-RGD (angiogenesis marker) allow hypoxia to be correlated with angiogenesis [298]. In another study, the combination of ^{18}F-FDG (glycolysis marker) and ^{18}F-FMISO (hypoxia marker) allow hypoxia to be corresponded with glycolysis [297]. Combination of DCE-MRI and PET imaging was used for noninvasive assessment of neck nodal tumor metastases [236, 285]. In PET/CT metabolic or biochemical activity can be correlated with anatomic imaging [224].

Cho *et al.* (2009) showed the spatial distribution of hypoxic regions in an animal model by combination of DCE-MRI (7 T) and PET using Gd-DTPA and ^{18}F-FMISO, respectively [285]. They also studied the hematoxylin and eosin (H&E) staining and uptake of pimonidazole hypoxia marker (Figure 2.24a). They used the Akep values which defined as (kep = rate constant of movement of Gd-DTPA between the interstitial space and plasma and A = amplitude in the two-compartment model) resulting from DCE-MRI studies indicated that tumor angiogenesis is a major determinant of early Gd-DTPA uptake. The correlation between DCE-MRI, DCE-Akep, H&E, and pimonidazole slices provided a powerful tool for imaging and characterizing the tumoral hypoxia, necrotic and well-oxygenated regions (Figure 2.24a).

Lewis *et al.* (2008) reported PET/CT imaging of uterine cervix cancer in which ^{64}Cu-ATSM and ^{18}F-FDG were served as a hypoxia radiopharmaceutical marker and metabolic marker, respectively (Figure 2.24b) [296].

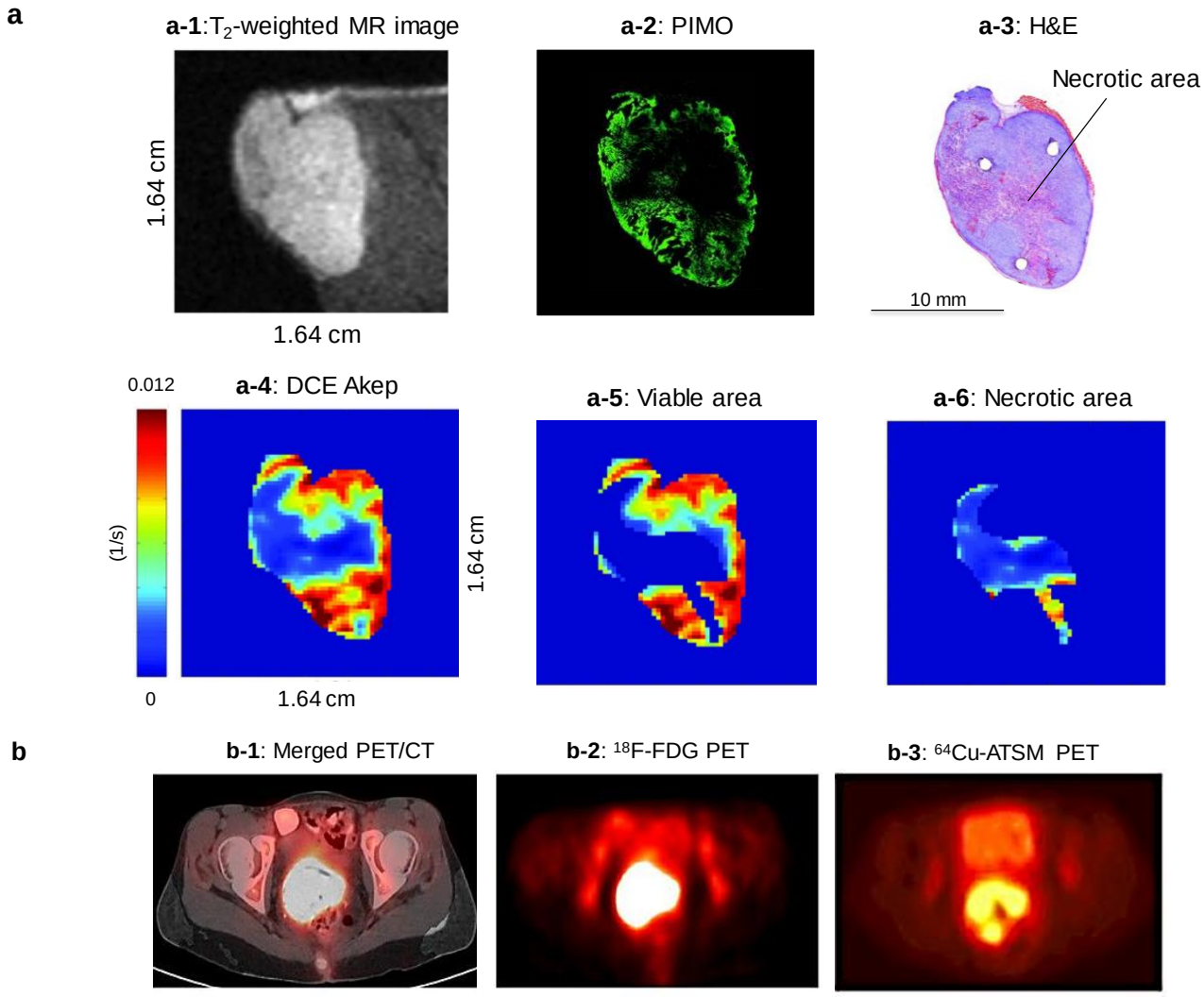

Figure 2.24: (**a**) Imaging of hypoxic, necrotic, and perfused areas in the tumor. T_2-weighted MR image using Gd-DTPA (a-1), corresponding pimonidazole-stained (PIMO) (a-2) and H&E-stained tissue section (a-3), corresponding DCE Akep map (a-4) and the masked Akep values for the viable tumor (a-5), and necrotic areas (a-6). Reproduced from [285], with permission from the Neoplasia. (**b**) Transaxial PET/CT (b-1), ^{18}F-FDG PET (b-2), and ^{64}Cu-ATSM PET (b-3) images of pelvis demonstrate markedly uptake of ATSM (hypoxia marker) and FDG (metabolic marker) within cervical tumor at site of cervical mass at same level on CT. Reproduced from [296].

Overall, although MRI, CT, and PET provide detailed information about size, angiogenesis, metabolism, and location of tumors, the sub-millimeter resolution of MRI and millimeter resolution of PET are insufficient to detect the microstructure of the tumors. The literature review of available imaging techniques revealed that currently there is no standard method in the clinical or pre-clinical setting to reliably image tumor microstructure and map the tumor hypoxia *in vivo*.

CHAPTER 3 ARTICLE 1: COVALENT BINDING OF NANOLIPOSOMES TO THE SURFACE OF MAGNETOTACTIC BACTERIA FOR THE SYNTHESIS OF SELF-PROPELLED THERAPEUTIC AGENTS

The following published journal article meets objective 1 of this thesis that is the formulation, functionalization, and conjugation of liposome nanoparticles on the surface of the MTB to be explored as a drug delivery system. To attain this objective, the bioconjugation was performed based on the carbodiimide chemistry, which resulted in the stable covalent bonding. The MTB-LP complexes were characterized in terms of attachment efficacy, swimming behavior, magnetic response, cytotoxicity, and cellar uptake. The attachment efficacy was found to be related to the incubation time and the concentration of the components. A substantial number of nanoliposomes (~70) were efficiently attached to MTB without compromising swimming behavior and their magnetic response. The cytotoxicity and cellular uptake capabilities of the MTB-LP were assessed in cancerous and non-cancerous cell lines. It was demonstrated that MTB-LP could be used as a drug delivery vehicle, and the attachment does not inhibit the liposomal uptake. That was the first published article featuring the bacteria as a bio-carrier that can be used for the different applications such as drug, genes, imaging agents, and so on.

The results of this study were published as a journal article entitled “Covalent Binding of Nanoliposomes to the Surface of Magnetotactic Bacteria for the Synthesis of Self-Propelled Therapeutic Agents” by the Journal of *ACS Nano* in 2014.

Covalent Binding of Nanoliposomes to the Surface of Magnetotactic Bacteria for the Synthesis of Self-Propelled Therapeutic Agents

Samira Taherkhani[1,2], Mahmood Mohammadi[1], Jamal Daoud[2],

Sylvain Martel[1,*], and Maryam Tabrizian[2,3,*]

[1] NanoRobotics Laboratory, Department of Computer and Software Engineering, Institute of Biomedical Engineering, Polytechnique Montréal, Montréal, Québec, Canada H3C3A7.

[2] Department of Biomedical Engineering, Faculty of Medicine, McGill University, Montréal, Québec, Canada H3A2B4.

[3] Faculty of Dentistry, McGill University, Montréal, Québec, Canada H3A0C7.

*Address correspondence to: (sylvain.martel@polymtl.ca) and (maryam.tabrizian@mcgill.ca).

The table of content graphic, which accompanied this article, is presented below.

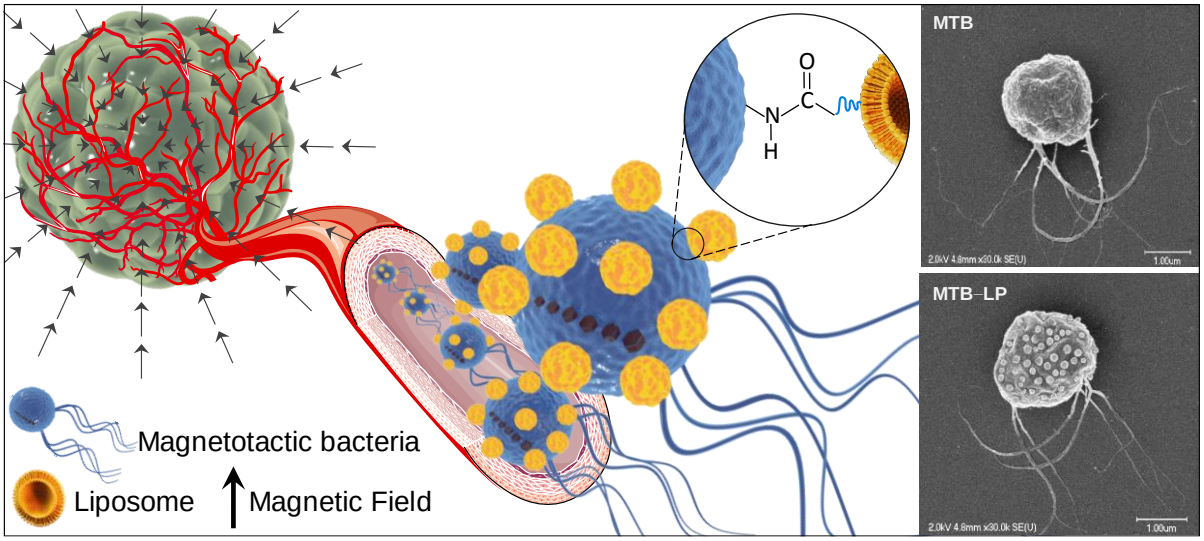

3.1 ABSTRACT

The targeted and effective delivery of therapeutic agents remains an unmet goal in the field of controlled release systems. *Magnetococcus Marinus* MC-1 magnetotactic bacteria (MTB) are investigated as potential therapeutic carriers. By combining directional magnetotaxis–microaerophilic control of these self-propelled agents, a larger amount of therapeutics can be delivered surpassing the diffusion limits of large drug molecules toward hard-to-treat hypoxic regions in solid tumors. The potential benefits of these carriers emphasize the need to develop an adequate method to attach therapeutic cargos, such as drug-loaded nanoliposomes, without substantially affecting the cell's ability to act as delivery agents. In this study, we report on a strategy for the attachment of liposomes to MTB (MTB–LP) through carbodiimide chemistry. The attachment efficacy, motility, and magnetic response of the MTB–LP were investigated. Results confirm that a substantial number of nanoliposomes (~70) are efficiently linked with MTB without compromising functionality and motility. Cytotoxicity assays using three different cell types (J774, NIH/3T3, and Colo205) reveal that liposomal attachments to MTB formulation improve the biocompatibility of MTB, whereas attachment does not interfere with liposomal uptake.

Keywords: magnetotactic bacteria; nanoliposome; bioconjugation; carbodiimide chemistry; self-propelled targeted delivery; bio-microcarrier

3.2 INTRODUCTION

Over the past several decades, various systems for the delivery of therapeutic agents such as polymeric micro/nanoparticles [67], liposomes [145], and magnetic-based nanoparticles [134], relying on active or passive targeting mechanisms [299] of therapeutics, have been designed and evaluated in animal models as well as in clinical trials [2]. However, nonspecific distribution throughout the systemic circulation can still cause substantial toxicity and adverse side effects [300]. Among nanosized delivery systems, liposomes [145] are of particular interest, since they are biocompatible, exhibit low immunogenicity and high flexibility, protect the body from potentially toxic cargo, shield therapeutic agents from premature degradation, control release kinetics [8], and may concurrently encapsulate a multitude of hydrophilic and/or hydrophobic drug cargos, pharmaceutical ingredients, imaging agents [133], and genetic material by virtue of

their aqueous interior and lipid exterior [40, 134]. Drawbacks of the systemic application of liposomes include poor pharmacokinetic profiles, incomplete local targeting, lack of deep tissue penetration, nonspecific biodistribution, and limited retention at sites of delivery [12]. The suboptimal concentration of such therapeutic agents reaching the region to be treated cannot generally diffuse deeper in the interstitial space due to a lack of flow caused by the Tumor Interstitial Fluid Pressure (TIFP) [54]. Therefore, conventional administration of such liposome-based systems often requires sustained levels of drugs to achieve therapeutic efficacy. Further from the diffusion limit of larger drug molecules, hypoxic microenvironments of tumors with approximately < 0.7% O_2, resulting from oxygen consumption caused by the rapid proliferation of cancer cells [13], are more resistant and highly difficult to treat. Such lacks of oxygenated regions not only impede radiotherapy treatments [301], but chemotherapy as well, since hypoxic cells are distant from blood vessels and beyond the diffusion limit of larger drug molecules [12, 13]. One strategy to minimize adverse side effects and enhance the therapeutic index in hypoxic regions is the use of targeting agents with propelling capabilities that can counteract TIFP effects, following a directionally guided transit toward the tumor with the additional capability of the agent to seek the hypoxic regions prior to the release of the therapeutics [107]. Self-propelled agents capable of some autonomy in navigating pathways, such as flagellated bacteria, could be potential candidates for targeted delivery to deep tumors. To date, bacteria including *Escherichia coli* [31], *Salmonella* [29], and other genera have been shown to preferentially accumulate in tissues by aerotaxis or chemotaxis suggesting the potential application of bacterial-based therapeutics. Although these bacteria can be used as therapeutic agents, they are not compatible with computer-based navigation toward tumoral regions, which would most likely enhance targeting efficacy.

In addition, to navigate and transport therapeutic agents within low Reynolds hydrodynamic conditions, such as the microvasculature (blood flow of few mm s^{-1} and diameter of approximately 4–8 μm) [104] and to reach deep inside tumors, a controllable propulsion and steering system with an appropriate size is required. Microcarriers should not exceed 2 μm in diameter [32, 36, 100]. Moreover, since the size of the openings in leaky tumor vessels are typically less than 2 μm in diameter between endothelial cells [60], the maximum diameter of each navigable microrobotic agent must remain below 2 μm if such openings are to be exploited to enhance targeting deeper within solid tumors.

To address this issue, flagellated *Magnetococcus Marinus* MC-1 magnetotactic bacteria (MTB) [33] with computer-based navigation compatibility along with appropriate steering and propulsion kinetics have been identified as such potential delivery agents with the aforementioned functionalities [36]. The combination of a flagella attached to a round cell body with a diameter around 1 to 2 μm is ideal for transiting effectively in the microvasculature, the angiogenesis network, and the interstitial space of solid tumors. Two bundles of flagella enable an average initial swimming velocity of approximately 200 μm s^{-1} (100–150 body (cell) lengths per second). Self-propulsion properties also enable the bacteria to penetrate regions that are inaccessible by passive therapies [36]. A chain of iron oxide nanoparticles, known as magnetosomes [34, 35], allows magnetotaxis control to entail such bacterial cells to aggregate in a specific region within 3D volume time-varying magnetic field sequences [108] prior to rely on the microaerophilic behavior of the MTB to target hypoxic regions. One of the many critical steps toward the potential use of such a carrier for delivering therapeutics is to develop a method of loading the bacteria while maintaining its capability for deep targeting of solid tumors. The approach presented herein relies on the fact that amine groups on the surface of gram-negative bacteria cells [302] such as MC-1 MTB enable them to covalently attach to various compounds, such as carboxylated liposomes, to allow design of the powerful targeted delivery systems. This is the grounding hypothesis of the work for developing a new drug delivery strategy using bacteria-conjugated nanoliposomes (MTB–LP) that can follow a navigation pattern, deeply penetrating tumors by propulsion from the flagella and external magnetic fields controls. A bioconjugation method based on a carbodiimide dehydrating agent [195, 303, 304] was developed for the covalent binding of amine containing molecules of bacteria to carboxylated liposomes. The MTB–LP complex was then thoroughly characterized for its structural properties, mobility in directional magnetic field, cellular uptake, and cytotoxicity in relevant cell models in order to demonstrate the feasibility of the proposed strategy for effective target drug delivery.

3.3 RESULTS

3.3.1 Characterization of the MTB–LP complex

The colocalization of TRITC-labeled nanoliposomes with MTB at excitation/emission wavelengths of ~555/580 nm indicate nanoliposome attachment on the surface of MTB and the

formation of the complex using confocal laser scanning microscopy (CLSM) (Figure 3.1a). To further confirm the successful formation of the complex, fluorescence-activated cell sorting (FACS) was performed. The density plots indicate that bare bacteria exhibit a higher forward scatter (FSC) and smaller amount of fluorescence than fluorescent nanoliposomes alone (Figure 3.1b, left). The MTB–LP plot combines the fluorescence intensity characteristic of nanoliposomes together with the forward scattering characteristics of bacteria cells, distinguished by a broad distribution of fluorescence intensity from that of bare bacteria. Considering that any fluorescent signal exclusively originates from attached liposomes, the percentage of the MTB–LP complex was determined by extracting its fluorescence intensity from controls. The events number and intensity distribution in four quadrants as a percentage of the total of 25,000 events are presented using FlowJo software. It can be concluded that more than 90% of the bacteria were associated with TRITC labeled nanoliposomes and considerable number of liposomes were attached homogeneously to bacteria. These results were also confirmed with the intensity distribution histograms of MTB–LP complexes (Figure 3.1b, right). Samples were characterized by comparing monomodal fluorescence intensities between each sample. Fluorescent nanoliposomes could clearly be differentiated from bacteria as the latter possess no or minimal background autofluorescence. In addition, the fluorescence intensity distributions of MTB–LP are broader and extend to higher intensities than those observed for bare bacteria indicating the successful bioconjugation between bacteria and nanoliposomes. The relative fluorescence intensity value of the fluorescent liposomes alone was approximately 160-fold higher than that of bacteria cells, while it was only 1.5-fold greater than MTB–LP.

To confirm confocal and FACS analyses and quantify the number of attached nanoliposomes to each bacteria, field-emission scanning transmission electron microscopy (FE-STEM) analysis was carried out. A comparison between SEM images of MTB–LP after multiple washing steps and those of bare MTB confirmed stable attachment of nanoliposomes to the bacterial cell membrane (Figure 3.1c).

The number of attached nanoliposomes to individual bacteria was dependent on concentration and incubation time (Figure 3.2). For a 1 h incubation time, the number of attached nanoliposomes increased gradually with liposome concentration from 0 to 400 μl of 15 mM liposomes. In the case of 2 h, results demonstrate that this number markedly increases with liposome concentrations from 0 to 100 μl. For a concentration of 4×10^7 MTB cells (10^7MTB ml$^-$

[1]), approximately ~70 ± 5 nanoliposomes could attach when 100 μl of 15 mM liposomes (250 μg ml^{-1}) were used. Further increasing the volume of liposomes up to 400 μl did not improve the efficiency of the attachment and it reached a plateau after a 250 μg ml^{-1} liposomal concentration. This concentration was therefore chosen for all further experiments and analyses.

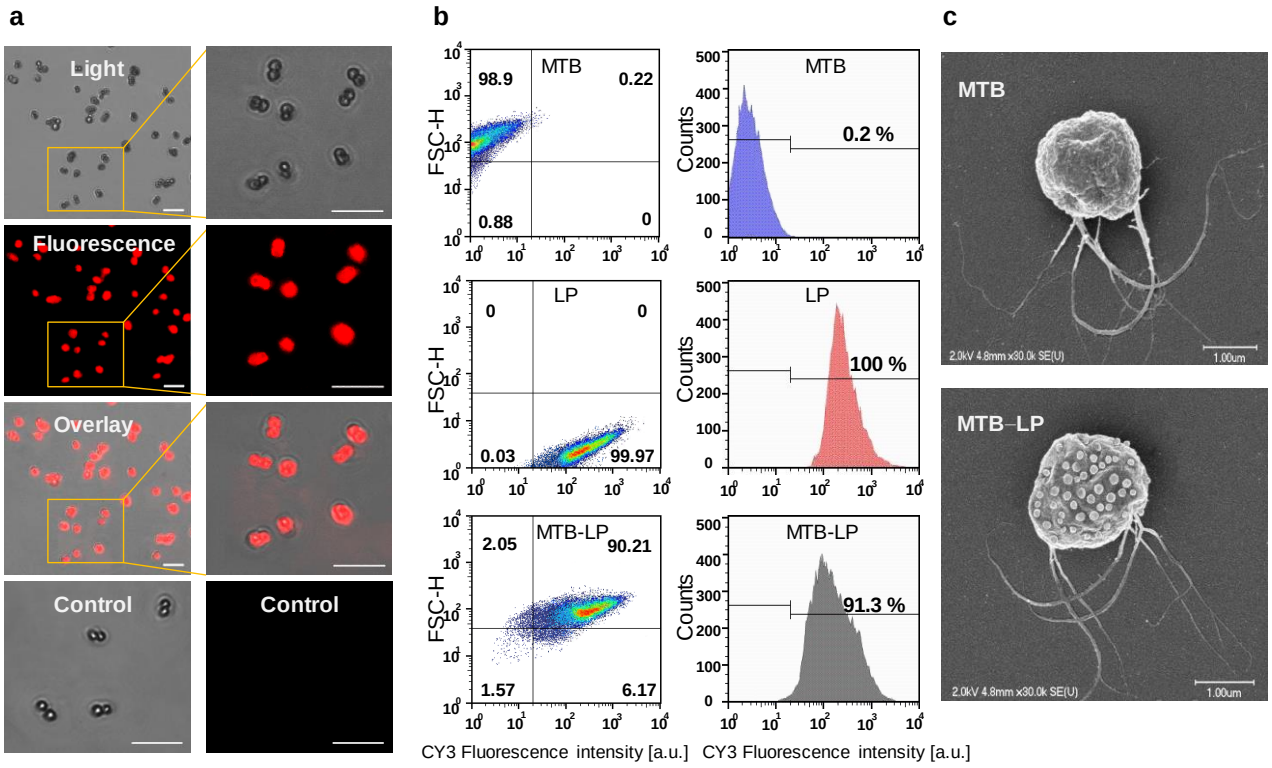

Figure 3.1: Characterization of nanoliposomes attached to the surface of MC-1 MTB. (**a**) Confocal microscopy images of TRITC labeled MTB–LP complexes. Photomicrographs show the phase contrast, fluorescence and overlay confocal images. Unlabeled bacteria were used as control. Scale bars show 5 μm at 60× magnification. (**b**) FACS density plots (left) and histograms (right) obtained from noncoated MC-1 bacteria, TRITC-labeled nanoliposomes, and MTB–LP complex show that bacteria are homogeneously coated with nanoliposomes and can be differentiated from bare bacteria by their fluorescence. Labeling efficacy was determined by dividing the percentage of labeled bacterial cells to total cells. (**c**) Field emission scanning electron microscopy images of bare MC-1 MTB and MTB–LP complex. The scale bar corresponds to 1 μm. All results are represented as the mean of five independent experiments.

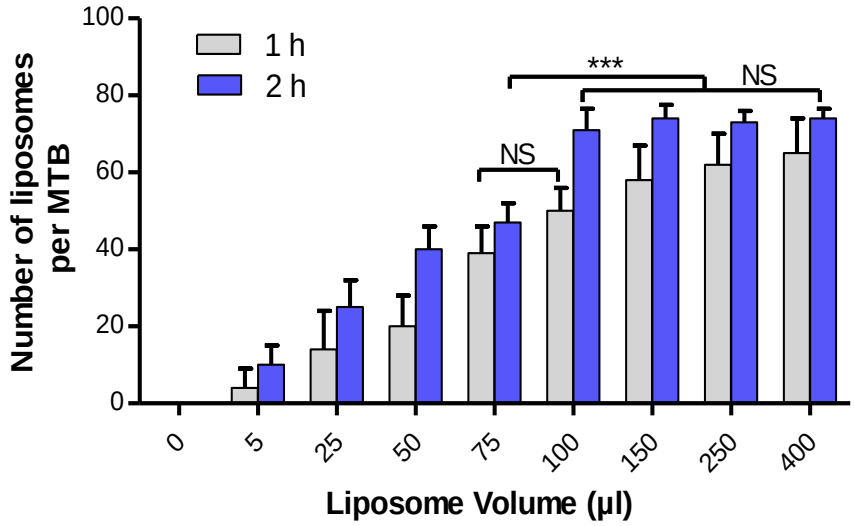

Figure 3.2: Quantification of the number of nanoliposomes attached to MTB cells by FE-STEM as a function of nanoliposome concentrations in volumes of 0, 5, 25, 50, 75, 100, 150, 250, and 400 μl (15 mM stock solution) for exposure times of 1 and 2 h. The results are presented as the mean number of attached nanoliposomes ± *SD*, $n = 3$. Results indicate that under 1 h incubation, the number of attached nanoliposomes gradually increases with liposome concentration. While after a 2 h incubation, bacterial surface saturates at volumes exceeding 100 μl. Statistical analysis was performed using two-way ANOVA. *P*-value < 0.001 marked with asterisk (***) is considered significantly different and $P > 0.05$ is not significant (NS).

3.3.2 Monitoring the magnetic response and swimming behavior of MTB–LP complex

To ascertain maximum loading of MTB while maintaining maximum velocity after the attachment of the nanoliposomes, the motility functions of MTB–LP such as swimming speed and response to applied magnetic fields were evaluated with a custom-made experimental magnetic component and an optical microscope (Figure 3.3a, b). The magnetic setup was composed of four permanent magnets facing each other two by two to generate a homogeneous two-dimensional magnetic gradient (Figure 3.3b). The magnetic gradient field direction was oriented toward the center with gradually decreasing magnitude to 0 G at the center. The magnet setup was placed under an optical microscope, and observation was carried out at the specific

position where a directional magnetic field of approximately 20 G resulted in straight swimming paths of the bacteria.

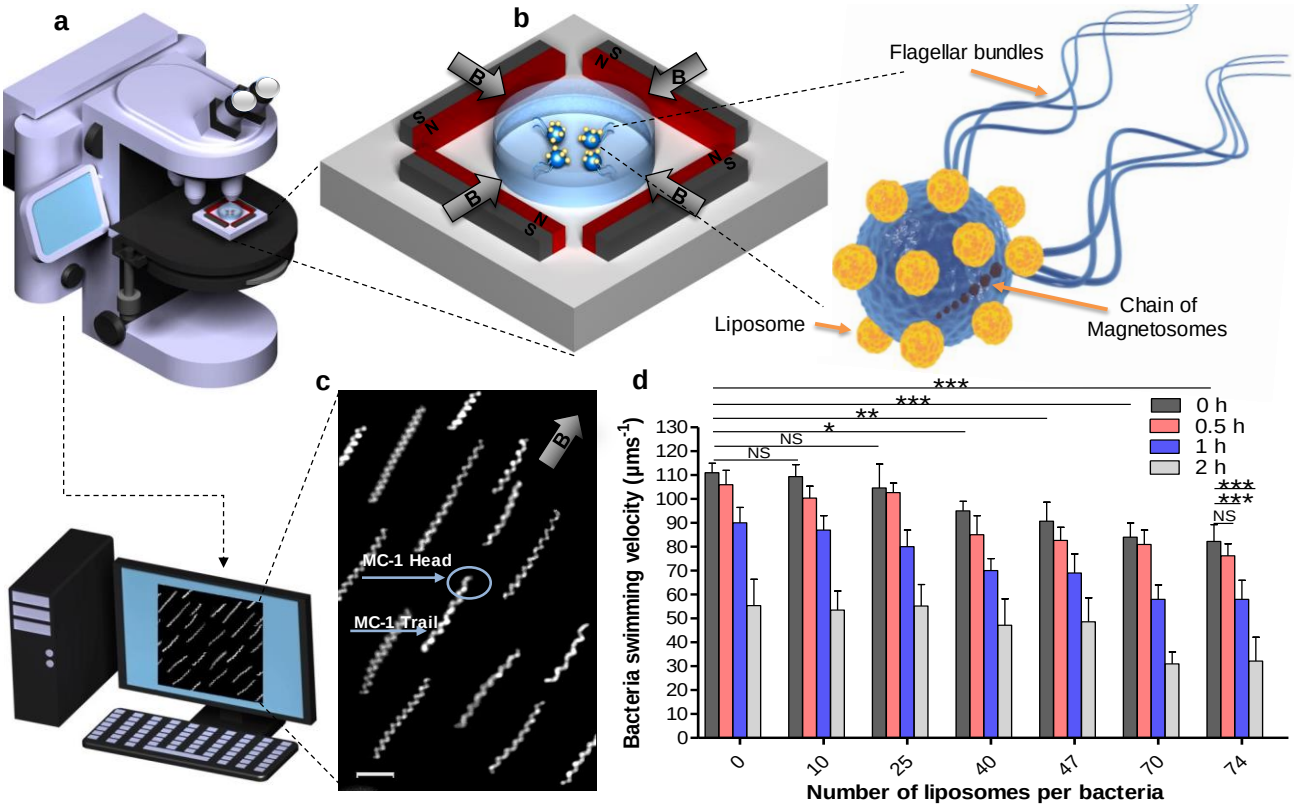

Figure 3.3: Schematic representation of the experimental setup used to track and visualize MTB–LP complex magnetotactic behavior. (**a**) Optical microscope. (**b**) Side view of the two-dimensional magnetic navigational setup including four permanent magnets that generate a homogeneous magnetic field toward the center of the device. Arrows depict the direction of the magnetic field. (**c**) Motility track of MTB–LP complex under the influence of the magnetic field. Images were recorded by dark field optical microscopy using a 200 ms exposure time for the helical motion in response to 20 G magnetic field. Scale bar indicates 5 μm. (**d**) The average terminal swimming speeds of loaded and bare MTB (none preselected) *versus* the number of attached nanoliposomes in PBS at room temperature 0, 0.5, 1, and 2 h after washing. Results indicate a decrease of bacterial motility caused by bioconjugation of nanoliposomes to the cell membrane. Data are presented as mean ± *SD*, $n = 3$. Statistical analysis was performed using two-way ANOVA. Significant difference was considered for $^{*}P < 0.05$, $^{**}P < 0.01$, $^{***}P < 0.001$ and not significant (NS) for $P > 0.05$.

The helical motion and trail left of the MTB could therefore be evaluated by decreasing the shutter speed of the camera to 200 ms (Figure 3.3c). Results show that the terminal swimming velocity of MTB–LP complexes is dependent on the number of nanoliposomes attached to bacteria, since the increased number of attached nanoliposomes reduces the motility (Figure 3.3d). MTB–LP complexes carrying up to approximately 70 liposomes responded to a similar magnitude of the magnetic field as compared to bare bacteria prepared and tested in the same conditions. At early time points *i.e.*, 30 min, the terminal velocity of these highly loaded complexes could reach around 80 μm s^{-1}. Results also indicate that the residency time of MTB–LP complexes in PBS has a major impact on the mobility of the bacteria. Long incubation times (more than 2 h) in buffer solution significantly decrease the motility of both MTB–LP and bare bacteria (Figure 3.3d). The motility of MTB–LP complexes with 70 nanoliposomes dropped to 32 μm s^{-1} after 2 h suggesting that the complex should be used for self-propelled target delivery purposes within 30 min of the preparation.

3.3.3 Biological characterization of MTB–LP complex

Cell viability graphs are presented for different concentrations of MTB–LP complexes at different incubation times (3, 6, 12, 24, and 48 h) using WST-1 assay (Figure 3.4). The viability of all tested cell lines (NIH/3T3, J774, and Colo205) were time, MTB–LP, and MTB bacteria dose dependent. Maximum cytotoxic levels were observed at highest bacterial concentration (10^8 MTB/well) after 48 h of incubation. No significant cell viability reduction could be observed between 24 and 48 h exposure times for NIH/3T3 and J774 (Figure 3.4a, b, d, e). Interestingly, the viability of MTB–LP was similar to bare nanoliposomes for Colo205 at MTB concentrations ranging from 2×10^5 to 6×10^6 (Figure 3.4h, i). In contrast, Colo205 cells demonstrated a significant increase in cytotoxicity for concentrations ranging from 6×10^6 to 10^8 MTB/well for both MTB–LP complex and bare MTB (Figure 3.4g, h). The MTB–LP exhibited a less cytotoxic effect on tested cell types at all concentrations compared to bare MTB (approximately 20–40%) indicating that the cell viability was improved through the attachment of nanoliposomes on the surface of bacteria. The free nanoliposomes in the experimental range of 0.07–40 μM did not induce significant cytotoxicity on tested cell types (Figure 3.4c, f, i).

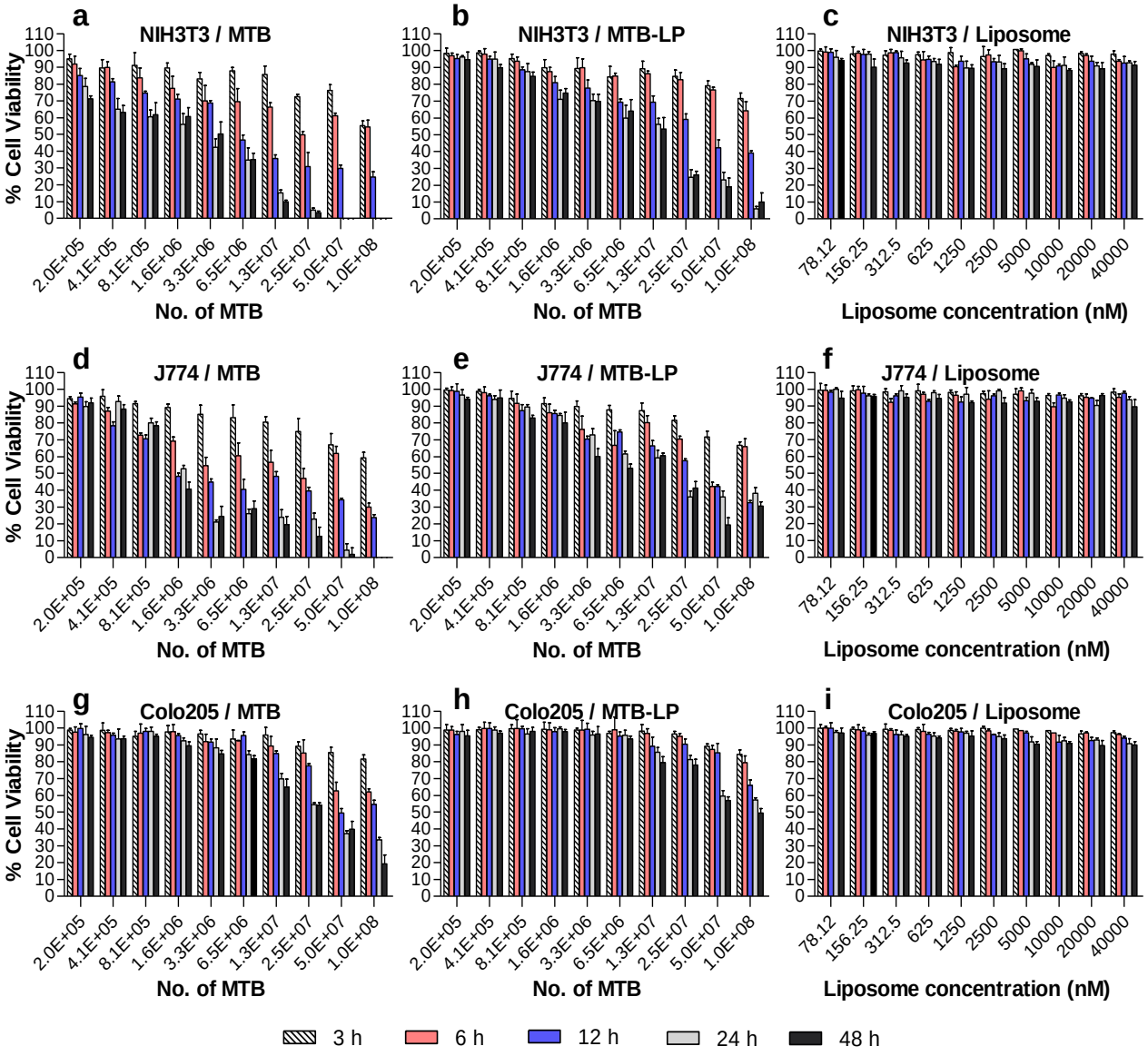

Figure 3.4: Inhibitory effects of MTB formulation on viability of tested cell lines. Effect of incubation time and concentration of MTB–LP complex on viability of NIH/3T3 (**a–c**), J774 (**d–f**), and Colo205 (**g–i**) cell lines as compared to bare MTB and bare nanoliposomes using the WST-1 assay. Cells were incubated for 3, 6, 12, 24, and 48 h at 37 °C with 2×10^5 to 10^8 (MTB/well) for MTB/MTB–LP and 0.07–40 μM for bare nanoliposomes. Viability responses were found to be cell-type, dose, and time dependent. While the results show that cells survive long after exposure to bare nanoliposomes, the bacterial formulations reduced viability of the tested cell lines. Cancer cells were shown to be less vulnerable than normal cells. Results demonstrate that cell viability was greater for MTB–LP compared to bare MTB. Data were normalized to untreated cell lines (controls). Error bars, mean ± *SD*, $n = 4$.

The comparison of half maximal inhibitory concentration (IC_{50}) values for MTB and MTB–LP in three tested cell lines indicates that a lower incubation time requires higher concentrations to reach the IC_{50} (Table 3.1). The rank order of IC_{50} associated with bare MTB and MTB–LP cytotoxicity was as follows: Colo205 > J774 > NIH/3T3. In addition, results reveal that the cytotoxicity is reduced when the biocompatible nanoliposomal moieties are attached to the bacteria. In this case, higher concentrations of MTB–LP complexes are needed to reach the 50% cell survival rates compared to bare MTB.

Table 3.1: IC_{50} Values of the MTB and MTB–LP for the tested cell lines [a]

		Incubation time				
Cell type	**Samples**	**3 h**	**6 h**	**12 h**	**24 h**	**48 h**
NIH/3T3 Fibroblast	**MTB- LP**	1.255×10^7	1.042×10^7	9.779×10^6	6.286×10^6	9.076×10^5
	MTB	3.289×10^6	3.149×10^6	1.980×10^6	1.172×10^6	7.179×10^5
J774 Macrophage	**MTB- LP**	4.838×10^7	2.727×10^7	1.506×10^7	9.639×10^6	6.720×10^6
	MTB	8.244×10^6	7.050×10^6	4.533×10^6	2.722×10^6	9.175×10^5
Colo205 Cancer cells	**MTB- LP**	1.945×10^8	1.784×10^8	8.164×10^7	4.047×10^7	1.284×10^7
	MTB	9.721×10^7	8.052×10^7	4.219×10^7	2.930×10^7	8.321×10^6

[a] Data are presented as the numbers of MTB in each well. MTB has growth-suppressive effects comparable with those of MTB–LP in tested cell lines. Data were normalized to untreated cell lines (controls) $n = 3$.

Incubation of fluorescent MTB–LP complexes with the cell lines and subsequent observation by confocal microscopy shows localization of complexes mainly in the cytoplasm and perinuclear region (Figure 3.5a). The same localization was also found for fluorescence bare liposomes used as control (Supporting information Figure S3.8). Overall, the samples internalized and migrated in a time-dependent manner toward the nucleus of cells but did not enter the nucleus. Z-stack

confocal images reconstructed using Imaris image analysis software (Bitplane AG) confirm that complexes are indeed internalized by the cells and not simply bound to their surface (data not shown). CellProfiler image analysis software was used to quantify the fluorescence signal intensity of uptaken nanoliposome alone and complexed. To derive an accurate quantification, the ratio of fluorescence intensity of internalized liposomes or MTB–LP relative to cell nuclei was calculated. As shown in Figure 3.5b, the MTB–LP uptake is cell-type dependent. J774 cells as a phagocytic cell model display the highest uptake capabilities for both free nanoliposomes and MTB–LP complexes compared to the two other nonphagocytic cells. Fluorescence signal related to MTB–LP uptake increased in nonphagocytic cell lines after a 6 h incubation.

Moreover, the complex exhibits significantly enhanced translocation into the J774 and NIH/3T3 cells as compared to Colo205 cancer cells. Interestingly, although free liposomes could generally be internalized faster relative to MTB–LP in nonphagocyte cells, the level of uptake is higher for the complex than for bare nanoliposomes, particularly by J774 cells. The fluorescent signal intensity increased gradually until 12 h incubation in J774 and NIH/3T3 cells and then reached a plateau suggesting that cells has reached their saturation capacity, while accumulation continued in cancer cells and significant uptake improvement was measured when the incubation time was extended to 24 h.

3.4 DISCUSSION

Despite advancements in targeted drug delivery, many relevant diagnostic and therapeutic products, including local and systemic administration by ligand-drug-conjugates [299, 305] or Magnetic Drug Targeting (MDT) [306, 307], have not been entirely effective, and clinical trials are still forthcoming. Various methods of MDT have investigated the applicability of superparamagnetic iron oxide nanoparticle (SPION) [307] and Fe–Co nanoparticles [67], as well as magnetosomes isolated from MTB [303, 308] for MR imaging, targeting, and drug delivery [307, 309]. To date, however, concerns regarding poor pharmacokinetic profiles, force limitations of small magnetic carriers in complex microvascular networks [68], lack of navigation to organs located deep in the body [32], poor depth penetration, and cytotoxicity remain barriers to clinical entry. The proposed MTB–LP complex combines several novel aspects that can overcome many of the aforementioned limitations relative to traditional polymeric and magneto-based platforms and render the system as a viable vehicle for target drug delivery.

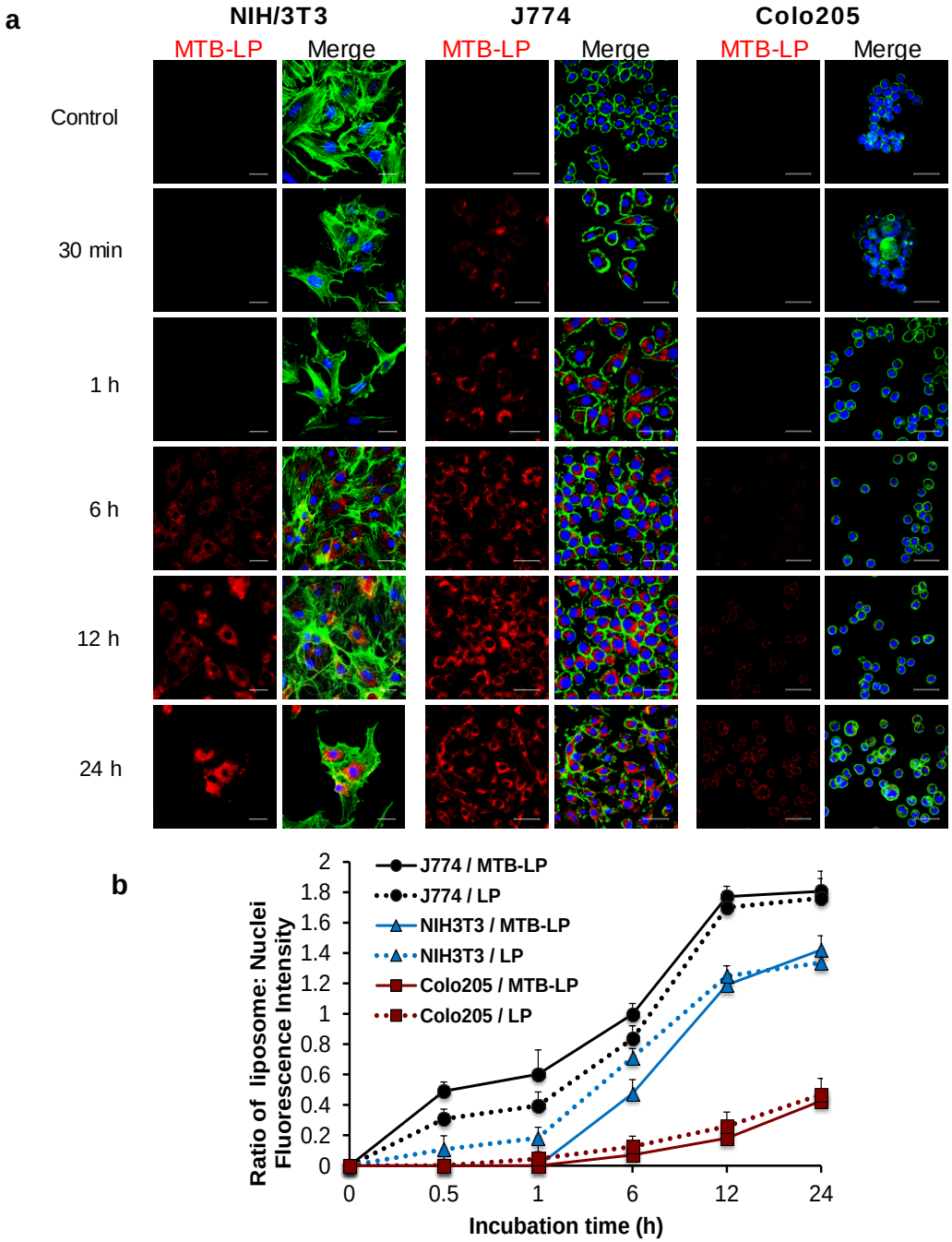

Figure 3.5: (**a**) Confocal microscopy images of time-dependent MTB–LP complex uptake by J774, NIH/3T3, and Colo205 cell lines at different incubation times. Fluorescently labeled nanoliposomes exhibit a very strong fluorescent signal. Actin filaments were visualized with Alexa Fluor 488 Phalloidin (green) and nuclei were stained with Hoechst 33342 (blue). The pictures were taken at the midsection of the cells. Bar indicates 30 μm. (**b**) The values reported are obtained by dividing the fluorescence intensity of bare liposomes or MTB–LP by that of nuclei in each fluorescence image over time. Values represent mean ± *SD*, $n = 3$.

The proposed route of injection for MTB–LP would be peritumoral (PT) injections for solid tumors that are accessible (*e.g.*, colorectal, prostate), to avoid the vasculature where the blood flow (ranging from a few tens of centimeters per second) [310] could carry the agents away from the intended target. For PT-based interventions, drug-loaded MTB can be directly injected in the vicinity of the tumor and as close as possible to the angiogenic microenvironment without touching the tumor mass to take advantage of the directional blood flow toward the tumor with minimal flow rate and to reduce the risk of systemic toxicity.

Bioconjugation was performed using a carbodiimide dehydrating agent [195, 303, 304] by taking advantage of terminal amine groups on the outer membrane of bacteria that are ideal docking sites for amide covalent attachment of carboxylated nanoliposomes to MTB cells. These functional amine groups are present as parts of organized phospholipids, lipopolysaccharides (LPS), lipoproteins and surface proteins assemblies such as lysine, *D*-alanine, or polypeptides [311, 312]. Carbodiimide cross-linking is a versatile technique used to prepare biomolecular probes, conjugate antibodies, peptides, proteins, and *etc.* onto nano/microparticle [313, 314], and immobilize macromolecules for use in numerous applications [213], demonstrating a stable chemical bond for *in vitro* and *in vivo* applications. The merits of the carbodiimide technique include the ease of sample preparation, high coupling efficiencies, reproducibility, reduced cost, and, most importantly, high strength bond. It should be noted that the enthalpies ($\Delta H°_{298}$) for amide bond formation using carbodiimide chemistry and bond dissociation enthalpies range from 375–422 and 305–440 kJ mol^{-1}, respectively [315]. The dissociation energy is much higher compared to other methods such as antibody–antigen affinity type bioconjugation including van der Waals forces, electrostatic forces, hydrogen bonds, and hydrophobic effects, which range from 4 to 30 kJ mol^{-1} [316]. Therefore, the covalent amide bonds are much stronger than affinity-based antibody conjugation and require considerable energy to break. It is robust in an *in vivo* environment and also compatible with MTB compared to other bioconjugation techniques. For instance, passive adsorption through electrostatic or van der Waals type attractions [317] suffers from poor stability for *in vivo* applications. Noncovalent affinity based bonds such as biotin–avidin [318] rely on manipulation of both bacteria and liposomes, which cause treated MTB to lose their functionality and viability due to the treatment processes and excessive use of chemical reagents. Antibody conjugation [319] for immunoliposome [203] preparation also has major drawbacks, specifically the cost involved in custom antibody production, especially for

monoclonal antibodies. The lack of specificity of polyclonal antibodies could result in targeting both the bacterial head and flagella, which can negatively affect the velocity and straight motility of the bacteria.

In physiological conditions, amide bonds are not affected by medium conditions such as pH or ions and are quite resistant to imposed mechanical forces. Moreover, hydrolysis and enzymatic cleavage (by serum proteins/cellular secreted products) of amide bonds is highly dependent on the microenvironment condition and exposure time [320]. Considering that the bacteria can only survive for 40 min at body temperature due to their nonpathogenic nature [36], the *in vivo* navigation would be performed in under 30 min, in which the covalent bonds would likely remain stable. This bioconjugation technique provides a one size fits all approach matching the experimental conditions required for the MTB cell bioconjugation.

Results from SEM, FACS, and confocal microscopy (Figure 3.1) reveal that the exogenous nanoliposomes are firmly linked to MTB cell membranes and remain on the bacterial cell surface, even after harsh washing conditions. Interestingly, as it can be observed on SEM images, most liposomes were localized on MTB main body, while a negligible number (less than 2%) were attached to the flagella. Optimizing the number of liposomes per bacteria was a key challenge in the development of the complex to carry sufficient concentrations of drug to exert therapeutic effects without compromising natural bacteria motility. Considering the surface area of a typical MTB (~1.5 μm in diameter), we found that coupling of up to 70 nanoliposomes with an average size of 170 nm to the surface of bacterial cells occludes only about 23% of the total cell surface without significantly altering MTB–LP mobility and responsiveness to the applied magnetic field.

Indeed, the swimming speed of the complexes only decreased by approximately 27% (from 110 down to approximately 80 μm s^{-1}) when ~70 liposomes are attached to the surface (Figure 3.3d). However, it should be noted that the terminal velocity of MTB–LP was still higher than that of typical morphotypes of magnetotactic bacteria such as *AMB-1* (49 μm s^{-1}), *MS-1* (40 μm s^{-1}), *etc.*, at the same magnitude of applied magnetic field [32] even after the bioconjugation process, weight of nanoliposomes, long-term exposure to PBS, and multiple turnovers of the culture environment. Moreover, the velocity of MTB–LP was greater than the linear swimming speed of some other non-magnetotactic flagellated bacteria strains such as *Salmonella* (20–50 μm s^{-1}) or

E. coli (10–40 μm s^{-1}), which can overcome diffusion resistances in solid tumors with this range of velocities [29, 31].

The uptake and internalization behaviors of free/attached liposomes were compared to those exhibited by macrophage, fibroblast, and colorectal cancer cells to assess whether tumor and nontumor cells exploit various uptake dynamics. The results show that the MTB–LP complex was rapidly internalized by J774 phagocytic cells, whereas the opposite was observed for nonphagocytic cells (NIH/3T3 and Colo205) (Figure 3.5; Supporting information Figure S3.8). Moreover, the level of uptake of negatively charged liposomes and MTB–LP in cancer cells (Colo205) was lower than that in normal cells (NIH/3T3, J774). As reported in the literature, cell phenotype (cancerous *vs* normal cells) [186, 187], the cell's endocytic capacity (phagocytosis *vs* nonphagocytosis) [321], bacteria type (pathogenic *vs* nonpathogenic) [189, 190], and attachment bond, as well as liposomal size [322] and surface charge [321], determine the mode and capacity of cellular uptake.

Negatively charged liposomes are believed to enter cells via nonspecific receptors present on a variety of cells, which in turn mediate particle recognition, adhesion, and the subsequent endocytotic-like internalization mechanisms [321, 323]. Conversely, cancer cell membranes possess an enhanced net negative surface charge compared to normal cells as a result of extensive sialylation [187], abundance of phosphatidylserine residues, heparan sulfate proteoglycans, and *O*-sialoglycoproteins [188]. This may lead to repulsion of negatively charged nanoparticles or complexes and reduced cellular uptake. Accordingly, the low MTB–LP uptake by Colo205 cell line can be explained by the presence of negatively charged nanoliposomes.

Bacteria, in their turn, exploit different pathways for cellular uptake such as phagocytosis. However, the uptake process of both pathogenic and nonpathogenic bacteria in epithelial cells or fibroblasts, representing classical nonphagocytic cells, is through nonselective internalization mechanisms, such as macropinocytosis [189, 190], which depend on external stimuli to trigger a signaling cascade. Only metabolically active bacteria can undergo this process since heat-treated bacteria did not induce any fluid-phase uptake [189, 190]. In our case, MTB bacteria are affected by mammalian cell culture conditions, mainly the 37 °C temperature. At this temperature, they cannot proliferate and remain active only for 30–40 min [36]. Therefore, we cannot conclude that MTB take advantage of macropinocytosis. Future studies will investigate whether nanoliposomes undergo detachment from bacteria in the cellular environment or if MTB–LP complexes

themselves can be internalized by nonphagocytic cells. The particular mechanisms involved in the entry of MTB into nonphagocytic cells remain to be elucidated. However, the lack of fluorescence signal from complexes at the initial incubation time indicates that liposomes should remain attached to the bacterial surface, and regardless of the underlying internalization mechanism, nanoliposomes containing therapeutic agents could enter the cell effectively for intracellular drug delivery applications.

Cell viability assays also support that MTB–LP show higher cell viability than MTB (Figure 3.4 and Table 3.1) due to the incorporation of biocompatible nanoliposomes [140]. Nonetheless, it is important to note that substances produced by the bacteria, certain degradation products, or competition for nutrients in the *in vitro* environment may also affect cell viability and result in concentration dependent cytotoxicity. Ultimately, benign concentrations of bacteria should be determined for *in vivo* assays, high enough to deliver sufficient therapeutic payload but lower than the cytotoxicity threshold.

3.5 CONCLUSION

We developed a new-generation of therapeutic vector by introducing a direct, reproducible, and clinically applicable chemical coupling of carboxylated nanoliposomes to pre-existing reactive groups naturally present on the surface of transporter MC-1 MTB via carbodiimide cross-linking chemistry. This bioconjugation strategy and the number of attached liposomes do not alter intrinsic bacterial motility and their behavior under a controlled magnetic field. The attachment of nanoliposomes improves the cellular viability of the complexes and does not interfere with their uptake. Through the combination of their suitable magneto-aerotaxis behavior, improved systemic biocompatibility, native bacteria cytotoxicity at tumor sites, therapeutic or diagnostic agents transport, and cellular uptake, this engineered MTB–LP system offers opportunity for their application in cellular tracking, medical imaging, and the ability to actively target areas of interest while increasing the maximum-tolerated dose of pharmacytes for cancer therapy, gene or vaccine delivery. Taking into account the encapsulation efficacy of drug within liposomes, the average number of liposomes carried by each bacteria, and the number of injected bacteria, it is possible to estimate the deliverable dosage of drug that will be released at the tumor site. Our system can potentially overcome targeting and diffusion limits by actively penetrating hypoxic

regions of tumors currently unattainable with conventional cancer drugs and effectively deliver active substances to solid tumors.

3.6 METHODS

3.6.1 Reagents and chemicals

The lipids distearoylphosphatidylcholine (DSPC), distearoylphosphatidylethanolamine derivatives of PEG with a terminal carboxyl group (DSPE-PEG2000-COOH) were purchased from Avanti Polar Lipids, Inc. (Alabaster, AL). Cholesterol, sulfo-*N*-hydroxysulfosuccinimide (sulfo-NHS), 1-ethyl-3-[3-(dimethylamino)propyl]-carbodiimide (EDC), 2-(*N*-morpholino)ethanesulfonic acid (MES), sepharose CL-4B, glutaraldehyde, trypsin–EDTA solution, and phosphate-buffered saline (PBS) were all acquired from Sigma-Aldrich (St. Louis, MO). Poly-L-lysine was purchased from Electron Microscopy Sciences, Inc. Rare earth magnets were purchased from Indigo Instruments (Waterloo, Canada). *N*-(6-Tetramethylrhodaminethiocarbamoyl)-1, 2-dihexadecanoyl-*sn*-glycero-3-phosphoethanolamine, triethylammonium salt (TRITC DHPE), Lissamine Rhodamine B 1, 2-dihexadecanoyl-*sn*-glycero-3-phosphoethanolamine, triethylammonium salt (Rhodamine DHPE), penicillin–streptomycin, bovine calf serum (BCS), and fetal bovine serum (FBS) were obtained from Invitrogen (Burlington, CA). NIH/3T3 (ATCC CRL-1658) mouse embryonic fibroblast cells, J774A.1 (ATCC TIB-67) murine macrophage cell lines, Colo205 (ATCC CCL-222) human colorectal adenocarcinoma cell line, Dulbecco's Modified Eagle's Medium (DMEM) (ATCC30-2002) and Roswell Park Memorial Institute 1640 medium (RPMI-1640) were purchased from American Type Culture Collection (Manassas, VA). 4-[3-(4-Iodophenyl)-2-(4-nitrophenyl)-2*H*-5-tetrazolio]-1, 3-benzene disulfonate (WST-1) was purchased from BioVision, Inc. A Milli-Q water system (Millipore, Bedford, MA), supplied with distilled water, provided high purity water (18 MΩ) for these experiments.

3.6.2 Culture growth conditions for MC-1 magnetotactic strain

Magnetococcus Marinus MC-1 strain from our laboratory stock was cultured microaerobically in chemoheterolithotrophic medium at room temperature, as previously reported [324]. Bacterial cultures were incubated statically under an oxygen concentration gradient ($[O_2]$-gradient) in an iron enrichment medium, which included 50 μM ferrous sulfate, $FeSO_4 \cdot 7H_2O$ (Sigma-Aldrich),

to allow the biomineralization of magnetic nanoparticles. The MC-1 culture was incubated for 48 h without agitation at 25 °C in the dark. Bacterial cells were harvested during the stationary phase of growth and used for direct observation or conjugation with liposomes in this study.

3.6.3 Fabrication and characterization of nanoliposomes

See supporting information.

3.6.4 Covalent coupling of carboxylated nanoliposomes to MTB cells using carbodiimide chemistry

To stably couple nanoliposomes to the surface of magnetotactic bacteria cells, we exploited the fact that many cells have high levels of intrinsic amine groups on their surfaces. The most straightforward approach to immobilize and maintain functionalized liposomes with reactive carboxylic acid groups (−COOH) in the range of 170 nm to the surface of bacteria was to use direct covalent chemical conjugation. To avoid loss of bacteria viability, conventional bioconjugation methods based on zero-length carbodiimide chemistry (EDC/NHS) were carefully adapted as a robust and highly versatile methodology for introducing functional surface of component to cell membrane [195].

The MTB–LP complex was achieved by a two-step process (Supporting Information Figure S3.7). First, the carboxylated nanoliposomes were activated using EDC/NHS chemistry by incubating 100 μl of a liposome solution (stock liposome solution; 15 mM) with the carbodiimide activating reagents EDC and sulfo-NHS (EDC/NHS/DSPE-PEG-COOH = 30:30:3, mol/mol) for 20 min in MES buffer (pH = 5.5) at room temperature. A Sepharose CL-4B column was used to remove the excess activating reagents. The carbodiimide-based coupling reagent can react with the carboxylic acid groups of liposomes to provide a highly active ester (*O*-acylisourea) intermediate that could then react with a nucleophile, such as a primary amine, to form an amide bond [195] (Supporting Information Figure S3.7). Subsequently, bioconjugation was achieved by incubating approximately 4×10^7 (~10^7 MTB ml^{-1}) MTB bacteria cells with activated nanoliposomes. The mixture was then incubated for 1 or 2 h at 25 °C under gentle agitation to permit amide coupling. Attached liposomes were separated from unbound liposomes using a two-dimensional magnetic field (Figure 3.3b) followed by three rinses with PBS. The sample was redispersed in PBS at pH 7.4. To develop an optimal protocol for MTB–LP complexes and

determine the maximum capacity for carrying liposomes, different liposome concentrations ranging from 0, 5, 25, 50, 75, 100, 150, 250, and 400 μl (15 mM) were added to an equal quantity of bacteria (4 ml of 10^7 MTB ml^{-1}) and incubated for 1 and 2 h at 25 °C with gentle mixing.

3.6.5 Assessment of nanoparticle attachment to MC-1 MTB bacteria

Construction and attachment efficacy of MTB–LP complexes were examined using confocal laser scanning microscopy (CLSM), scanning electron microscopy (SEM) and fluorescence activated cell sorting (FACS) flow cytometry techniques. All the experiments were performed in triplicate in order to ensure consistency and reproducibility through statistical significance.

Fluorescence signals from MTB–LP were acquired using confocal laser scanning microscopy (CLSM: Carl Zeiss LSM 510-META with Axiovert inverted microscope, Jena, Germany). TRITC labeled liposomes were visualized with a He/Ne laser (543 nm excitation and a 560–615 nm band-pass emission filter), while scattered incident light was simultaneously observed via the transmitted light detector. Images were obtained through a high numerical aperture (NA) 63.0× 1.4 oil-immersion objective and Carl Zeiss LSM imaging software.

In addition, fluorescence and scattering intensity distributions of bacteria treated with nanoliposomes were measured by TRITC tagged lipids using fluorescence activated cell sorting analysis (FACS: BD FACSCalibur; BD Biosciences) with a laser excitation wavelength of 543 nm. Samples were diluted 1 in 10 in PBS and the measurement was carried out using forward scatter *versus* fluorescence (FSC/FL1) plots for 25000 events. Bare bacteria were used as a control. FACS data was analyzed by FlowJo software (Tree Star, Inc., Ashland, OR), using appropriate gates and controls to generate density plots and histograms of each sample.

The number of liposomes attached to the MTB surface was assessed by FE-STEM. After each incubation time point, a suspension of MTB–LP was fixed with 3% glutaraldehyde (Sigma-Aldrich, Oakville, Ontario) in 0.12 M PBS (pH 7.2) at 4 °C. A suspension of fixed samples (20 μl) was placed onto a poly-L-lysine coated 12 mm glass slide and incubated for 30 min. The slides were then rinsed with ultrapure water. Samples were dehydrated in a series of ethanol/water solutions of increasing ethanol content from 30% to 100%. Dehydration was followed by critical point drying to remove ethanol from the sample (Leica Microsystems Critical Point Dryer Model CPD030). Samples were finally mounted on carbon tape and wafer sputtered with gold/palladium prior to imaging (Anatech Hummer VI sputtering coater, Arlington, VA).

High-resolution images were obtained using a Hitachi S-4700 FE-STEM at an accelerating voltage from 2 to 5 kV and working distances of < 5.3 mm. To determine the average number of attached liposomes to the surface, their number was counted on 100 bacterial cells at each concentration.

3.6.6 Investigation of magnetotaxis behavior of MTB–LP complexes by optical microscopy

The swimming velocity and magnetotaxis-based behavior of MTB–LP complexes at different number of attached liposomes per MTB (0, 10, 25, 40, 47, 70 and 74) after 0, 0.5, 1, and 2 h sample preparation were examined using a phase contrast microscope (AxioImager Z1, Imaging Solutions Carl ZEISS) with a resolution of 1388 × 1040 pixels and a dynamic range of 12-bits. Images were acquired by AxioCamMRm CCD camera (Zeiss) bearing a long distance objective Ediplan 50×, dark-field illumination in reflection-mode while applying 20 G external magnetic field. A gaussmeter probe (model 450, Lake Shore Cryotronics, Inc.) was used to quantify the magnetic field at this position. To obtain consistent results, the exposure time of the camera was set to 200 ms, allowing the visualization of the trail left by bacterial motion. All measurements were made using AxioVision v.4.6.0 software. As mentioned earlier, the initial swimming velocity of unloaded MC-1 bacteria in complete growth medium at room temperature can exceed 200 μm s^{-1}. However, bare MTB bacteria, washed three times in PBS-1× (pH = 7.4), showed velocity decrease to about 110 μm s^{-1} using 2D magnetic field. This was set as a reference velocity to compare the swimming speed of bare MTB and MTB–LP complexes from ~500 non-preselected bacteria images.

3.6.7 Evaluation of cellular toxicity and uptake

3.6.7.1 Cell culture

The Colo205 was cultured in RPMI-1640 medium. J774A.1 and NIH/3T3 were grown in DMEM under recommended conditions. NIH/3T3 cells were supplemented with 10% BCS and 1% penicillin/streptomycin. Colo205 and J774A.1 cell lines were supplemented with 10% FBS and 1% penicillin/streptomycin. All cells were cultured in an atmosphere of 5% CO_2 at 37 °C in a fully humidified incubator. NIH/3T3 and Colo205 cells were harvested using commercial trypsin

(0.05% trypsin-EDTA; Gibco). J774.A cells were scraped and viable cell concentrations were determined by 0.4% Trypan blue staining.

3.6.7.2 WST-1 Based cell inhibition and cytotoxicity assays

The growth inhibitory effect of the MTB–LP complex was evaluated with a WST-1 colorimetric assay [325]. MTB alone and blank liposomes were used as control. First, J774, Colo205, and NIH/3T3 cells were seeded in growth medium at a density of 1×10^5 cells/well into 96-well flat bottom plates (Costar, Corning, NY) in triplicates and incubated overnight to allow adhesion to plates. Non-adherent cells were removed by washing with media just before addition of the MTB–LP complex. Incubation time and concentration were considered as effective variables to determine cytotoxicity. Cytotoxicity on a panel of tumor and nontumor cells was determined by exposing cells to serial dilutions of liposomes (0.07–40 μM), MTB–LP (2×10^5 to 10^8; 0.022–11.6 μM ((MTB/well); liposome) and MTB (2×10^5 to 10^8 MTB/well) from the stock in the appropriate growth medium (without penicillin). Cells were treated with the formulations for variable time periods 3, 6, 12, 24, and 48 h and incubated in a humidified incubator. Then, a WST-1 cytotoxicity assay (G-Biosciences) was performed according to the manufacturer's instructions. Briefly, after the planned incubation time, 10 μl of cell viability proliferation reagent WST-1 (1:10 dilution) was added to each well and the sample was incubated for an additional 2 h at 37 °C under 5% CO_2. Absorbance of formazan dye produced by viable cells was then measured in a microplate reader (Biotek μQuant Monochromatic Microplate Spectrophometer) at 450 nm with a reference wavelength of 620 nm. Wells with cells alone (without bacteria and/or liposome) served as controls to determine the percentage of cytotoxicity in bacterial infected wells. The same amounts of culture medium and WST-1 reagent in empty wells were also included in every experiment as a blank control. The WST-1 reagent incubation time of 2 h was found to be optimum since the color intensity did not change after 2 h (data not shown), and this condition was used in all subsequent assays. Three independent experiments were performed, each in triplicate and viability values were expressed as a percentage of control and plotted *versus* concentration. Cell viability was calculated with respect to cells as control. A sigmoidal dose-response curve was fitted to the data and a half maximal inhibitory concentration (IC_{50}) value was calculated for each replicate, using GraphPad Prism software (version 6.0).

3.6.7.3 *In vitro* cell uptake study

To visualize and determine cellular uptake, the liposomes were fluorescently labeled by incorporating 1 mol% Rhodamine-DHPE (head groups marker) into the original formulation with excitation/emission maxima ~560/580 nm. To study the effect of attachment on the liposomal uptake, all viable cell lines were seeded in complete growth medium at a density of 1×10^4 cells/well in a poly-L-lysine coated 35 mm confocal glass bottom Petri dishes with a 14 mm cover glass center (Mattek Corp.). Cells were incubated overnight at 37 °C under 5% CO_2 in a humidified incubator to allow for uniform cell attachment. Following incubation, the medium was then aspirated from the wells and replaced with the stock liposome suspension (200 nM) or MTB–LP complex (10^6 MTB/Petri) in complete growth medium (without penicillin). The quantity of MTB–LP samples for the uptake study was selected based on the lowest IC_{50} concentration measured among all three cell lines after 24 h incubation. Moreover, liposomes alone were used as control with the same concentration as attached liposomes to MTB. Cells incubated with plain growth medium served as controls. The cells and samples were then incubated for different time intervals (0.5, 1, 6, 12, and 24 h) to allow for sufficient uptake.

3.6.7.4 Assessment of cellular uptake by confocal imaging

Confocal microscopy on each cell monolayer from randomly selected areas was performed to investigate the internalization and intracellular distribution of the MTB–LP complex and liposomes alone. Following incubation of cells with each formulation, the medium was aspirated and cells were washed three times with cold phosphate buffered saline (PBS) to eliminate traces of liposomes and bacteria left in the wells. Cells were fixed with 10% formalin (Sigma-Aldrich, Oakville, Ontario) for 20 min and washed another three times with PBS. Cells were then permeabilized with 0.1% Triton-X (Invitrogen, Carlsbad, CA) for 5 min and stained with Hoechst 33342 (Molecular Probes, Eugene, OR) and Alexa-488 conjugated Phalloidin (Molecular Probes R, Invitrogen) for nuclei and F-actin visualization, respectively. The cell-containing cover glass at the center of the confocal glass bottom dishes was then mounted with Clear-Mount mounting solution (Invitrogen, Carlsbad, CA).

Microscopic observation of the fluorescent probes delivered to cells was performed with the previously mentioned confocal laser-scanning microscope. All images were acquired while maintaining a constant laser intensity and detector gain. Following image acquisition, the

composite images were assembled using ImageJ (MacBiophotonics) software (NIH, Bethesda, MD). The intensity of fluorescence was evaluated for uptaken liposomes and cell nuclei using CellProfiler image analysis software (Broad Institute, Cambridge, MA). The ratio of fluorescence intensity of uptaken vesicles relative to cell nuclei was then determined to give a quantitative analysis of cellular uptake.

3.7 Statistical analysis

Quantitative data are expressed as a mean ± standard deviation (SD) and the number of independent replicates is indicated in the figure legends. Statistical significance was evaluated with the use of a one- or two-way ANOVA as appropriate followed by a post-hoc Bonferroni test to compare individual means using GraphPad Prism version 6.0 software. The level of statistically significance was set at *P*-values of 0.05 or less for all of the tests.

3.8 Acknowledgment

This project is funded by the Quebec Consortium for Drug Discovery (CQDM) and in part by a Discover Grant from the Natural Sciences and Engineering Research Council of Canada (NSERC), Mathematics of Information Technology and Complex Systems (MITACS) and the Research Chair of École Polytechnique in NanoRobotics.

3.9 SUPPORTING INFORMATION

3.9.1 Preparation of fluorescently labeled carboxylated liposomes

A well-established reverse phase evaporation (REV) method was used for the preparation of fluorescently labeled carboxylated liposomes composed of DSPC/CH (3:2, molar ratio) with distal terminal groups of DSPE-PEG-COOH (6 mol%). As a tracer, 1 mol% of a fluorescently labeled lipid TRITC-DHPE or Rhodamine-DHPE was included in the liposome formulation for flow cytometry and fluorescence microscopy experiments. First, lipids were dissolved in a round-bottomed glass flask with 2 ml of a 4:1 (vol/vol) chloroform/methanol mixture. To produce a thin lipid film, the solvent was removed under vacuum by a rotary evaporator (Rotavapor; Büchi) at a

water bath temperature of 60 °C for 2 h, then overnight under high vacuum to eliminate any solvent traces. Dried lipid films were hydrated at a concentration of 15 mM phospholipid in MES buffer (100 mM; pH = 5.5) by heating in a 60 °C water bath with occasional gentle vortexing. Afterward, multilamellar liposomes were sequentially extruded 30 times using an extruder (Avanti Polar Lipids, AL) through a series of PTFE membranes with pore sizes ranging from 0.8 μm to 0.2 μm.

3.9.2 Physicochemical characterization of nanoliposomes

The mean hydrodynamic diameter and size distribution of the nanoliposomes [polydispersity index; (PDI)] were ascertained by photon correlation spectroscopy (PCS) using the 90Plus multiangle particle sizer (Brookhaven Instruments Corp., Holtsville, NY) at room temperature. The PCS measurements were carried out using a solid state laser diode (15 mW) operating at 670 nm as light source in a fixed scattering angle of 90 degrees. The real and imaginary refractive indexes were set at 1.59 and 0.0, respectively. Nanoliposomes were diluted 50-fold in distilled water to avoid multiscattering phenomena and to obtain appropriate viscosities. The resultant liposome size was 169.3 ± 1.31 nm with a polydispersity index of 0.12 ± 0.014 (Supporting Information Figure S3.6a, b), which only increased slightly after three weeks confirming the stability of the nanoliposomes.

The net surface charge was determined by zeta (ζ) potential analysis by laser Doppler anemometry and conducted using a ZetaPlus analyzer (Brookhaven Instruments Corp., Holtsville, NY) at 25 °C. Carboxylated nanoliposomes were diluted 50-fold in distilled water and zeta potentials were calculated for an average of ten measurements at the stationary level using the measured electrophoretic mobility distributions with the Smoluchowski equation. Obtained negative values of 34.3 ± 1.4 mV indicated that negatively charged carboxylic groups were successfully inserted into the outer monolayer of the nanoliposomes (Supporting Information Figure S3.6a).

The TEM micrograph of the nanoliposomes revealed a narrow size distribution as well as their characteristic spherical morphology (Supporting Information Figure S3.6c). A 5 μl droplet of liposome suspension was placed onto a pretreated quantifoil R2/2 holey carbon coated on 400 mesh copper grids (Quantifoil Micro Tools). Samples were kept in a controlled environment at FEI Vitrobot Grid Cryo-Plunging System (FEI Company, Hillsboro, OR) where humidity and

temperature were maintained at 100% and 4 °C, respectively, to allow the liposomes to be fixed on the grid. The excess solution was removed by blotting with paper filter and the vitrification was achieved by rapidly plunging the samples into liquid ethane which was kept in a liquid nitrogen container. Finally, the samples were transferred to a grid holder and kept frozen in liquid nitrogen until observation to prevent the formation of ice crystals and sample perturbation. Cryo-TEM was performed with a FEI Tecnai G2 F20 (FEI Company, Hillsboro, OR) operating at 120 kV acceleration voltages. Images were recorded with a Gatan Ultrascan 4000 (4k × 4k) CCD Camera System Model 895.

a

	Day 1	Day 20
Particle Size (nm)	169.3 ± 5.31	169.2 ± 7.43
PDI	0.12 ± 0.014	0.144 ± 0.051
Zeta Potential (mV)	-34.3 ± 1.4	-33.5 ± 1.3

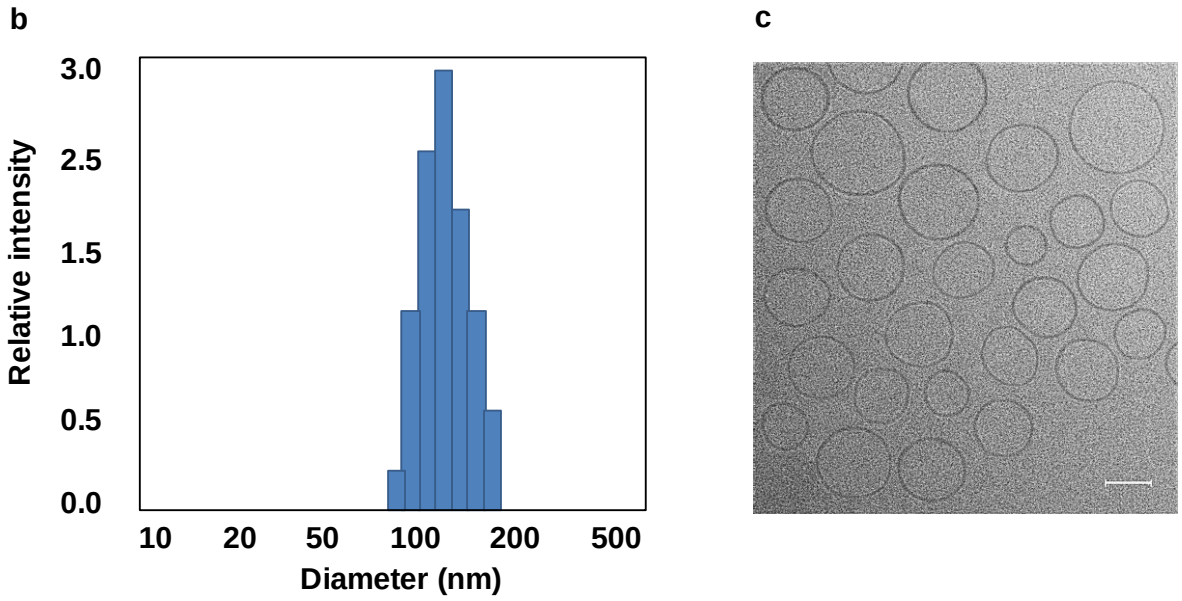

Figure S3.6: Physicochemical characterization of nanoliposomes. (**a**) Data presenting size, PDI and zeta potential of carboxylated nanoliposomes (mean ± *SD*, *n* = 10). (**b**) Size distribution of nanoliposomes (average size ~170 nm). (**c**) TEM photograph of nanoliposomes (bar = 100 nm).

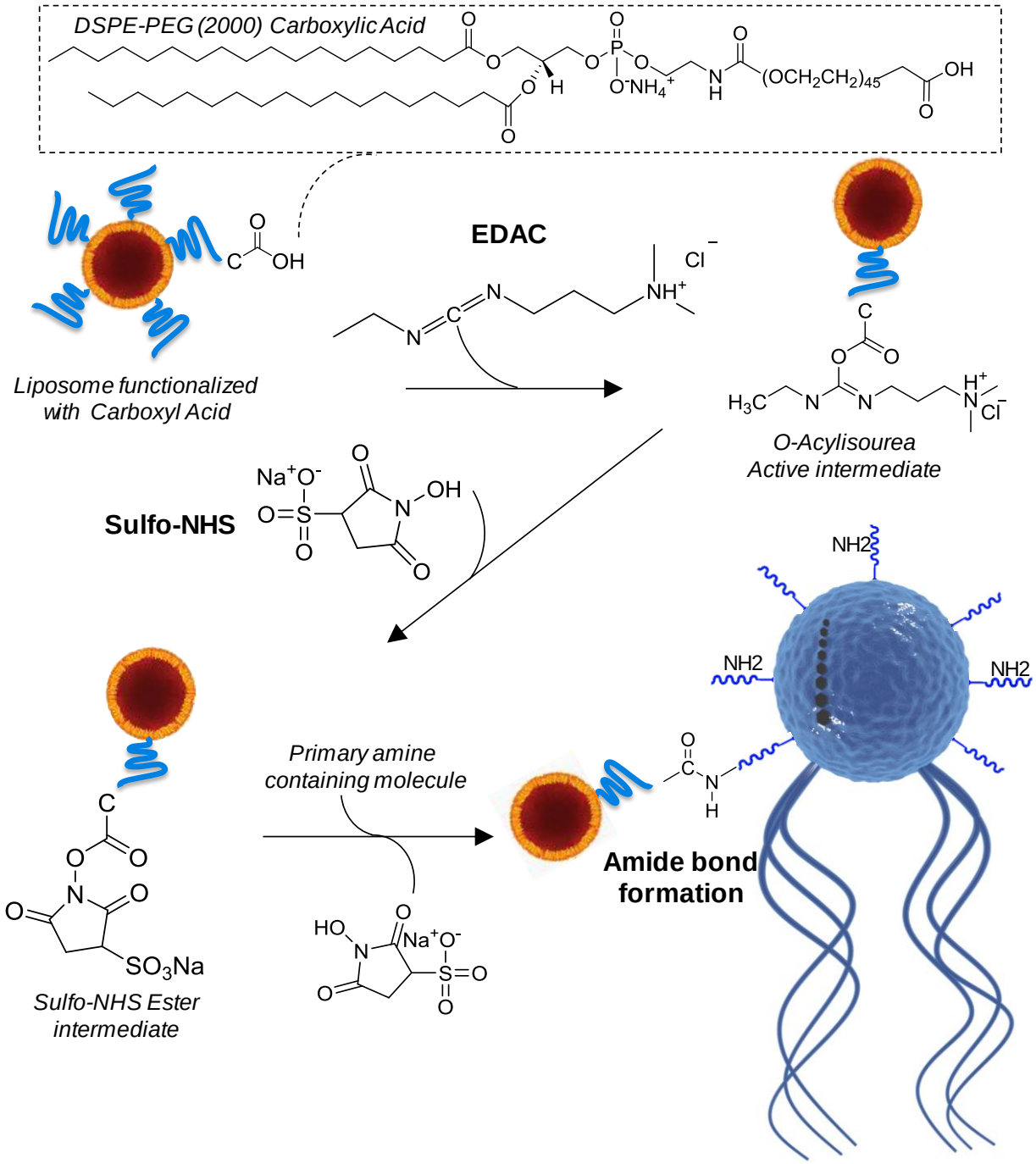

Figure S3.7: Schematic representation of carbodiimide-based conjugation of the nanoliposomes to MTB cells. First, EDC/NHS reacts with the available carboxyl groups on the nanoliposomes surface. The activated nanoliposomes that are highly reactive toward the amino groups can then covalently attach to the surface of the magnetic bacteria (bottom pathway).

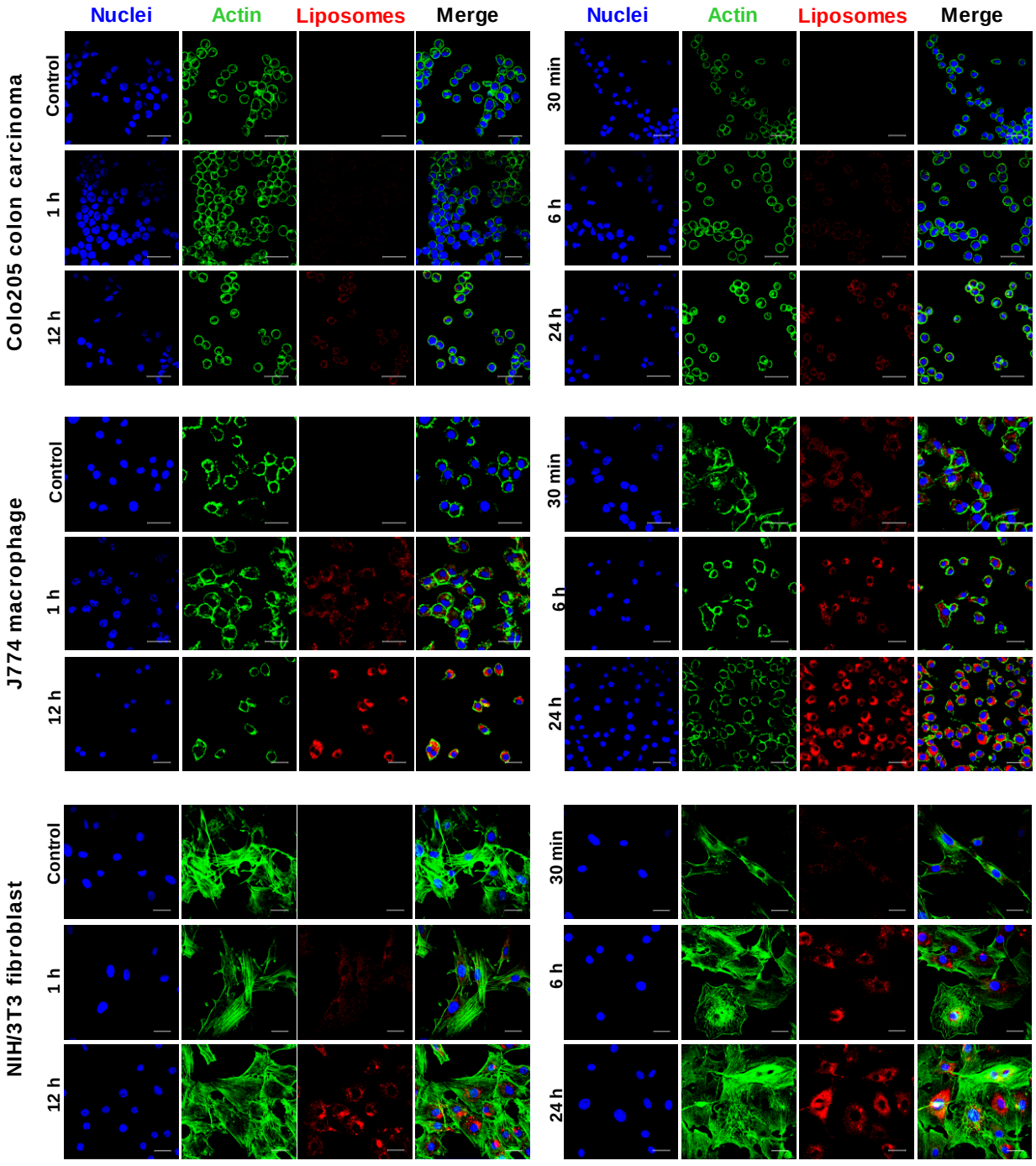

Figure S3.8: Confocal images of NIH/3T3, Colo205 and J774 cells showing uptake of Rhodamine labeled nanoliposomes. Nuclei were stained blue with Hoechst 33342, actin filaments were labeled green with Phalloidin-Alexa Fluor 488 and nanoliposomes were marked red by Rhodamine. Uptake of bare nanoliposomes was initiated rapidly within 30 min for J774 and NIH/3T3, which increased gradually with the incubation time. The uptakes of nanoliposomes were occurred after 1 h in Colo205 cells. Scale bars represent 30 μm.

CHAPTER 4 MAGNETIC RESONANCE IMAGING OF TUMOR HYPOXIA USING COMPUTER-ASSISTED MAGNETO-AEROTACTIC BACTERIA-MEDIATED SUPERPARAMAGNETIC IRON-OXIDE NANOPARTICLES

This chapter presents objective 2 that is the application of MC-1 MTB carrying MRI contrast agents for imaging the hypoxic regions of tumors. To validate the feasibility of this objective, an antibody-mediated attachment strategy was developed to conjugate the magnetite nanoparticles to the surface of the MTB to form a navigable contrast agent. The *in vivo* results obtained from the magnetic navigation of superparamagnetic attached to MTB in HCT116 colorectal tumor xenograft demonstrated that the attachment was reliable and the MTB complexes were capable of accumulating into the hypoxic regions causing the local field heterogeneity detectable by clinical MRI. Corresponding histopathology analyses such as IF and HPS confirmed the MRI results regarding the location of the loaded MTB in the tumor hypoxia. The MTB complexes offer an unprecedented approach for targeting and transporting the imaging agents to distal tumor regions in a more directed and controlled manner while providing the capability for tracking the loaded MTB inside the tumor.

4.1 INTRODUCTION

Tumor hypoxia has been recognized as a decisive factor in the impairment of tumor response to therapeutic and diagnostic schemes and yet, an efficient method to visualize hypoxic regions for *in vivo* diagnostics, drug delivery targeting assessment, or treatment efficacy monitoring, to name but a few applications, is still lacking. *In vivo* information gathering of the spatial structures of tumor microenvironments can not only prove to be a valuable tool to assess factors that influence responses to treatments but also in determining the appropriate dosage and the type of agents required to yield optimal therapeutic outcomes. Hypoxic tumors are generally associated with a more aggressive tumor phenotype and are known to promote angiogenesis and metastasize [13].

They also significantly reduce tumor sensitivity to radiation and chemotherapy that very often ultimately lead to treatment failures [13]. Therefore, major determinants of individual tumor hypoxic structures can provide prognostic information for improving not only treatment planning for regimen of therapeutic agents but also intensity-modulated radiotherapy, to name but only two examples of commonly used interventional procedures.

Current clinically invasive methods to measure hypoxia such as immunohistochemistry of exogenous markers or hypoxia-related proteins in tumor biopsy samples [13] and oxygen tension (pO_2) electrode measurements [277] are restricted to easily accessible tumor sites and lack spatial coverage due to a limited number of samples. Considerable effort is being made to investigate the use of *in vivo* clinical imaging modalities to overcome the aforementioned limitations. For instance, MRI, PET, and CT scan are used to identify the location and volume of tumors and to evaluate the structure and different physiological processes of the tumor milieu [228, 229, 285]. Despite advances in medical imaging technologies, to date, the internal hypoxic tumor microenvironments still remain inaccessible to such clinical imaging modalities.

For instance, MRI is currently under intense investigations as a robust technique with unlimited tissue penetration and a relatively high spatial resolution for determining the tumor location and size [326] or tumor angiogenesis [228, 232]. MRI contrast agents such as gadolinium derivatives [232] and magnetic nanoparticles (MNPs) [327], particularly superparamagnetic iron-oxide nanoparticles (SPIONs), are widely used in biological assays and have become an indispensable part of clinical MRI. Such contrast agents alter the MR signal due to the magnetic field perturbation, which affects T_1- and T_2-relaxation times that can be of assistance in distinguishing disease from normal tissue. Currently, contrast agents including SPIONs share the same limitations as for drug delivery where a suboptimal accumulation around the leaky tumor vasculature by EPR effect [61, 233] and limited intratumoral penetration through the tumor extracellular matrix [6, 11, 12], are observed. The prior systemic circulation, the tumor interstitial fluid pressure [54], the irregular and disorganized angiogenesis capillary networks [61], the heterogeneous blood flow, the relatively large distances between the tumor cells and the functional blood vessels , and the lack of an oxygen gradient-based targeting and retention capability are all major obstacles to the effective diffusion and high-specificity targeting of contrast and therapeutic agents towards the tumor hypoxic areas. Developing special micro-bio robots as carriers for targeting and delivering therapeutic payloads to a cancer mass with high

specificity and ability to penetrate into all tumor regions could be curative in many medical tasks such as delivery of MRI contrast agents, highly localized drug delivery for chemotherapy, and thermal treatment of tumors at selected sites. Previous studies on biological microorganisms such as bacteria have proven their potential to reach tumor region following a systemic injection and to proliferate in the solid tumors [29, 80]. However, to minimize systemic circulation of these bacteria and to guide their migration path for targeting interventions, no external computer-based control can be used.

To overcome these obstacles, a new steerable carrier based on live *Magnetococcus Marinus* flagellated MC-1 magnetotactic bacteria was proposed with experimental results showing that large populations of MTB were able to migrate non-systematically in the tumor hypoxic regions when operating in an artificial environment enabling the exploitation of their magneto-aerotactic migration behavior (See Appendix A). MTB cells with intrinsic magneto-aerotactic behavior are promising candidate and efficient for computer-based navigation and have a potential to preferentially penetrate deep, accumulate and deliver medicine in hypoxic regions ($< 0.7\%$ O_2) of the solid tumors [36, 109]. Despite the potential implementations of this bio-carrier, *in situ* targeting assessment of deeply penetrated MTB into the tumor tissue could not be achieved due to the absence of traceable agents being linked to such a carrier. To overcome the aforementioned problem as well as visualizing the tumor hypoxic areas, MTB-mediated contrast agents could prove to be a highly valuable imaging addition to the arsenal already available in clinical settings.

In this respect, here we assess a suitable ~200 nm clusters of SPIONs loading capacity for such MTB carriers to yield contrast levels that are compatible with clinical MRI scanners while maintaining their capability to migrate effectively through the potential physiological routes leading towards the tumor hypoxic areas. Such new MRI contrast assemblies are acting as nanorobotic agents with self-propelling and magneto-aerotactic sensing capabilities. These MRI contrast assemblies enable non-systemic delivery of contrast agents to tumor hypoxic regions that were injected peritumorally into SCID-Beige mice bearing HCT116 colorectal tumor xenografts prior to conduct *in vivo* computer-assisted magnetotactic guidance followed by MTB-autonomous aerotactic targeting of hypoxic regions. Hypoxic areas identified through T_1- and T_2^*-weighted images were subsequently validated by *in vitro* studies featuring staining with immunofluorescence (IF) together with hematoxylin-phloxine-saffron (HPS) prior to being accurately registered to the corresponding MRI slices. Besides *in vivo* MRI-mapping of hypoxic

areas, opportunities also exist for other medical imaging modalities and the synthesis of new markers and theranostic agents.

4.2 METHODS

4.2.1 Culture growth conditions of MC-1 magnetotactic bacteria

The *Magnetococcus Marinus* MTB MC-1 cells from our laboratory stock strain were cultured as previously reported [324]. This microorganism grows in a specific chemoheterolithotrophic liquid medium under microaerobic growth conditions. The MTB cells in culture medium were incubated statically without agitation in the dark, for 48 h at 25 °C and under an oxygen concentration gradient of 0.1-0.5%, a precise neutral pH at 7.0, and a controlled input of 7.5% CO_2. The medium was also supplied with 50 μM of ferrous sulfate heptahydrate ($FeSO_4 \cdot 7H_2O$) prior to inoculation to allow the synthesis of bacterial magnetosomes. All these parameters were controlled precisely to insure the high yield, high motility, and high magnetic sensitivity that are essential to using the MTB as biocarriers for drug delivery. The MTB typically are used at day seven, which corresponds to the end of their exponential growth phase. A typical successful MTB culture batch provides ~10^7 MTB per ml that can be used for the preparation of polyclonal antibodies or bioconjugation with particles. Bacterial cell concentration was determined by counting under optical microscopy (AxioImager Z1, Imaging Solutions Carl ZEISS).

4.2.2 Covalent immobilization of anti-MC-1 antibody on magnetic particles

Four types of magnetic particles (MPs) with different sizes and magnetic properties including superparamagnetic 200 nm (S200), ferromagnetic 200 nm (F200), superparamagnetic 500 nm (S500), and ferromagnetic 500 nm (F500) particles (Chemicell GmbH, Germany) were utilized for their applicability as contrast agents as introduced in Table 4.1. All of the employed MPs including FluidMAG-ARA-COOH and SiMAG-COOH, are ferrofluids consisting of an aqueous dispersion of individual magnetic iron oxide particles (Fe_3O_4) embedded in a polysaccharide substrate (S200, F200) or silica matrix (S500, F500), respectively (Figure 4.1a). The MPs contain terminal carboxyl acids for covalent immobilization of biomolecules. The numbers of particles per mg are 2.2×10^{14} and 1.5×10^{13} for S200/F200 and S500/F500, respectively.

Covalent binding of the amino-group containing IgG antibody (AB) specific against MC-1 MTB to the distal terminal of carboxylated MPs by the carbodiimide chemistry method provides MP-AB complexes (S200-AB, S500-AB, F200-AB, and F500-AB), as depicted in Figure 4.1b. The carboxyl sites of MPs were activated with EADC. EDAC coupling reagent in the presence of sulfo-NHS is commonly used to convert carboxyl groups to amine-reactive sulfo-NHS esters [195] for efficient AB attachment. In brief, 2 mg of particles were washed twice and resuspended in 2.5 ml of 2-(N-morpholino) ethanesulfonic acid (MES) buffer (50 mM, pH = 5.5; Sigma-Aldrich). All the washing steps for the superparamagnetic particles were performed using a NdFeB magnetic separator (MagnetoPURE, Chemicell).

Ferromagnetic particles were washed by centrifugation (5 min, 4000 rpm) to prevent aggregation caused by the magnetic interaction. That is due to the fact that, once ferromagnetic particles are magnetized, the particles behave like small permanent magnets, forming irreversible aggregates or lattices due to magnetic interactions. 4 mg of EDC (Sigma-Aldrich) and 6 mg of Sulfo-NHS (Sigma-Aldrich) were dispersed in 2.5 ml of MES buffer and mixed with resuspended MPs. The mixture was shaken at room temperature for 30 min. The particles were washed three times with MES buffer to remove any excess of activated agents. Then, the pH was raised to around 7 to 7.4 to link functionalized particles to antibodies. In fact, the kinetics of the hydrolysis of the Sulfo-NHS activated -COOH group increases at non-acidic pH. However, based on the isoelectric point of IgG antibody (7.3 ± 1.2) the pH needs to be increased to around 7-8 (not larger than 8.0) to avoid protein denaturation. Then, 50 μl of 2 mg ml^{-1} of AB (FITC-labeled or unlabeled) was added to the activated particles. The mixture was incubated for 4 hours at room temperature with gentle stirring. The unconjugated antibodies were separated from the conjugated ones as before. Finally, the MP-AB samples were dispersed in phosphate buffer saline (PBS, pH = 7.4) with the final concentration of 400 μg [MP] ml^{-1}. The MP-AB was stored at 4 °C until use.

4.2.3 MP-AB attachment to the MTB membrane to form MTB-MP complexes

For preparation of the MTB-MP complexes (MTB-S200, MTB-S500, MTB-F200, and MTB-F500), the 50 ml of 10^6 MTB ml^{-1} was incubated with 2.8 ml of S200/F200-AB and 4.15 ml of S500/F500-AB at a concentration of 400 μg [MP] ml^{-1} for 2 h at 25 °C under gentle agitation.

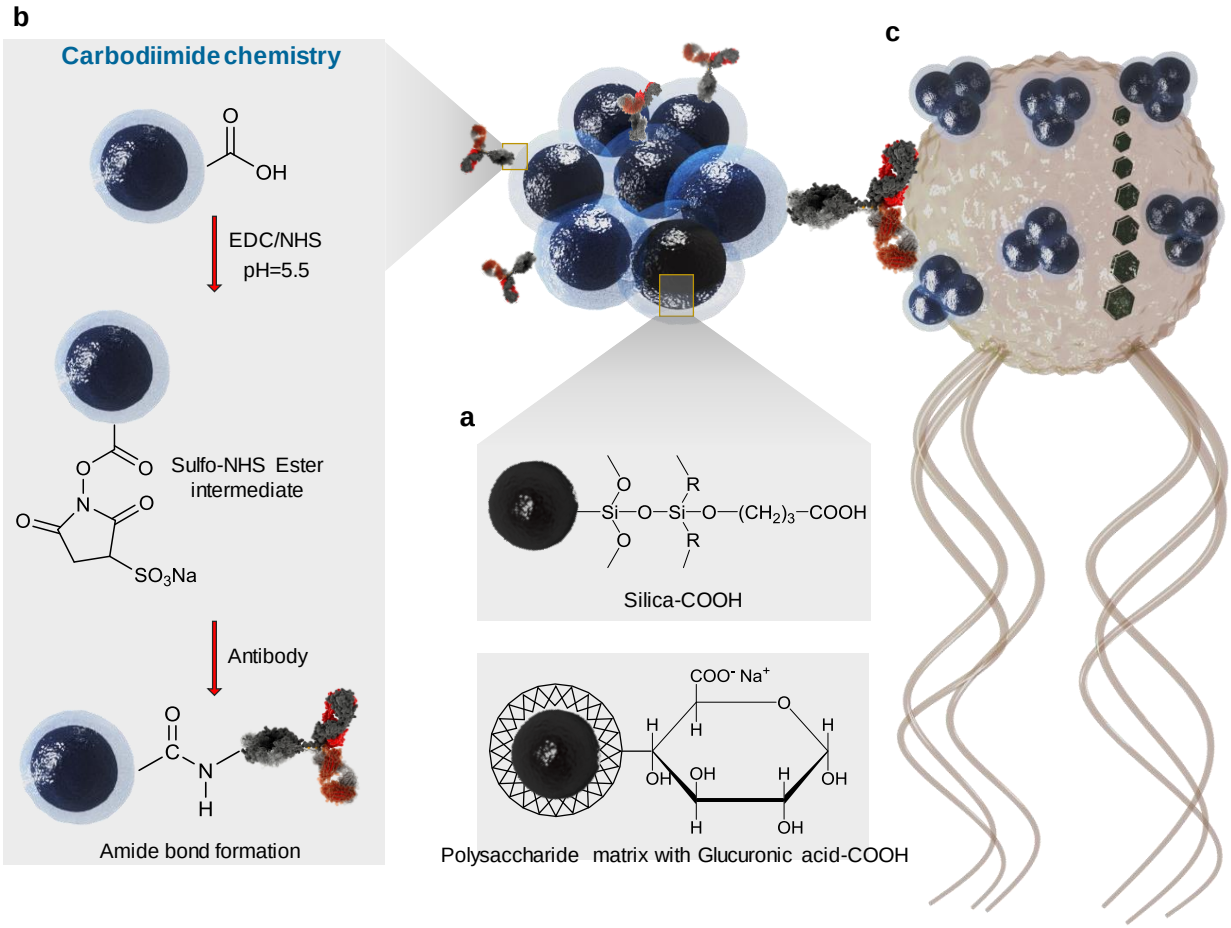

Figure 4.1: Schematic representation of MTB-MP complexes preparation. (**a**) SiMAG (top) and FluidMAG magnetic particle (bottom) with terminal carboxyl groups. (**b**) Covalent coupling of amino group-containing AB to carboxylated MPs by the carbodiimide method. (**c**) Attachment of the MP-AB to MTB cell membrane.

Subsequently, the complexes were washed three times with PBS (pH = 7.4) to remove non-attached particles using a magnetic setup designed to generate a homogenous magnetic gradient in two-dimensional space (Figure 4.2a). The magnetic field direction was oriented towards the center of each petri dish by decreasing its magnitude from 60 Gauss at the edges to zero Gauss at the center where the swarm of MTB-MP complexes was to form. This magnetic field strength is sufficient to accumulate the magnetic bacteria; however, it does not result in the aggregate formation of any super/ferromagnetic particles.

4.2.4 Physicochemical characterization of MP, MP-AB, and MTB-MP

The physical characteristics of MP and MP-AB were investigated using TEM, confocal microscopy, dynamic light scattering, and zeta potential. The chemical analysis of MP-AB was performed by FTIR. The MP-AB attachment to MTB (MTB-MP) complex was qualitatively analyzed using TEM and confocal microscopy. The specific affinity of MTB to MP-AB was investigated by μCP techniques.

4.2.4.1 Quantification of surface carboxyl groups of MPs using toluidine blue O

In this study, AB conjugation to the MP surface is mediated by COOH groups. The degree of carboxylation (in molarity per mg of MP) was measured using the toluidine blue O (TBO) (technical grade, Sigma–Aldrich, St. Louis, MO) assay. The cationic TBO blue dye derivative of phenothiazine ($C_{12}H_9NS$) [328] interacts with ionized, negatively-charged COOH functional groups via electrostatic interaction and shows an absorption peak at a wavelength of around 600-630 nm.

In the current study, two calibration curves at pH = 2 and 11 were prepared based on the TBO absorption at 630 nm using a microplate reader (SpectraMax i3, Molecular devices). In brief, dry TBO powder was dissolved into a reacting solution of 0.2 M NaCl (0.5 ml) at pH 2, and a reacting solution of 0.02 M NaCl (0.5 ml) at pH 11 to prepare two different TBO solutions at different concentrations. The pH of the reacting solutions was adjusted using hydrochloric acid (HCl) and sodium hydroxide (NaOH). Briefly, 0.6 mg MP was immersed into the freshly prepared TBO solution (2 mM in 0.02 M NaCl, pH 11) and followed by bath-sonication at room temperature for 1h, forcing TBO molecules to react with COOH groups by electrostatic interaction. The resultant MP-TBO complex was rinsed with 0.02 M NaCl (pH 11) and placed in the same solution for an extended time of 1 h, during which the unbound dye collected as a supernatant to measure. Subsequently, the MP-TBO complex was immersed in 0.5 ml of 0.2 M NaCl solution at pH 2 for 30 min under bath-sonication, promoting the release of TBO from the carboxyl groups into the solution, coloring it blue. Since the carboxyl groups of the MP could be ionized at pH 11 and protonated at pH 2, TBO molecules physically bind to ionized carboxyl groups (COO^-) at a pH of 11 and are released when immersed in pH 2 condition. The molarity of the release dyes could be served as the molarity of the surface carboxyl groups. Here, the molarity of COOH groups was determined by measuring both the unbounded TBO as well as the

released TBO after immersion at pH 2 conditions. A best-fit polynomial equation rather than a linear equation was fitted to the standard curve. Each measurement was compared to the calibration curve in reference to the corresponding pH, and the average value of the three measurements was reported.

4.2.4.2 Particle size and zeta potential analysis

The average hydrodynamic diameter and size distribution (polydispersity index) of MPs before and after AB conjugation were determined by a size analyzer using dynamic light scatter (DLS, Brookhaven instrument Corporation, USA). The stock suspensions of MP and MP-AB were diluted with Milli-Q water at a concentration of 0.01 mg ml^{-1} to eliminate concentration-dependent effects. Size measurements were recorded at a temperature of 25 ºC and a scattering angle of 90º. Size distribution data were obtained from the autocorrelation functions of the instrument. A ZetaPlus analyzer using laser Doppler anemometry (Brookhaven Instruments Corp., Holtsville, NY) was employed to determine the net zeta potential (ζ) in Milli-Q water at 25 ºC. The electrophoretic mobility of the particles diluted to a concentration of 0.01 mg ml^{-1} was measured. Zeta potentials were then estimated at the stationary level using the Smoluchowski equation. All measurements were conducted in triplicate from ten independent experiments.

4.2.4.3 Transmission electron microscopy (TEM) observation and image analysis

The morphology characteristics and size of the MP-AB, bare MTB, MPs alone, and MTB-MP complex were determined by TEM. The MTB-MP complexes or bare MTB suspensions were fixed with 2.5% glutaraldehyde in 0.1 M phosphate buffer solution pH 7.4 (Electron Microscopy Sciences). Formvar/carbon-coated copper grid (200 mesh, SPI Supplies) was ionized by argon plasma discharge. A 5 μl drop of the fixed suspension was then deposited on a grid and allowed to adhere for 10 min at room temperature. When some of the cells adhered to the grid, the excess liquid was blotted with filter paper. The grids were washed with water three times. Then, as before, the excess liquid was removed, and the grids were allowed to dry slowly. In the case of MP-AB and MP alone, 10 μl of samples (400 μg ml^{-1}) in Milli-Q water were placed on carbon-coated copper grid and dried at room temperature. Observations were carried out using an FEI Tecnai 12 BioTwin TEM (AMT XR80C CCD camera system) operated at 120 kV. Images were captured with a Gatan Ultrascan (2k × 2k) digital camera.

4.2.4.4 Confocal laser scanning microscopy and image acquisition

The success of MTB-MP complex formation and also the efficiency of FITC-AB conjugation to the fluorescent-MP surface were further confirmed by observation under confocal laser scanning microscopy (CLSM: Carl Zeiss LSM 628 510-META with Axiovert inverted microscope, Jena, Germany). FITC-AB (ex/em: 495/525 nm), Lumogen-S200/F200 (ex/em: 578/613 nm) and Rhodamine B-S500/F500 (ex/em: 540/625 nm) were visualized upon excitation with Ar-ion laser and He-Ne laser, respectively. Images were acquired using a 63× magnification with 1.4 numerical aperture (NA) oil-immersion objective and Carl Zeiss LSM imaging software.

4.2.4.5 Fourier transform infrared spectroscopy (FTIR)

Characterization of the MP-AB conjugation was performed using FTIR spectrophotometer (Spectrum two, Perkin Elmer, UK) equipped with the attenuated total reflection (ATR) cell. Approximately 10 mg of lyophilized samples were introduced onto the ATR crystal followed by an acquisition of spectra in the range of 400-4000 cm^{-1} at a resolution of 4 cm^{-1}. Background measurements were carried on before the analysis of each sample.

4.2.4.6 Microcontact printing (μCP)

Soft lithographic approaches, such as μCP, have been explored to identify the selective binding of MTB to substrate-immobilized MP-AB. The mold for soft lithography was fabricated by curing negative photoresist SU-8 2025 (Microchem Corp, Boston, MA) on a silicon wafer [329]. Standard photolithography was performed on the wafer using the design printed on a chrome mask. This patterned master was then used to fabricate the poly (dimethylsiloxane) (PDMS; Essex Chemical, Boston, MA) elastomer stamps. After curing, the PDMS elastomer was peeled off from the master and cut to 1 cm^2. The resulting PDMS stamps had a line shape pattern of 25 μm wide bars and 40 μm wide gaps that extended the length of each stamp. The PDMS stamp was first plasma treated in an O_2 plasma for 1 min (200 mTorr O_2, 200 W) to increase in hydrophilicity and antibody adsorption. Subsequently, it was covered with 20 μl (400 μg ml^{-1}) of anti-MC1 MTB antibodies attached to particles (S200-AB) for 10 min at 25 °C. To avoid evaporation of the solution, a coverslip was placed on the stamp. After rinsing with PBS and drying under N_2 gas for 30 s, the stamp was gently brought into contact with the plasma treated glass surface. After 1 min, the PDMS stamp was removed carefully, while the S200-AB samples

remained on the substrate. After patterning of fluorescence-labeled S200-AB onto substrates, the resulting micropattern was visualized using confocal microscopy. In order to reduce the nonspecific binding of bacteria to the bare silicon spaces between the sample-stamped lines, the surface was blocked using 2 ml blocking buffer (*i.e.*, BSA, PLLA-PEG, goat serum) for 30 min. After washing with PBS, 2 ml of MTB (5×10^6 MTB ml^{-1}) was allowed to bind for 1 h. Then, the surface was washed to remove non-attached bacteria and visualized under a microscope.

4.2.4.7 Fluorescence spectroscopy analysis of MP-AB and MTB-MP complex

Coupling efficacy of AB to MP was assessed using fluorescence-based characterization techniques, including fluorescence-UV/Vis spectroscopy and fluorescamine (FL-amine) protein detection assay. Fluorescence spectroscopy was utilized for quantification of fluorescein isothiocyanate (FITC) labeled AB raised against MC-1 MTB (GenScript Inc., Piscataway, NJ, USA) covalently coupled to the surface of fluorescent MPs. Nano-screenMAG/R-ARA (200 nm), Nano-screenMAG/MP/R-ARA (200 nm), screenMAG/RR-carboxyl (500 nm), and screenMAG/MP/RR-Carboxyl (500 nm) particles (Chemicell, Germany) were used. The iron oxide cores are covered by the fluorescence dye Lumogen/F Red 300 (ex/em: 578/613 nm) and Rhodamine B (ex/em: 540/625) for nano-screenMAG and screenMAG, respectively. Considering the initial concentration of AB (20 μg ml^{-1}) used for attachment, the calibration curve was constructed by preparing a serial dilution of FITC-AB in PBS (1-50 μg ml^{-1}). The samples were excited at 495 nm while fluorescent emission was recorded at 525 nm using a Multi-Mode Microplate Reader (SpectraMax i3, Molecular devices). Different fractions of MP-AB and non-covalently coupled AB were collected and analyzed for protein content. The amount of ABs covalently coupled to the MP was determined by comparing the fluorescent intensity of MP-AB sample to the prepared calibration curve. The amount of unbounded antibody was also determined by subtracting the calculated amount of covalently coupled AB to MP from the initial amount of AB that was added to the MP solution during preparation.

FL-amine protein assay was also utilized for quantification of attached AB to the surface of MP. FL-amine, a heterocyclic Dione, is a sensitive fluorescence-based colorimetric assay used to detect primary amine functional groups and measure protein concentrations. Non-fluorescent FL-amine dye reacts rapidly with primary amines of ABs to form a fluorescent product, which emits strongly at around 480 nm under excitation at 400 nm [330]. The fluorescence of MP-AB

samples plus FL-amine is proportional to the quantity of AB conjugated to MP. A standard curve was plotted based on reaction of different AB concentrations (1-50 μg ml^{-1}) in phosphate buffer (100 μl, pH 7.4) with 32 μl of freshly prepared FL-amine solutions (3 mg ml^{-1}) (Sigma) in acetonitrile. For MP-AB samples, 20 μl of sample solution (400 μg ml^{-1}) was diluted in 80 μl of PBS followed by the addition of 32 μl of FL-amine solution. Fluorescence emission was recorded rapidly after adding the FL-amine reagent to the sample using microplate reader. To quantify the AB concentration per mg of MP, the recorded values were compared to the calibration curve.

Beside TEM observation, for quantification analysis of MTB-MP bio-complexes, the fluorescence spectroscopy was used. The MP-AB was synthesized using the fluorescent MPs and FITC-AB according to the procedure described previously. A standard curve for various concentrations of MP-AB (20-400 μg ml^{-1}) was plotted against fluorescent values recorded at ex/em peak at 578/613 nm for Lumogen, 540/625 nm for Rhodamine B, and 495/525 nm for FITC. After MTB-MP formation, the complexes were washed three times with PBS and subsequently concentrated 50 times. 100 μl of the complex was loaded into a 96-well plate, and the emission was recorded using a microplate reader at the same wavelengths as used for fluorescent-MP and FITC-AB. The concentration of MP and AB in the complex was estimated based on the obtained value compared to the standard curve.

4.2.4.8 Magnetic properties of MP, MP-AB, and MTB

Magnetic characterization of the MTB cells, MPs (S200, S500, F200, F500) and MP-ABs (S200-AB, S500-AB, F200-AB, F500-AB) was performed using a vibrating sample magnetometer (VSM: Microsense EV9). 40 μl (10 mg ml^{-1}) of each MP sample and MP-AB diluted in PBS were measured in a glass container at room temperature. The magnetic moment, saturation magnetization and coercive field strength were measured for whole particle mass by applying field ranging from -20 to 20 kOe at a precision of about 10^{-7} emu.

The amount, size, and a number of magnetic materials in the magnetosome chain of MTB are important factors that influence the relaxivity of MRI. To quantify the amount of magnetic material in each MTB, direct magnetic measurement using VSM as well as theoretical calculations based on magnetosome properties was performed. The magnetic moment per bacterium can be calculated knowing that magnetosomes of MC-1 MTB are composed of magnetite (Fe_3O_4) with a magnetic moment per unit volume (M_v) of 480 emu ml^{-1} and density of

5.2 g ml^{-1} [80]. To measure the magnetic moment of the MTB using VSM, the cells were washed three times using a two-dimensional magnetic field and resuspended in PBS. Then, 40 μl of MTB (~4.2×10^7 MTB) were placed in a glass container and measured at 6.82×10^{-5} emu (~1.62×10^{-12} emu per MTB). The magnetic moment was then converted into mass magnetization σ_M (emu g^{-1}). Dividing the magnetic moment values by the known magnetic moment of magnetite and multiplying by magnetite density provided the amount of magnetite per bacteria. Iron content is the molar ratio (168/232) of iron in magnetite.

To confirm the VSM results, TEM images were obtained from MTB and their magnetosome. The average diameter and size distributions of magnetosomes were determined from multiple TEM images (approximately 1500 particles) using ImageJ software (National Institutes of Health, Bethesda, MD, USA). The magnetosomes were considered as a chain of single domain magnetite spheres with an average number of 15 ± 5 magnetosomes per chain, and an average radius of 34 ± 13 nm (68 nm in diameter). Therefore, for a single particle of volume 1.64×10^{-16} cm^3, the magnetic moment is obtained at around 7.89×10^{-14} emu. For an MTB containing an average of 15 particles, the total magnetic moment per bacterium is calculated about 1.184×10^{-12} emu. Using the same formulation, the amount of magnetite per bacteria is estimated at around $1.28 \pm 0.7 \times 10^{-14}$ g per MTB, which is close to the VSM measurement.

4.2.5 Tumor model

For *in vivo* studies, human colorectal tumors implanted into the flank of SCID-beige mice (Charles Rivers) were established as xenograft models. HCT116 (CCL-247) parental mammary colorectal carcinoma cells (ATCC; Manassas, VA) were maintained at 37 °C, 5% CO_2 in McCoy's 5A medium (MULTICELL) with 10% fetal bovine serum (FBS). Trypsinized cells (0.25% (w/v) Trypsin-0.53 mM EDTA) were resuspended in PBS at a final concentration of 5×10^7 cells per ml immediately prior to use. Two mice were used for each experimental arm, in two independent experiments. Experimental procedure and animal care were conducted in accordance with the Canadian Council on Animal Care guidelines and with the approval of the Animal Care Committee of the McGill University Health Center. All the animals were pathogen-, murine virus-, helicobacter-, and parasite-free. At 8 weeks of age and around 25 g of body weight, SCID mice received 100 μl of 5×10^7 tumor cells per ml subcutaneously in the flank resulting in tumors with sizes of approximately 700–800 mm^3 within 4 weeks. During the 30 days of tumor

growth, the animal weight and volume of the tumor were assessed. Tumor volume was estimated with measurements obtained from an electronic caliper using the following formula [331]: [(length) × (width)^2 × 0.5].

4.2.6 *In vivo* magnetically targeting of MTB-S200 complex

Each MTB sample injection was prepared from an initial quantity of 200 ml of MTB (5×10^6 MTB ml^{-1}) suspended in the culture medium. MTB and MTB-MPs were concentrated using the two-dimensional magnetic setup, causing a swarm of bacteria to appear in the center of petri dishes after a few minutes (Figure 4.2a, b). The culture medium surrounding the cluster was then gently removed, and the samples were washed three times with PBS. Finally, samples were concentrated to maximize the number of injected bacteria. Prior to injection, a homogeneous sample of the final solution was collected, and the exact concentration of injected bacteria into each mouse was quantified by counting under optical microscopy (Carl ZEISS). Fifteen minutes before the sample injection and prior to the actual magnetic navigation process, each animal was anesthetized with an intraperitoneal (*i.p.*) injection of Xylazine/Ketamine at the appropriate dose based on their individual weight. A 200 μl of 5×10^9 MTB ml^{-1} in PBS of freshly concentrated MTB-S200 were injected peritumorally (*p.t.*) in one side of the tumor.

Using three-dimensional magnetic fields generated by a pair of orthogonal magnetic coils, the MTBs were magnetically navigated for 1 hour towards the center of the tumor. The magnetic set-up was designed and built especially for the *in vivo* experiments to accumulate the bacteria in the tumor (Figure 4.2d). The motion guidance of MTB was obtained using custom-designed computer software to control the amplitude of the electrical current delivered by GPIB power supplies to the coils. Bare MTB and MPs alone were used as a control with the quantity adjusted on the basis of MTB-S200 equivalents. At the end of the navigation, animals were euthanized with CO_2 overdose and tumors were harvested immediately from the sacrificed animals. The marker served as a reference to properly orient the immunofluorescence tumor sections with respect to the MR image slices. Tumors were washed once with PBS to remove any unbound samples and then fixed in 10% neutral buffered formalin for MRI and histology studies.

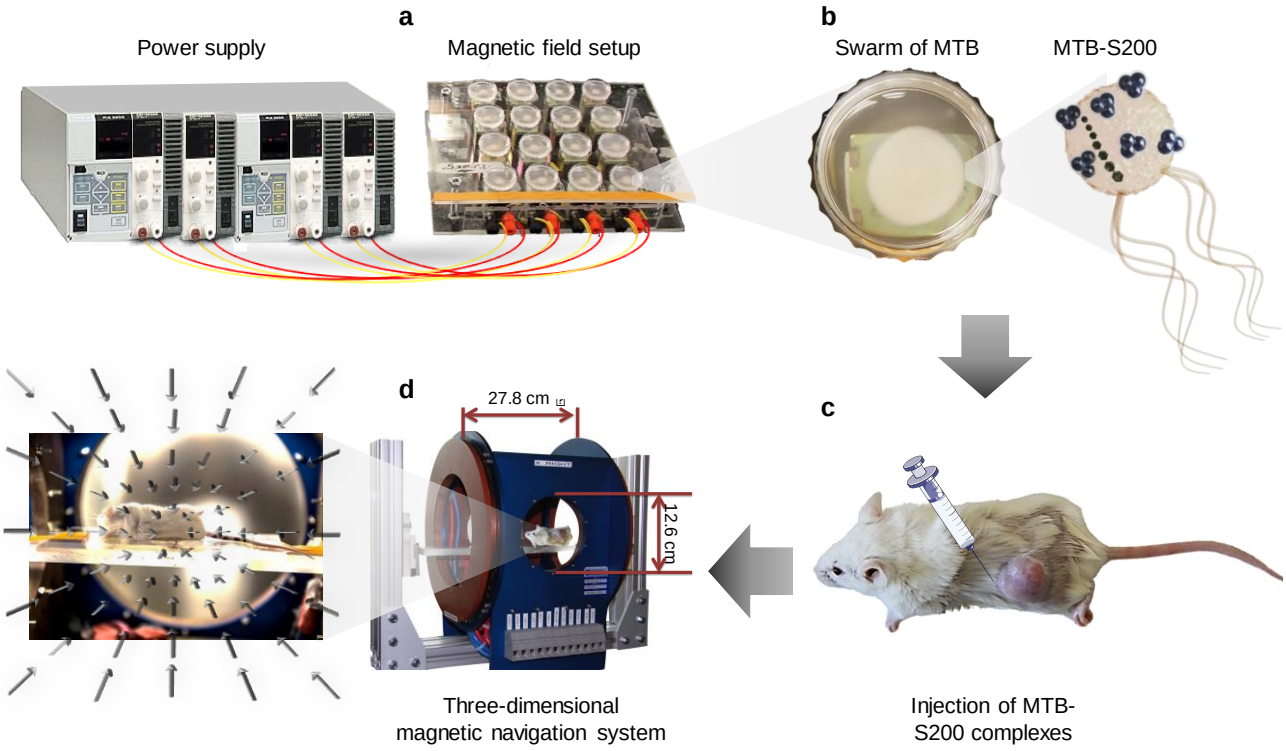

Figure 4.2: Schematic illustrating magnetically navigation process of MTB-MP complex in tumor xenograft. (**a**) Two-dimensional magnetic setup to accumulate and wash the MTB and their complexes. (**b**) An enlarged picture of the swarm of MTB-MP. (**c**) Photographs of mice with xenografts receiving MP-loaded MTB. (**d**) Side view of the home built three–dimensional magnetic navigation system and animal placement.

4.2.7 Relaxivity measurement

T_1 and T_2 relaxivities were measured at 3 Tesla on a clinical MR scanner (Siemens Skyra) at room temperature using a 32-channel head coil. For *in vitro* phantom studies, several concentrations of MTB-MP (MTB-S200 and MTB-S500) were prepared ranging from (10^8, 5×10^7, 2.5×10^7, 1.25×10^7, 6.25×10^6, and 3.12×10^6 MTB ml^{-1}). Bare MTB and MP alone with the equal concentration corresponding to the MTB-MP samples were used as a control. Concentration of the MTB samples was determined by direct counting under optical microscopy. Each 500 μl of concentrated sample was inserted into a 1 ml microtube. The phantoms were aligned inside a container, which was subsequently filled with gel and solidified at 4 °C to maintain a homogenous cellular distribution. For T_1 measurements, an inversion-recovery fast-

spin echo sequence was performed with inversion times (TI) of 50, 100, 150, 200, 400, 800, 1500, 2500, and 4000 ms and the following imaging parameter: TR/TE = 10000/8.6, flip angle = 150°, bandwidth = 245 Hz/pixel, voxel size = 0.46 × 0.46 × 3 mm, imaging matrix = 256 × 256. T_1 values were estimated using a non-linear function least-square curve fitting according to the following equation:

$$S(TI) = S_0\,[1 - 2\exp\,(-\frac{TI}{T_1})] \tag{4.1}$$

where $S(TI)$ is the MRI signal intensity at inversion time TI, and S_0 is the MRI signal magnitude at equilibrium.

T_2 maps were calculated using a fast spin-echo sequence at various echo times (TE) of 10, 20, 30, 40, 60, 100, 150 and 180 ms and the following imaging parameters TR = 10000, flip angle = 150°, bandwidth = 260 Hz/pixel, voxel size = 0.46 × 0.46 × 3 mm, imaging matrix = 256 × 256. T_2 values were estimated using a non-linear function least-square curve fitting according to the following equation:

$$S(TE) = S_0\,\exp\,(-\frac{TE}{T_2})] \tag{4.2}$$

where $S(TE)$ is the MRI signal intensity at which TE is used. The signal intensity for each sample was averaged over multiple cross-sectional slices, which were acquired along the height of each sample. Relaxation rates ($r_1 = 1/T_1$ and $r_2 = 1/T_2$) were plotted against the concentration of the solutions, and then the slopes were used to determine the relaxivities.

4.2.8 *Ex vivo* MRI

The *ex vivo* MR imaging of the formalin-fixed tumors was acquired to confirm the magnetically targeting and distribution pattern of the MTB-S200 complex inside the human colorectal mouse tumor xenografts. Bare MTB, S200 alone, and tumors without injection were served as control. Fixed tumors were put in a gelatin solution and solidified at 4 °C. MR imaging of the tumors was performed on a 3 Tesla MAGNETOM Skyra scanner (Siemens, Erlangen, Germany) equipped with self-shielded gradient coils (45 mT/m@200 T/m/s). Coronal and axial images were acquired from xenografts using a typical 16-channel hand/wrist coil and a spoiled gradient echo sequence (FLASH). The imaging parameters were set to TR/TE = 250/4.73, flip angle = 70°, bandwidth =

220 Hz/pixel, voxel size = 0.25 × 0.25 × 2 mm and imaging matrix = 320 × 320 to obtain T_1-weighted contrast and to TR/TE = 700/10, flip angle = 25°, bandwidth = 210 Hz/pixel, voxel size = 0.20 × 0.20 × 1.5 mm and imaging matrix = 384 × 384 to acquire T_2^*-weighted contrast.

4.2.9 Histology analysis

For histology analysis, fixed tumors were sectioned into longitudinal slices following navigation trajectory to view possible MTB migration inside tumor tissue. Oriented paraffin embedded tissues, which are corresponding to slices of the MRI were cut using microtome (Leica RM2255) into 4 μm thick sections. The sections from each block were subsequently layered on two slides, which each was stained with HPS or submitted to immunofluorescence for further assessment of the presence of MTB. For immunofluorescence studies, representative sections were submitted to automated immunostainer (Discovery XT system, Ventana Medical Systems, Roche group, Tucson, AZ) following fluorescence *in situ* hybridization (FISH) procedure and manual titrations by using proprietary reagents ready to use from Ventana Medical Systems. After deparaffinization and rehydration of the sections, antigen recovery was conducted using heat retrieval and cell conditioning 1 (CC1) standard option, in Tris/EDTA buffer (pH = 9) for 30 min in a bath at 95 °C. Then, rabbit anti-MC1 antibody (2 mg ml^{-1}, GenScript Inc.) with 1:300 dilutions in PBS was applied on every slide for 60 min at room temperature. Afterward, the slides were incubated with an FITC-labelled secondary anti-rabbit antibody for 32 minutes to visualize MC1 receptors in green. Finally, sections were washed and mounted using ProLong® Gold Antifade Reagent with DAPI (Invitrogen). Images were obtained using a digital camera (DP71) mounted on an Olympus BX61 microscope. The other tissue sections were stained with HPS. Immunostained and HPS slides were scanned using the NanoZoomer Digital Pathology system (Hamamatsu, Bridgewater, NJ).

4.3 RESULTS AND DISCUSSION

4.3.1 Physicochemical characterization of the MRI contrast agents

Magnetite (Fe_3O_4) nanoparticles with ferromagnetic or superparamagnetic property with each MNP being embedded in a polymeric matrix and clustered as larger MPs with diameter of approximately 200 nm and 500 nm (designated S200, S500, F200, and F500 for 200 nm and 500

nm superparamagnetic and ferromagnetic MPs, respectively) with functional carboxyl groups were used as MRI contrast agents. Covalent conjugation of IgG antibody to the surface of each MP provides excellent MP-AB bio-complexes for specific attachments to the surface of the MC-1 MTB cells. Although a number of conjugation methods have been developed for covalent coupling amine- containing molecules to carboxylate particles [195], in the current study, the carbodiimide EDAC/NHS [332, 333] was used as an aqueous dehydrating agents to preserves optimal activity and significant immobilization while guaranteeing reproducibility to prepare MTB-MP-AB complex into desirable configurations for the proposed application.

Prior to conjugation of biomolecules, quantification of surface functional groups on nanoparticles that are responsible for covalent attachment can provide good insight into designing the reaction conditions. The carboxylation degree of MPs was measured by a colorimetric assay based on quantification of the amount of toluidine blue O molecules bonded to the carboxyl groups (Table 4.1). The carboxylation degree was ~583 μmol [COOH] g^{-1} particle for Fluid-MAG (200 nm) and ~850 μmol g^{-1} particle for Si-MAG (500 nm). As shown in Table 4.1, the degree of carboxylation is dependent on the type of particle coating and size, while it is independent of the magnetic property (ferromagnetic or superparamagnetic). A greater number of carboxylic groups are presented on the larger particles, offering a higher level of surface functionalization degree.

Fourier transform infrared spectroscopy, transmission electron microscopy, dynamic light scattering, zeta potential, confocal microscopy, as well as quantitative spectroscopy data confirmed the successful formation of MP-AB with high dispersity and stability (Figure 4.3, Table 4.1).

The covalent chemical attachment of AB to MPs using carbodiimide chemistry was assessed by FTIR spectroscopy. The results provide evidence of successful MP-AB conjugations with the presence of peaks assigned to amide bond formations within the amines and carboxyl acid during the reaction (Figure 4.3a). The spectrum of MP with carboxyl acid displays significant rise of the characteristic peak owing to the free COOH (C=O) stretching vibration with strong intensity at 1749 cm^{-1}, the presence of O–H at 3386 cm^{-1}, and C–O at 1150 cm^{-1}. Furthermore, the MP characteristic peak of the Fe–O bond is observed at 556 cm^{-1} as well as distinct Fe–OH stretching (960 cm^{-1}) and bending (864 cm^{-1}) vibrations. A weak peak of 1380 cm^{-1} is also observed and corresponds to aromatic ether groups introduced by glucuronic acid coating on the surface of the

MPs. After AB conjugation, the disappearance of characteristic peaks of oxide groups in MP surface (1749 cm^{-1}) indicates that COOH groups were bonded to the ABs. In a more specific approach, the FTIR spectrum of MP-AB exhibits AB absorption features located in the zone related to amide (–CONH–) that corresponds to the N–H stretching (νN–H at 3331 cm^{-1}) and C=O (νC=O at 1658 cm^{-1}) [334]. Compared to pure particles and antibodies, the intensity of the N–H bending band of an amide at 1690 cm^{-1} increases remarkably. Indeed, the primary amines specific peaks of AB (1550 cm^{-1}) vanish after conjugation to surface carboxyl groups. The obtained results confirm that the AB is covalently grafted to the MP surface through an amide bridge.

Table 4.1: Physicochemical characterization of MP-AB and MTB-MP complexes. Size distribution, zeta potential, carboxylation degree, and saturation magnetization (M_s) of MPs after AB attachment are shown. Moreover, quantification of AB conjugated to MP and MP-AB attached to MTB (MTB-MP) are also presented.

Magnetic particle types		**S200**	**F200**	**S500**	**F500**
		FluidMAG-ARA	FluidMAG/MP-ARA	SiMAG-carboxyl	SiMAG/MP-carboxyl
		Superpara magnetic	Ferromagnetic	Superpara magnetic	Ferromagnetic
Size (nm)	MP	203 ± 11		507 ± 18	
	MP-AB	267 ± 15		596 ± 32	
Zeta potential (mV)	MP	-34 ± 2.94		-41 ± 4.15	
	MP-AB	-18 ± 3.87		-23 ± 2.09	
Degree of carboxylation [COOH (μmol)/MP(g)]	MP	583		850	
M_s (emu/g)	MP-AB	46.73	73.41	30.45	51.77
AB(μg)/MP(μg)		0.0027	0.0015	0.0086	0.0024
MP(μg)/MTB		3.6×10^{-6}	4.8×10^{-6}	5.5×10^{-6}	11.6×10^{-6}

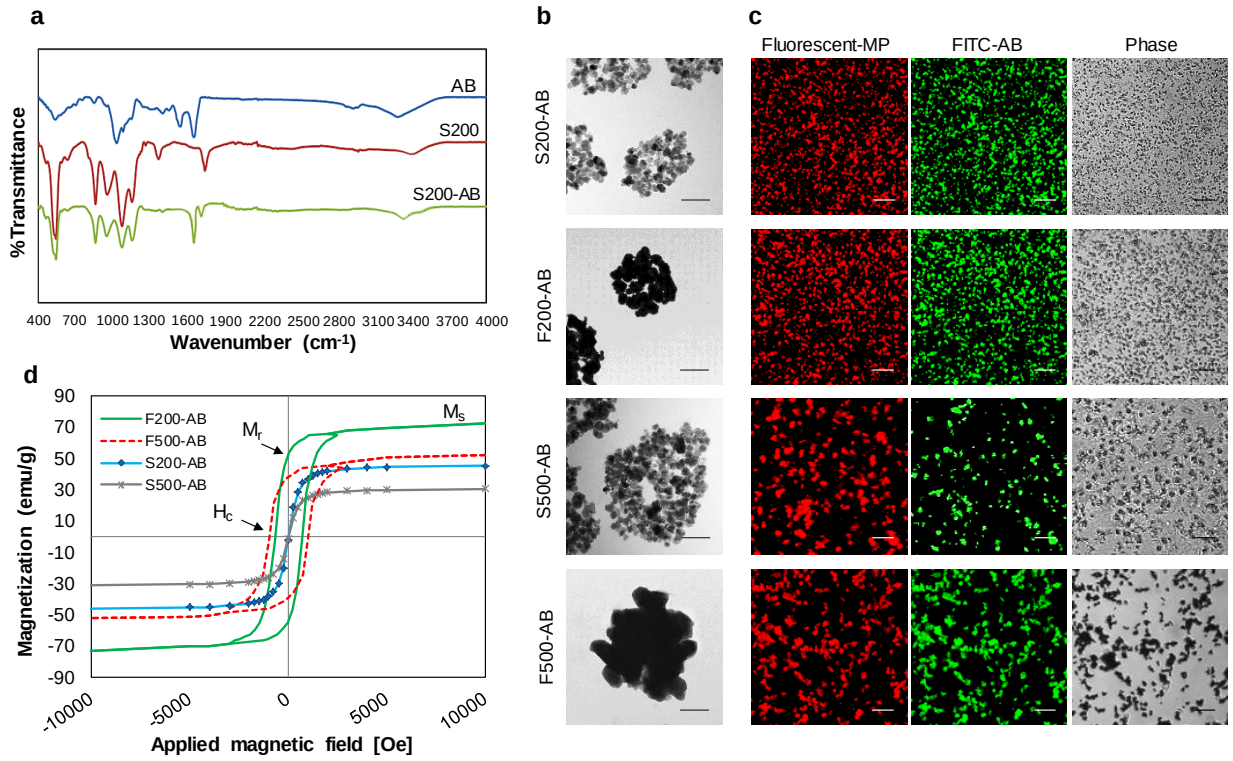

Figure 4.3: Characterization of the MP-ABs. (**a**) Comparison of FTIR spectra of the S200-AB, S200, and AB. For S200-AB, the peaks at 1658, 1690, and 3331 cm^{-1} represent C=O, N-H bending, and N-H stretching bonds of the amide group, respectively. For S200, the acid peaks appear at 1749 and 3386 cm^{-1} that shows the C=O and O-H bond, respectively, hence confirming the functionalization of the particles. In the AB graph, the peak at 1550 cm^{-1} shows the amine of non-attached antibodies. (**b**) TEM images of S200-AB, S500-AB, F200-AB, and F500-AB are depicted. The MPs are comprised of individual magnetite particle cores embedded in a matrix. Scale bar 100 nm. (**c**) Confocal microscopy images of Lumogen-S200/F200 and Rhodamine-S500/F500 MPs (red) with conjugated FITC-labelled AB (green). Scale bar 2 μm. (**d**) Magnetic hysteresis curves (M-H) of MP-AB at 25 °C. The hysteresis loop indicates nearly zero value for coercivity (H_c) and magnetic remanence (M_r) for S200 and S500 while hysteresis is presented for the F200, F500.

The mean sizes of different MPs including S200, F200, S500, and F500 particles before and after AB attachment are presented in Table 4.1. As depicted, the results indicated that the AB conjugation causes slight increases of the size of the MPs. The mean size of S200-AB and F200-AB particles were around 267 ± 15 nm from 203 nm in average with a polydispersity index of

0.14. The average diameter of S500-AB and F500-AB were approximately 596 ± 32 nm from 507 nm with a polydispersity index of 0.25, indicating successful conjugation and minimal aggregation. To assess the surface charge as it plays an important role in determining the colloidal stability of the particles, zeta-potential measurements (before and after attachment) were performed. The negative zeta potential values displayed by particles can be explained by the potential ionization of the COOH groups, leading to a negative surface charge. It can be seen from Table 4.1 that the zeta potential values of S200 and F200 after AB attachment was raised from -34 to -18 mV, while S500 and F500 was altered from -41 to -23 mV. The absolute zeta potential for MP-AB resulted in less negative values than those without AB on the surface that correlated with an increase in size while the MP-ABs still having a low tendency to aggregate. This reduction in negative surface charge is due to the attachment of IgG ABs carrying a net positive charge at neutral pH as well as a decrease in MP surface carboxyl groups due to amidation reaction.

The TEM was performed to observe the structure and size distribution of MP-AB particles (Figure 4.3b). The obtained TEM images confirmed that the MPs consisted of a cluster of polymer coated superparamagnetic or ferromagnetic nanoparticles and displayed a diameter of approximately 200 and 500 nm for S200/F200-AB and S500/F500-AB, respectively, confirming the dynamic light scattering data. For the S200-AB and S500-AB, the core diameters of the MNPs in each cluster vary in a narrow size distribution ranging between 12-15 nm. The individual particles were visible, whereas the shell did not provide sufficient contrast. Confocal microscopy visualization of the coated FITC-labelled anti-MC1 AB (FITC-AB) on the surface of Lumogen-labelled S200/F200 and Rhodamine-labelled S500/F500 MPs was also performed and depicted in the Figure 4.3c. The results indicate that the particles are coated with antibodies.

The M_s values were measured by vibrating sample magnetometer (VSM) and are presented in Table 4.1. The relationship between magnetization (M) and the applied magnetic field (H) is expressed in the M-H curve depicted in Figure 4.3d. The M_s was measured at 46.73 and 30.45 emu g^{-1} for S200 and S500, respectively, and through the hysteresis curve it was confirmed that the particles will be saturated at 3T MR scanner. Magnetite particles can act both as a ferromagnetic and superparamagnetic material depending on the particle's size [335]. Ferromagnetic crystals are composed of magnetized domains. Superparamagnetism occurs when the size of particle is smaller than the ferromagnetic domain (~30 nm). The lack of magnetic

hysteresis loops confirms the superparamagnetic behavior of the particles. Therefore, in the absence of an external magnetic field these particles have zero magnetization and fewer tendencies to agglomerate, which is a key factor for *in vivo* applications. Ferromagnetic particles show M_s values of 73.41 and 51.77 emu g^{-1} for F200 and F500, respectively, somewhat lower than the magnetite bulk value (~92 emu g^{-1}). The recorded hysteresis loops show that these ferromagnetic particles have a remanent magnetization, which may lead to unwanted aggregations after removal of the applied magnetic field. The results indicate that the magnetization measurements of MPs after functionalization with the ABs show negligible changes in the magnetic properties (around 2-4%).

To quantify the amount of AB conjugated to two different sizes of MPs with superparamagnetic or ferromagnetic properties, different fluorescent-based techniques were employed (Table 4.1). Fluorescent spectroscopy results confirm that the attachment method can provide enough ligands to interact with the MTB specific receptors. More than 60-70% FITC-AB coupling efficiency is observed for various MP-AB formulations. The FL-amine assay was also used to measure the amount of AB (non-fluorescent) per mg of MPs. The FL-amine reagent reacts rapidly with primary amines of ABs and makes fluorescent molecules emit strongly around 480 nm under excitation of 400 nm. Compared to the AB calibration curve, ABs are successfully conjugated to the MP surface. This result is in accordance with estimated fluorescence AB attachments measured by fluorescent spectroscopy. The effect of the particle size on AB binding at equal solid mass is presented in Table 4.1. The density of carboxyl group for different-sized particles was not the same as determined by TBO assay. Considering that the degree of carboxylation was 850 and 583 μmol g^{-1} for 500 and 200 nm MPs, respectively, the amounts of attached ABs were greater for larger MPs. Moreover, the superparamagnetic particles show higher attachment efficacy compared to ferromagnetic particles. In fact, S200 and S500 allow for almost 1.8-fold and 3.5-fold higher AB attachment than F200 and F500, respectively. This difference could be due to the easy resuspension, the slow sedimentation, and the uniform distribution of superparamagnetic particles during the attachment process.

4.3.2 Characterization of the MTB-MP complexes

As shown in Figure 4.4 and Table 4.1, qualitative and quantitative analyzes demonstrate the successful and specific attachment of MP-AB to the surface of the MTB cells. TEM and confocal

images provide evidence for AB-functionalized MP attachment to MTB after 2h incubation as depicted in Figure 4.4a, b. The images show that the conjugated ABs are preserving their specific activity and availability for binding to MTB antigens, which results in overlapping of MP-AB particles with MTB in the confocal images.

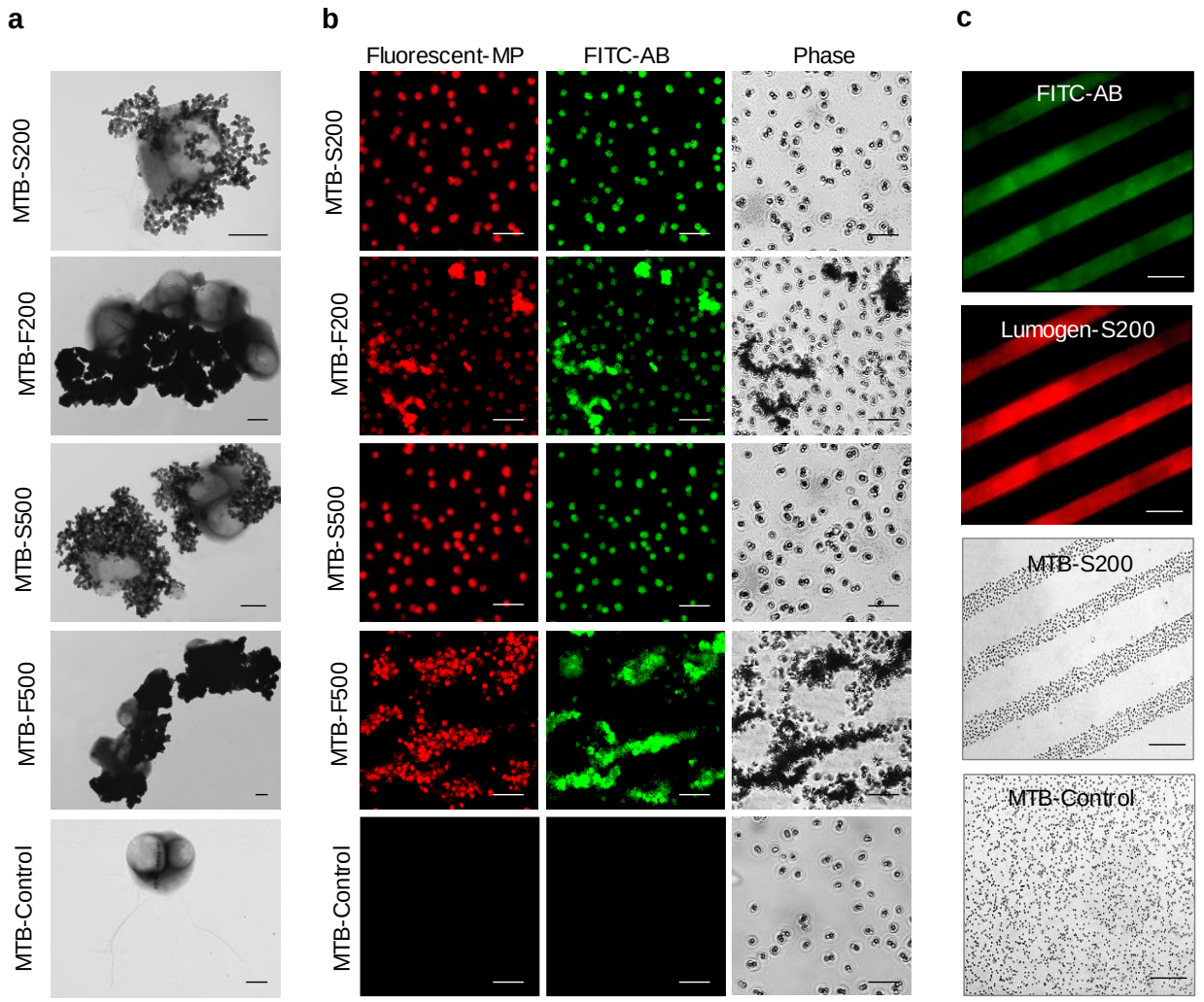

Figure 4.4: Characterization of MTB-MP complexes. (**a**) TEM images of MTB-MPs and bare MTB. Scale bar 0.5 μm. (**b**) Confocal microscopy images of FITC-AB conjugated Lumogen-S200/F200 or Rhodamine-S500/F500 attached to MTB. MTB-S200 and MTB-S500 show the uniform distribution while aggregation was observed in MTB-F200 and MTB-F500. Bare MTB was used as a control. Scale bar 10 μm. 60× magnification. (**c**) Fluorescence photomicrograph of patterning MTB-S200 to the surface. Photomicrographs depict the FITC-AB stamped surface (top), Lumogen-labelled S200 particles stamped the surface (middle top), patterned MTB-S200 complex (middle bottom), and non-patterned MTB as control (bottom). Scale bar 40 μm.

Microcontact printing of MTB-S200 was performed to generate patterns of MTB by binding on patterned FITC-AB attached to Lumogen-S200 (Figure 4.4c). Due to a specific interaction between AB and MTB's antigen, the bacteria follow the bait redistribution on the patterned surface. Phase and fluorescence images clearly show that the MTBs bind specifically and only on the stamped MP-AB regions. In the control, where an equivalent number of bacteria were incubated with non-treated surfaces, MTBs did not form a pattern on the surface (Figure 4.4c).

Fluorometric assay was used for quantifying the attachment efficacy. As presented in Table 4.1, the amounts of MP attached to MTB were approximately 3.6×10^{-6}, 4.8×10^{-6}, 5.5×10^{-6}, and 11.6×10^{-6} μg per each MTB for MTB-S200, MTB-F200, MTB-S500, and MTB-F500, respectively. The amount of attached MPs per each MTB for the MTB-F200 was slightly higher than that of MTB-S200 (~1.33-fold) while it was ~2-fold greater for MTB-F500 compared to MTB-S500. Even though the results indicate that the attachment efficacy was greater for ferromagnetic particles compared to SPIONs, TEM and confocal images showed the aggregations following conjugation to MTB with this type of particles. Considering that the MTB-MP complexes must transit through the tumor tissue followed by the penetration through cellular barriers and the effective distribution in the extracellular matrix, they should remain as an individual magnetic carrier system prior the navigation procedure.

In addition, while higher concentration of the MPs may result in higher MRI contrast ability, the loading capacity and overall sizes of the MPs per bacteria is however limited not only by the transport capacity of the cell itself but also by the overall diameters of the physiological routes and openings that must be transited to target effectively the hypoxic areas. Therefore, in addition to the contrast ability, the quantity and the overall sizes of the MPs attached per MC-1 cell need to be adjusted appropriately.

Further, ferromagnetic iron oxide particles are composed of magnetized domains with a very large magnetic susceptibility, which persists upon removal of the external magnetic field of MRI. In some studies, the application of ferromagnetic particles as MRI contrast agents for blood pool, liver and spleen imaging [336], and cell labeling have been suggested [337]. Despite the strong magnetic properties and higher M_s values of ferromagnetic particles compared to SPIONs (Table 4.1), the clinical application of such particles as MRI contrast agents is limited due to their remanent magnetization. Our experimental results indicate that the aggregates formation of

ferromagnetic particles after attachment to the MTB leads to a considerable reduction of MTB motility. In contrast, SPIONs present many advantageous properties over ferromagnetic particles such as a slow sedimentation and a uniform particle distribution before and after attachment, which provides the ability for the loaded MTB to achieve the appropriate penetration and distribution in the tumor milieu. In addition, they lose their magnetization in the absence of an external field while responding quickly to an external magnetic field and also exhibiting relatively high saturation magnetization [338, 339]. A cluster of SPIONs can be used to enhance the contrast in MR images for several biomedical applications such as cell labeling, drug delivery, MRI, and hyperthermia [67, 340, 341].

When addressing the possible *in vivo* application of MPs, it is important to consider their fate after target delivery. Further issues arise when evaluating the degradation products and clearance of MPs from the tissues [342]. While aggregates of ferromagnetic particles may take longer to be washed away, demagnetized SPIONs could re-disperse into individual particles and be cleared from the circulatory system [250]. Collectively, these results demonstrate that SPIONs with their superior contrast properties have great potential to meet the main criteria for *in vivo* applications as a compromise between the desire to achieve good magnetization and the need to avoid particle aggregations after the attachment procedure to the MTB cells.

4.3.3 MRI contrast properties of MTB-MP complexes

Longitudinal (T_1)- and transversal (T_2)-relaxation rates at different TI and TE values, respectively, were studied to validate the possibility of detecting MTB-MP complexes with a clinical MRI scanner. The effects of MTB-S200 and MTB-S500 on the MR signal at different concentrations *in vitro* are presented in Figure 4.5. The SPIONs attached to MTB cause a perturbation of the homogenous MRI's magnetic field and amplification in the signal intensity. Even though the samples cause a decrease in both T_1 and T_2 values in a manner inversely proportional to their concentration, T_2-relaxation is more affected than T_1-relaxation rate as it is the case with superparamagnetic MRI contrast agents [343].

As depicted in Figure 4.5a, the relaxivities were determined to be r_1 = 96.2 and r_2 = 198.6 $ms^{-1}\mu g^{-1}ml$ for MTB-S200, and r_1 = 59.8 and r_2 = 154.4 $ms^{-1}\mu g^{-1}ml$ for MTB-S500, while it was found to be r_1 = 47.2 and r_2 = 144.9 $ms^{-1}\mu g^{-1}ml$ for the S200 (Figure 4.5a). A 37.8% and 22.25% improvement in r_1 and r_2 relaxivity of MTB-S200, respectively, is found when compared to the

MTB-S500. As mentioned in Table 4.1, magnetic property measurements indicate an enhancement in the M_s value with a reduction of the particle size ranging from 500 to 200 nm, which may be due to a higher amount of iron in the S200 samples.

On the other hand, MTB-S200 shows an increase of ~50.93% in r_1 relaxivity and 27.03% in r_2 relaxivity compared with S200 alone for the same quantity of nanoparticles. Moreover, as depicted in Figure 4.5b, the signal intensity of the MTB-S200 was slightly higher on the T_1- and T_2-weighted images compared to the same concentration of S200, which could be due to the bacterial iron content present in the tested samples. Each MC-1 MTB cell possesses a Fe_3O_4 content of approximately $1.76 \pm 0.4 \times 10^{-14}$ g per MTB as determined by magnetic moment measurements using VSM. Therefore, the bare MTB with the maximum used concentration of 10^8 MTB ml^{-1} contained ~1.26 μg ml^{-1} of iron.

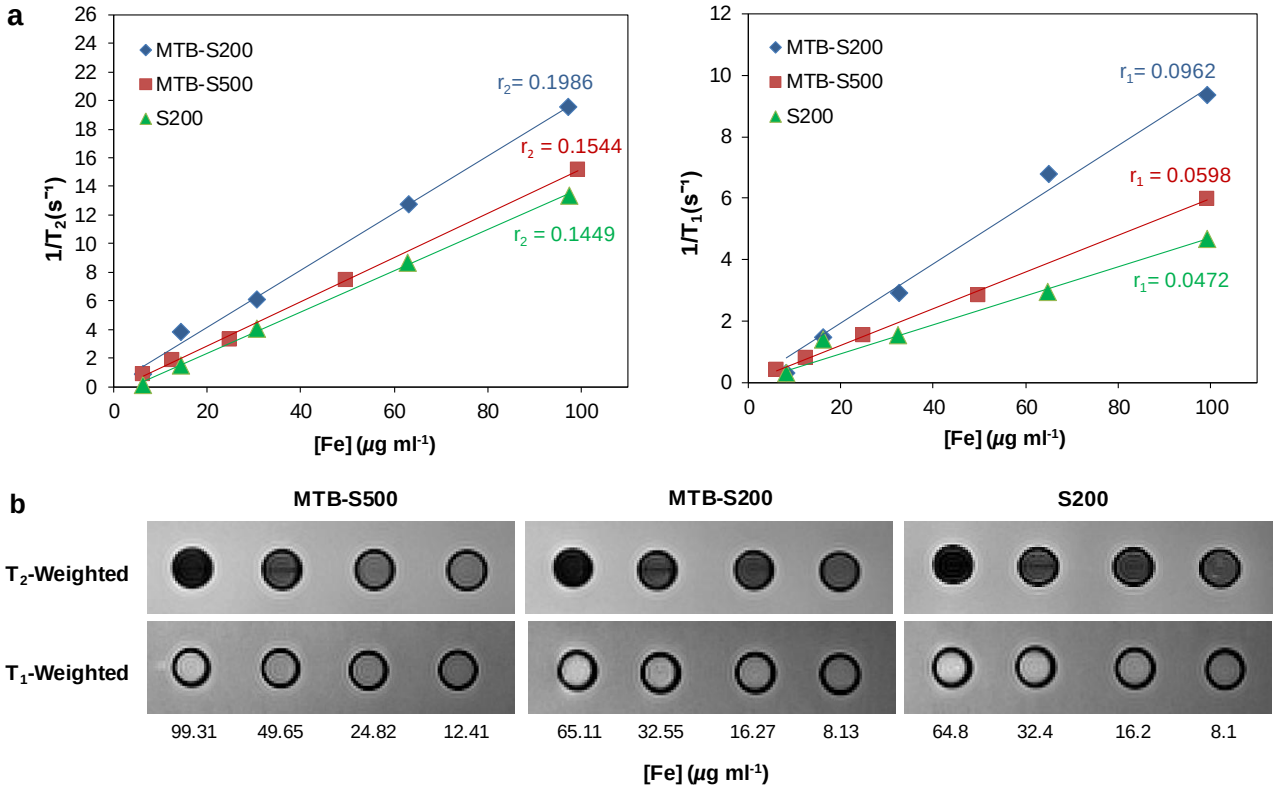

Figure 4.5: (**a**) r_2 (left) and r_1 (right) relaxation rates of MTB-S500, MTB-S200 and S200 solutions as a function of Fe concentration (μg ml^{-1}). (**b**) T_2– (top) (TR/TE = 10000/150 ms) and T_1–weighted (bottom) (TR/TI/TE = 10000/2500/8.6 ms) MR images of MTB-S500, MTB-S200 and S200 solutions at various concentrations. The amount of the susceptibility artifact was found to be related to the scan parameters and the concentration of samples.

A concentration of MTB at this scale does not produce a signal loss in the MR signal detectable in the images, which was confirmed by our data and previous studies [73]. The MTB-S200 complexes produced a distinct contrast at the total iron concentrations range of 65.11 to 8.13 μg ml^{-1}, which corresponds to 2.5×10^7 to 3.12×10^6 MTB ml^{-1}, respectively. Studies conducted on the effect of particle sizes on the MR signal *in vitro* helped to choose the most appropriate particles for *in vivo* evaluation. T_1 and T_2 MRI contrast properties of navigable MTB-S200 demonstrated their potential as contrast agents for MR imaging with high r_1- and r_2-relaxivity rates.

4.3.4 Visualization of MTB-S200 complex in tumor xenografts

In the current study, MTB-S200 complex was developed as navigable and controllable contrast agents to transport the S200 particles toward the center of the tumor along with a 3T clinical MRI scanner as a non-invasive tool for therapeutic aspects and visualization of hypoxic regions.

Targeting of non-systemic peritumorally injected MC-1 MTBs toward the center of the tumor could initially be achieved with magnetotaxis-based navigation. Subsequently, the poorly oxygenated hypoxic regions (< 0.7% O_2) provide a privileged environment for directional aerotaxis to dominate and incite microaerophilic MTBs with their embedded oxygen sensor to detect oxygen gradient and migrate toward the oxic-anoxic transition zone (OATZ) [33].

Ex vivo MR images of MTB-S200 complexes with the corresponding immunofluorescence and HPS stained tissue sections are presented in Figure 4.6. Bare MTB were used as a control. Figure 4.6a presents the T_2^*-weighted images of the tumor lesions to visualize the tumor structure through the *p.t.* injection of MTB-S200 complexes (~200 μl of 5×10^9 MTB ml^{-1}). The implications of the MRI data suggest that the accumulated MTB-S200 complexes in tumor affect the relaxation times by locally altering the magnetic field during MR imaging and can generate contrast. On the contrary, the tumors remain largely unaffected by bare MTB and do not show any sign of signal improvement in hypoxic regions (Figure 4.6d). Even though the MTB possess embedded magnetosomes, the concentration of distributed MTB inside the tumor does not provide sufficient contrast to be detected by MRI. Therefore, the MR signal needs to be improved by attaching contrast agents to the surface of the MTB. A previous study showed that the MR signal intensity would not be affected by fixation [344], therefore, the obtained *ex vivo* MR results could be achievable for *in vivo* experiments.

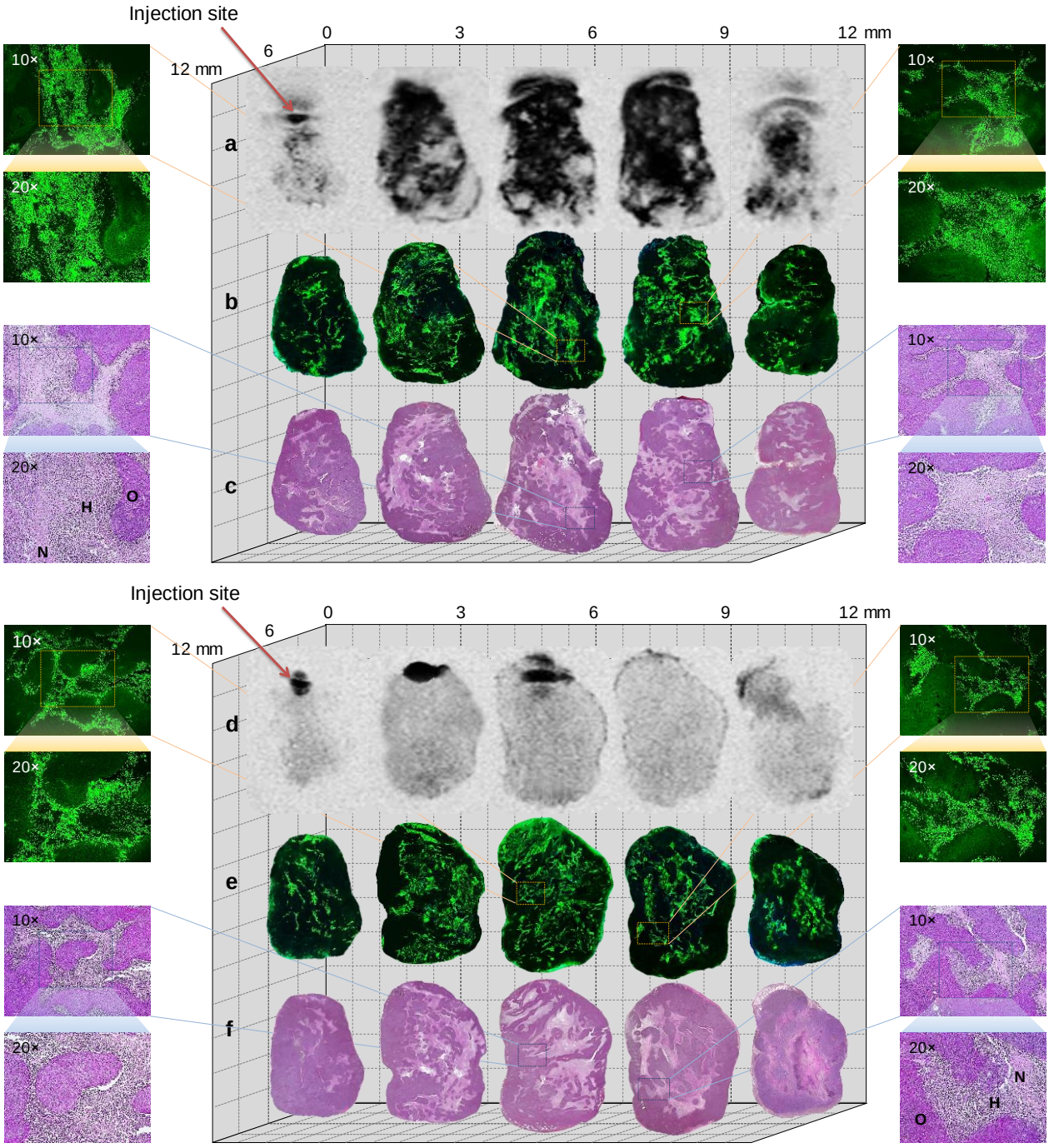

Figure 4.6: Tumor mapping using navigable MTB-S200 contrast agent in HCT116 colorectal tumor xenografts. (**a**, **d**) T_2^*-weighted MR imaging of MTB-S200 (**a**) and bare MTB (**d**) are presented. The locations of the intense signal indicate the injection site (arrowheads). MR images for MTB-S200 are evidence of the presence of contrast agents within the tumor while the hypointense signal was not observed in bare MTB images. (**b**, **e**) immunofluorescence assessment of longitudinal tumor sections for the MTB-S200 (**b**) and MTB (**e**) injected tumor. Green

fluorescent dots represent the bacteria inside the tumor at 10× and 20× magnifications. (**c**, **f**) Histological examinations of an adjusted serial section of HCT116 tumor xenografts using HPS staining reveal islands of well oxygenated viable tumor cells (O) sprinkled within hypoxic regions (H) and necrotic regions (N). $n = 2$ animals in each arm, in two independent experiments. Extensive penetrations of MTB-S200 into the tumor are evident in both MRI and immunofluorescence images.

Our MRI approach, beyond its translatability into the clinic, promises many advantages from providing high quality images with decipherable tumor heterogeneity patterns to eliminating the need for systemic exposure to toxic agents (*e.g.* radioactive tracers in PET or gadolinium in MRI [345]) or invasive biopsy procedures lacking inadequate spatial sampling. The current microscopic invasive techniques such as immunofluorescence and HPS entail major disadvantages because of their complexity, their non-real-time monitoring, and their requirement of time-consuming tissue processing procedures.

The MR imaging results were validated by staining the tumor tissue sections of the corresponding MRI slices with HPS and immunofluorescence (using a fluorescent-labeled antibody against MTB). As presented in Figure 4.6b, e, immunofluorescence tumor sections provide detailed information about locations of loaded and unloaded MTB (stained green) and facilitate the interpretation of the MRI data. Analyzes of immunofluorescence images demonstrated the ability to magnetically navigate significant numbers of MTB and their particle complexes from the injection site toward the center of tumor xenografts. The results also provide evidence of the aerotactic behavior of the MTB, which led to their accumulation in hypoxic regions.

Negative controls including tumors without injected MTB confirmed staining is specificity for MTBs (Figure 4.7).

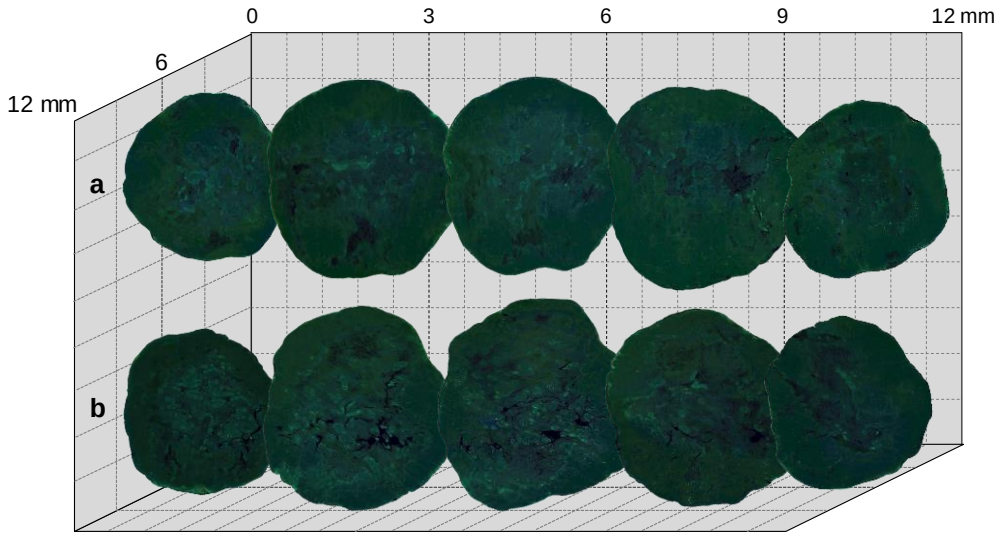

Figure 4.7: (**a**, **b**) Immunofluorescence images of tumor xenografts injected with S200 alone (**a**) and tumor without any injection (**b**).

Figure 4.6c, f shows representative sections of tumors from each group stained with HPS as a technique of marking tissues to discriminate between viable, hypoxic and necrotic tissue and to demonstrate the heterogeneous pattern of tumor structure. All tested xenografts, grown to a volume of around 700–800 mm^3, consisted of poorly differentiated tumor cells, hypoxic and necrotic regions. Nuclear changes that sometimes extended to the periphery of the tumor were observed in the images. Higher fluorescence signal and MR hypointensity were apparent in tissue sections corresponding to hypoxic areas. On the other hand, dark areas in immunofluorescence images and hyperintensity signal in the MR images matched with the viable tumor regions, as shown on corresponding HPS stained slices.

It should be emphasized that most of the tumor cells such as HCT116 colorectal cancer cells used in this study are originated from epithelial cells. A key feature of epithelial cells is the presence of intracellular junctions [3], which act as a virtually impermeable barrier to control cellular permeability and prevent penetration of foreign agents or large particles into living tissues [7]. These type of cancer cells are also known to have a high level of cellular adhesion to matrix proteins, stabilized β-catenin and E-cadherin localization at cell–cell junctions [346], an increased cellular packing density, enhanced TIFP, vascular disorganization and aberrant or lack of lymphatic system [6, 7]. According to our results, self-propelled flagellated MC-1 MTB with

thrust force could overcome the aforementioned obstacles and penetrate deep into the tissue. As shown in Figure 4.6, immunofluorescence and corresponding HPS results clearly demonstrate that the MC-1 MTB accumulated within the tumor interstitial fluid at the hypoxic regions between the well-oxygenated angiogenic network (oxic) and the tumor necrotic (anoxic) zones. The presence of vasculogenic mimicry in tumors [233] could also provide routes for MTB to penetrate and distribute in the tumor's interstitial space.

SPIONs offer several advantages by providing high signal contrast in T_2/T_2^*-weighted imaging, biodegradability, and non-toxicity [347, 348]. The T_2^*-based contrast mechanism is used in several MRI applications such as functional imaging, MR perfusion imaging and contrast-enhanced imaging using SPIONs [349]. The principal effect of the SPIONs is on T_2^* relaxation time and as such T_2^*-weighted sequences can be used with SPIONs to depict their accumulation sites in a tissue. The imaging sequences that exploit T_2^* contrast are faster and more sensitive to the presence of SPIONs compared with those that use T_2 contrast. A major challenge in T_2^* imaging is the need to distinguish regions of signal void due to SPIONs from other sources of signal loss such as susceptibility artifacts, imperfect shimming or chemical shift. Several techniques have been developed to generate hyperintensities in the vicinity of SPION [256], which provide a more accurate estimation of SPIONs concentration. Enhancement on T_1-weighted images can also be observed with SPIONs to a lesser degree compared to T_2^*-weighted ones. However, T_1 contrast provides a hyperintense signal of the tumor lesion and as such, a higher contrast to noise ratio in the presence of SPIONs can be achieved, and also tumor margins within a tissue are more clearly demonstrated. A combination of MR imaging technique using T_1- and T_2^* imaging criteria appears to provide clinically more useful patterns of SPIONs signal enhancement in a tumor lesion. Therefore, to verify the effectiveness of the MTB-S200 for *in vivo* applications, T_1- and T_2^*-weighted images were obtained (Figure 4.8).

Controls including bare MTB, particles alone and tumors without any injection were examined. We found that MTB-S200 complexes affect both the T_1- and T_2- relaxation rates (Figure 4.8a). As shown in Figure 4.8c, no magnetosome-induced signal is observed when bare MTBs are applied due to an insufficient amount of distributed MTBs in the tumor to induce a detectable distortion in the MRI's magnetic field. However, the injection sites show high signal intensity around the tumor rim, due to the accumulation of highly concentrated and non-fully penetrated MTBs during the injection and navigation procedure. As reported by our group, the mean

magnetic targeting ratio of detected MTB to injected MTB in the tumor was estimated at around 50% (See Appendix A and Chapter 5).

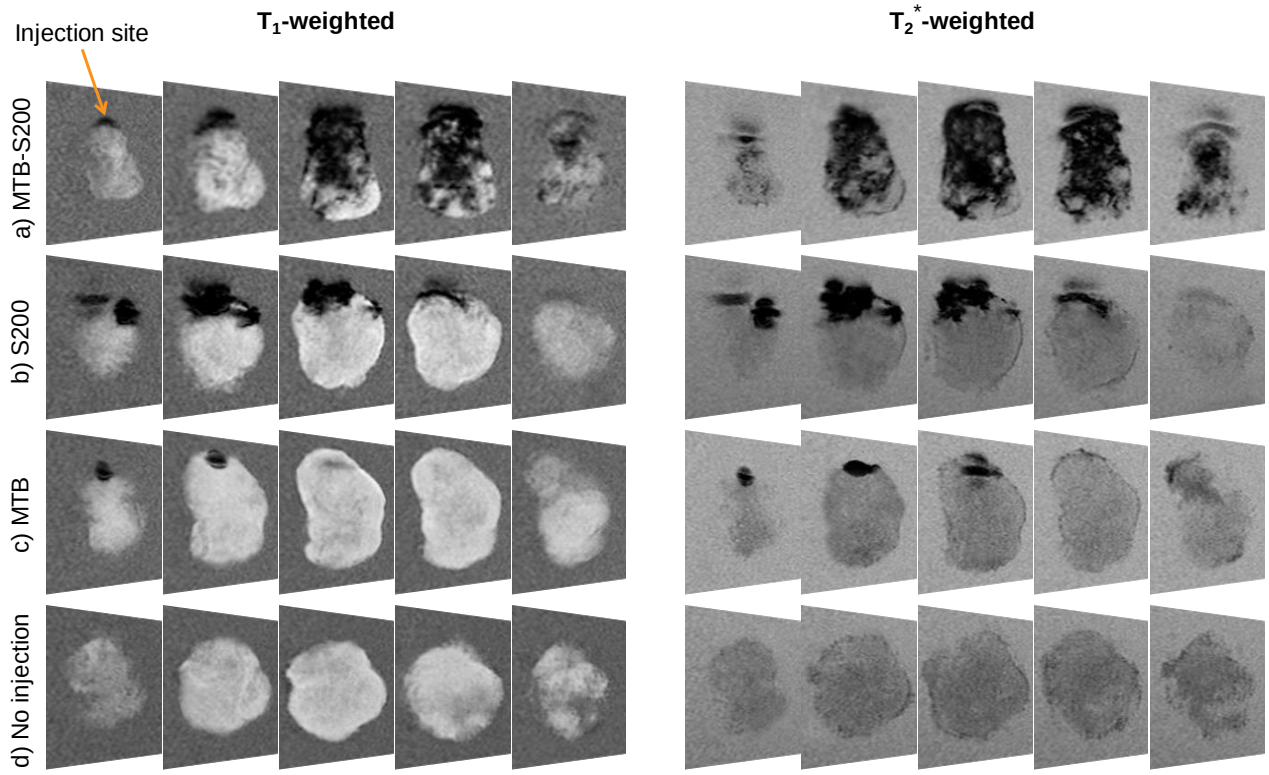

Figure 4.8: MR images of MTB-S200 complexes in HCT116 tumor xenografts. T_1/T_2^* weighted coronal MR imaging (Siemens, Skyra, 3T) of MTB-S200 (**a**), S200 (**b**), MTB (**c**), and control without an injection (**d**) are shown. T_1-weighted images acquired with 2D-FLASH sequence (TR/TE, 250/4.73; flip angle, 70°; bandwidth, 220 Hz/pixel; voxel size, 0.25 × 0.25 × 2 mm; imaging matrix, 320 × 320; number of averages [NA], 3) and T_2^*-weighted images acquired with 2D-FLASH pulse sequence (TR/TE, 700/10; flip angle, 25°; bandwidth, 210 Hz/pixel; voxel size, 0.20 × 0.20 × 1.5 mm; imaging matrix, 384 × 384, NA, 1). MR signals clearly demonstrate penetration of the MTB-S200 into the tumor, whereas S200 remains at the rim of the injection site. No pronounced contrast in the images of MTB or the non-treated xenograft is observed.

In the case of S200 particles alone, no signal changes are observed inside the tumor (Figure 4.8b). The TIFP pressure and lack of propulsion system prevent the particles alone from penetrating

deep into the tissue during the time course of the magnetic navigation, which causing them only to reside around the injection site.

In routine clinical treatment, after intravenous injection of pharmaceutical agents with long circulating properties (PEGylation) [10], very limited accumulation (less than 2%) occurs at the tumor site [10]. These agents have been shown to concentrate around the broken blood vessels by EPR effect [8, 9] with limited tissue penetration [6, 11, 12]. Encapsulated conventional cancer therapies in particles greater than 100 nm are mostly trapped within physiological barriers such as dense interstitial matrix (composed of collagen, glycosaminoglycans, and proteoglycans) [4, 5]. Aforementioned barriers lead to an impeded delivery of the pharmaceutical agents in an optimal concentration to the entire tumor [19], which renders most efficient theranostic agents clinically ineffective. Loading particles on self-propelled bio-carriers is a promising approach to improve the penetration of therapeutic and imaging agents into an inaccessible site within a tumor.

4.4 CONCLUSION

Advances in targeted delivery and deep penetration of pharmaceutical agents allow improved assessment of tumor microenvironment. As validated in this work through the experiments, the SPIONs delivered by MTB can serve as a source of contrast to allow visualization the tumor regions in implanted mouse tumor xenografts below the spatial resolution of medical imaging modalities using a 3T clinical MRI scanner and a commercial receiver coils. Indeed, for *in vivo* drug delivery into tumor microenvironment and hypoxic regions, the overall swimming direction of the polar MC-1 MTB is influenced by magnetotaxis in conjunction with aerotaxis and caused the bacteria reacts according to a balance of these stimuli. The results indicate that these trackable bacteria can readily penetrate into the tumor's interstitial space toward hypoxic regions and alter the accumulation rate and distribution pattern of imaging agents in tumor regions.

It was observed that aggregations were more pronounced for MTB-F200/F500 complexes than for MTB-S200/S500. The attachment of the 200 nm SPIONs as contrast agents to the surface of MTB gave the sufficient magnetic properties for MR imaging without compromising bacterial motility or migration. Moreover, the superparamagnetism behavior is well adapted to the conjugation technique, which resulting in uniform and disperses bio-complexes. The MTB-S200

complexes can generate a high contrast in both T_1- and T_2/T_2^*-weighted images, enhancing their visualization pattern in tumor hypoxic regions.

Considering the multiple physiological barriers that pharmaceutical agents must encounter, MTB as a sophisticated cargo carrier loaded with pharmaceutical agents could provide tenability in spatial control for targeted delivery for various biomedical applications. This approach can be further extended by incorporating a therapeutic to our developed imaging agent to enhance the effect of treatment by facilitating the delivery and tracking of the therapeutics to inaccessible sites of solid tumors *in vivo*. Such an advanced system can not only improve the efficacy of current cancer therapies by overcoming current limitations but also make theranostic agents that have been abandoned due to delivery problems clinically practical. The developed technique offers several possibilities as a non-invasive tool to provide clinical spatial images of hypoxic and quiescence areas of tumors, tracking anatomical changes during a treatment, obtain prognostic information about tumor progression in response to a treatment, and allowing image-guided therapy plan to be made in radiation therapy or numerous medical theranostic applications such as gene and vaccine delivery, drug targeting, PET, and MRI.

CHAPTER 5 DRUG-LOADED NANOLIPOSOMES ATTACHED TO MAGNETO-AEROTACTIC BACTERIA FOR TARGETED DELIVERY IN TUMOR XENOGRAFT

The following chapter deliberates the objective 3 of this thesis that was to develop drug-loaded liposomes covalently attached to the surface of the MC-1 MTB (MTB-LSC) using carbodiimide chemistry and also to assess the attachment stability during targeting in the tumor microenvironment. After physico-chemical characterization, the optimized MTB-LSC were targeted in HCT116 colorectal tumor xenograft model. The deeply penetrated MTB complexes were visualized by immunofluorescence staining. The results demonstrated that the therapeutic payloads can overcome the diffusion limits in tumor microenvironment through the stable attachment on the MTB and can be delivered in the hard-to-treat tumor hypoxic regions.

This chapter is devoted to elaborate the specific contribution of the candidate in multidisciplinary *in vivo* experiment. The full-length article entitled “Non-Systemic Magneto-Aerotactic Bacteria-Mediated Delivery of Drug-Loaded Nanoliposomes in Tumor Hypoxic Regions” under revision by the journal of *Nature Nanotechnology* as a result of teamwork is presented in Appendix A. The details of contributions of authors are described in section 1.1.

5.1 INTRODUCTION

Effective delivery of nanocarriers in regions leading to optimized therapeutic outcomes such as within tumoral hypoxic regions remains unmet. With a low therapeutic index and increased systemic toxicity, nanocarriers could greatly benefit from the actuation-navigation-sensory capability envisioned for futuristic nanorobots to enhance distribution in hard-to-reach tumoral regions following transports through the most direct physiological routes.

Hypoxia facilitates the survival of tumor cells and is a cause of malignant transformation. It is the consequence of oxygen consumption by the rapid proliferation of tumor cells which results in approximately < 0.7% O_2 in highly difficult treatable hypoxic regions [350]. Such hypoxic

environments negatively impact treatments based on radiotherapy [14, 351, 352] while for chemotherapy, larger drug molecules including nanocarriers cannot generally target and diffuse effectively [54, 353] towards the hypoxic cells within the absence of flow caused by the tumor interstitial fluid pressure [354]. The resulting limited drug and macromolecule distribution within tumors significantly reduces the therapeutic index [12].

The two main approaches to the selective killing of hypoxic cells in tumors [13, 355], the bio-reductive prodrugs [16, 17] and small molecule inhibitors against molecular targets involved in the survival of hypoxic cells [355, 356], need to overcome the problem of drug-loaded nanocarriers penetration through poorly perfused hypoxic tissue [357]. While reducing the TIFP is known to enhance the uptake and homogeneous distribution of many therapeutic compounds, available pharmacologic and physical therapies used to reduce tumor pressure have their side effects and their application in clinical practice is not yet validated [18] while suffering from the low targeting efficacy when using the systemic routes. Indeed, currently used pharmaceutical nanocarriers such as liposomes, micelles, polymeric nanoparticles and many others, result in very low tumor site accumulation. Combining the EPR effect of nanocarriers with the longer systemic circulation properties that are achieved following PEGylation has increased the targeting ratio but still result in a very limited fraction of nanocarriers entering tumors. This is due to the facts that usually only about 5% of the administered nanocarriers remain in the systemic circulation after 12 h with 90% of these PEGylated nanocarriers being removed from the systemic circulation within several hours, resulting to only ~2% of the total administered dose being deposited in the tumor after 4 h of circulation [10].

But since the overall maximum size of nanocarriers is an obstacle to the integration of advanced functionalities that would correct for such deficiencies, the overall sizes of intercellular openings responsible for the leakiness of tumor vessels provide sufficient spaces for such nanocarriers to be transported by larger and more capable self-propelled carriers. The development of a common carrier capable of transporting such therapeutic nanocarriers to the most effective site of treatment with embedded functionalities that would enhance the targeting capability beyond what is possible using existing nanocarriers alone is the focus of this study. Such functionalities would include navigation capability towards the sites of treatment in order to avoid systemic circulation, self-actuation providing a propelling force sufficient to penetrate the tumor volume beyond the diffusion limits of nanocarriers and larger drug molecules, and sensory capability to target

regions such as the hypoxic zones that would lead to the best treatment outcomes. Although these are functionalities generally used in robotics, implementing them at the scale required to transit through the physiological environments to reach deep inside a tumor is well beyond what is technically feasible for the implementation of an artificial nanorobotic agent, but possible with the use of a natural agent.

For instance, the MC-1 MTB [324, 358] contains a chain of magnetosomes acting like a nano-compass needle entails the bacteria to swim persistently along local magnetic field lines in a preferred direction [99, 359]. In their natural environment, such direction corresponds to a downward migration along geomagnetic field lines in conjunction with aerotaxis to efficiently migrate to and maintain position at their preferred low oxygen concentrations. Such magnetically-assisted aerotaxis known as magneto- aerotaxis [33] results in the formation of microaerophilic bands of MC-1 cells at O_2 concentrations equivalent to the ones observed in the hypoxic regions of solid tumors. Most microaerophilic bacteria form aerotactic bands using a temporal sensory mechanism [360] that samples the environment as they swim while comparing the present O_2 level with the O_2 level of the previous sample. Unlike M. magnetotacticum which is consistent with such temporal sensory mechanism, the aerotactic behavior of MC-1 cells is based on a two-state aerotactic sensory system in which the O_2 concentration determines the sense of flagellar rotation and hence the swimming direction along the geomagnetic field lines. Such polar magneto-aerotaxis accounts for the ability of the MC-1 bacteria to migrate and to maintain position at the preferred O_2 concentration at the oxic-anoxic transition zone in chemically-stratified, semi-anaerobic basins [33].

Our hypothesis was that a similar OATZ present in the fluid interstitial regions (tumor interstitium) between the angiogenic network (oxic) and the tumor necrotic (anoxic) zones could be exploited to enhance drug targeting in hypoxic regions using live MC-1 cells after being guided toward the site of treatment by an external magnetic source. Indeed, unlike previous bacterial therapies [93], minimizing systemic circulation of drug-loaded MC-1 cells was achieved by initially guiding their migration path towards such OATZ where an oxygen gradient was present and could be detected by the bacteria. Unlike hypoxic zones, since the location of the tumoral volume can generally be precisely determined, magnetotaxis was first prioritized over aerotaxis considering that the latter could not initially benefit from such spatial information.

The targeting procedure consisted of an assisted magnetotactic directional navigation [108] using a magnetic field sensibly higher than the geomagnetic field to induce a stronger directional torque on the chain of magnetosomes towards the tumor when in the peritumoral regions, followed by a MTB-autonomous aerotactic directional phase in the absence of a sufficient level of interactive magnetic energy required for prioritizing magnetotactic directional control when in the predefined targeted tumoral volume. Since the physiological environments encountered by the MTB during travel would be different from the ones found along their natural migrating paths, the experiments were aimed at assessing the ability of the MTB and MTB-LSC to migrate effectively towards the hypoxic zones following peritumoral injection. More specifically, to examine whether a large ratio of injected MTB spherical cells whose diameter ranges between 1-2 μm would be able to migrate through physiological routes such as the interstitial spaces, and the intercellular openings of typically less than 2 μm in diameter between endothelial cells [60] responsible for much of the vessel leakiness in solid tumors.

5.2 METHODS

5.2.1 Covalent attachment of liposome-SN38 to the surface of MTB cells

The direct chemical conjugation strategy presented in Chapter 3 was optimized for the covalent attachment of SN38 encapsulated into functionalized liposomes (LP-SN38) on the MTB cell membrane.

To obtain high attachment efficacy and also prevent the leakage of encapsulated SN38 during the attachment procedure, the chemical environments such as the pH, type of buffer, and quantity of reagents were adjusted for the LP-SN38 system compared to the liposomes alone. The LP-SN38 was prepared using pH gradient method at pH = 8 outside and pH = 4 inside. It should be noted that EDC and NHS crosslinking agents are more efficient in acidic conditions (pH = 5.5-6.7, 20 °C) using MES buffer as a suitable carbodiimide reaction buffer. However, decreasing the outside pH of LP-SN38 to 5.5 reduces the pH gradient of liposomes and may leads to the leakage of the drug. On the other hand, for preparation of a saturated solution of SN38 for encapsulation steps a high pH is required (pH ~11), which is not possible with MES buffer (pK_a = 6.16). To address these issues, PBS was used as a compatible coupling buffer with the reaction chemistry, albeit with lower efficiency. Increasing the amount of EDC in a reaction solution in combination

with NHS or Sulfo-NHS can compensate for the reduced efficiency. In fact, PBS with pH 11 and 8 was used for SN38-LP preparation and then at crosslinking steps the pH was adjusted to 6-6.5 to avoid hydrolysis and EDC deactivation and also minimize the drug leakage. Briefly, dehydrated agents such as EDC and Sulfo-NHS were added to 3 ml of 0.5 mM liposomes suspension (EDC: NHS: DSPE-PEG-COOH = 35: 35: 3, molar ratio) in PBS buffer (pH 6.5). The mixture was incubated at room temperature for 20 min. The free activating reagents were removed using Sephadex G-50 column. Then, activated liposomes were added to 4×10^7 MTB ($\sim 10^7$ MTB ml^{-1}) and incubated for 2 h at room temperature, under gentle mixing. MTB-LSC were separated from non-attached liposomes by applying a 2D magnetic field. The sample was washed three times with PBS and finally resuspended in PBS (pH = 7.4). The MTB-LSC samples were prepared in daily batches and separately for each animal injection.

5.2.2 *In vivo* navigation of MTB-LSC

In vivo experiments were conducted by implantation of HCT116 colorectal xenografts in SCID-Beige mice. Approximately, 2.9×10^7 MTB-LSC in 20 μl PBS were injected peritumorally. MTB with the same quantity were also used a control. After injection, the animals were placed in the center of a tridimensional magnetotaxis platform designed by Dr. Felfoul [103]. After magnetic navigation, the tumors were extracted and fixed in 10% neutral buffer formalin. After fixation, paraffin embedded tissue section were stained with FITC- or Texas red-labeled antibody to visualize MC-1 in green or red, respectively.

5.2.3 MTB-LSC count in tumor

To visualize the variation in distribution of the injected MTB complexes within the tumor and estimate the relative amounts of MTB complexes present in each histological section sampled from each tumor, images of each section were acquired using a fluorescence optical microscope equipped with a 40× magnification objective lens. The acquired images were then processed using automated software to count the number of stained MTB in each histological section (See more details in Appendix A).

5.3 RESULTS AND DISCUSSION

5.3.1 Navigation, assessment the stability, and targeting ratio of MTB-LSC in tumor xenograft

Figure 5.1 shows the MTB-LSC as a drug delivery biocarrier. *In vivo* experiments were conducted in HCT116 tumoral tissue to evaluate the mean targeting ratio of MTB-LSC and to obtain statistical data of the quantity of MTB-LSC *versus* the total amount injected peritumorally.

Among all potential nanocarriers, liposomes were initially selected as a first proof-of-concept because they are biocompatible, exhibit low immunogenicity and high flexibility, protect the body from potential toxic cargo, shield therapeutic agents from premature degradation, control release kinetics, and may concurrently encapsulate a multitude of hydrophilic and/or hydrophobic drug cargos, pharmaceutical ingredients, imaging agents, and genetic material by virtue of their aqueous interior and lipid exterior [37, 131, 139, 145]. The diameter of each liposome was set to the maximum possible synthesized value of ~170 nm to maximize the quantity of drug-cargo being transported per MTB. The amount of bacteria intended for injection was predetermined prior to the experiments. The dosage of the delivered active agents can be controlled by the encapsulation efficacy of drug within liposomes, the average number of liposomes carried by each bacterium, and the number of injected bacteria.

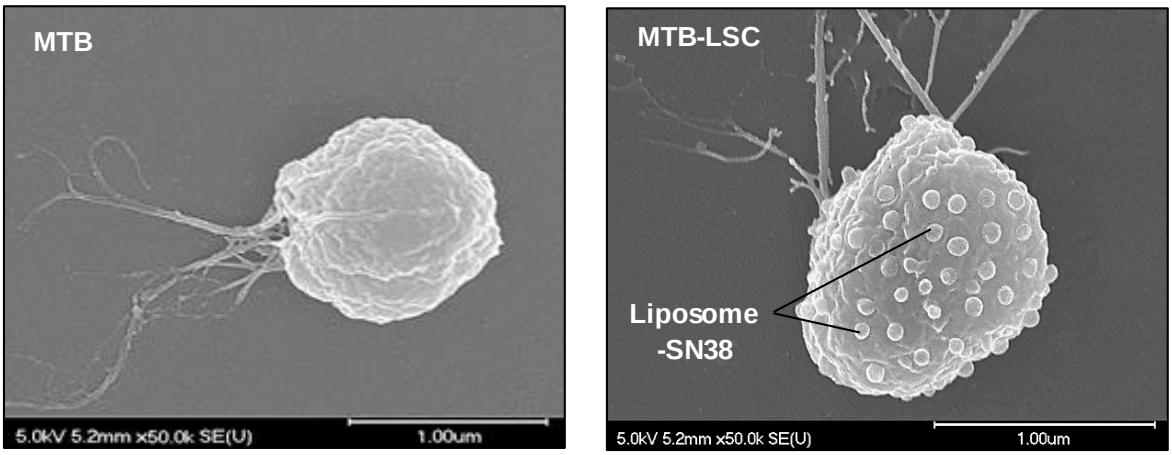

Figure 5.1: Unloaded MTB (left) and MTB-LSC (right) with ~70 SN38-loaded liposomes attached to the surface of each MC-1 MTB cell.

To assess magnetically-guided live MC-1 MTB and MTB-LSC targeting profile in HCT116 xenograft, the peritumoral injections of ~2.92 × 10^7 bacteria in 20 μl PBS for a total of 10 mice were performed. Relatively large populations of MTB in the middle section of the tumor were observed after the mice exposed to a directional magnetic field toward the center of the xenograft for a period of 30 min. When the MTB come close enough to the target to be influenced by decreasing oxygen gradients, aerotactic directional motion toward the hypoxic regions takes effect. Figure 5.2 shows the penetration and distribution of MTB and MTB-LSC in the tumor. The live MTB alone appear to swim and move effectively through necrotic tissues as assessed by the observation of several adjacent histology slides (4 μm apart), one stained with green FITC-secondary antibody immunofluorescence targeting a specific protein at the MTB membrane (Figure 5.2a) and the second stained with HPS (Figure 5.2b).

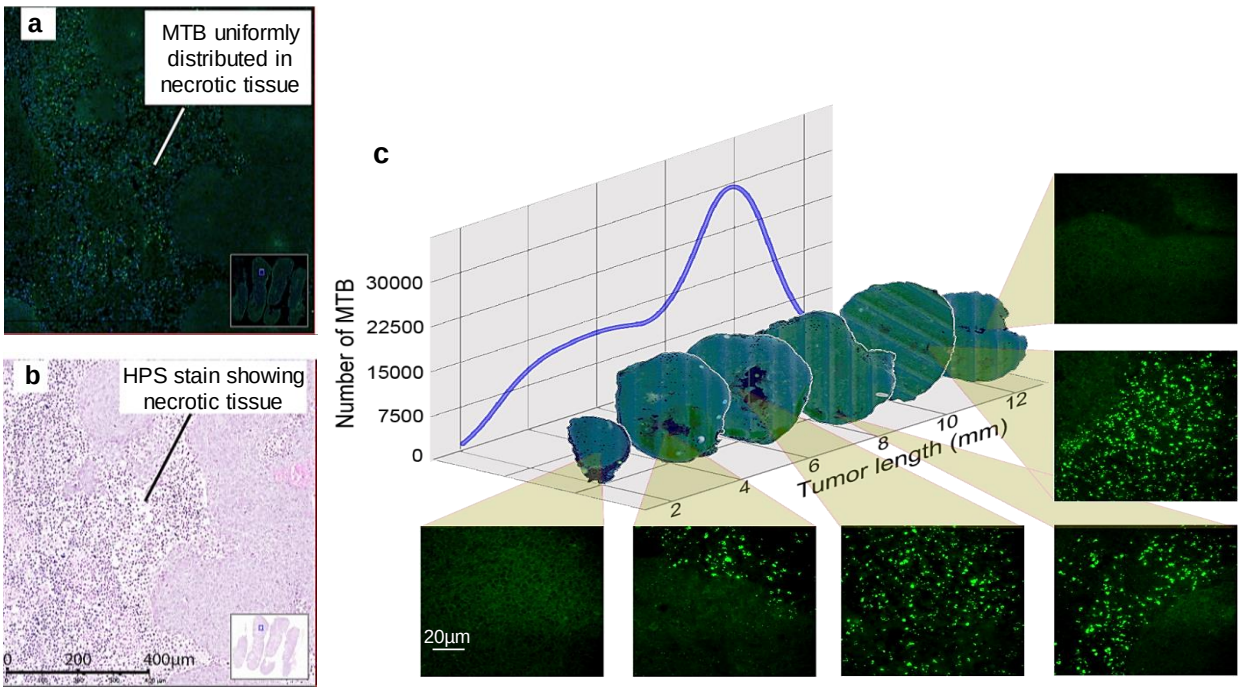

Figure 5.2: Penetration of live MTB-LSC in HCT116 xenografts following a peritumoral injection after a directional magnetic field targeting toward the center of the tumor. (**a, b**) An immunohistology analysis of the middle section of the tumors reveals the presence of MTB, as green FITC fluorescent dots (top), in uniformly distributed within the vicinity of the same regions recognized to be necrotic with the HPS stain necrotic region (bottom). (**c**) Transverse tumor sections of MTB-LSC (group MBC-8) after targeting. Insert graph shows the MTB-LSC distribution inside the tumor.

Histological sections of the magnetotactic bacterial count (MBC) samples also revealed that the large populations of MTB-LSC were distributed throughout the xenografts (Figure 5.2c) mainly where necrosis and hypoxic were more predominant.

Since some of the bacteria injected peritumorally might not have ended up inside the tumor, an exact percentage of bacteria which actually could be found in the excised tumors were estimated. At that point, some of the injected bacteria might have been dead and/or partly cleared from the tumor tissue, so obtained counts represent only estimates performed for comparative purposes. Two different approaches for bacteria counting were investigated to validate and confirm the navigation capabilities of MTB in a colorectal tumor model. The tissue homogenization was performed as a rapid approach followed by optical microscopy for bacteria counting (Figure 5.3a). Also, some tumors were cut in seven fragments, and all fragments were paraffin-embedded, sectioned, stained, and then histology slides were evaluated using fluorescence microscopy (Figure 5.3b). Similar to the results achieved with the unloaded MTB, high targeting ratios of MTB-LSC were obtained. The mean tumor targeting ratio (~50%) estimated from the MBC samples by image processing techniques (See details in Appendix A) allowing to assess the distribution of the MTB-LSC complexes in the HCT116 xenografts which was coherent with the mean targeting tumor ratio (~59%) obtained by homogenization extracted after experiments performed under similar conditions.

5.3.2 Tumor penetration of active MTB *versus* passive marker

Although the preceding section showed that in general the combination of magnetic and aerotactic guidance leads to much superior targeting ratios in hypoxic regions of tumor xenografts, the targeting profile needs to be compared with passive agents, *i.e.* agents lacking the three functionalities mentioned earlier namely, navigation such as magnetotactic guidance, propelling force, and sensory-based displacement such as aerotactic motion behavior.

As such, the peritumoral injections of a mixture consisting of live MTB and passive marker (polymer microspheres (PS)) was performed to be more confident on the concluding results. The simultaneous injection of MTB and passive marker was to compare their ability to diffuse and remain inside the tumor within the same experimental conditions using the same injection site and the same injection rate.

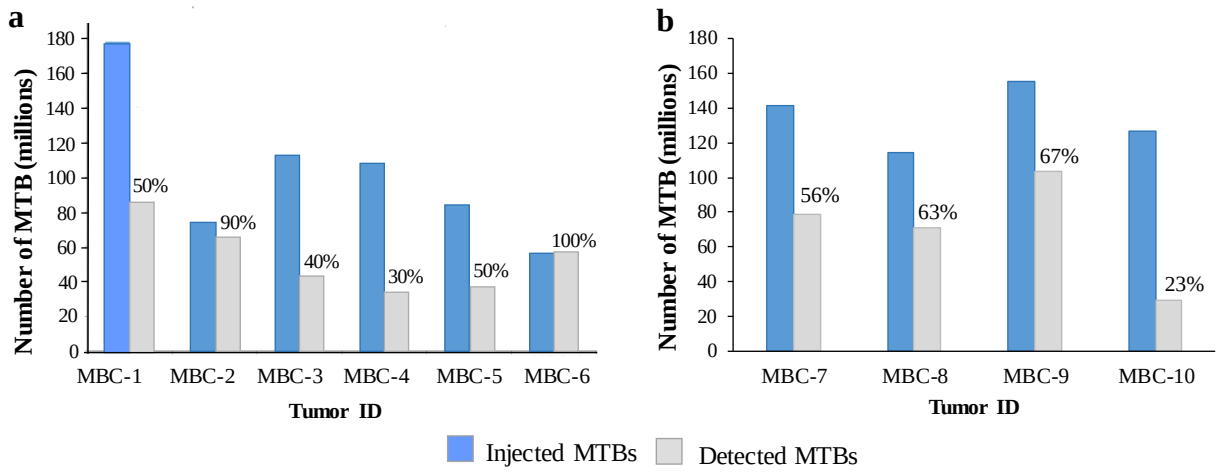

Figure 5.3: Targeting ratios of MTB-LSC (MBC-groups) in HCT116 xenografts. (**a**) Ratios of MTB-LSC in the tumoral tissue obtained by homogenization followed by counting using optical microscopy. (**b**) Estimated mean ratios of MTB-LSC found in each histological section sampled from each tumor using a fluorescent optical microscope.

20 μl of Dragon green fluorescent PS (ex/em: 480/520) 1.9 μm polymer microspheres, similar in size to the MC-1 spherical cells, and 20 μl of live MTB were injected, which in term of numbers consisted of ~2.92×10^7 bacteria and ~1.35×10^7 beads, followed by 30 min magnetic guidance. The targeted MC-1 MTB were stained with Texas-red secondary antibody (ex/em: 595/613) making the MTB red on the histological slides with the beads alone showing in green. The active directional motility through magnetotaxis and aerotaxis of the MTB resulted in superior penetration depths in HCT116 xenografts compared to passive marker as depicted by the polymeric beads (Figure 5.4). Figure 5.4 shows a substantial decrease in the number of microspheres as moved deeper into the tumor while the number of MTB increased significantly. In fact, when such passive marker is injected in the peritumoral region, it exhibits a limited diffusion due to the tumor interstitial fluid pressure.

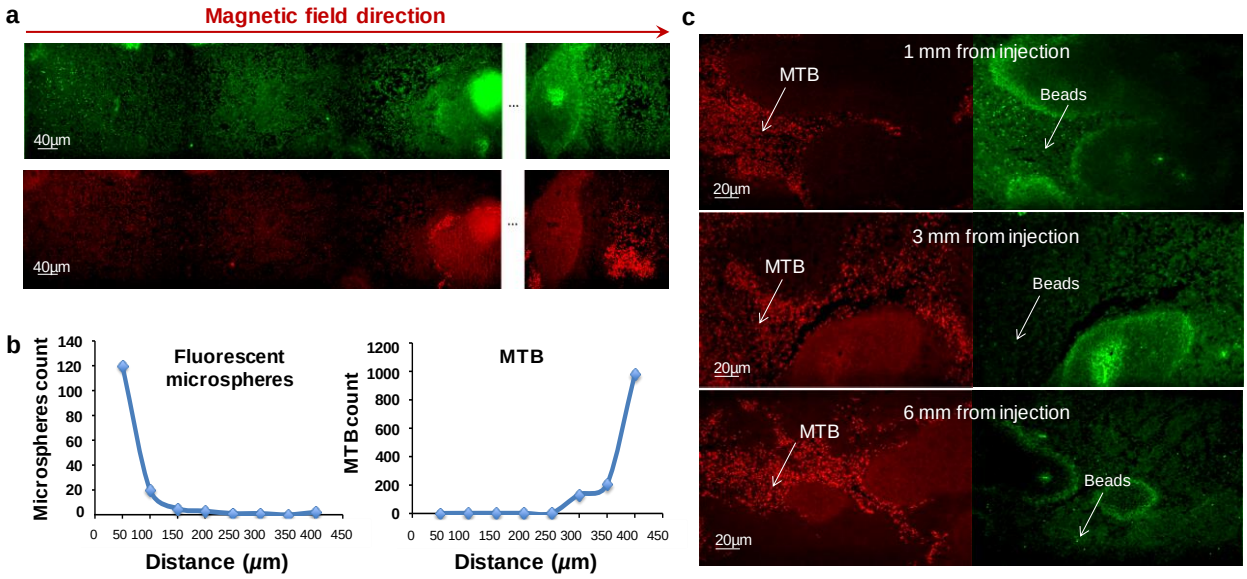

Figure 5.4: Penetration of live MC-1 cells over the passive diffusion of polymeric beads in HCT116 xenografts. (**a**) 20× images of MTB and fluorescent beads at different tumoral depths. (**b**) Quantity of fluorescent microspheres *vs.* MTB at various tumoral depths. (**c**) 20× images of MTB and fluorescent beads at 1, 3, and 6 mm inside the HCT116 xenograft.

5.4 CONCLUSION

The results demonstrated that magneto-aerotactic MC-1 MTB covalently attached to ~70 170 nm SN38-encapsulated nanoliposomes are capable of being magnetically navigated toward the center of the tumor. The experiments performed in HCT116 colorectal tumor xenograft implanted in SCID-Beige mice resulted in a ~50% mean targeting ratio of the ~2 × 10^7 peritumorally injected MTB-LSC in hypoxic regions. These initial findings based on the stably attached cargos on the MTB cells may influence medical interventional methods and provide opportunities for the synthesis of new navigable therapeutic and imaging agents to achieve maximum effectiveness of treatment for various diseases.

CHAPTER 6 GENERAL DISCUSSION

The overall aim of this thesis was to develop MC-1 MTB-based complexes with targeting and tracking abilities for potential applications in cancer treatment. To this end, the achievements of this thesis include: (i) development of bioconjugation technique for the attachment of liposomes to the surface of the MC-1 MTB, (ii) development of MTB-S200 as a navigable MRI contrast agent for visualizing the tumor hypoxic regions as well as using its tracking capability for feedback control of complex location in tumor microenvironment, and (iii) development of MTB-LSC and assessment the attachment stability during targeting in the tumor milieu. In following sections, main results related to each objective obtained during this PhD work, are presented.

6.1 Development, physico-chemical characterization, uptake and cytotoxicity assessment of MTB-LP delivery system

The most suitable attachment strategy for the MTB-LP complex was covalent binding of negatively charged carboxylated liposomes to the pre-existing amine reactive groups naturally present on the surface of MTB through direct carbodiimide (EDC/NHS) chemistry to form amide-linkage [195, 303, 304]. The terminal amine functional groups are as a part of phospholipids (*e.g.* phosphatidylserine), lipopolysaccharides, lipoproteins and surface proteins assemblies that abundantly and seamlessly incorporate into the outer membrane of gram-negative bacteria [311, 312].

The rationale behind using the liposome as a drug carrier system was due to their biocompatibility, biodegradability, versatility, low immunogenicity, and controlled release [37, 139, 145]. Furthermore, in our particular context, liposomes can be engineered to provide surface functionality for attachment (for instance by incorporation of DSPE-PEG-COOH groups) and, also is very suitable for encapsulation of the active metabolite form of pH sensitive SN38 within its acidic core by a pH-gradient technique [111, 112, 127]. Even though the liposome-based vehicles are being extensively used for the delivery of pharmaceutical agents, their bioconjugation as a drug-loading moiety to live bio-carrier such as magnetic bacteria was not reported in the literature.

Various bioconjugation methods were examined prior to the demonstration of carbodiimide chemistry as a suitable technique for the attachment of liposomes to MTB cells. Although oppositely charged particles may spontaneously adsorb on the abundantly charged sites on the surface of MTB cells [317], the physically adsorbed particles showed a lack of stability and detached during washing steps which were not suitable for *in vivo* conditions. In other conjugation technique, functional groups were grafted on the surface of MTB (*e.g.* biotin-avidin [361] or maleimide-thiol interaction). This approach affected the MTB cells viability due to extensive manipulation of the bacteria and also due to their exposure to chemicals needed for conjugation. In general, like all other biological cell types, changes in pH, osmolarity, exposure of bacterial cells to organic solvents, and excessive agitation have profound effects on MTB cell movement, as well as on their response to magnetic field and viability.

Carbodiimide crosslinking is a versatile chemistry for various *in vitro* and *in vivo* applications such as bioconjugation of antibody, peptide, and protein to nano/micro particle [313, 314] and immobilization of other biomacromolecules [213]. This technique induces the formation of the covalent amide bond (-NH-CO-) without producing any byproduct that may interfere with viability and motility of bacteria after the attachment. The relatively high bond dissociation enthalpies (ΔH°_{298}) of the amide bond which is ~305-440 kJ mol^{-1}, results in a strong and robust covalent bond [315, 362] enable to remain stable in biological conditions [315, 320]. In a physiological environment, the hydrolysis mechanism for degradation of amide bonds is very slow [320] and the bond is not affected by environment conditions such as pH or ionic strength. Moreover, hydrolysis and enzymatic cleavage of amide bonds by serum proteins/cellular secreted products (such as proteases) are highly dependent on the microenvironment condition and typically requires a long exposure time [320]. These characteristics insure the liposomes to remain attached covalently on the surface of MTB until reaching the site of interest.

Our results demonstrated that the attachment of 70 liposomes having an average diameter of ~170 nm to the MTB does not significantly affect the desired MTB functions such as mobility, viability, swimming speeds, and response to the magnetic field. However, this "optimized number" of attached liposomes on the MTB led to ~60% reduction in swimming velocity of MTB-LP from 200 to 80 μm s^{-1} as a result of bacteria exposure to the non-origin culture media and also repeated washing steps during the attachment process. It should be noted that this number of liposomal attachment was considered optimal, since the swimming velocity of MTB-

LP was still greater than that of some of the other magnetic bacteria *MS-1* (40 μm s^{-1}) and *AMB-1* (49 μm s^{-1}) [32] or that of non-magnetic bacteria used in cancer therapy such as *E. coli* (10-40 μm s^{-1}) or *Salmonella* (20-50 μm s^{-1}) having the capacity to overcome the tumor barriers [29, 31].

The cellular uptake and cytotoxicity of MTB-LP delivery system was investigated in different cell lines including Colo205 colorectal cancer cells and non-cancerous NIH/3T3 fibroblast and J774 macrophages cells. The effect of concentration and incubation time on uptake and toxicity were investigated on the MTB-LP, liposome alone, and bare MTB. The uptake results showed intact internalization of fluorescent liposomes, which were mainly localized in the cytoplasm and perinuclear region following incubation in both phagocytic cells (J774) and non-phagocytic cells (NIH/3T3 and Colo205). The uptake rate was lower in cancer cells as compared to the non-cancerous cells. This might be explained by literature finding that states extensive sialylation [187], heparan sulfate proteoglycans, abundance of phosphatidylserine residues, and *O*-sialoglycoproteins [188] enhance net negative surface charge on the cancerous cell, thereby induce a repulsive force towards the negatively charged liposome. The uptake of liposomes occurs via endocytotic-like mechanisms [321, 323]. The studies showed that live bacteria can stimulate and enter the nonphagocytic cells through macropinocytosis [189, 190]. Since the MC-1 MTB will only survive for 40 min at 37 °C [36], the uptake mechanism of MTB-LP needs to be further investigated. However, we showed that the attachment does not interfere with the liposome internalization and MTB-LP upon arrival to the tumor regions can deliver their drug content intracellularly. The *in vitro* cytotoxicity results revealed that the incorporation of liposomes on the MTB surface improved the biocompatibility of the MTB-LP complex compared to MTB alone in the examined cell types. The concentration-dependent cytotoxicity can be originated from substances produced by the bacteria, certain degradation products, and their competition for nutrients.

6.2 Development of MTB-magnetic particles as MRI contrast agents to track loaded MTB and visualize hypoxic regions of tumor xenograft

The absence of tracking feedback control during the *in vivo* targeting process of the bacteria is one of the major limitations of using MTB-LP for targeting. Currently, to confirm the presence and distribution of MTB-LP inside the target site, the tumor needs to proceed with invasive and prolonged histopathology analyses. Moreover, current noninvasive *in vivo* tumor imaging

modalities (*e.g.* MRI, PET, CT) [229, 285, 292] do not provide all required criteria for imaging due to the lack of spatial resolution, systemic side effects, and limited penetration of imaging agents toward tumor hypoxic regions [249, 250, 260]. Therefore, during this PhD thesis we aimed at developing a straightforward strategy for tracking the imaging agents-loaded MTB to address some of these limitations.

Iron oxide particles with the different particle sizes (200 and 500 nm) and magnetic properties (SPIONs and ferromagnetic) were used as MRI contrast agents to prepare the MTB-MP complexes. TEM images showed that the MPs consisted of a sub-particle cluster embedded in a polymeric matrix. Unlike MTB-LP, the direct attachment method for MTB-MP samples resulted in low attachment efficiency. This is may be due to the fact that COOH-functional groups at the terminal ending of irregularly shaped magnetic particles were sterically less accessible for direct binding. Therefore, for the preparation of MTB-MPs, two step bioconjugation procedures were developed. First IgG AB was grafted to the surface of the MPs using carbodiimide chemistry to covalently bind carboxyl groups to amine groups to form amide bonds [332, 333], and then the MP-AB were attached to the MTB through affinity binding. This attachment technique has been used vastly in many *in vitro* and *in vivo* applications [195, 213, 313]. The results demonstrated that the incorporating a spacer such as antibody compensates for the low attachment efficiency by providing the particles with higher chemical reactivity towards MTB.

The samples were further characterized by confocal microscopy, dynamic light scattering, zeta potential, fluorescence-based spectroscopy, FTIR, VSM, and MRI. For *in vitro* MR contrast characterization of MTB-MPs, T_1 and T_2-relaxation rates at different TI and TE values were performed and results validated the possibility of detecting MTB-S200/S500/F200/F500 complexes in the GRE images of a 3T clinical MR scanner. All four types of MTB-magnetic particles lead to shortening both T_1 and T_2 values in a manner inversely proportional to their concentration. The results indicated that T_1-relaxation is less affected than T_2-relaxation rate as is the case with superparamagnetic MRI contrast agents [343]. MTB-S200 showed higher relaxivity compared to MTB-S500, which corresponds well with VSM results showing higher saturation magnetization of S200 particles. Also, MTB-S200 showed higher signal intensity and relaxivities compared to S200 alone. This signal enhancement is due to the influence of the MTB iron content ($1.76 \pm 0.4 \times 10^{-14}$ g per MTB) that was determined by VSM. Moreover, MTB alone at the maximum tested concentration (10^8 MTB ml^{-1}) was contained ~1.26 μg ml^{-1} of iron and did

not generate a detectable signal loss in MR images. This result was in concordance with previous literature finding on bare MTB imaging [73]. MTB-S200 with the 3.6×10^{-6} μg (S200) per each MTB can generate appropriate magnetic properties (46.73 emu g^{-1}) with high relaxivity rates (r_1 = 96.2 and r_2 = 198.6 ($ms^{-1}\mu g^{-1}ml$)).

Despite high magnetic susceptibility, F200 and F500 showed high remanent magnetization that also led to the formation of aggregates during MR imaging. The previous studies demonstrated that these aggregates have a limited clearance from the body [59, 336]. Moreover, the F200 and F500 tended to form aggregates during bioconjugation to the MTB, which significantly affected their swimming behavior. Conversely, unlike ferromagnetic agents, S200 and S500 did not retain any significant amount of coercivity and remanent magnetization. Most importantly, they did not aggregate after the attachment process and the MTB-S200 complexes remained dispersed as individual magnetic carriers, making them more suitable for navigation into the tumor tissue. In addition, literature reports on SPIONs high biodegradability, low toxicity [347, 348], easy clearance from the body [250], and high signal contrast in T_2/T_2^*-weighted images [239, 247]. All these properties make SPIONs promising as an MRI contrast agents for various applications such as visualization of tumor location or angiogenesis [242, 244]. These are the reasons why MTB-200 complex was chosen for further *in vivo* investigation.

The tracking and imaging ability of the MTB-S200 complexes were performed in HCT116 human colorectal mouse tumor xenograft implanted into SCID-beige mice using 3T MRI's magnetic field and commercial receiver coils. The attachment of IgG antibody and MTB's antigen performed through affinity and non-covalent binding [363]. The results demonstrated that the bond remained stable through penetrating of MTB complexes in tumor tissue.

For MR image acquisition and improve the signal-to-noise ratio, the optimal concentration of MTB-S200 needs to be accumulated at the tumor site [70, 101]. Based on the initial concentration of injected MTB-S200 (200 μl of 5×10^9 MTB ml^{-1} in PBS) and the experimental results that showed around 50% of injected bacteria can reach the target side (Chapter 5 and Appendix A), it was concluded that 5×10^8 MTB-S200 (~1.8 mg Fe_3O_4) of distributed sample was visible in 3T MRI. In fact, the attached SPIONs were found to have a strong effect on the proton's relaxation time which resulted in susceptibility artifact by distortions of homogenous magnetic field and caused signal loss in a much greater scale than their actual size [244, 255].

According to the literature, T_2*-weighted GRE acquisitions provide the greatest sensitivity to the SPIONs as well as other sources of susceptibility (*e.g.* hemorrhage), shimming artifact, or chemical shift that make them less specific in the detection of SPIONs [230, 349]. On the other hand, the T_1-weighted imaging is less sensitive but more specific in detection of SPIONs and can provide greater signal-to-noise ratio in the presence of SPIONs and generate a hyperintense signal of the tumor [364]. Detection of MTB-S200 in hypoxic regions was successfully achieved through the combination of T_1- and T_2*-weighted images in *ex vivo* experiments to take advantage of the sensitivity of T_2*-weighted and specificity of T_1-weighted images to the presence of the SPIONs. The IF images were also addressed crucial information about the success of targeting, the state of localization and the accumulation of MTB inside the tumor, which correlates well with MR images.

To demonstrate the synergic effect of S200 particles once attached to MTB, the MRI was performed on the S200 particles alone. No signal improvement of tumor was observed and S200 particles were accumulated at the rim of the tissue and exhibited a limited diffusion ability due to the tumor interstitial fluid pressure and lack of propulsion force to overcome this barrier. This result was in concordance with previous studies that showed particles > 100 nm typically could be remained trapped in the extracellular matrix [4, 5]. Interestingly, our results demonstrated that MC-1 MTB could potentially be detected at the tumor site by MRI if a sufficient quantity of the magnetic materials attaches to their surface. In fact, no magnetosome-induced signal and detectable distortion in the MRI's magnetic field was observed for the bare MTBs due to the inadequate amount of iron content in the chains of magnetosomes. As depicted in TEM images, the magnetosome chain embedded in MC-1 MTB consists of 10-15 magnetosomes with a mean diameter of 70 nm, which provides quite a small volume of magnetic material for the population density of used MTB.

6.3 Development of the MTB-LSC complex and investigation of its stability during navigation in tumor xenograft

To prevent drug leakage during the attachment process, chemical environments such as the pH and type of reagents were adjusted to the pH-gradient liposome-SN38 formulation during the preparation of MTB-LSC for *in vivo* assays. The stability of the attachment during targeting was then examined within the HCT116 mouse tumor xenografts. The results from the IF combined

with HPS staining showed the penetration capability of MTB-LSC and their accumulation in hypoxic and necrotic regions. Two detection methods were validated for quantification of MTB complexes in tissue samples: (i) the rapid homogenization technique followed by optical microscopy observation and (ii) immunofluorescence staining technique. Both techniques were coherent for the ratio of injected bacteria to detected MTB in tumor tissue (~59% for homogenization compared to ~50% for the image-processing technique of fluorescence images). These convincing results validated that approximately half of the peritumorally injected MTB-LSC can be penetrated through the cellular barriers of the tumor xenografts such as extracellular matrix (composed of collagen, glycosaminoglycans, and proteoglycans) [12, 44] and tight junctions [52], and overcome the tumor interstitial fluid pressure [54, 365] while carrying their therapeutic payloads.

The MTB-LSC system showed promising potential to overcome the delivery concerns and improve therapeutic effects of SN38 by delivering the active lactone form through enhancing SN38 solubility and its encapsulation in the acidic core of liposome [111, 112, 127] using pH gradient method [111, 127] (See Appendix B). The results demonstrated that multiple dose injections of MTB-LSC with the final cumulative dose of ~6.4 μg SN38 have the therapeutic effect on tumor growth, and also produce a statistically significant reduction in tumor size compared to all controls (MTB, LP-SN38, LP, CPT-11, and PBS). Observing the therapeutic effectiveness of the drug evidenced that the LP-SN38 remained attached during the navigation process. The plausible mechanism of drug release from the liposomes in the tumor environment can be degradation-dependent drug release (*e.g.* hydrolysis or enzymatically [141, 178, 179]) or drug diffusion from liposomes, which should be further explored in future work. The overall results suggest that the MTB-LSC system enhances therapeutic index with the possibility to reduce systemic circulation by direct targeting of unattainable sites of tumors and is more effective as compared to currently used passive and active targeting methods [366] as well as compared to more recent finding with MDT [306, 307] and MRN [20] delivery methods.

CHAPTER 7 CONCLUSION AND RECOMMENDATIONS

A novel MTB-based navigable targeted delivery system was introduced as a viable therapeutic and imaging modality to transport payloads into distal tumor regions for treating purposes and visualization of tumor structure. We demonstrated that peritumorally administered magneto-aerotactic MTB associated drug or contrast agents can profoundly navigate toward the center of the tumor, pass the cellular barrier, penetrate deeply into the tumors xenograft, alter biodistribution and accumulate in hypoxic and necrotic zone. The attached therapeutic and contrast agent through both direct covalent amide bonds in MTB-LSC and antibody affinity bond in MTB-S200 were stable during the navigation in tumor environment and did not cause any adverse effect on migration of the MTB into the tissue. Indeed, high targeting ratios (~50-59%) were obtained for both loaded and unloaded MTB.

We confirmed that the pairing of MTB carrier with 200 nm SPIONs is a promising candidate for tracking and tumor microstructure imaging by the production of susceptibility artifact inside the tumor hypoxic regions using a 3T clinical MRI scanner. SPIONs are more suitable for attachment due to the better magnetic characteristics, generating a high contrast in both T_1- and T_2/T_2^*-weighted images, and fewer tendencies to cause agglomerate formation with MTB during attachment process, which are crucial for the performance of the navigable agents *in vivo*. The versatility of MTB bio-carrier combined with suitable attached agents is a significant breakthrough in the field of microrobotics and targeting delivery systems in medical interventions for oncological care or other different types of diseases.

Recommendations and future perspectives

The purpose of this thesis was to establish the foundation for the application of magnetic bacteria-based system with targeting and tracking capabilities as viable navigable drug delivery systems. Through an innovative design and straightforward chemistry, we prepared the bacterial complexes and successfully showed the feasibility of this approach. Given the wealth of this sophisticated carrier, attached cargos to MTB can be extended far beyond the liposome and magnetic nanoparticle illustrated here. The MTB-based technology may open further opportunities for delivering a vast variety of therapeutics (*e.g.* drugs, genes, vaccines, and

markers) or imaging agents (*e.g.* magnetic materials, gold, fluorescence, radiosensitizers). Some examples of the future directions along with the limitation of this study are presented below:

- Labeling the MTB with the trackable chemicals gives the opportunity for *in vivo* image-guided therapy plan for the inaccessible disease sites as well as noninvasive tracking for feedback control of the position of drug-loaded MTB.
- The MTB-based drug delivery system presented here was either featured for targeting or tracking. Future work can envision attaching and incorporating therapeutic and imaging modalities into the same MTB biocarriers to increase the potential application of the complex as multifunctional theranostic agents with the ability to simultaneously target, track, and treat the diseased tissue *in vivo*.
- The optimizations of experiments are required to further investigate the therapeutic dose of drug, its mechanism of release and pharmacokinetics. This should be also accompanied with a better characterization of MTB complexes *in vivo* and its biodistribution after reaching the targets.
- Future plan can also include loading a combination of chemotherapy compounds with radiosensitizers such as gold nanoparticles on same MTB to take advantage of magneto-aerotaxis platform along with external beam radiation therapy to improve the therapeutic index of cancer therapy.
- Future studies can explore targeting magnetic nanoparticle-loaded MTB (MTB-MP) for localized hyperthermia. The hyperthermia could heat up the targeted MTB-MP and raise the temperature by a few degrees at the cellular level in the vicinity of a region needs to be treated to minimize overheating of the surrounding healthy tissues. For instance, targeted MTB-MP in brain's vessels offer the possibility for reversible and transient disruption of the blood-brain barrier via localized hyperthermia to allow delivery of brain chemotherapy drugs. The heat-triggered release of drug embedded hydrogel attached to the MTB-MP is just another example of the many possible applications.
- The targeting and tracking ability of the MTB complexes should be validated for application in a human for its clinical translation. An enormous scale-up is needed to adapt the magnetic navigation protocol platform as well as the effective drug dosage.
- The applications of developed MTB systems are limited to localized therapy and only applicable for accessible solid tumors such as colorectal and prostate by peritumorally injection

of MTB complexes closest to the microvessels and bypassing the artery and larger vessels. This is due to the fact that bacteria cannot be controlled in the bloodstream due to the high blood velocity. For the diseases that are not accessible, the targeted delivery needs to be done through the bloodstream. Therefore, encapsulation of MTB loaded with both magnetic particles and drugs in the larger hollow carriers (~50 μm) could be designed as MRI-navigable complex. The complexes should be released via a catheter closest to the microvasculature feeding the tissue and then be followed by magnetic guidance. When it reaches the desired site, magnetotaxis platform can take place and navigate the bacteria to the site of interest. However, the aerotactic behavior depends on the type of the disease that present appropriate level of oxygen for MTB to penetrate.

- As a potential for clinical application, in-depth investigations of the safety assessment and inflammatory responses of the MTB complexes, bacteria residual, and all free compounds need be conducted. Specifically, an experiment quantifying hematology and biochemistry biomarkers, immunotoxicity, toxicokinetic, carcinogenicity, and genotoxicity need to be undertaken to achieve a detailed understanding of effects of MTB system on safety.

Social and economic impact

The developed technology can provide tremendous potential and holds substantial promise to improve the efficacy of therapy in patients suffering from cancer. Effective pathways can be developed to transfer the results and outputs of this technology to the potential end-users in a timely manner. Successful accomplishment and pharmacoeconomics effects of developed drug targeting approach using MTB will result in:

- An augmentation of the efficacy of established chemotherapy and imaging compounds by targeting them directly in the tumor;
- An increase in the accumulation and diffusion of drugs in the tumor site;
- The enabling of safe and repeated administration of doses higher than the other MTD or unencapsulated drug, while simultaneously the decrease of adverse side-effects;
- The reduction of the risk of tumor reformation or metastases to other organs of the body;
- The decrease of costs incurred by the patients and the taxpayer;
- The massive impacts and concomitant benefits on life expectancy and survival of the patients fighting cancer while improving their life quality during the treatment.

BIBLIOGRAPHY

[1] Canadian Cancer Society's Advisory Committee on Cancer Statistics, *Canadian Cancer Statistics 2015*. Toronto, ON: Government of canada, 2015.

[2] L. Brannon-Peppas and J. O. Blanchette, "Nanoparticle and targeted systems for cancer therapy," *Advanced Drug Delivery Reviews,* vol. 64, pp. 206-212, Dec 2012.

[3] I. K. Choi, R. Strauss, M. Richter, C. O. Yun, and A. Lieber, "Strategies to increase drug penetration in solid tumors," *Front Oncol,* vol. 3, p. 193, 2013.

[4] W. J. Gradishar, S. Tjulandin, N. Davidson, H. Shaw, N. Desai, P. Bhar, *et al.*, "Phase III trial of nanoparticle albumin-bound paclitaxel compared with polyethylated castor oil-based paclitaxel in women with breast cancer," *Journal of Clinical Oncology,* vol. 23, pp. 7794-7803, Nov 1 2005.

[5] E. P. Winer, D. A. Berry, S. Woolf, W. Duggan, A. Kornblith, L. N. Harris, *et al.*, "Failure of higher-dose paclitaxel to improve outcome in patients with metastatic breast cancer: Cancer and Leukemia Group B Trial 9342," *Journal of Clinical Oncology,* vol. 22, pp. 2061-2068, Jun 1 2004.

[6] O. Tredan, C. M. Galmarini, K. Patel, and I. F. Tannock, "Drug resistance and the solid tumor microenvironment," *Journal of the National Cancer Institute,* vol. 99, pp. 1441-1454, Oct 3 2007.

[7] M. R. Junttila and F. J. de Sauvage, "Influence of tumour micro-environment heterogeneity on therapeutic response," *Nature,* vol. 501, pp. 346-354, Sep 19 2013.

[8] L. M. Kaminskas, V. M. McLeod, B. D. Kelly, G. Sberna, B. J. Boyd, M. Williamson, *et al.*, "A comparison of changes to doxorubicin pharmacokinetics, antitumor activity, and toxicity mediated by PEGylated dendrimer and PEGylated liposome drug delivery systems," *Nanomedicine-Nanotechnology Biology and Medicine,* vol. 8, pp. 103-111, Jan 2012.

[9] M. M. Yallapu, S. P. Foy, T. K. Jain, and V. Labhasetwar, "PEG-Functionalized Magnetic Nanoparticles for Drug Delivery and Magnetic Resonance Imaging Applications," *Pharmaceutical Research,* vol. 27, pp. 2283-2295, Nov 2010.

[10] M. H. Hong, S. J. Zhu, Y. Y. Jiang, G. T. Tang, and Y. Y. Pei, "Efficient tumor targeting of hydroxycamptothecin loaded PEGylated niosomes modified with transferrin," *Journal of Controlled Release,* vol. 133, pp. 96-102, Jan 19 2009.

[11] R. K. Jain, "Delivery of molecular and cellular medicine to solid tumors," *Advanced Drug Delivery Reviews,* vol. 64, pp. 353-365, Dec 2012.

[12] A. I. Minchinton and I. F. Tannock, "Drug penetration in solid tumours," *Nature Reviews Cancer,* vol. 6, pp. 583-592, Aug 2006.

[13] J. M. Brown and W. R. William, "Exploiting tumour hypoxia in cancer treatment," *Nature Reviews Cancer,* vol. 4, pp. 437-447, Jun 2004.

[14] B. J. Moeller, R. A. Richardson, and M. W. Dewhirst, "Hypoxia and radiotherapy: opportunities for improved outcomes in cancer treatment," *Cancer and Metastasis Reviews,* vol. 26, pp. 241-248, Jun 2007.

[15] J. Bussink, J. H. A. M. Kaanders, and A. J. van der Kogel, "Tumor hypoxia at the micro-regional level: clinical relevance and predictive value of exogenous and endogenous hypoxic cell markers," *Radiotherapy and Oncology,* vol. 67, pp. 3-15, Apr 2003.

[16] G. J. Weiss, J. R. Infante, E. G. Chiorean, M. J. Borad, J. C. Bendell, J. R. Molina, *et al.*, "Phase 1 Study of the Safety, Tolerability, and Pharmacokinetics of TH-302, a Hypoxia-Activated Prodrug, in Patients with Advanced Solid Malignancies," *Clinical Cancer Research,* vol. 17, pp. 2997-3004, May 1 2011.

[17] G. O. Ahn and M. Brown, "Targeting tumors with hypoxia-activated cytotoxins," *Frontiers in Bioscience,* vol. 12, pp. 3483-3501, May 1 2007.

[18] A. B. Ariffin, P. F. Forde, S. Jahangeer, D. M. Soden, and J. Hinchion, "Releasing Pressure in Tumors: What Do We Know So Far and Where Do We Go from Here ? A Review," *Cancer Research,* vol. 74, pp. 2655-2662, May 15 2014.

[19] C. Wong, T. Stylianopoulos, J. A. Cui, J. Martin, V. P. Chauhan, W. Jiang, *et al.*, "Multistage nanoparticle delivery system for deep penetration into tumor tissue," *Proceedings of the National Academy of Sciences of the United States of America,* vol. 108, pp. 2426-2431, Feb 8 2011.

[20] S. Martel, J. B. Mathieu, O. Felfoul, A. Chanu, E. Aboussouan, S. Tamaz, *et al.*, "Automatic navigation of an untethered device in the artery of a living animal using a conventional clinical magnetic resonance imaging system," *Applied Physics Letters,* vol. 90, Mar 12 2007.

[21] O. Rotariu and N. J. C. Strachan, "Modelling magnetic carrier particle targeting in the tumor microvasculature for cancer treatment," *Journal of Magnetism and Magnetic Materials,* vol. 293, pp. 639-646, May 1 2005.

[22] B. Polyak and G. Friedman, "Magnetic targeting for site-specific drug delivery: applications and clinical potential," *Expert Opinion on Drug Delivery,* vol. 6, pp. 53-70, Jan 2009.

[23] L. Zhang, J. J. Abbott, L. X. Dong, K. E. Peyer, B. E. Kratochvil, H. X. Zhang, *et al.*, "Characterizing the Swimming Properties of Artificial Bacterial Flagella," *Nano Letters,* vol. 9, pp. 3663-3667, Oct 2009.

[24] L. Zhang, J. J. Abbott, L. X. Dong, B. E. Kratochvil, D. Bell, and B. J. Nelson, "Artificial bacterial flagella: Fabrication and magnetic control," *Applied Physics Letters,* vol. 94, Feb 9 2009.

[25] M. E. Fox, M. J. Lemmon, M. L. Mauchline, T. O. Davis, A. J. Giaccia, N. P. Minton, *et al.*, "Anaerobic bacteria as a delivery system for cancer gene therapy: In vitro activation of 5-fluorocytosine by genetically engineered clostridia (vol 3, pg 173, 1996)," *Gene Therapy,* vol. 3, pp. 741-741, Aug 1996.

[26] A. T. St Jean, M. M. Zhang, and N. S. Forbes, "Bacterial therapies: completing the cancer treatment toolbox," *Current Opinion in Biotechnology,* vol. 19, pp. 511-517, Oct 2008.

[27] R. W. Kasinskas and N. S. Forbes, "Salmonella typhimurium specifically chemotax and proliferate in heterogeneous tumor tissue in vitro," *Biotechnology and Bioengineering,* vol. 94, pp. 710-721, Jul 5 2006.

[28] N. S. Forbes, L. L. Munn, D. Fukumura, and R. K. Jain, "Sparse initial entrapment of systemically injected Salmonella typhimurium leads to heterogeneous accumulation within tumors," *Cancer Research,* vol. 63, pp. 5188-5193, Sep 1 2003.

[29] S. Ganai, R. B. Arenas, J. P. Sauer, B. Bentley, and N. S. Forbes, "In tumors Salmonella migrate away from vasculature toward the transition zone and induce apoptosis," *Cancer Gene Therapy,* vol. 18, pp. 457-466, Jul 2011.

[30] X. Yin, B. Yu, Z. Tang, B. He, J. Ren, X. Xiao, *et al.*, "Bifidobacterium infantis-mediated HSV-TK/GCV suicide gene therapy induces both extrinsic and intrinsic apoptosis in a rat model of bladder cancer," *Cancer Gene Therapy,* vol. 20, pp. 77-81, Feb 2013.

[31] N. S. Forbes, "Engineering the perfect (bacterial) cancer therapy," *Nat Rev Cancer,* vol. 10, pp. 785-94, Nov 2010.

[32] O. Felfoul, J. B. Mathieu, and S. Martel, "A Comparative Study between MC-1 Cells and Magnetic Microparticles Used for Enhanced Target Delivery of Therapeutic Agents in the Microvasculature," in *2008 2nd Ieee Ras & Embs International Conference on Biomedical Robotics and Biomechatronics (Biorob 2008), Vols 1 and 2*, 2008, pp. 694-699.

[33] R. B. Frankel, D. A. Bazylinski, M. S. Johnson, and B. L. Taylor, "Magneto-aerotaxis in marine coccoid bacteria," *Biophysical Journal,* vol. 73, pp. 994-1000, Aug 1997.

[34] A. Arakaki, H. Nakazawa, M. Nemoto, T. Mori, and T. Matsunaga, "Formation of magnetite by bacteria and its application," *Journal of the Royal Society Interface,* vol. 5, pp. 977-999, Sep 6 2008.

[35] D. Faivre and D. Schuler, "Magnetotactic Bacteria and Magnetosomes," *Chemical Reviews,* vol. 108, pp. 4875-4898, Nov 2008.

[36] S. Martel, M. Mohammadi, O. Felfoul, Z. Lu, and P. Pouponneau, "Flagellated Magnetotactic Bacteria as Controlled MRI-trackable Propulsion and Steering Systems for Medical Nanorobots Operating in the Human Microvasculature," *International Journal of Robotics Research,* vol. 28, pp. 571-582, Apr 2009.

[37] Y. Malam, M. Loizidou, and A. M. Seifalian, "Liposomes and nanoparticles: nanosized vehicles for drug delivery in cancer," *Trends in Pharmacological Sciences,* vol. 30, pp. 592-599, Nov 2009.

[38] A. Kumari, S. K. Yadav, and S. C. Yadav, "Biodegradable polymeric nanoparticles based drug delivery systems," *Colloids and Surfaces B-Biointerfaces,* vol. 75, pp. 1-18, Jan 1 2010.

[39] O. C. Farokhzad and R. Langer, "Impact of Nanotechnology on Drug Delivery," *Acs Nano,* vol. 3, pp. 16-20, Jan 2009.

[40] V. P. Torchilin, "Recent advances with liposomes as pharmaceutical carriers," *Nature Reviews Drug Discovery,* vol. 4, pp. 145-160, Feb 2005.

[41] S. A. Hussain, D. R. Ferry, G. El-Gazzaz, D. F. Mirza, N. D. James, P. McMaster, *et al.*, "Hepatocellular carcinoma," *Annals of Oncology,* vol. 12, pp. 161-172, Feb 2001.

[42] C. A. Znati, M. Rosenstein, Y. Boucher, M. W. Epperly, W. D. Bloomer, and R. K. Jain, "Effect of radiation on interstitial fluid pressure and oxygenation in a human tumor xenograft," *Cancer Res,* vol. 56, pp. 964-68, Mar 1 1996.

[43] M. Oconnell, J. A. Martenson, H. S. Wieand, J. E. Krook, J. S. Macdonald, D. G. Haller, *et al.*, "Improving Adjuvant Therapy for Rectal-Cancer by Combining Protracted-Infusion Fluorouracil with Radiation-Therapy after Curative Surgery," *New England Journal of Medicine,* vol. 331, pp. 502-507, Aug 25 1994.

[44] V. G. Peddareddigari, D. Wang, and R. N. Dubois, "The tumor microenvironment in colorectal carcinogenesis," *Cancer Microenviron,* vol. 3, pp. 149-66, 2010.

[45] R. Stoyanova, K. Huang, K. Sandler, H. Cho, S. Carlin, P. B. Zanzonico, *et al.*, "Mapping Tumor Hypoxia In Vivo Using Pattern Recognition of Dynamic Contrast-enhanced MRI Data," *Translational Oncology,* vol. 5, pp. 437-U114, Dec 2012.

[46] S. K. Hobbs, W. L. Monsky, F. Yuan, W. G. Roberts, L. Griffith, V. P. Torchilin, *et al.*, "Regulation of transport pathways in tumor vessels: role of tumor type and microenvironment," *Proc Natl Acad Sci U S A,* vol. 95, pp. 4607-12, Apr 14 1998.

[47] F. Yuan, M. Dellian, D. Fukumura, M. Leunig, D. A. Berk, V. P. Torchilin, *et al.*, "Vascular-Permeability in a Human Tumor Xenograft - Molecular-Size Dependence and Cutoff Size," *Cancer Research,* vol. 55, pp. 3752-3756, Sep 1 1995.

[48] A. K. Iyer, G. Khaled, J. Fang, and H. Maeda, "Exploiting the enhanced permeability and retention effect for tumor targeting," *Drug Discovery Today,* vol. 11, pp. 812-818, Sep 2006.

[49] F. Yuan, M. Leunig, S. K. Huang, D. A. Berk, D. Papahadjopoulos, and R. K. Jain, "Microvascular permeability and interstitial penetration of sterically stabilized (stealth) liposomes in a human tumor xenograft," *Cancer Res,* vol. 54, pp. 3352-6, Jul 1 1994.

[50] H. Kobayashi, R. Watanabe, and P. L. Choyke, "Improving Conventional Enhanced Permeability and Retention (EPR) Effects; What Is the Appropriate Target?," *Theranostics,* vol. 4, pp. 81-89, 2014.

[51] M. A. Konerding, A. J. Miodonski, and A. Lametschwandtner, "Microvascular corrosion casting in the study of tumor vascularity: A review," *Scanning Microscopy,* vol. 9, pp. 1233-1244, 1995.

[52] R. Ancillotti, L. Goto-Silva, G. Montesano, S. Oliveira, P. A. Redondo, L. A. Barbosa, *et al.*, "Assembly and functional analysis of tight junction in a colon adenocarcinoma cell line: Effect of glucose depletion," *Cellular and Molecular Biology,* vol. 49, pp. 113-122, Feb 2003.

[53] S. K. Green, M. C. Karlsson, J. V. Ravetch, and R. S. Kerbel, "Disruption of cell-cell adhesion enhances antibody-dependent cellular cytotoxicity: implications for antibody-based therapeutics of cancer," *Cancer Res,* vol. 62, pp. 6891-900, Dec 1 2002.

[54] C. H. Heldin, K. Rubin, K. Pietras, and A. Ostman, "High interstitial fluid pressure - An obstacle in cancer therapy," *Nature Reviews Cancer,* vol. 4, pp. 806-813, Oct 2004.

[55] R. K. Jain, "Transport of molecules in the tumor interstitium: a review," *Cancer Res,* vol. 47, pp. 3039-51, Jun 15 1987.

[56] M. I. Koukourakis, A. Giatromanolaki, A. Polychronidis, C. Simopoulos, K. C. Gatter, A. L. Harris, *et al.*, "Endogenous markers of hypoxia/anaerobic metabolism and anemia in primary colorectal cancer," *Cancer Science,* vol. 97, pp. 582-588, Jul 2006.

[57] G. Maleux, H. van Malenstein, V. Vandecaveye, S. Heye, J. Vaninbroukx, F. Nevens, *et al.*, "Transcatheter Chemoembolization of Unresectable Hepatocellular Carcinoma: Current Knowledge and Future Directions," *Digestive Diseases,* vol. 27, pp. 157-163, 2009.

[58] E. J. Furlani and E. P. Furlani, "A model for predicting magnetic targeting of multifunctional particles in the microvasculature," *Journal of Magnetism and Magnetic Materials,* vol. 312, pp. 187-193, May 1 2007.

[59] F. Mishima, S. Takeda, Y. Izumi, and S. Nishijima, "Three dimensional motion control system of ferromagnetic particles for magnetically targeted drug delivery systems," *Ieee Transactions on Applied Superconductivity,* vol. 16, pp. 1539-1542, Jun 2006.

[60] D. M. McDonald and P. Baluk, "Significance of blood vessel leakiness in cancer," *Cancer Research,* vol. 62, pp. 5381-5385, Sep 15 2002.

[61] H. Hashizume, P. Baluk, S. Morikawa, J. W. McLean, G. Thurston, S. Roberge, *et al.*, "Openings between defective endothelial cells explain tumor vessel leakiness," *American Journal of Pathology,* vol. 156, pp. 1363-1380, Apr 2000.

[62] J. Szebeni, F. Muggia, A. Gabizon, and Y. Barenholz, "Activation of complement by therapeutic liposomes and other lipid excipient-based therapeutic products: Prediction and prevention," *Advanced Drug Delivery Reviews,* vol. 63, pp. 1020-1030, Sep 16 2011.

[63] M. Longmire, P. L. Choyke, and H. Kobayashi, "Clearance properties of nano-sized particles and molecules as imaging agents: considerations and caveats," *Nanomedicine,* vol. 3, pp. 703-717, Oct 2008.

[64] B. Gleich, N. Hellwig, H. Bridell, R. Jurgons, C. Seliger, C. Alexiou, *et al.*, "Design and evaluation of magnetic fields for nanoparticle drug targeting in cancer," *Ieee Transactions on Nanotechnology,* vol. 6, pp. 164-170, Mar 2007.

[65] P. Pouponneau, J. C. Leroux, and S. Martel, "Magnetic nanoparticles encapsulated into biodegradable microparticles steered with an upgraded magnetic resonance imaging system for tumor chemoembolization," *Biomaterials,* vol. 30, pp. 6327-6332, Nov 2009.

[66] S. Martel, J. B. Mathieu, O. Felfoul, A. Chanu, E. Aboussouan, S. Tamaz, *et al.*, "A computer-assisted protocol for endovascular target interventions using a clinical MRI system for controlling untethered microdevices and future nanorobots," *Computer Aided Surgery,* vol. 13, pp. 340-352, Nov 2008.

[67] P. Pouponneau, J. C. Leroux, G. Soulez, L. Gaboury, and S. Martel, "Co-encapsulation of magnetic nanoparticles and doxorubicin into biodegradable microcarriers for deep tissue targeting by vascular MRI navigation," *Biomaterials,* vol. 32, pp. 3481-3486, May 2011.

[68] S. Martel, "Combining Pulsed and DC Gradients in a Clinical MRI-Based Microrobotic Platform to Guide Therapeutic Magnetic Agents in the Vascular Network," *International Journal of Advanced Robotic Systems*, vol. 10, Jan 11 2013.

[69] S. Tamaz, R. Gourdeau, A. Chanu, J. B. Mathieu, and S. Martel, "Real-time MRI-based control of a ferromagnetic core for endovascular navigation," *Ieee Transactions on Biomedical Engineering*, vol. 55, pp. 1854-1863, Jul 2008.

[70] S. Martel, O. Felfoul, J. B. Mathieu, A. Chanu, S. Tamaz, M. Mohammadi, *et al.*, "MRI-based Medical Nanorobotic Platform for the Control of Magnetic Nanoparticles and Flagellated Bacteria for Target Interventions in Human Capillaries," *Int J Rob Res*, vol. 28, pp. 1169-1182, Sep 1 2009.

[71] P. Pouponneau, G. Soulez, G. Beaudoin, J. C. Leroux, and S. Martel, "MR Imaging of Therapeutic Magnetic Microcarriers Guided by Magnetic Resonance Navigation for Targeted Liver Chemoembolization," *Cardiovascular and Interventional Radiology*, vol. 37, pp. 784-790, Jun 2014.

[72] J. Edd, S. Payen, B. Rubinsky, M. L. Stoller, and M. Sitti, "Biomimetic propulsion for a swimming surgical micro-robot," *Iros 2003: Proceedings of the 2003 Ieee/Rsj International Conference on Intelligent Robots and Systems, Vols 1-4*, pp. 2583-2588, 2003.

[73] O. Felfoul, P. Pouponneau, J. B. Mathieu, and S. Martel, "MR Imaging of Fe-Co Nanoparticles, Magnetotactic Bacteria and Fe(3)O(4) Microparticles for Future Drug Delivery Applications," *2007 7th Ieee Conference on Nanotechnology, Vol 1-3*, pp. 308-311, 2007.

[74] S. Martel, "Targeted delivery of therapeutic agents with controlled bacterial carriers in the human blood vessels," *2006 Bio- Micro- and Nanosystems Conference*, pp. 9-9, 2006.

[75] P. Kodati, J. Hinkle, and X. Y. Deng, "Micro autonomous robotic ostraciiform (MARCO): Design and fabrication," *Proceedings of the 2007 Ieee International Conference on Robotics and Automation, Vols 1-10*, pp. 960-965, 2007.

[76] J. T. Wei, L. C. Xiong, and H. Wang, "The Study of Thermoelectric Power Generation in The Cooling of Fin and Vibration Heat Pipe," *2012 International Conference on Future Electrical Power and Energy System, Pt B*, vol. 17, pp. 1570-1577, 2012.

[77] Y. Tanaka, K. Hirano, H. Nagata, and M. Ishikawa, "Real-time three-dimensional orientation control of non-spherical micro-objects using laser trapping," *Electronics Letters*, vol. 43, pp. 412-414, Mar 29 2007.

[78] B. Behkam and M. Sitti, "Bacterial flagella-based propulsion and on/off motion control of microscale objects," *Applied Physics Letters*, vol. 90, Jan 8 2007.

[79] A. S. Bahaj, P. A. B. James, and F. D. Moeschler, "High gradient magnetic separation of motile and non-motile magnetotactic bacteria," *Ieee Transactions on Magnetics*, vol. 32, pp. 5106-5108, Sep 1996.

[80] M. R. Benoit, D. Mayer, Y. Barak, I. Y. Chen, W. Hu, Z. Cheng, *et al.*, "Visualizing Implanted Tumors in Mice with Magnetic Resonance Imaging Using Magnetotactic Bacteria," *Clinical Cancer Research*, vol. 15, pp. 5170-5177, Aug 15 2009.

[81] Y. Hiratsuka, M. Miyata, T. Tada, and T. Q. P. Uyeda, "A microrotary motor powered by bacteria," *Proceedings of the National Academy of Sciences of the United States of America,* vol. 103, pp. 13618-13623, Sep 12 2006.

[82] S. Martel, C. C. Tremblay, S. Ngakeng, and G. Langlois, "Controlled manipulation and actuation of micro-objects with magnetotactic bacteria," *Applied Physics Letters,* vol. 89, Dec 4 2006.

[83] B. Behkam and M. Sitti, "Design methodology for biomimetic propulsion of miniature swimming robots," *Journal of Dynamic Systems Measurement and Control-Transactions of the Asme,* vol. 128, pp. 36-43, Mar 2006.

[84] S. Martel and M. Mohammadi, "A Robotic Micro-assembly Process Inspired by the Construction of the Ancient Pyramids and Relying on Several Thousand Flagellated Bacteria Acting as Micro-workers," *2009 Ieee-Rsj International Conference on Intelligent Robots and Systems,* pp. 426-427, 2009.

[85] E. Steager, C. B. Kim, J. Patel, S. Bith, C. Naik, L. Reber, *et al.*, "Control of microfabricated structures powered by flagellated bacteria using phototaxis," *Applied Physics Letters,* vol. 90, Jun 25 2007.

[86] R. P. Blakemore, "Magnetotactic bacteria," *Annu Rev Microbiol,* vol. 36, pp. 217-38, 1982.

[87] H. Lee, A. M. Purdon, V. Chu, and R. M. Westervelt, "Controlled assembly of magnetic nanoparticles from magnetotactic bacteria using microelectromagnets arrays," *Nano Letters,* vol. 4, pp. 995-998, May 2004.

[88] S. Martel, "Controlled bacterial micro-actuation," *2006 International Conference on Microtechnologies in Medicine and Biology,* pp. 89-92, 2006.

[89] S. Martel and M. Mohammadi, "Using a Swarm of Self-propelled Natural Microrobots in the Form of Flagellated Bacteria to Perform Complex Micro-assembly Tasks," *2010 Ieee International Conference on Robotics and Automation (Icra),* pp. 500-505, 2010.

[90] W. B. Coley, "II. Contribution to the Knowledge of Sarcoma," *Ann Surg,* vol. 14, pp. 199-220, Sep 1891.

[91] R. Gardlik, M. Behuliak, R. Palffy, P. Celec, and C. J. Li, "Gene therapy for cancer: bacteria-mediated anti-angiogenesis therapy," *Gene Ther,* vol. 18, pp. 425-31, May 2011.

[92] C. Bettegowda, L. H. Dang, R. Abrams, D. L. Huson, L. Dillehay, I. Cheong, *et al.*, "Overcoming the hypoxic barrier to radiation therapy with anaerobic bacteria," *Proceedings of the National Academy of Sciences of the United States of America,* vol. 100, pp. 15083-15088, Dec 9 2003.

[93] S. Patyar, R. Joshi, D. S. P. Byrav, A. Prakash, B. Medhi, and B. K. Das, "Bacteria in cancer therapy: a novel experimental strategy," *Journal of Biomedical Science,* vol. 17, Mar 23 2010.

[94] C. K. Baban, M. Cronin, D. O'Hanlon, G. C. O'Sullivan, and M. Tangney, "Bacteria as vectors for gene therapy of cancer," *Bioeng Bugs,* vol. 1, pp. 385-94, Nov-Dec 2010.

[95] S. Liu, X. Xu, X. Zeng, L. Li, Q. Chen, and J. Li, "Tumor-targeting bacterial therapy: A potential treatment for oral cancer (Review)," *Oncol Lett,* vol. 8, pp. 2359-2366, Dec 2014.

[96] J. F. Toso, V. J. Gill, P. Hwu, F. M. Marincola, N. P. Restifo, D. J. Schwartzentruber, *et al.*, "Phase I study of the intravenous administration of attenuated Salmonella typhimurium to patients with metastatic melanoma," *Journal of Clinical Oncology,* vol. 20, pp. 142-152, Jan 1 2002.

[97] L. H. Dang, C. Bettegowda, D. L. Huso, K. W. Kinzler, and B. Vogelstein, "Combination bacteriolytic therapy for the treatment of experimental tumors," *Proceedings of the National Academy of Sciences of the United States of America,* vol. 98, pp. 15155-15160, Dec 18 2001.

[98] I. Cheong, X. Huang, C. Bettegowda, L. A. Diaz, K. W. Kinzler, S. B. Zhou, *et al.*, "A bacterial protein enhances the release and efficacy of liposomal cancer drugs," *Science,* vol. 314, pp. 1308-1311, Nov 24 2006.

[99] R. Blakemore, "Magnetotactic bacteria," *Science,* vol. 190, pp. 377-9, Oct 24 1975.

[100] S. Martel, "Magnetic Navigation Control of Microagents in the Vascular Network: Challenges and Strategies for Endovascular Magnetic Navigation Control of Microscale Drug Delivery Carriers," *Ieee Control Systems Magazine,* vol. 33, pp. 119-134, Dec 2013.

[101] R. Hergt, R. Hiergeist, M. Zeisberger, D. Schuler, U. Heyen, I. Hilger, *et al.*, "Magnetic properties of bacterial magnetosomes as potential diagnostic and therapeutic tools," *Journal of Magnetism and Magnetic Materials,* vol. 293, pp. 80-86, May 1 2005.

[102] I. S. M. Khalil, V. Magdanz, S. Sanchez, O. G. Schmidt, L. Abelmann, and S. Misra, "Magnetic Control of Potential Microrobotic Drug Delivery Systems: Nanoparticles, Magnetotactic Bacteria and Self-Propelled Microjets," *2013 35th Annual International Conference of the Ieee Engineering in Medicine and Biology Society (Embc),* pp. 5299-5302, 2013.

[103] O. Felfoul, "MRI-Based Tumour Targeting Enhancement with Magnetotactic Bacterial Carriers," Ph.D. Thesis, Computer and Software Engineering, École Polytechnique de Montréal, Montreal, 2011.

[104] P. Koumoutsakos, I. Pivkin, and F. Milde, "The Fluid Mechanics of Cancer and Its Therapy," *Annual Review of Fluid Mechanics, Vol 45,* vol. 45, pp. 325-355, 2013.

[105] D. de Lanauze, "Contrôle tridimensionnel de bactéries magnétotactiques agissant comme microrobots pour le transport actif de médicament vers une tumeur," Master Thesis, Computer and Software Engineering, Institute of Biomedical Engineering, École Polytechnique de Montréal, Montréal, 2013.

[106] R. Nadkarni, S. Barkley, and C. Fradin, "A Comparison of Methods to Measure the Magnetic Moment of Magnetotactic Bacteria through Analysis of Their Trajectories in External Magnetic Fields," *Plos One,* vol. 8, Dec 12 2013.

[107] S. Martel, "Magnetic therapeutic delivery using navigable agents," *Ther Deliv,* vol. 5, pp. 189-204, 2014.

[108] D. de Lanauze, O. Felfoul, J. P. Turcot, M. Mohammadi, and S. Martel, "Three-dimensional remote aggregation and steering of magnetotactic bacteria microrobots for drug delivery applications," *International Journal of Robotics Research,* vol. 33, pp. 359-374, Mar 2014.

[109] S. Martel, "Presenting a new paradigm in cancer therapy: delivering therapeutic agents using navigable microcarriers," *IEEE Pulse,* vol. 5, pp. 48-55, May-Jun 2014.

[110] E. Calvo, J. Cortes, J. Rodriguez, O. Fernandez-Hidalgo, J. Rebollo, S. Martin-Algarra, *et al.*, "Irinotecan, oxaliplatin, and 5-fluorouracil/leucovorin combination chemotherapy in advanced colorectal carcinoma: a phase II study," *Clin Colorectal Cancer,* vol. 2, pp. 104-10, Aug 2002.

[111] J. A. Zhang, T. Xuan, M. Parmar, L. Ma, S. Ugwu, S. Ali, *et al.*, "Development and characterization of a novel liposome-based formulation of SN-38," *International Journal of Pharmaceutics,* vol. 270, pp. 93-107, Feb 11 2004.

[112] T. Xuan, J. A. Zhang, and I. Ahmad, "HPLC method for determination of SN-38 content and SN-38 entrapment efficiency in a novel liposome-based formulation, LE-SN38," *Journal of Pharmaceutical and Biomedical Analysis,* vol. 41, pp. 582-588, May 3 2006.

[113] P. Tobin, S. Clarke, J. P. Seale, S. Lee, M. Solomon, S. Aulds, *et al.*, "The in vitro metabolism of irinotecan (CPT-11) by carboxylesterase and beta-glucuronidase in human colorectal tumours," *Br J Clin Pharmacol,* vol. 62, pp. 122-9, Jul 2006.

[114] S. J. Chen, M. F. Yueh, C. Bigo, O. Barbier, K. P. Wang, M. Karin, *et al.*, "Intestinal glucuronidation protects against chemotherapy-induced toxicity by irinotecan (CPT-11)," *Proceedings of the National Academy of Sciences of the United States of America,* vol. 110, pp. 19143-19148, Nov 19 2013.

[115] J. Williams, R. Lansdown, R. Sweitzer, M. Romanowski, R. LaBell, R. Ramaswami, *et al.*, "Nanoparticle drug delivery system for intravenous delivery of topoisomerase inhibitors," *Journal of Controlled Release,* vol. 91, pp. 167-172, Aug 28 2003.

[116] S. Frese and B. Diamond, "Structural modification of DNA--a therapeutic option in SLE?," *Nat Rev Rheumatol,* vol. 7, pp. 733-8, Dec 2011.

[117] K. R. Duan, X. L. Zhang, X. X. Tang, J. H. Yu, S. Y. Liu, D. X. Wang, *et al.*, "Fabrication of cationic nanomicelle from chitosan-graft-polycaprolactone as the carrier of 7-ethyl-10-hydroxy-camptothecin," *Colloids and Surfaces B-Biointerfaces,* vol. 76, pp. 475-482, Apr 1 2010.

[118] C. Manaspon, S. Hongeng, A. Boongird, and N. Nasongkla, "Preparation and in vitro characterization of SN-38-loaded, self-forming polymeric depots as an injectable drug delivery system," *Journal of Pharmaceutical Sciences,* vol. 101, pp. 3708-3717, Oct 2012.

[119] X. X. Yang, Z. P. Hu, S. Y. Chan, B. C. Goh, W. Duan, E. Chan, *et al.*, "Simultaneous determination of the lactone and carboxylate forms of irinotecan (CPT-11) and its active metabolite SN-38 by high-performance liquid chromatography: Application to plasma pharmacokinetic studies in the rat," *Journal of Chromatography B-Analytical Technologies in the Biomedical and Life Sciences,* vol. 821, pp. 221-228, Jul 25 2005.

[120] M. N. Tallman, J. K. Ritter, and P. C. Smith, "Differential rates of glucuronidation for 7-ethyl-10-hydroxy-camptothecin (SN-38) lactone and carboxylate in human and rat microsomes and recombinant UDP-glucuronosyltransferase isoforms," *Drug Metabolism and Disposition,* vol. 33, pp. 977-983, Jul 2005.

[121] Z. H. Mi and T. G. Burke, "Differential Interactions of Camptothecin Lactone and Carboxylate Forms with Human Blood Components," *Biochemistry,* vol. 33, pp. 10325-10336, Aug 30 1994.

[122] F. Meyer-Losic, C. Nicolazzi, J. Quinonero, F. Ribes, M. Michel, V. Dubois, *et al.*, "DTS-108, a novel peptidic prodrug of SN38: In vivo efficacy and toxicokinetic studies," *Clinical Cancer Research,* vol. 14, pp. 2145-2153, Apr 1 2008.

[123] H. Zhao, B. Rubio, P. Sapra, D. C. Wu, P. Reddy, P. Sai, *et al.*, "Novel prodrugs of SN38 using multiarm poly(ethylene glycol) linkers," *Bioconjugate Chemistry,* vol. 19, pp. 849-859, Apr 2008.

[124] Q. R. Gu, J. Z. Xing, M. Huang, C. He, and J. Chen, "SN-38 loaded polymeric micelles to enhance cancer therapy," *Nanotechnology,* vol. 23, May 25 2012.

[125] R. B. Kolhatkar, P. Swaan, and H. Ghandehari, "Potential oral delivery of 7-Ethyl-10-hydroxy-camptothecin (SN-38) using poly(amidoamine) dendrimers," *Pharmaceutical Research,* vol. 25, pp. 1723-1729, Jul 2008.

[126] H. W. Wang, T. B. Shrestha, M. T. Basel, R. K. Dani, G. M. Seo, S. Balivada, *et al.*, "Magnetic-Fe/Fe3O4-nanoparticle-bound SN38 as carboxylesterase-cleavable prodrug for the delivery to tumors within monocytes/macrophages," *Beilstein Journal of Nanotechnology,* vol. 3, pp. 444-455, Jun 13 2012.

[127] Y. Sadzuka, H. Takabe, and T. Sonobe, "Liposomalization of SN-38 as active metabolite of CPT-11," *Journal of Controlled Release,* vol. 108, pp. 453-459, Nov 28 2005.

[128] P. Ebrahimnejad, R. Dinarvand, M. R. Jafari, S. A. S. Tabasi, and F. Atyabi, "Characterization, blood profile and biodistribution properties of surface modified PLGA nanoparticles of SN-38," *International Journal of Pharmaceutics,* vol. 406, pp. 122-127, Mar 15 2011.

[129] D. Papahadjopoulos and N. Miller, "Phospholipid model membranes. I. Structural characteristics of hydrated liquid crystals," *Biochim Biophys Acta,* vol. 135, pp. 624-38, Sep 9 1967.

[130] A. D. Bangham, M. M. Standish, and J. C. Watkins, "Diffusion of univalent ions across the lamellae of swollen phospholipids," *J Mol Biol,* vol. 13, pp. 238-52, Aug 1965.

[131] A. Jesorka and O. Orwar, "Liposomes: Technologies and Analytical Applications," *Annual Review of Analytical Chemistry,* vol. 1, pp. 801-832, 2008.

[132] Y. Rahimpour and H. Hamishehkar, "Liposomes in cosmeceutics," *Expert Opinion on Drug Delivery,* vol. 9, pp. 443-455, Apr 2012.

[133] N. Mitchell, T. L. Kalber, M. S. Cooper, K. Sunassee, S. L. Chalker, K. P. Shaw, *et al.*, "Incorporation of paramagnetic, fluorescent and PET/SPECT contrast agents into liposomes for multimodal imaging," *Biomaterials,* vol. 34, pp. 1179-1192, Jan 2013.

[134] G. Mikhaylov, U. Mikac, A. A. Magaeva, V. I. Itin, E. P. Naiden, I. Psakhye, *et al.*, "Ferri-liposomes as an MRI-visible drug-delivery system for targeting tumours and their microenvironment," *Nature Nanotechnology,* vol. 6, pp. 594-602, Sep 2011.

[135] K. Ma, H. J. Shen, S. Shen, M. Xie, C. B. Mao, L. Y. Qiu, *et al.*, "Development of a successive targeting liposome with multi-ligand for efficient targeting gene delivery," *Journal of Gene Medicine,* vol. 13, pp. 290-301, May 2011.

[136] X. Yun, V. D. Maximov, J. Yu, H. Zhu, A. A. Vertegel, and M. S. Kindy, "Nanoparticles for targeted delivery of antioxidant enzymes to the brain after cerebral ischemia and reperfusion injury," *Journal of Cerebral Blood Flow and Metabolism,* vol. 33, pp. 583-592, Apr 2013.

[137] S. Channarong, W. Chaicumpa, N. Sinchaipanid, and A. Mitrevej, "Development and Evaluation of Chitosan-Coated Liposomes for Oral DNA Vaccine: The Improvement of Peyer's Patch Targeting Using a Polyplex-Loaded Liposomes," *Aaps Pharmscitech,* vol. 12, pp. 192-200, Mar 2011.

[138] E. Afergan, M. Ben David, H. Epstein, N. Koroukhov, D. Gilhar, K. Rohekar, *et al.*, "Liposomal Simvastatin Attenuates Neointimal Hyperplasia in Rats," *Aaps Journal,* vol. 12, pp. 181-187, Jun 2010.

[139] R. R. Sawant and V. P. Torchilin, "Liposomes as 'smart' pharmaceutical nanocarriers," *Soft Matter,* vol. 6, pp. 4026-4044, 2010.

[140] M. L. Immordino, F. Dosio, and L. Cattel, "Stealth liposomes: review of the basic science, rationale, and clinical applications, existing and potential," *International Journal of Nanomedicine,* vol. 1, pp. 297-315, 2006.

[141] T. L. Andresen, S. S. Jensen, and K. Jorgensen, "Advanced strategies in liposomal cancer therapy: Problems and prospects of active and tumor specific drug release," *Progress in Lipid Research,* vol. 44, pp. 68-97, Jan 2005.

[142] J. P. Wang and G. H. Huang, "Preparation of itraconazole-loaded liposomes coated by carboxymethyl chitosan and its pharmacokinetics and tissue distribution," *Drug Delivery,* vol. 18, pp. 631-638, Nov 2011.

[143] A. Kocer, "Functional liposomal membranes for triggered release," *Methods Mol Biol,* vol. 605, pp. 243-55, 2010.

[144] H. Takahama, T. Minamino, H. Asanuma, M. Fujita, T. Asai, M. Wakeno, *et al.*, "Prolonged Targeting of Ischemic/Reperfused Myocardium by Liposomal Adenosine Augments Cardioprotection in Rats," *Journal of the American College of Cardiology,* vol. 53, pp. 709-717, Feb 24 2009.

[145] W. T. Al-Jamal and K. Kostarelos, "Liposomes: From a Clinically Established Drug Delivery System to a Nanoparticle Platform for Theranostic Nanomedicine," *Accounts of Chemical Research,* vol. 44, pp. 1094-1104, Oct 2011.

[146] A. V. Yadav, M. S. Murthy, A. S. Shete, and S. Sakhare, "Stability Aspects of Liposomes," *Indian Journal of Pharmaceutical Education and Research,* vol. 45, pp. 402-413, Oct-Dec 2011.

[147] S. Y. Yang, Y. Zheng, J. Y. Chen, Q. Y. Zhang, D. Zhao, D. E. Han, *et al.*, "Comprehensive study of cationic liposomes composed of DC-Chol and cholesterol with different mole ratios for gene transfection," *Colloids and Surfaces B-Biointerfaces,* vol. 101, pp. 6-13, Jan 1 2013.

[148] D. Papahadjopoulos, S. Nir, and S. Oki, "Permeability properties of phospholipid membranes: effect of cholesterol and temperature," *Biochim Biophys Acta,* vol. 266, pp. 561-83, Jun 20 1972.

[149] P. Rivera Gil and W. J. Parak, "Composite Nanoparticles Take Aim at Cancer," *Acs Nano,* vol. 2, pp. 2200-2205, Nov 2008.

[150] K. Maruyama, "PEG-immunoliposome," *Bioscience Reports,* vol. 22, pp. 251-266, Apr 2002.

[151] K. Maruyama, T. Takizawa, N. Takahashi, T. Tagawa, K. Nagaike, and M. Iwatsuru, "Targeting efficiency of PEG-immunoliposome-conjugated antibodies at PEG terminals," *Advanced Drug Delivery Reviews,* vol. 24, pp. 235-242, Mar 17 1997.

[152] R. A. Sperling and W. J. Parak, "Surface modification, functionalization and bioconjugation of colloidal inorganic nanoparticles," *Therapeutic Innovation & Regulatory Science,* vol. 47, pp. 1333-1383, Jan 2013.

[153] J. Barar and Y. Omidi, "Surface modified multifunctional nanomedicines for simultaneous imaging and therapy of cancer," *Bioimpacts,* vol. 4, pp. 3-14, 2014.

[154] H. H. P. Yiu, "Engineering the multifunctional surface on magnetic nanoparticles for targeted biomedical applications: a chemical approach," *Nanomedicine,* vol. 6, pp. 1429-1446, Oct 2011.

[155] L. A. Meure, N. R. Foster, and F. Dehghani, "Conventional and dense gas techniques for the production of liposomes: a review," *AAPS PharmSciTech,* vol. 9, pp. 798-809, 2008.

[156] P. Gentine, L. Bourel-Bonnet, and B. Frisch, "Modified and derived ethanol injection toward liposomes: development of the process," *Journal of Liposome Research,* vol. 23, pp. 11-19, Mar 2013.

[157] M. R. Mozafari, C. J. Reed, C. Rostron, C. Kocum, and E. Piskin, "Construction of stable anionic liposome-plasmid particles using the heating method: A preliminary investigation," *Cellular & Molecular Biology Letters,* vol. 7, pp. 923-927, 2002.

[158] F. C. S. F. Szoka Jr., CA), "Preparation of liposome and lipid complex compositions," United States Patent, 1996.

[159] J. Jing, Y. Li, J. Liu, and S. H. Zhan, "Liposome Formation with Electroformation Method," *Progress in Chemistry,* vol. 23, pp. 2598-2606, Dec 24 2011.

[160] K. Otake, T. Imura, H. Sakai, and M. Abe, "Development of a new preparation method of liposomes using supercritical carbon dioxide," *Langmuir,* vol. 17, pp. 3898-3901, Jun 26 2001.

[161] R. Barnadas-Rodriguez and M. Sabes, "Factors involved in the production of liposomes with a high-pressure homogenizer," *International Journal of Pharmaceutics,* vol. 213, pp. 175-186, Feb 1 2001.

[162] U. Massing, S. Cicko, and V. Ziroli, "Dual asymmetric centrifugation (DAC) - A new technique for liposome preparation," *Journal of Controlled Release,* vol. 125, pp. 16-24, Jan 4 2008.

[163] T. Wang, Y. J. Deng, Y. H. Geng, Z. B. Gao, H. P. Zou, and Z. Z. Wang, "Preparation of submicron unilamellar liposomes by freeze-drying double emulsions," *Biochimica Et Biophysica Acta-Biomembranes,* vol. 1758, pp. 222-231, Feb 2006.

[164] A. P. Costa, X. M. Xu, and D. J. Burgess, "Freeze-Anneal-Thaw Cycling of Unilamellar Liposomes: Effect on Encapsulation Efficiency," *Pharmaceutical Research,* vol. 31, pp. 97-103, Jan 2014.

[165] R. R. Hood, D. L. DeVoe, J. Atencia, W. N. Vreeland, and D. M. Omiatek, "A facile route to the synthesis of monodisperse nanoscale liposomes using 3D microfluidic hydrodynamic focusing in a concentric capillary array," *Lab on a Chip,* vol. 14, pp. 2403-2409, 2014.

[166] B. Maherani, E. Arab-Tehrany, M. R. Mozafari, C. Gaiani, and M. Linder, "Liposomes: A Review of Manufacturing Techniques and Targeting Strategies," *Current Nanoscience,* vol. 7, pp. 436-452, Jun 2011.

[167] E. Hernandez-Zapata, L. Martinez-Balbuena, and I. Santamaria-Holek, "Thermodynamics and Dynamics of the Formation of Spherical Lipid Vesicles," *Biophysical Journal,* vol. 98, pp. 481a-481a, Jan 2010.

[168] Sávia Caldeira de Araújo Lopes, Cristiane dos Santos Giuberti, Talita Guieiro Ribeiro Rocha, Diêgo dos Santos Ferreira, Elaine Amaral Leite, and M. C. Oliveira, "Liposomes as Carriers of Anticancer Drugs," in *Cancer Treatment - Conventional and Innovative Approaches*, L. Rangel, Ed., ed: InTech, 2013.

[169] A. Mahapatro and D. K. Singh, "Biodegradable nanoparticles are excellent vehicle for site directed in-vivo delivery of drugs and vaccines," *Journal of Nanobiotechnology,* vol. 9, Nov 28 2011.

[170] D. C. Drummond, C. O. Noble, M. E. Hayes, J. W. Park, and D. B. Kirpotin, "Pharmacokinetics and In Vivo Drug Release Rates in Liposomal Nanocarrier Development," *Journal of Pharmaceutical Sciences,* vol. 97, pp. 4696-4740, Nov 2008.

[171] S. Sur, A. C. Fries, K. W. Kinzler, S. B. Zhou, and B. Vogelstein, "Remote loading of preencapsulated drugs into stealth liposomes," *Proceedings of the National Academy of Sciences of the United States of America,* vol. 111, pp. 2283-2288, Feb 11 2014.

[172] A. Fritze, F. Hens, A. Kimpfler, R. Schubert, and R. Peschka-Suss, "Remote loading of doxorubicin into liposomes driven by a transmembrane phosphate gradient," *Biochimica Et Biophysica Acta-Biomembranes,* vol. 1758, pp. 1633-1640, Oct 2006.

[173] G. Haran, R. Cohen, L. K. Bar, and Y. Barenholz, "Transmembrane Ammonium-Sulfate Gradients in Liposomes Produce Efficient and Stable Entrapment of Amphipathic Weak Bases (Vol 1151, Pg 201, 1993)," *Biochimica Et Biophysica Acta-Biomembranes,* vol. 1190, pp. 197-197, Feb 23 1994.

[174] J. Gubernator, G. Chwastek, M. Korycinska, M. Stasiuk, G. Grynkiewicz, F. Lewrick, *et al.*, "The encapsulation of idarubicin within liposomes using the novel EDTA ion gradient

method ensures improved drug retention in vitro and in vivo," *Journal of Controlled Release,* vol. 146, pp. 68-75, Aug 17 2010.

[175] P. G. Tardi, N. L. Boman, and P. R. Cullis, "Liposomal doxorubicin," *Journal of Drug Targeting,* vol. 4, pp. 129-140, 1996.

[176] M. J. W. Johnston, S. C. Semple, S. K. Klimuk, K. Edwards, M. L. Eisenhardt, E. C. Leng*, et al.,* "Therapeutically optimized rates of drug release can be achieved by varying the drug-to-lipid ratio in liposomal vincristine formulations," *Biochimica Et Biophysica Acta-Biomembranes,* vol. 1758, pp. 55-64, Jan 2006.

[177] M. J. W. Johnston, K. Edwards, G. Karlsson, and P. R. Cullis, "Influence of drug-to-lipid ratio on drug release properties and liposome integrity in liposomal doxorubicin formulations," *Journal of Liposome Research,* vol. 18, pp. 145-157, 2008.

[178] V. Panel, P. Y. Boelle, J. Ayala-Sanmartin, A. M. Jouniaux, R. Hamelin, J. Masliah*, et al.,* "Cytoplasmic phospholipase A2 expression in human colon adenocarcinoma is correlated with cyclooxygenase-2 expression and contributes to prostaglandin E2 production," *Cancer Letters,* vol. 243, pp. 255-263, Nov 18 2006.

[179] K. Jorgensen, J. Davidsen, and O. G. Mouritsen, "Biophysical mechanisms of phospholipase A2 activation and their use in liposome-based drug delivery," *Febs Letters,* vol. 531, pp. 23-27, Oct 30 2002.

[180] A. Schroeder, J. Kost, and Y. Barenholz, "Ultrasound, liposomes, and drug delivery: principles for using ultrasound to control the release of drugs from liposomes," *Chemistry and Physics of Lipids,* vol. 162, pp. 1-16, Nov 2009.

[181] A. Schroeder, Y. Avnir, S. Weisman, Y. Najajreh, A. Gabizon, Y. Talmon*, et al.,* "Controlling liposomal drug release with low frequency ultrasound: Mechanism and feasibility," *Langmuir,* vol. 23, pp. 4019-4025, Mar 27 2007.

[182] S. Naahidi, M. Jafari, F. Edalat, K. Raymond, A. Khademhosseini, and P. Chen, "Biocompatibility of engineered nanoparticles for drug delivery," *Journal of Controlled Release,* vol. 166, pp. 182-194, Mar 10 2013.

[183] M. T. Zhu, G. J. Nie, H. Meng, T. Xia, A. Nel, and Y. L. Zhao, "Physicochemical Properties Determine Nanomaterial Cellular Uptake, Transport, and Fate," *Accounts of Chemical Research,* vol. 46, pp. 622-631, Mar 19 2013.

[184] T. Boulikas, "Clinical overview on Lipoplatin (TM): a successful liposomal formulation of cisplatin," *Expert Opinion on Investigational Drugs,* vol. 18, pp. 1197-1218, Aug 2009.

[185] J. Rejman, V. Oberle, I. S. Zuhorn, and D. Hoekstra, "Size-dependent internalization of particles via the pathways of clathrin- and caveolae-mediated endocytosis," *Biochem J,* vol. 377, pp. 159-69, Jan 1 2004.

[186] T. Osaka, T. Nakanishi, S. Shanmugam, S. Takahama, and H. Zhang, "Effect of surface charge of magnetite nanoparticles on their internalization into breast cancer and umbilical vein endothelial cells," *Colloids and Surfaces B-Biointerfaces,* vol. 71, pp. 325-330, Jul 1 2009.

[187] M. Marquez, S. Nilsson, L. Lennartsson, Z. X. Liu, T. Tammela, M. Raitanen, *et al.*, "Charge-dependent targeting: Results in six tumor cell lines," *Anticancer Research,* vol. 24, pp. 1347-1351, May-Jun 2004.

[188] D. W. Hoskin and A. Ramamoorthy, "Studies on anticancer activities of antimicrobial peptides," *Biochimica Et Biophysica Acta-Biomembranes,* vol. 1778, pp. 357-375, Feb 2008.

[189] B. E. Garcia-Perez, J. C. Hernandez-Gonzalez, S. Garcia-Nieto, and J. Luna-Herrera, "Internalization of a non-pathogenic mycobacteria by macropinocytosis in human alveolar epithelial A549 cells," *Microbial Pathogenesis,* vol. 45, pp. 1-6, Jul 2008.

[190] B. E. Garcia-Perez, J. J. De la Cruz-Lopez, J. I. Castaneda-Sanchez, A. R. Munoz-Duarte, A. D. Hernandez-Perez, H. Villegas-Castrejon, *et al.*, "Macropinocytosis is responsible for the uptake of pathogenic and non-pathogenic mycobacteria by B lymphocytes (Raji cells)," *Bmc Microbiology,* vol. 12, Oct 31 2012.

[191] H. X. Li and L. J. Rothberg, "Label-free colorimetric detection of specific sequences in genomic DNA amplified by the polymerase chain reaction," *Journal of the American Chemical Society,* vol. 126, pp. 10958-10961, Sep 8 2004.

[192] E. R. Goldman, E. D. Balighian, H. Mattoussi, M. K. Kuno, J. M. Mauro, P. T. Tran, *et al.*, "Avidin: A natural bridge for quantum dot-antibody conjugates," *Journal of the American Chemical Society,* vol. 124, pp. 6378-6382, Jun 5 2002.

[193] L. Davalos-Pantoja, J. L. Ortega-Vinuesa, D. Bastos-Gonzalez, and R. Hidalgo-Alvarez, "Colloidal stability of IgG- and IgY-coated latex microspheres," *Colloids and Surfaces B-Biointerfaces,* vol. 20, pp. 165-175, Feb 2001.

[194] T. Tsukagoshi, Y. Kondo, and N. Yoshino, "Protein adsorption on polymer-modified silica particle surface," *Colloids and Surfaces B-Biointerfaces,* vol. 54, pp. 101-107, Jan 15 2007.

[195] G. T. Hermanson, *Bioconjugate techniques*, 2th ed. Amsterdam, Boston: Elsevier Academic Press, 2008.

[196] L. Chen, "Surface Functionalization and Bioconjugation of Nanoparticles for Biomedical Applications," Ph.D. Thesis, The School of Graduate and Postdoctoral Studies, The University of Western Ontario, London, Ontario, Canada, 2013.

[197] K. A. Whitehead, R. Langer, and D. G. Anderson, "Knocking down barriers: advances in siRNA delivery," *Nat Rev Drug Discov,* vol. 8, pp. 129-38, Feb 2009.

[198] K. C. Ho, P. J. Tsai, Y. S. Lin, and Y. C. Chen, "Using biofunctionalized nanoparticles to probe pathogenic bacteria," *Analytical Chemistry,* vol. 76, pp. 7162-7168, Dec 15 2004.

[199] M. Howarth and A. Y. Ting, "Imaging proteins in live mammalian cells with biotin ligase and monovalent streptavidin," *Nature Protocols,* vol. 3, pp. 534-545, 2008.

[200] Y. C. Li, Y. S. Lin, P. J. Tsai, C. T. Chen, W. Y. Chen, and Y. C. Chen, "Nitrilotriacetic acid-coated magnetic nanoparticles as affinity probes for enrichment of histidine-tagged proteins and phosphorylated peptides," *Analytical Chemistry,* vol. 79, pp. 7519-7525, Oct 1 2007.

[201] L. Tian, C. Shi, and J. Zhu, "Reversible formation of hybrid nanostructures via an organic linkage," *Chemical Communications*, pp. 3850-3852, 2007.

[202] W. X. Xi, T. F. Scott, C. J. Kloxin, and C. N. Bowman, "Click Chemistry in Materials Science," *Advanced Functional Materials*, vol. 24, pp. 2572-2590, May 2014.

[203] D. Danila, R. Partha, D. B. Elrod, M. Lackey, S. W. Casscells, and J. L. Conyers, "Antibody-Labeled Liposomes for CT Imaging of Atherosclerotic Plaques In Vitro Investigation of an Anti-ICAM Antibody-Labeled Liposome Containing Iohexol for Molecular Imaging of Atherosclerotic Plaques via Computed Tomography," *Texas Heart Institute Journal*, vol. 36, pp. 393-403, Oct 2009.

[204] Y. S. Sohn and Y. K. Lee, "Site-directed immobilization of antibody using EDC-NHS-activated protein A on a bimetallic-based surface plasmon resonance chip," *Journal of Biomedical Optics*, vol. 19, May 2014.

[205] S. Sam, L. Touahir, J. S. Andresa, P. Allongue, J. N. Chazalviel, A. C. Gouget-Laemmel, *et al.*, "Semiquantitative Study of the EDC/NHS Activation of Acid Terminal Groups at Modified Porous Silicon Surfaces," *Langmuir*, vol. 26, pp. 809-814, Jan 19 2010.

[206] V. R. Pattabiraman and J. W. Bode, "Rethinking amide bond synthesis," *Nature*, vol. 480, pp. 471-479, Dec 22 2011.

[207] I. Freitag, U. Neugebauer, A. Csaki, W. Fritzsche, C. Krafft, and J. Popp, "Preparation and characterization of multicore SERS labels by controlled aggregation of gold nanoparticles," *Vibrational Spectroscopy*, vol. 60, pp. 79-84, May 2012.

[208] Z. Grabarek and J. Gergely, "Zero-Length Crosslinking Procedure with the Use of Active Esters," *Analytical Biochemistry*, vol. 185, pp. 131-135, Feb 15 1990.

[209] J. V. Staros, R. W. Wright, and D. M. Swingle, "Enhancement by N-hydroxysulfosuccinimide of water-soluble carbodiimide-mediated coupling reactions," *Anal Biochem*, vol. 156, pp. 220-2, Jul 1986.

[210] S. S. Wong, D. M. Jameson, and S. S. Wong, *Chemistry of protein and nucleic acid cross-linking and conjugation*, 2nd ed. Boca Raton: Taylor & Francis/CRC Press, 2012.

[211] C. K. Joung, H. N. Kim, M. C. Lim, T. J. Jeon, H. Y. Kim, and Y. R. Kim, "A nanoporous membrane-based impedimetric immunosensor for label-free detection of pathogenic bacteria in whole milk," *Biosensors & Bioelectronics*, vol. 44, pp. 210-215, Jun 15 2013.

[212] R. Jackeray, C. K. V. Z. Abid, G. Singh, S. Jain, S. Chattopadhyaya, S. Sapra, *et al.*, "Selective capturing and detection of Salmonella typhi on polycarbonate membrane using bioconjugated quantum dots," *Talanta*, vol. 84, pp. 952-962, May 15 2011.

[213] R. L. Meyer, X. F. Zhou, L. N. Tang, A. Arpanaei, P. Kingshott, and F. Besenbacher, "Immobilisation of living bacteria for AFM imaging under physiological conditions," *Ultramicroscopy*, vol. 110, pp. 1349-1357, Oct 2010.

[214] T. W. Chang, Y. M. Lin, C. F. Wang, and Y. D. Liao, "Outer Membrane Lipoprotein Lpp Is Gram-negative Bacterial Cell Surface Receptor for Cationic Antimicrobial Peptides," *Journal of Biological Chemistry*, vol. 287, pp. 418-428, Jan 2 2012.

[215] E. Mahon, A. Salvati, F. B. Bombelli, I. Lynch, and K. A. Dawson, "Designing the nanoparticle-biomolecule interface for "targeting and therapeutic delivery"," *Journal of Controlled Release,* vol. 161, pp. 164-174, Jul 20 2012.

[216] F. Shamsipour, A. H. Zarnani, R. Ghods, M. Chamankhah, F. Forouzesh, S. Vafaei, *et al.*, "Conjugation of Monoclonal Antibodies to Super Paramagnetic Iron Oxide Nanoparticles for Detection of her2/neu Antigen on Breast Cancer Cell Lines," *Avicenna J Med Biotechnol,* vol. 1, pp. 27-31, Apr 2009.

[217] P. H. Yang, W. Wei, H. H. Cai, J. Feng, and J. Y. Cai, "Immobilization of Anti-Transferrin On Nano-Gold and Its Immune Recognition of Transferrin," *Spectroscopy and Spectral Analysis,* vol. 29, pp. 1398-1401, May 2009.

[218] H. Shang, W. S. Chang, S. Kan, S. A. Majetich, and G. U. Lee, "Synthesis and characterization of paramagnetic microparticles through emulsion-templated free radical polymerization," *Langmuir,* vol. 22, pp. 2516-2522, Mar 14 2006.

[219] M. A. Sesay, "Monoclonal antibody conjugation via chemical modification," *Biopharm International-the Applied Technologies of Biopharmaceutical Development,* vol. 16, pp. 32-39, Dec 2003.

[220] C. R. Behrens and B. Liu, "Methods for site-specific drug conjugation to antibodies," *Mabs,* vol. 6, pp. 46-53, Jan-Feb 2014.

[221] B. J. Olson and J. Markwell, "Assays for determination of protein concentration," *Curr Protoc Protein Sci,* vol. Chapter 3, p. Unit 3 4, May 2007.

[222] I. Tessmer, P. Kaur, J. G. Lin, and H. Wang, "Investigating bioconjugation by atomic force microscopy," *Journal of Nanobiotechnology,* vol. 11, Jul 15 2013.

[223] C. Alric, J. Taleb, G. Le Duc, C. Mandon, C. Billotey, A. Le Meur-Herland, *et al.*, "Gadolinium chelate coated gold nanoparticles as contrast agents for both X-ray computed tomography and magnetic resonance imaging," *Journal of the American Chemical Society,* vol. 130, pp. 5908-5915, May 7 2008.

[224] R. Boellaard, R. Delgado-Bolton, W. J. G. Oyen, F. Giammarile, K. Tatsch, W. Eschner, *et al.*, "FDG PET/CT: EANM procedure guidelines for tumour imaging: version 2.0," *European Journal of Nuclear Medicine and Molecular Imaging,* vol. 42, pp. 328-354, Feb 2015.

[225] H. Leong-Poi, J. Christiansen, A. L. Klibanov, S. Kaul, and J. R. Lindner, "Noninvasive assessment of angiogenesis by ultrasound and microbubbles targeted to alpha(v)-integrins," *Circulation,* vol. 107, pp. 455-460, Jan 28 2003.

[226] H. Harada, S. Kizaka-Kondoh, and M. Hiraoka, "Optical Imaging of Tumor Hypoxia and Evaluation of Efficacy of a Hypoxia-Targeting Drug in Living Animals," *Molecular Imaging,* vol. 4, pp. 182-193, Jul 2005.

[227] Y. Wu, W. Zhang, J. Li, and Y. Zhang, "Optical imaging of tumor microenvironment," *Am J Nucl Med Mol Imaging,* vol. 3, pp. 1-15, 2013.

[228] T. Barrett, M. Brechbiel, M. Bernardo, and P. L. Choyke, "MRI of tumor angiogenesis," *Journal of Magnetic Resonance Imaging,* vol. 26, pp. 235-249, Aug 2007.

[229] R. J. Gillies, N. Raghunand, G. S. Karczmar, and Z. M. Bhujwalla, "MRI of the tumor microenvironment," *Journal of Magnetic Resonance Imaging*, vol. 16, pp. 430-450, Oct 2002.

[230] E. M. Shapiro, S. Skrtic, K. Sharer, J. M. Hill, C. E. Dunbar, and A. P. Koretsky, "MRI detection of single particles for cellular imaging," *Proceedings of the National Academy of Sciences of the United States of America*, vol. 101, pp. 10901-10906, Jul 27 2004.

[231] J. W. M. Bulte and D. L. Kraitchman, "Iron oxide MR contrast agents for molecular and cellular imaging," *Nmr in Biomedicine*, vol. 17, pp. 484-499, Nov 2004.

[232] A. Kassner, R. E. Thornhill, F. Liu, P. M. Winter, S. D. Caruthers, S. A. Wickline, *et al.*, "Assessment of tumor angiogenesis: dynamic contrast-enhanced MRI with paramagnetic nanoparticles compared with Gd-DTPA in a rabbit Vx-2 tumor model," *Contrast Media & Molecular Imaging*, vol. 5, pp. 155-161, May-Jun 2010.

[233] R. Folberg, M. J. C. Hendrix, and A. J. Maniotis, "Vasculogenic mimicry and tumor angiogenesis," *American Journal of Pathology*, vol. 156, pp. 361-381, Feb 2000.

[234] T. F. Massoud and S. S. Gambhir, "Molecular imaging in living subjects: seeing fundamental biological processes in a new light," *Genes & Development*, vol. 17, pp. 545-580, Mar 1 2003.

[235] T. Wittlinger, I. Martinovic, A. Moritz, and S. Romanzetti, "Evaluation of the spatial resolution with 1.5-4 tesla in a stenosis model," *Asian Cardiovasc Thorac Ann*, vol. 14, pp. 387-93, Oct 2006.

[236] J. F. A. Jansen, H. Schoder, N. Y. Lee, Y. Wang, D. G. Pfister, M. G. Fury, *et al.*, "Noninvasive Assessment of Tumor Microenvironment Using Dynamic Contrast-Enhanced Magnetic Resonance Imaging and (18)F-Fluoromisonidazole Positron Emission Tomography Imaging in Neck Nodal Metastases," *International Journal of Radiation Oncology Biology Physics*, vol. 77, pp. 1403-1410, Aug 1 2010.

[237] C. J. G. Bakker, R. Bhagwandien, M. A. Moerland, and L. M. P. Ramos, "Simulation of Susceptibility Artifacts in 2d and 3d Fourier-Transform Spin-Echo and Gradient-Echo Magnetic-Resonance-Imaging," *Magnetic Resonance Imaging*, vol. 12, pp. 767-774, 1994.

[238] J. R. Reichenbach, R. Venkatesan, D. A. Yablonskiy, M. R. Thompson, S. Lai, and E. M. Haacke, "Theory and application of static field inhomogeneity effects in gradient-echo imaging," *Jmri-Journal of Magnetic Resonance Imaging*, vol. 7, pp. 266-279, Mar-Apr 1997.

[239] M. K. Yu, Y. Y. Jeong, J. Park, S. Park, J. W. Kim, J. J. Min, *et al.*, "Drug-loaded superparamagnetic iron oxide nanoparticles for combined cancer imaging and therapy in vivo," *Angewandte Chemie-International Edition*, vol. 47, pp. 5362-5365, 2008.

[240] S. C. McBain, H. H. P. Yiu, and J. Dobson, "Magnetic nanoparticles for gene and drug delivery," *International Journal of Nanomedicine*, vol. 3, pp. 169-180, 2008.

[241] C. L. Dennis, A. J. Jackson, J. A. Borchers, R. Ivkov, A. R. Foreman, P. J. Hoopes, *et al.*, "The influence of magnetic and physiological behaviour on the effectiveness of iron oxide

nanoparticles for hyperthermia," *Journal of Physics D-Applied Physics,* vol. 41, Jul 7 2008.

[242] T. Allkemper, C. Bremer, L. Matuszewski, W. Ebert, and P. Reimer, "Contrast-enhanced blood-pool MR angiography with optimized iron oxides: Effect of size and dose on vascular contrast enhancement in rabbits," *Radiology,* vol. 223, pp. 432-438, May 2002.

[243] S. Kinner, S. Maderwald, N. Parohl, J. Albert, C. Corot, P. Robert, *et al.,* "Contrast-Enhanced Magnetic Resonance Angiography in Rabbits Evaluation of the Gadolinium-Based Agent P846 and the Iron-Based Blood Pool Agent P904 in Comparison With Gadoterate Meglumine," *Investigative Radiology,* vol. 46, pp. 524-529, Aug 2011.

[244] V. Demas and T. J. Lowery, "Magnetic resonance for in vitro medical diagnostics: superparamagnetic nanoparticle-based magnetic relaxation switches," *New Journal of Physics,* vol. 13, Feb 4 2011.

[245] A. G. Kolhatkar, A. C. Jamison, D. Litvinov, R. C. Willson, and T. R. Lee, "Tuning the magnetic properties of nanoparticles," *Int J Mol Sci,* vol. 14, pp. 15977-6009, 2013.

[246] M. M. Lin, D. K. Kim, A. J. El Haj, and J. Dobson, "Development of Superparamagnetic Iron Oxide Nanoparticles (SPIONS) for Translation to Clinical Applications," *Ieee Transactions on Nanobioscience,* vol. 7, pp. 298-305, Dec 2008.

[247] M. Mahmoudi, S. Sant, B. Wang, S. Laurent, and T. Sen, "Superparamagnetic iron oxide nanoparticles (SPIONs): Development, surface modification and applications in chemotherapy," *Advanced Drug Delivery Reviews,* vol. 63, pp. 24-46, Jan-Feb 2011.

[248] M. A. Sieber, H. Pietsch, J. Walter, W. Haider, T. Frenzel, and H. J. Weinmann, "A preclinical study to investigate the development of nephrogenic systemic fibrosis: A possible role for gadolinium-based contrast media," *Investigative Radiology,* vol. 43, pp. 65-75, Jan 2008.

[249] M. A. Sieber, T. Steger-Hartmann, P. Lengsfeld, and H. Pietsch, "Gadolinium-Based Contrast Agents and NSF: Evidence from Animal Experience," *Journal of Magnetic Resonance Imaging,* vol. 30, pp. 1268-1276, Dec 2009.

[250] T. K. Jain, M. K. Reddy, M. A. Morales, D. L. Leslie-Pelecky, and V. Labhasetwar, "Biodistribution, clearance, and biocompatibility of iron oxide magnetic nanoparticles in rats," *Mol Pharm,* vol. 5, pp. 316-27, Mar-Apr 2008.

[251] J. R. McCarthy, J. Bhaumik, M. R. Karver, S. S. Erdem, and R. Weissleder, "Targeted nanoagents for the detection of cancers," *Molecular Oncology,* vol. 4, pp. 511-528, Dec 2010.

[252] K. Tanabe, Z. Zhang, T. Ito, H. Hatta, and S. Nishimoto, "Current molecular design of intelligent drugs and imaging probes targeting tumor-specific microenvironments," *Org Biomol Chem,* vol. 5, pp. 3745-57, Dec 7 2007.

[253] P. Reimer and T. Balzer, "Ferucarbotran (Resovist): a new clinically approved RES-specific contrast agent for contrast-enhanced MRI of the liver: properties, clinical development, and applications," *European Radiology,* vol. 13, pp. 1266-1276, Jun 2003.

[254] K. Leung, "Ferumoxides," in *Molecular Imaging and Contrast Agent Database (MICAD),* ed Bethesda (MD), 2004.

[255] Y. X. J. Wang, S. M. Hussain, and G. P. Krestin, "Superparamagnetic iron oxide contrast agents: physicochemical characteristics and applications in MR imaging," *European Radiology,* vol. 11, pp. 2319-2331, 2001.

[256] S. Patil, D. Jirak, F. Saudek, M. Hajek, and K. Scheffler, "Positive contrast visualization of SPIO-labeled pancreatic islets using echo-dephased steady-state free precession," *European Radiology,* vol. 21, pp. 214-220, Jan 2011.

[257] C. Diwoky, D. Liebmann, B. Neumayer, A. Reinisch, F. Knoll, D. Strunk, *et al.*, "Positive contrast of SPIO-labeled cells by off-resonant reconstruction of 3D radial half-echo bSSFP," *Nmr in Biomedicine,* vol. 28, pp. 79-88, Jan 2015.

[258] F. D. Knollmann, J. C. Bock, K. Rautenberg, J. Beier, W. Ebert, and R. Felix, "Differences in predominant enhancement mechanisms of superparamagnetic iron oxide and ultrasmall superparamagnetic iron oxide for contrast-enhanced portal magnetic resonance angiography - Preliminary results of an animal study original investigation," *Investigative Radiology,* vol. 33, pp. 637-643, Sep 1998.

[259] O. Felfoul, M. Mohammadi, and S. Martel, "Magnetic resonance imaging of Fe(3)O(4) nanoparticles embedded in living magnetotactic bacteria for potential use as carriers for in vivo applications," *2007 Annual International Conference of the Ieee Engineering in Medicine and Biology Society, Vols 1-16,* pp. 1463-1466, 2007.

[260] L. K. Griffeth, "Use of PET/CT scanning in cancer patients: technical and practical considerations," *Proc (Bayl Univ Med Cent),* vol. 18, pp. 321-330, 2005.

[261] T. C. Kwee, S. Basu, B. Saboury, V. Ambrosini, D. A. Torigian, and A. Alavi, "A new dimension of FDG-PET interpretation: assessment of tumor biology," *European Journal of Nuclear Medicine and Molecular Imaging,* vol. 38, pp. 1158-1170, Jun 2011.

[262] I. N. Fleming, R. Manavaki, P. J. Blower, C. West, K. J. Williams, A. L. Harris, *et al.*, "Imaging tumour hypoxia with positron emission tomography," *British Journal of Cancer,* vol. 112, pp. 238-250, Jan 20 2015.

[263] F. Dehdashti, R. Laforest, F. Gao, K. I. Shoghi, R. L. Aft, B. Nussenbaum, *et al.*, "Assessment of Cellular Proliferation in Tumors by PET Using F-18-ISO-1," *Journal of Nuclear Medicine,* vol. 54, pp. 350-357, Mar 1 2013.

[264] M. D. Farwell, D. A. Pryma, and D. A. Mankoff, "PET/CT Imaging in Cancer: Current Applications and Future Directions," *Cancer,* vol. 120, pp. 3433-3445, Nov 15 2014.

[265] D. M. McDonald and P. L. Choyke, "Imaging of angiogenesis: from microscope to clinic," *Nature Medicine,* vol. 9, pp. 713-725, Jun 2003.

[266] I. Iordanescu, C. Becker, B. Zetter, P. Dunning, and G. A. Taylor, "Tumor vascularity: Evaluation in a murine model with contrast-enhanced color Doppler US - Effect of angiogenesis inhibitors," *Radiology,* vol. 222, pp. 460-467, Feb 2002.

[267] S. L. Bacharach and S. K. Sundaram, "F-18-FDG in cardiology and oncology: The bitter with the sweet," *Journal of Nuclear Medicine,* vol. 43, pp. 1542-1544, Nov 2002.

[268] H. Kobayashi, N. Sato, A. Hiraga, T. Saga, Y. Nakamoto, H. Ueda, *et al.*, "3D-micro-MR angiography of mice using macromolecular MR contrast agents with polyamidoamine

dendrimer core with reference to their pharmacokinetic properties," *Magnetic Resonance in Medicine,* vol. 45, pp. 454-460, Mar 2001.

[269] R. Savai, A. C. Langheinrich, R. T. Schermuly, S. S. Pullamsetti, R. Dumitrascu, H. Traupe, *et al.*, "Evaluation of Angiogenesis Using Micro-Computed Tomography in a Xenograft Mouse Model of Lung Cancer," *Neoplasia,* vol. 11, pp. 48-56, Jan 2009.

[270] C. A. Berrios-Otero, Y. Z. Wadghiri, B. J. Nieman, A. L. Joyner, and D. H. Turnbull, "Three-dimensional micro-MRI analysis of cerebral artery development in mouse embryos," *Magn Reson Med,* vol. 62, pp. 1431-9, Dec 2009.

[271] Y. T. Chen, H. L. Sun, J. H. Luo, J. Y. Ni, D. Chen, X. Y. Jiang, *et al.*, "Interventional digital subtraction angiography for small bowel gastrointestinal stromal tumors with bleeding," *World Journal of Gastroenterology,* vol. 20, pp. 17955-17961, Dec 21 2014.

[272] P. J. Nederkoorn, Y. van der Graaf, and M. Hunink, "Duplex ultrasound and magnetic resonance angiography compared with digital subtraction angiography in carotid artery stenosis - A systematic review," *Stroke,* vol. 34, pp. 1324-1331, May 2003.

[273] H. K. Pannu, R. E. Thompson, J. Phelps, C. A. Magee, and E. K. Fishman, "Optimal contrast agents for vascular imaging on computed tomography: iodixanol versus iohexol," *Acad Radiol,* vol. 12, pp. 576-84, May 2005.

[274] M. Bache, M. Kappler, H. M. Said, A. Staab, and D. Vordermark, "Detection and specific targeting of hypoxic regions within solid tumors: Current preclinical and clinical strategies," *Current Medicinal Chemistry,* vol. 15, pp. 322-338, Feb 2008.

[275] A. S. E. Ljungkvist, J. Bussink, J. H. A. M. Kaanders, and A. J. Van der Kogel, "Dynamics of tumor hypoxia measured with bioreductive hypoxic cell markers," *Radiation Research,* vol. 167, pp. 127-145, Feb 2007.

[276] X. L. Sun, G. Niu, N. Chan, B. Z. Shen, and X. Y. Chen, "Tumor Hypoxia Imaging," *Molecular Imaging and Biology,* vol. 13, pp. 399-410, Jun 2011.

[277] H. Lyng, K. Sundfor, and E. K. Rofstad, "Oxygen tension in human tumours measured with polarographic needle electrodes and its relationship to vascular density, necrosis and hypoxia," *Radiotherapy and Oncology,* vol. 44, pp. 163-169, Aug 1997.

[278] J. A. Raleigh, S. C. Chou, G. E. Arteel, and M. R. Horsman, "Comparisons among pimonidazole binding, oxygen electrode measurements, and radiation response in C3H mouse tumors," *Radiation Research,* vol. 151, pp. 580-589, May 1999.

[279] S. Davda and T. Bezabeh, "Advances in methods for assessing tumor hypoxia in vivo: Implications for treatment planning," *Cancer and Metastasis Reviews,* vol. 25, pp. 469-480, Sep 2006.

[280] D. Saha, H. Dunn, H. L. Zhou, H. Harada, M. Hiraoka, R. P. Mason, *et al.*, "In vivo Bioluminescence Imaging of Tumor Hypoxia Dynamics of Breast Cancer Brain Metastasis in a Mouse Model," *Jove-Journal of Visualized Experiments,* Oct 2011.

[281] S. A. Vinogradov, P. Grosul, V. Rozhkov, I. Dunphy, L. Shuman, B. W. Dugan, *et al.*, "Oxygen distributions in tissue measured by phosphorescence quenching," *Oxygen Transport to Tissue Volume Xxiii,* vol. 510, pp. 181-185, 2003.

[282] T. W. H. Meijer, J. H. A. M. Kaanders, P. N. Span, and J. Bussink, "Targeting Hypoxia, HIF-1, and Tumor Glucose Metabolism to Improve Radiotherapy Efficacy," *Clinical Cancer Research,* vol. 18, pp. 5585-5594, Oct 15 2012.

[283] B. F. Jordan, J. Magat, F. Colliez, E. Ozel, A. C. Fruytier, V. Marchand, *et al.*, "Mapping of oxygen by imaging lipids relaxation enhancement: a potential sensitive endogenous MRI contrast to map variations in tissue oxygenation," *Magn Reson Med,* vol. 70, pp. 732-44, Sep 2013.

[284] S. H. Crayton and A. Tsourkas, "pH-Titratable Superparamagnetic Iron Oxide for Improved Nanoparticle Accumulation in Acidic Tumor Microenvironments," *Acs Nano,* vol. 5, pp. 9592-9601, Dec 2011.

[285] H. J. Cho, E. Ackerstaff, S. Carlin, M. E. Lupu, Y. Wang, A. Rizwan, *et al.*, "Noninvasive Multimodality Imaging of the Tumor Microenvironment: Registered Dynamic Magnetic Resonance Imaging and Positron Emission Tomography Studies of a Preclinical Tumor Model of Tumor Hypoxia," *Neoplasia,* vol. 11, pp. 247-U45, Mar 2009.

[286] R. R. Hallac, H. L. Zhou, R. Pidikiti, K. Song, S. Stojadinovic, D. W. Zhao, *et al.*, "Correlations of Noninvasive BOLD and TOLD MRI with pO(2) and Relevance to Tumor Radiation Response," *Magnetic Resonance in Medicine,* vol. 71, pp. 1863-1873, May 2014.

[287] J. P. B. O'Connor, J. H. Naish, G. J. M. Parker, J. C. Waterton, Y. Watson, G. C. Jayson, *et al.*, "Preliminary Study of Oxygen-Enhanced Longitudinal Relaxation in Mri: A Potential Novel Biomarker of Oxygenation Changes in Solid Tumors," *International Journal of Radiation Oncology Biology Physics,* vol. 75, pp. 1209-1215, Nov 15 2009.

[288] F. A. Howe, S. P. Robinson, D. J. O. McIntyre, M. Stubbs, and J. R. Griffiths, "Issues in flow and oxygenation dependent contrast (FLOOD) imaging of tumours," *Nmr in Biomedicine,* vol. 14, pp. 497-506, Nov-Dec 2001.

[289] J. D. Winter, M. K. Akens, and H. L. M. Cheng, "Quantitative MRI assessment of VX2 tumour oxygenation changes in response to hyperoxia and hypercapnia," *Physics in Medicine and Biology,* vol. 56, pp. 1225-1242, Mar 7 2011.

[290] R. P. Mason, H. Shukla, and P. P. Antich, "Invivo Oxygen-Tension and Temperature - Simultaneous Determination Using F-19 Nmr-Spectroscopy of Perfluorocarbon," *Magnetic Resonance in Medicine,* vol. 29, pp. 296-302, Mar 1993.

[291] J. X. Yu, V. D. Kodibagkar, W. Cui, and R. P. Mason, "19F: a versatile reporter for non-invasive physiology and pharmacology using magnetic resonance," *Curr Med Chem,* vol. 12, pp. 819-48, 2005.

[292] I. V. Linnik, M. L. J. Scott, K. F. Holliday, N. Woodhouse, J. C. Waterton, J. P. B. O'Connor, *et al.*, "Noninvasive Tumor Hypoxia Measurement Using Magnetic Resonance Imaging in Murine U87 Glioma Xenografts and in Patients with Glioblastoma," *Magnetic Resonance in Medicine,* vol. 71, pp. 1854-1862, May 2014.

[293] C. C. Riedl, P. Brader, P. Zanzonico, V. Reid, Y. Woo, B. Wen, *et al.*, "Tumor hypoxia imaging in orthotopic liver tumors and peritoneal metastasis: a comparative study featuring dynamic 18F-MISO and 124I-IAZG PET in the same study cohort," *Eur J Nucl Med Mol Imaging,* vol. 35, pp. 39-46, Jan 2008.

[294] G. Komar, M. Seppanen, O. Eskola, P. Lindholm, T. J. Gronroos, S. Forsback, *et al.*, "18F-EF5: a new PET tracer for imaging hypoxia in head and neck cancer," *J Nucl Med,* vol. 49, pp. 1944-51, Dec 2008.

[295] H. Barthel, H. Wilson, D. R. Collingridge, G. Brown, S. Osman, S. K. Luthra, *et al.*, "In vivo evaluation of [18F]fluoroetanidazole as a new marker for imaging tumour hypoxia with positron emission tomography," *Br J Cancer,* vol. 90, pp. 2232-42, Jun 1 2004.

[296] J. S. Lewis, R. Laforest, F. Dehdashti, P. W. Grigsby, M. J. Welch, and B. A. Siegel, "An imaging comparison of 64Cu-ATSM and 60Cu-ATSM in cancer of the uterine cervix," *J Nucl Med,* vol. 49, pp. 1177-82, Jul 2008.

[297] J. G. Rajendran, D. C. Wilson, E. U. Conrad, L. M. Peterson, J. D. Bruckner, J. S. Rasey, *et al.*, "[F-18]FMISO and [F-18]FDG PET imaging in soft tissue sarcomas: correlation of hypoxia, metabolism and VEGF expression," *European Journal of Nuclear Medicine and Molecular Imaging,* vol. 30, pp. 695-704, May 2003.

[298] M. H. W. Starmans, D. Zips, B. G. Wouters, M. Baumann, and P. Lambin, "The use of a comprehensive tumour xenograft dataset to validate gene signatures relevant for radiation response," *Radiotherapy and Oncology,* vol. 92, pp. 417-422, Sep 2009.

[299] V. P. Torchilin, "Passive and active drug targeting: drug delivery to tumors as an example," in *Handbook of experimental pharmacology*. vol. 197, F. B. Hofmann, Ed., ed New York: Springer, 2010, pp. 3-53.

[300] D. E. Owens and N. A. Peppas, "Opsonization, biodistribution, and pharmacokinetics of polymeric nanoparticles," *International Journal of Pharmaceutics,* vol. 307, pp. 93-102, Jan 3 2006.

[301] L. Harrison and K. Blackwell, "Hypoxia and anemia: factors in decreased sensitivity to radiation therapy and chemotherapy?," *Oncologist,* vol. 9 Suppl 5, pp. 31-40, 2004.

[302] G. E. Schulz, "The structure of bacterial outer membrane proteins," *Biochimica Et Biophysica Acta-Biomembranes,* vol. 1565, pp. 308-317, Oct 11 2002.

[303] J. B. Sun, Y. Li, X. J. Liang, and P. C. Wang, "Bacterial Magnetosome: A Novel Biogenetic Magnetic Targeted Drug Carrier with Potential Multifunctions," *Journal of Nanomaterials,* 2011.

[304] J. Kalia and R. T. Raines, "Advances in Bioconjugation," *Current Organic Chemistry,* vol. 14, pp. 138-147, Jan 2010.

[305] M. T. Stephan, J. J. Moon, S. H. Um, A. Bershteyn, and D. J. Irvine, "Therapeutic cell engineering with surface-conjugated synthetic nanoparticles," *Nat Med,* vol. 16, pp. 1035-41, Sep 2010.

[306] C. C. Berry, "Progress in functionalization of magnetic nanoparticles for applications in biomedicine," *Journal of Physics D-Applied Physics,* vol. 42, Nov 21 2009.

[307] C. Sun, J. S. H. Lee, and M. Q. Zhang, "Magnetic nanoparticles in MR imaging and drug delivery," *Advanced Drug Delivery Reviews,* vol. 60, pp. 1252-1265, Aug 17 2008.

[308] C. Lang, D. Schuler, and D. Faivre, "Synthesis of magnetite nanoparticles for bio- and nanotechnology: Genetic engineering and biomimetics of bacterial magnetosomes," *Macromolecular Bioscience,* vol. 7, pp. 144-151, Feb 12 2007.

[309] O. Veiseh, J. W. Gunn, and M. Q. Zhang, "Design and fabrication of magnetic nanoparticles for targeted drug delivery and imaging," *Advanced Drug Delivery Reviews,* vol. 62, pp. 284-304, Mar 8 2010.

[310] R. E. Klabunde, *Cardiovascular physiology concepts*, 2nd ed. Philadelphia, PA: Lippincott Williams & Wilkins/Wolters Kluwer, 2012.

[311] W. Jiang, A. Saxena, B. Song, B. B. Ward, T. J. Beveridge, and S. C. B. Myneni, "Elucidation of functional groups on gram-positive and gram-negative bacterial surfaces using infrared spectroscopy," *Langmuir,* vol. 20, pp. 11433-11442, Dec 21 2004.

[312] T. J. Silhavy, D. Kahne, and S. Walker, "The Bacterial Cell Envelope," *Cold Spring Harbor Perspectives in Biology,* vol. 2, May 2010.

[313] O. C. Farokhzad, J. J. Cheng, B. A. Teply, I. Sherifi, S. Jon, P. W. Kantoff, *et al.*, "Targeted nanoparticle-aptamer bioconjugates for cancer chemotherapy in vivo," *Proceedings of the National Academy of Sciences of the United States of America,* vol. 103, pp. 6315-6320, Apr 18 2006.

[314] X. H. Gao, Y. Y. Cui, R. M. Levenson, L. W. K. Chung, and S. M. Nie, "In vivo cancer targeting and imaging with semiconductor quantum dots," *Nature Biotechnology,* vol. 22, pp. 969-976, Aug 2004.

[315] Y. R. Luo, *Comprehensive Handbook of Chemical Bond Energies*. Boca Raton, Florida: CRC Press, Taylor and Francis Group, 2007.

[316] H. R. Garrett and C. M. Grisham, *Biochemistry*, 5 th ed. Belmont, CA: Brooks/Cole, Cengage Learning, 2012.

[317] Y. F. Huang, Y. F. Wang, and X. P. Yan, "Amine-Functionalized Magnetic Nanoparticles for Rapid Capture and Removal of Bacterial Pathogens," *Environmental Science & Technology,* vol. 44, pp. 7908-7913, Oct 15 2010.

[318] A. T. Marttila, O. H. Laitinen, K. J. Airenne, T. Kulik, E. A. Bayer, M. Wilchek, *et al.*, "Recombinant NeutraLite Avidin: a non-glycosylated, acidic mutant of chicken avidin that exhibits high affinity for biotin and low non-specific binding properties," *Febs Letters,* vol. 467, pp. 31-36, Feb 4 2000.

[319] D. L. J. Thorek, D. R. Elias, and A. Tsourkas, "Comparative Analysis of Nanoparticle-Antibody Conjugations: Carbodiimide versus Click Chemistry," *Molecular Imaging,* vol. 8, pp. 221-229, Jul-Aug 2009.

[320] R. B. Martin, "Free energies and equilibria of peptide bond hydrolysis and formation," *Biopolymers,* vol. 45, pp. 351-353, Apr 15 1998.

[321] C. R. Miller, B. Bondurant, S. D. McLean, K. A. McGovern, and D. F. O'Brien, "Liposome-cell interactions in vitro: Effect of liposome surface charge on the binding and endocytosis of conventional and sterically stabilized liposomes," *Biochemistry,* vol. 37, pp. 12875-12883, Sep 15 1998.

[322] A. U. Andar, R. R. Hood, W. N. Vreeland, D. L. Devoe, and P. W. Swaan, "Microfluidic Preparation of Liposomes to Determine Particle Size Influence on Cellular Uptake Mechanisms," *Pharmaceutical Research,* vol. 31, pp. 401-413, Feb 2014.

[323] M. S. Martina, V. Nicolas, C. Wilhelm, C. Meenager, G. Barratt, and S. Lesieur, "The in vitro kinetics of the interactions between PEG-ylated magnetic-fluid-loaded liposomes and macrophages," *Biomaterials,* vol. 28, pp. 4143-4153, Oct 2007.

[324] D. A. Bazylinski, T. J. Williams, C. T. Lefevre, R. J. Berg, C. L. L. Zhang, S. S. Bowser, *et al.*, "Magnetococcus marinus gen. nov., sp nov., a marine, magnetotactic bacterium that represents a novel lineage (Magnetococcaceae fam. nov., Magnetococcales ord. nov.) at the base of the Alphaproteobacteria," *International Journal of Systematic and Evolutionary Microbiology,* vol. 63, pp. 801-808, Mar 2013.

[325] P. Ngamwongsatit, P. P. Banada, W. Panbangred, and A. K. Bhunia, "WST-1-based cell cytotoxicity assay as a substitute for MTT-based assay for rapid detection of toxigenic Bacillus species using CHO cell line," *Journal of Microbiological Methods,* vol. 73, pp. 211-215, Jun 2008.

[326] M. Montelius, M. Ljungberg, M. Horn, and E. Forssell-Aronsson, "Tumour size measurement in a mouse model using high resolution MRI," *Bmc Medical Imaging,* vol. 12, May 30 2012.

[327] K. W. Huang, S. Y. Yang, H. E. Horng, J. J. Chieh, H. H. Chen, C. C. Wu, *et al.*, "Time-Evolution Contrast of Target MRI Using High-Stability Antibody Functionalized Magnetic Nanoparticles: An Animal Model," *Journal of Nanomaterials,* 2014.

[328] A. Tiraferri and M. Elimelech, "Direct quantification of negatively charged functional groups on membrane surfaces," *Journal of Membrane Science,* vol. 389, pp. 499-508, Feb 1 2012.

[329] M. Thery and M. Piel, "Adhesive micropatterns for cells: a microcontact printing protocol," *Cold Spring Harb Protoc,* vol. 2009, p. pdb prot5255, Jul 2009.

[330] Y. Chen and Y. Q. Zhang, "Fluorescent quantification of amino groups on silica nanoparticle surfaces," *Analytical and Bioanalytical Chemistry,* vol. 399, pp. 2503-2509, Mar 2011.

[331] N. Q. N. Nguyen, A. Cornet, S. Blacher, S. P. Tabruyn, J. M. Foidart, A. Noel, *et al.*, "Inhibition of tumor growth and metastasis establishment by adenovirus-mediated gene transfer delivery of the antiangiogenic factor 16K hPRL," *Molecular Therapy,* vol. 15, pp. 2094-2100, Dec 2007.

[332] S. Puertas, P. Batalla, M. Moros, E. Polo, P. Del Pino, J. M. Guisan, *et al.*, "Taking advantage of unspecific interactions to produce highly active magnetic nanoparticle-antibody conjugates," *ACS Nano,* vol. 5, pp. 4521-8, Jun 28 2011.

[333] E. Amstad, S. Zurcher, A. Mashaghi, J. Y. Wong, M. Textor, and E. Reimhult, "Surface Functionalization of Single Superparamagnetic Iron Oxide Nanoparticles for Targeted Magnetic Resonance Imaging," *Small,* vol. 5, pp. 1334-1342, Jun 5 2009.

[334] C. C. Moura, M. A. Segundo, J. das Neves, S. Reis, and B. Sarmento, "Co-association of methotrexate and SPIONs into anti-CD64 antibody-conjugated PLGA nanoparticles for theranostic application," *International Journal of Nanomedicine,* vol. 9, pp. 4911-4922, 2014.

[335] A. P. Zhu, L. H. Yuan, and S. Dai, "Preparation of well-dispersed superparamagnetic iron oxide nanoparticles in aqueous solution with biocompatible N-succinyl-O-carboxymethylchitosan," *Journal of Physical Chemistry C,* vol. 112, pp. 5432-5438, Apr 10 2008.

[336] M. H. Mendonca Dias and P. C. Lauterbur, "Ferromagnetic particles as contrast agents for magnetic resonance imaging of liver and spleen," *Magn Reson Med,* vol. 3, pp. 328-330, 1986.

[337] Z. G. Zheng, Q. Jiang, R. L. Zhang, L. Zhang, L. Wang, L. J. Zhang, *et al.*, "Magnetic resonance imaging and neurosphere therapy of stroke in rat," *Annals of Neurology,* vol. 53, pp. 259-263, Feb 2003.

[338] C. C. Berry and A. S. G. Curtis, "Functionalisation of magnetic nanoparticles for applications in biomedicine," *Journal of Physics D-Applied Physics,* vol. 36, pp. R198-R206, Jul 7 2003.

[339] T. Neuberger, B. Schopf, H. Hofmann, M. Hofmann, and B. von Rechenberg, "Superparamagnetic nanoparticles for biomedical applications: Possibilities and limitations of a new drug delivery system," *Journal of Magnetism and Magnetic Materials,* vol. 293, pp. 483-496, May 1 2005.

[340] A. S. Arbab, L. A. Bashaw, B. R. Miller, E. K. Jordan, B. K. Lewis, H. Kalish, *et al.*, "Characterization of biophysical and metabolic properties of cells labeled with superparamagnetic iron oxide nanoparticles and transfection agent for cellular MR imaging," *Radiology,* vol. 229, pp. 838-846, Dec 2003.

[341] K. Hayashi, M. Nakamura, W. Sakamoto, T. Yogo, H. Miki, S. Ozaki, *et al.*, "Superparamagnetic Nanoparticle Clusters for Cancer Theranostics Combining Magnetic Resonance Imaging and Hyperthermia Treatment," *Theranostics,* vol. 3, pp. 366-376, 2013.

[342] A. S. Arbab, L. B. Wilson, P. Ashari, E. K. Jordan, B. K. Lewis, and J. A. Frank, "A model of lysosomal metabolism of dextran coated superparamagnetic iron oxide (SPIO) nanoparticles: implications for cellular magnetic resonance imaging," *Nmr in Biomedicine,* vol. 18, pp. 383-389, Oct 2005.

[343] C. Paquet, H. W. de Haan, D. M. Leek, H. Y. Lin, B. Xiang, G. H. Tian, *et al.*, "Clusters of Superparamagnetic Iron Oxide Nanoparticles Encapsulated in a Hydrogel: A Particle Architecture Generating a Synergistic Enhancement of the T-2 Relaxation," *Acs Nano,* vol. 5, pp. 3104-3112, Apr 2011.

[344] S. W. Sun, J. J. Neil, and S. K. Song, "Relative indices of water diffusion anisotropy are equivalent in live and formalin-fixed mouse brains," *Magnetic Resonance in Medicine,* vol. 50, pp. 743-748, Oct 2003.

[345] C. L. Bennett, Z. P. Qureshi, A. O. Sartor, L. B. Norris, A. Murday, S. Xirasagar, *et al.*, "Gadolinium-induced nephrogenic systemic fibrosis: the rise and fall of an iatrogenic disease," *Clin Kidney J,* vol. 5, pp. 82-88, Feb 2012.

[346] M. Conacci-Sorrell, I. Simcha, T. Ben-Yedidia, J. Blechman, P. Savagner, and A. Ben-Ze'ev, "Autoregulation of E-cadherin expression by cadherin-cadherin interactions: the

roles of beta-catenin signaling, Slug, and MAPK," *Journal of Cell Biology,* vol. 163, pp. 847-857, Nov 24 2003.

[347] R. R. Qiao, C. H. Yang, and M. Y. Gao, "Superparamagnetic iron oxide nanoparticles: from preparations to in vivo MRI applications," *Journal of Materials Chemistry,* vol. 19, pp. 6274-6293, 2009.

[348] S. Laurent, D. Forge, M. Port, A. Roch, C. Robic, L. V. Elst, *et al.*, "Magnetic Iron Oxide Nanoparticles: Synthesis, Stabilization, Vectorization, Physicochemical Characterizations, and Biological Applications (vol 108, pg 2064, 2008)," *Chemical Reviews,* vol. 110, pp. 2574-2574, Apr 2010.

[349] T. Tonan, K. Fujimoto, S. Azuma, N. Ono, S. Matsushita, M. Kojiro, *et al.*, "Evaluation of small (<= 2 cm) dysplastic nodules and well-differentiated hepatocellular carcinomas with ferucarbotran-enhanced MRI in a 1.0-T MRI unit: Utility of T2*-weighted gradient echo sequences with an intermediate-echo time," *European Journal of Radiology,* vol. 64, pp. 133-139, Oct 2007.

[350] P. Vaupel and A. Mayer, "Hypoxia in cancer: significance and impact on clinical outcome," *Cancer and Metastasis Reviews,* vol. 26, pp. 225-239, Jun 2007.

[351] L. B. Harrison, M. Chadha, R. J. Hill, K. Hu, and D. Shasha, "Impact of tumor hypoxia and anemia on radiation therapy outcomes," *Oncologist,* vol. 7, pp. 492-508, 2002.

[352] C. Peitzsch, R. Perrin, R. P. Hill, A. Dubrovska, and I. Kurth, "Hypoxia as a biomarker for radioresistant cancer stem cells," *International Journal of Radiation Biology,* vol. 90, pp. 636-652, Aug 2014.

[353] I. F. Tannock, C. M. Lee, J. K. Tunggal, D. S. M. Cowan, and M. J. Egorin, "Limited penetration of anticancer drugs through tumor tissue: A potential cause of resistance of solid tumors to chemotherapy," *Clinical Cancer Research,* vol. 8, pp. 878-884, Mar 2002.

[354] Padera T.P., Stoll B.R., Tooredman J.B., Capen D., di Tomase E., and J. R.K., "Cancer cells compress intratumour vessels: pressure from proliferating cells impedes transport of therapeutic drugs into tumors," *Nature,* vol. 247: 695, 2004.

[355] W. R. Wilson and M. P. Hay, "Targeting hypoxia in cancer therapy," *Nature Reviews Cancer,* vol. 11, pp. 393-410, Jun 2011.

[356] G. L. Semenza, "Targeting HIF-1 for cancer therapy," *Nature Reviews Cancer,* vol. 3, pp. 721-732, Oct 2003.

[357] K. O. Hicks, F. B. Pruijn, T. W. Secomb, M. P. Hay, R. Hsu, J. M. Brown, *et al.*, "Use of three-dimensional tissue cultures to model extravascular transport and predict in vivo activity of hypoxia-targeted anticancer drugs," *Journal of the National Cancer Institute,* vol. 98, pp. 1118-1128, Aug 16 2006.

[358] S. Schubbe, T. J. Williams, G. Xie, H. E. Kiss, T. S. Brettin, D. Martinez, *et al.*, "Complete Genome Sequence of the Chemolithoautotrophic Marine Magnetotactic Coccus Strain MC-1," *Applied and Environmental Microbiology,* vol. 75, pp. 4835-4852, Jul 15 2009.

[359] D. A. Bazylinski, R. B. Frankel, and H. W. Jannasch, "Anaerobic magnetite production by a marine, magnetotactic bacterium," *Nature,* vol. 334, pp. 518-519 1988.

[360] J. E. Segall, S. M. Block, and H. C. Berg, "Temporal comparisons in bacterial chemotaxis," *Proc Natl Acad Sci U S A,* vol. 83, pp. 8987-91, Dec 1986.

[361] S. J. Park, S. H. Park, S. Cho, D. M. Kim, Y. Lee, S. Y. Ko, *et al.*, "New paradigm for tumor theranostic methodology using bacteria-based microrobot," *Scientific Reports,* vol. 3, Dec 2 2013.

[362] I. I. Marochkin and O. V. Dorofeeva, "Amide bond dissociation enthalpies: Effect of substitution on Nsingle bondC bond strength," *Computational and Theoretical Chemistry,* vol. 991, pp. 182-191, 2012.

[363] R. Reverberi and L. Reverberi, "Factors affecting the antigen-antibody reaction," *Blood Transfus,* vol. 5, pp. 227-240, 2007.

[364] A. Moore, E. Marecos, A. Bogdanov, and R. Weissleder, "Tumoral distribution of long-circulating dextran-coated iron oxide nanoparticles in a rodent model," *Radiology,* vol. 214, pp. 568-574, Feb 2000.

[365] J. M. Munson and A. C. Shieh, "Interstitial fluid flow in cancer: implications for disease progression and treatment," *Cancer Manag Res,* vol. 6, pp. 317-28, 2014.

[366] F. Danhier, O. Feron, and V. Preat, "To exploit the tumor microenvironment: Passive and active tumor targeting of nanocarriers for anti-cancer drug delivery," *Journal of Controlled Release,* vol. 148, pp. 135-146, Dec 1 2010.

[367] S. Taherkhani, M. Mohammadi, J. Daoud, S. Martel, and M. Tabrizian, "Covalent binding of nanoliposomes to the surface of magnetotactic bacteria for the synthesis of self-propelled therapeutic agents," *ACS Nano,* vol. 8, pp. 5049-60, May 27 2014.

[368] R. Dreyfus, J. Baudry, M. L. Roper, M. Fermigier, H. A. Stone, and J. Bibette, "Microscopic artificial swimmers," *Nature,* vol. 437, pp. 862-865, Oct 6 2005.

[369] D. Akin, J. Sturgis, K. Ragheb, D. Sherman, K. Burkholder, J. P. Robinson, *et al.*, "Bacteria-mediated delivery of nanoparticles and cargo into cells," *Nature Nanotechnology,* vol. 2, pp. 441-449, Jul 2007.

[370] R. K. Jain and N. S. Forbes, "Commentary - Can engineered bacteria help control cancer?," *Proceedings of the National Academy of Sciences of the United States of America,* vol. 98, pp. 14748-14750, Dec 18 2001.

[371] P. Sapra, P. Kraft, M. Mehlig, J. Malaby, H. Zhao, L. M. Greenberger, *et al.*, "Marked therapeutic efficacy of a novel polyethylene glycol-SN38 conjugate, EZN-2208, in xenograft models of B-cell non-Hodgkin's lymphoma," *Haematologica-the Hematology Journal,* vol. 94, pp. 1456-1459, Oct 2009.

[372] R. M. Sharkey, S. V. Govindan, T. M. Cardillo, and D. M. Goldenberg, "Epratuzumab-SN-38: a new antibody-drug conjugate for the therapy of hematologic malignancies," *Mol Cancer Ther,* vol. 11, pp. 224-34, Jan 2012.

[373] A. Pal, S. Khan, Y. F. Wang, N. Kamath, A. K. Sarkar, A. Ahmad, *et al.*, "Preclinical safety, pharmacokinetics and antitumor efficacy profile of liposome-entrapped SN-38 formulation," *Anticancer Research,* vol. 25, pp. 331-341, Jan-Feb 2005.

Contributions for Appendix A and Appendix B

Appendix A and Appendix B gather the results of a multidisciplinary teamwork *in vivo* experiments in which the contribution of the candidate was determined to be 20%. Appendix A presents the non-systemic magneto-aerotactic bacteria-mediated delivery of drug-loaded nanoliposomes in tumor hypoxic regions. Appendix B describes the preliminary investigation on the therapeutic effect of MTB-LSC system on tumor. The experiments were conducted with different collaborators from various disciplines including clinical oncologists, chemists, physicians, pathologists, and immunologists from different institutional research priorities (McGill University, Jewish General Hospital, Institute for Research in Immunology and Cancer, and University de Montréal).

In this multidisciplinary project, the contributions of the candidate consisted of design and attachment of SN38-loaded liposomes to the MTB cells supervised by Dr. Maryam Tabrizian. In addition, the candidate was also involved to perform the *in vivo* experiments including writing the related *in vivo* protocols, the daily batch preparation of MTB complexes for the injection, post-evaluation of the complexes using electron microscopy, and also assisting to evaluate the targeting, counting, and biodistribution capabilities of the complexes in tumor tissue by performing fluorescence microscopic imaging for immunostained histological slides, tumor homogenization followed by optical microscopy, and data analyses. Dr. Sylvain Martel acted as principal investigator and developed the general principles and methods. The three-dimensional navigation magnetic platforms and the software control system was designed and performed by Dr. Ouajdi Felfoul. The magnetotactic control sequences was tested by Mr. Dominic De Lanauze and executed by Mr. Dumitru Loghin. The bacteria were provided by Dr. Mahmood Mohammadi. The histopathological analyses were performed by Dr. Louis Gaboury. Liposome-SN38 was prepared by Dr. Sherief Essa working under supervision of Dr. Michel Lafleur and Dr. Maryam Tabrizian. Dr. Danuta Radzioch did preliminary analyses on cytotoxicity and immune system responses and help in the coordination for the *in vivo* tests. Dr. Nicole Beauchemin coordinated the implantations of tumor xenografts. The peritumoral injections in animals were performed by Mr. Daniel Houle. Dr. Yong Zhong Xu implanted the xenografts and performed tumor measurements. Dr. Neila Kaou, Mr. Michael Atkin, and Dr. Mahmood Mohammadi acted as project managers. Dr. Té Vuong and Dr. Gerald Batist provided clinical insights.

APPENDIX A – NON-SYSTEMIC MAGNETO-AEROTACTIC BACTERIA-MEDIATED DELIVERY OF DRUG-LOADED NANOLIPOSOMES IN TUMOR HYPOXIC REGIONS

Effective delivery of nanocarriers in regions leading to optimized therapeutic outcomes such as within tumoral hypoxic regions remains unmet. With a low therapeutic index and increased systemic toxicity, nanocarriers could greatly benefit from the actuation-navigation-sensory capability envisioned for futuristic nanorobots to enhance distribution in hard-to-reach tumoral regions following transports through the most direct physiological routes. Here we report that large populations of MC-1 magnetotactic bacteria (MTB) directionally-guided using their intracellular chain of iron-oxide nanoparticles, were able to mimic swarms of such futuristic transporters when operating in a computer-controlled artificial environment enabling the exploitation of their magneto-aerotactic migration behavior. Experiments conducted with SCID Beige mice resulted in a > 50% mean targeting ratio of the ~2×10^7 peritumorally injected drug-loaded nanoliposomal MTB-complexes (MTB-LP) in hypoxic regions of HCT116 colorectal xenografts. The results obtained with ~70 170 nm SN38 loaded nanoliposomes being attached per MTB suggest that harnessing microorganisms exhibiting magneto-aerotactic behavior can improve significantly the therapeutic index to tumor hypoxic regions for a variety of nanocarriers.

A.1 INTRODUCTION

Hypoxia facilitates the survival of tumor cells and is a cause of malignant transformation. It is the consequence of oxygen consumption by the rapid proliferation of tumor cells which results in approximately < 0.7% O_2 in highly difficult treatable hypoxic regions [350]. Such hypoxic environments negatively impact treatments based on radiotherapy [14, 351, 352] while for chemotherapy, larger drug molecules including nanocarriers cannot generally target and diffuse effectively [54, 353] towards the hypoxic cells within the absence of flow caused by the tumor

interstitial fluid pressure (TIFP) [354]. The resulting limited drug and macromolecule distribution within tumors significantly reduces the therapeutic index [12].

The two main approaches to the selective killing of hypoxic cells in tumors [13, 355], the bio-reductive prodrugs [16, 17] and small molecule inhibitors against molecular targets involved in the survival of hypoxic cells [355, 356], need to overcome the problem of drug-loaded nanocarriers penetration through poorly perfused hypoxic tissue [357]. While reducing the TIFP is known to enhance the uptake and homogeneous distribution of many therapeutic compounds, available pharmacologic and physical therapies used to reduce tumor pressure have their side effects and their application in clinical practice is not yet validated [18] while suffering from the low targeting efficacy when using the systemic routes. Indeed, currently used pharmaceutical nanocarriers such as liposomes, micelles, polymeric nanoparticles and many others, result in very low tumor site accumulation. Combining the enhanced permeability and retention (EPR) effect of nanocarriers with the longer systemic circulation properties that are achieved following PEGylation has increased the targeting ratio but still result in a very limited fraction of nanocarriers entering tumors. This is due to the facts that usually only about 5% of the administered nanocarriers remain in the systemic circulation after 12 h with 90% of these PEGylated nanocarriers being removed from the systemic circulation within several hours, resulting to only ~2% of the total administered dose being deposited in the tumor [10].

But since the overall maximum size of nanocarriers is an obstacle to the integration of advanced functionalities that would correct for such deficiencies, the overall sizes of intercellular openings responsible for the leakiness of tumor vessels provide sufficient spaces for such nanocarriers to be transported by larger and more capable self-propelled carriers. The development of a common carrier capable of transporting such therapeutic nanocarriers to the most effective site of treatment with embedded functionalities that would enhance the targeting capability beyond what is possible using existing nanocarriers alone is the focus of this study. Such functionalities would include navigation capability towards the sites of treatment in order to avoid systemic circulation, self-actuation providing a propelling force sufficient to penetrate the tumor volume beyond the diffusion limits of nanocarriers and larger drug molecules, and sensory capability to target regions such as the hypoxic zones that would lead to the best treatment outcomes. Although these are functionalities generally used in robotics, implementing them at the scale required to transit through the physiological environments to reach deep inside a tumor is well beyond what is

technically feasible for the implementation of an artificial nanorobotic agent, but possible with the use of a natural agent.

For instance, the MC-1 strain *Magnetococcus Marinus* [324, 358] contains a chain of magnetic iron-oxide (Fe_3O_4) nano-crystals enclosed in membranes known as magnetosomes [359]. Such chain of magnetosomes acting like a nano-compass needle entails the bacteria to swim persistently along local magnetic field lines in a preferred direction [99]. In their natural environment, such direction corresponds to a downward migration along geomagnetic field lines in conjunction with aerotaxis to efficiently migrate to and maintain position at their preferred low oxygen concentrations. Such magnetically-assisted aerotaxis known as magneto- aerotaxis [33] results in the formation of microaerophilic bands of MC-1 cells at O_2 concentrations equivalent to the ones observed in the hypoxic regions of solid tumors. Most microaerophilic bacteria form aerotactic bands using a temporal sensory mechanism [360] that samples the environment as they swim while comparing the present O_2 level with the O_2 level of the previous sample. Unlike M. magnetotacticum which is consistent with such temporal sensory mechanism, the aerotactic behavior of MC-1 cells is based on a two-state aerotactic sensory system in which the O_2 concentration determines the sense of flagellar rotation and hence the swimming direction along the geomagnetic field lines. Such polar magneto-aerotaxis accounts for the ability of the MC-1 bacteria to migrate and to maintain position at the preferred O_2 concentration at the oxic-anoxic transition zone (OATZ) in chemically-stratified, semi-anaerobic basins [33].

Our hypothesis was that a similar OATZ present in the fluid interstitial regions (tumor interstitium) between the angiogenic network (oxic) and the tumor necrotic (anoxic) zones could be exploited to enhance drug targeting in hypoxic regions using live MC-1 cells after being guided toward the site of treatment by an external magnetic source. Indeed, unlike previous bacterial therapies [93], minimizing systemic circulation of drug-loaded MC-1 cells was achieved by initially guiding their migration path towards such OATZ where an oxygen gradient was present and could be detected by the bacteria. Unlike hypoxic zones, since the location of the tumoral volume can generally be precisely determined, magnetotaxis was first prioritized over aerotaxis considering that the latter could not initially benefit from such spatial information.

Based on the Langevin function, the level of magnetotactic directional control characterized by the alignment of the chain of single magnetic domain nanoparticles (magnetosomes) in the MC-1

cells in the applied directional magnetic field would be determined by the ratio of the interactive magnetic energy with the applied field to the thermal energy. Such thermal energy in the form of thermal forces associated with Brownian motions would tend to randomize the cell orientation after a sufficient reduction of the magnetotactic component unless in this particular case, another taxis-compatible directional source such as an oxygen gradient in the tumor interstitium would be detected by the bacteria. Following such a concept, the targeting procedure consisted of an assisted magnetotactic directional control phase [108] using a magnetic field sensibly higher than the geomagnetic field to induce a stronger directional torque on the chain of magnetosomes towards the tumor when in the peritumoral regions, followed by a MTB-autonomous aerotactic directional phase in the absence of a sufficient level of interactive magnetic energy required for prioritizing magnetotactic directional control when in the predefined targeted tumoral volume. Since the physiological environments encountered by the MTB during travel would be different from the ones found along their natural migrating paths, the experiments were aimed at assessing the ability of the MC-1 cells to migrate effectively towards the hypoxic zones following peritumoral injection. More specifically, we questioned whether a large ratio of injected MC-1 spherical cells whose diameter ranges between 1 and 2 μm would be able to migrate through physiological routes such as the irregular and disorganized angiogenic network, the interstitial spaces, and the intercellular openings of typically less than 2 μm in diameter between endothelial cells [60] responsible for much of the vessel leakiness in solid tumors.

A.2 RESULTS AND DISCUSSION

In order to assess magnetically-guided live MC-1 MTB targeting profile in HCT116 xenograft, we performed peritumoral injections of ~2.92×10^7 bacteria in 20 μl PBS solution for a total of 8 mice. Depending on whether or not a magnetic field was applied to guide the bacteria, two groups were discerned namely, an experimental group (MS1 to 4) with a 30 minutes applied magnetic field targeting the center of the tumor following the MC-1 injection; and a control group (MS5 to 8) that was not exposed to the magnetic field. A color map graph showing the distribution of the MC-1 cells in the xenograft for mice MS1 to 8 is depicted in Figure A.1a, b while an approximate MTB count for each tumor's section is shown in Figure A.1e.

We notice a higher population of MC-1 cells in the middle section of the tumor for the group exposed to the magnetic field for 3 out of 4 mice. The lack of targeting level in one mouse may be due to experimental errors such as a magnetic pole position being set outside of the tumor volume. With nonmagnetically guided bacteria, only 1 of 4 mice showed a high penetration ratio for the control group. This high ratio for one mouse may be due to a relatively large population of bacteria to come close enough to the target to be influenced by decreasing oxygen gradients, resulting in aerotactic directional motion toward the hypoxic regions. But also of interest in the fact that when guided appropriately, the MTB appear to swim and move effectively through necrotic tissues as assessed by the observation of several adjacent histology slides (4 μm apart), one stained with hematoxylin phloxine saffron (HPS) (Figure A.1c) and the second stained with green FITC-secondary antibody immunofluorescence targeting a specific protein at the MC-1 cell membrane (Figure A.1d).

Although the preceding section showed that in general the combination of magnetic and aerotactic guidance leads to much superior targeting ratios in hypoxic regions of tumor xenografts, the targeting profile needs to be compared with passive agents, *i.e.* agents lacking the three functionalities mentioned earlier namely, navigation such as magnetotactic guidance, propelling force, and sensory-based displacement such as aerotactic motion behavior. As such, we performed peritumoral injections of a mixture consisting of live MTB and two types of passive markers to be more confident on the concluding results.

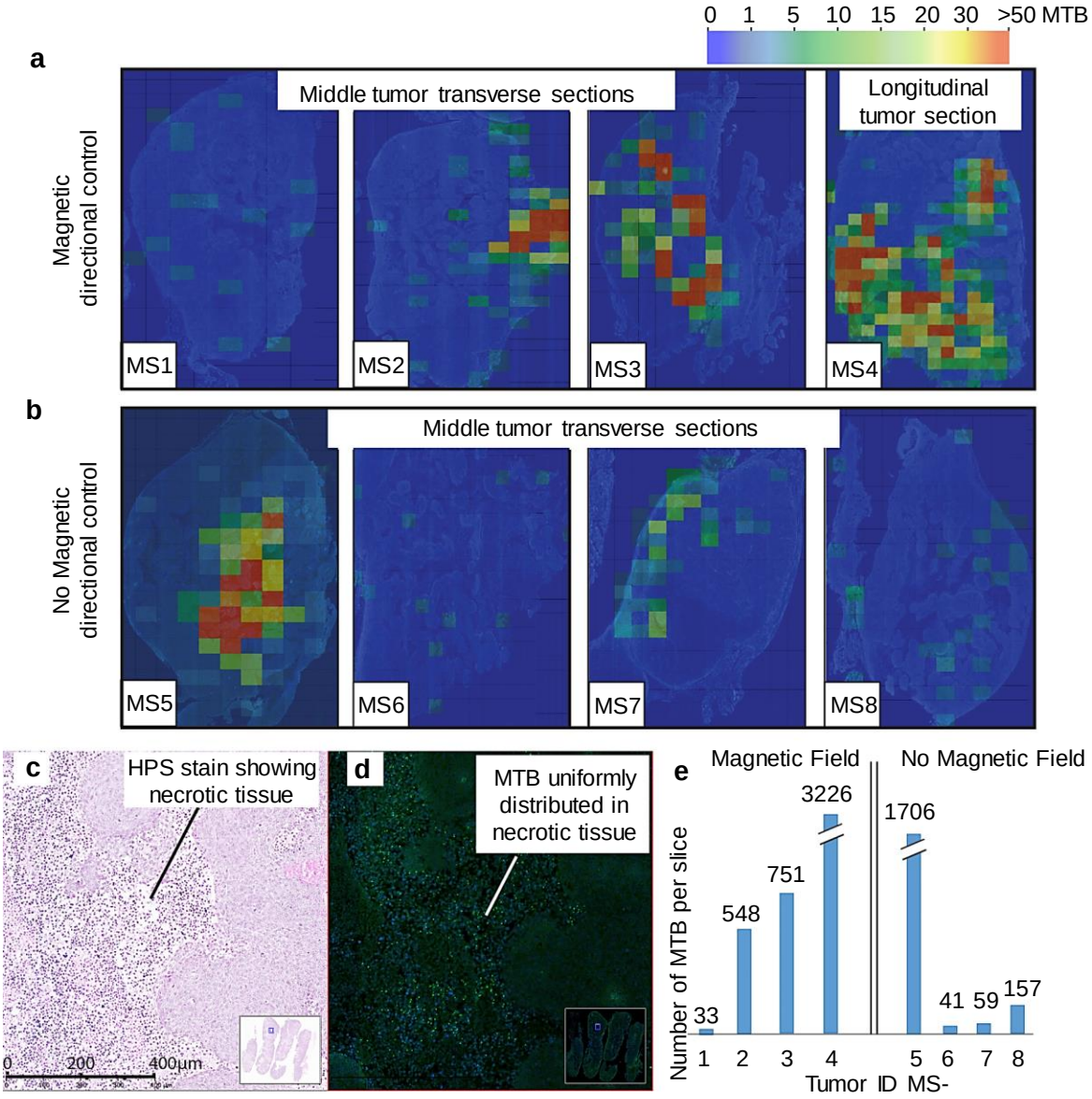

Figure A.1: Penetration of live MC-1 cells with and without magnetic field exposure in HCT116 xenografts following a peritumoral injection. (**a**) Mice labeled as MS1 to 4 were exposed to 30 minutes of a directional magnetic field targeting the center of the tumor. An immunohistology analysis of the middle section of these tumors reveals the presence of MTB in the vicinity of the necrotic region and in high number in 3 out of 4 mice. (**b**) Mice labeled as MS5 to 8 were not exposed to a magnetic field following peritumoral injection. Immunohistology analysis of the middle section of these tumors shows limited MTB penetration in 3 out of 4 mice. (**c**) HPS stain of a tumor section showing necrotic zones. (**d**) Adjacent section to C showing the MTB, as green FITC fluorescent dots, uniformly distributed within the same regions recognized to be necrotic with the HPS stain. (**e**) Total MC-1 MTB count for the middle section of MS1 to 8.

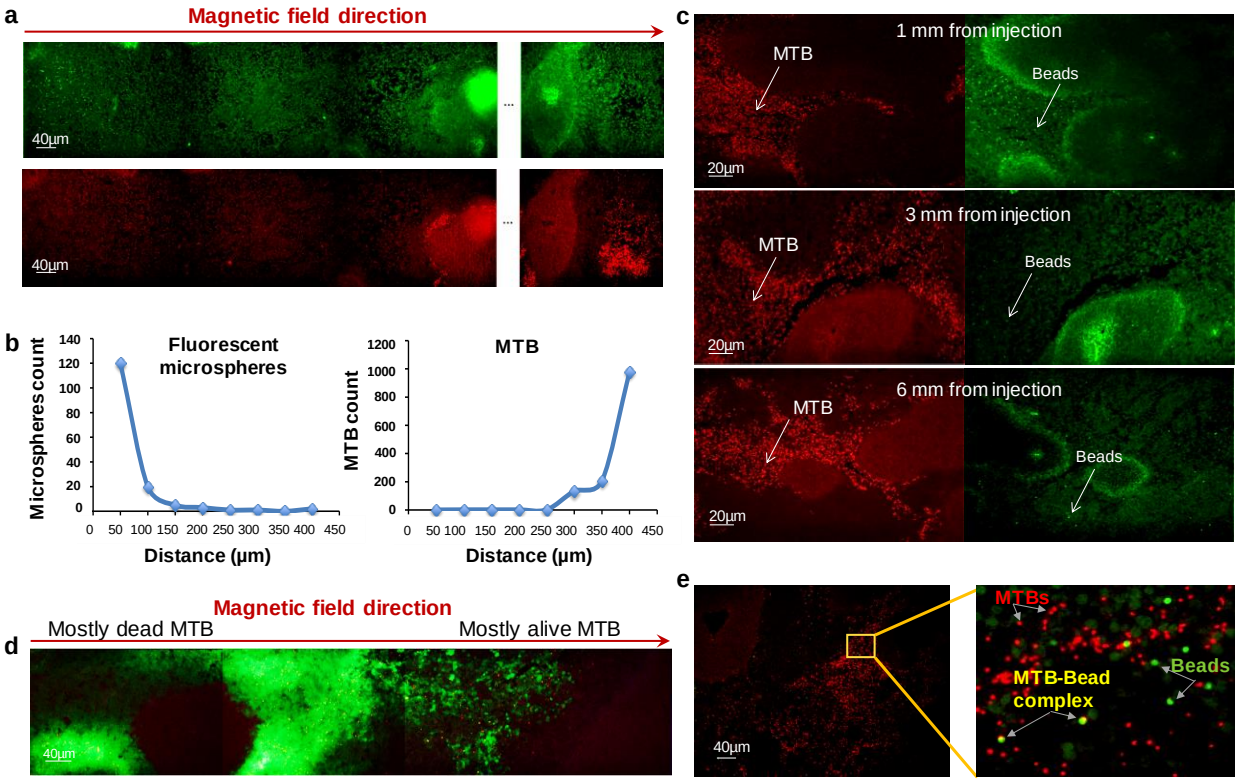

Figure A.2: Penetration of live MC-1 cells over passive diffusion in HCT116 xenografts. (**a**) 20× images of MTB and fluorescent beads at different tumoral depths. (**b**) Quantity of fluorescent microspheres *vs.* MTB at various tumoral depths. (**c**) 20× images of MTB and fluorescent at 1, 3, and 6 mm inside the HCT116 xenograft. (**d**) 20× images of live and dead MTB at different tumoral depths. (**e**) Co-localization of MTB-bead complexes at a tumoral depth of 4 mm.

When such passive markers are injected in the peritumoral region, they exhibit a limited diffusion due to the tumor interstitial fluid pressure. The simultaneous injection of live MTB and passive markers was to compare their ability to diffuse and remain inside the tumor within the same experimental conditions using the same injection site and the same injection rate. The first marker consists of polymer microspheres (PS) and the second marker consists of dead MC-1 cells that have undergone prior staining with a fluorescent cell penetrating peptide (CellTrace, CFSE Cell Proliferation Kit). 20 μl of Dragon green fluorescent PS (480, 520) 1.9 μm polymer microspheres, similar in size to the MC-1 spherical cells, and 20 μl of live MTB were injected, which in term of numbers consisted of ~2.92 × 10^7 bacteria and ~1.35 × 10^7 beads, followed by 30 min. magnetic guidance. In a separate set of experiments, 20 μl of dead MTB were used instead of the polymer

microspheres. Texas-red secondary antibody was coupled to MC-1 MTB making the live MTB red on the histological slides with the beads alone showing in green. The dead MTB appear yellow. The active directional motility through magnetotaxis and aerotaxis of the MTB resulted in superior penetration depths in HCT116 xenografts compared to passive markers as depicted by the dead MTB and the polymeric beads (Figure A.2a-d). We observed a substantial decrease in the number of microspheres as we move deeper into the tumor, while the number of MTB increased significantly (Figure A.2b). The co-localization of MTB-bead complexes (Figure A.2e) that occurred from the surface interaction of some beads with MTB suggests the potential for each MTB to carry a large load deeply inside tumoral tissues. Similarly, live MTB outnumber dead MTB as we move far from the injection site. The injection site exhibited a strong passive diffusion of the CellTrace making the background fluorescent in which mostly dead MTB (yellow dots) and few live MTB (red dots) are found. Deeper, mostly live bacteria were found and shown to compete in penetration with the diffusion of the CellTrace.

To evaluate the mean targeting ratio of MTB-LP (Figure A.3a) with covalently-attached SN38 drug-loaded liposomes to the cell surface through carbodiimide chemistry [367], we conducted additional *in vivo* experiments in SCID Beige mice to obtain statistical data of the quantity of MTB-LP in HCT116 tumoral tissue *versus* the total amount injected peritumorally. Among all potential nanocarriers, liposomes were initially selected as a first-proof-of-concept because they are biocompatible, exhibit low immunogenicity and high flexibility, protect the body from potential toxic cargo, shield therapeutic agents from premature degradation, control release kinetics, and may concurrently encapsulate a multitude of hydrophilic and/or hydrophobic drug cargos, pharmaceutical ingredients, imaging agents, and genetic material by virtue of their aqueous interior and lipid exterior. Furthermore, cytotoxicity assays reveal that liposomal attachments to the MC-1 MTB formulation improve the biocompatibility of the MTB, whereas attachment does not interfere with liposomal uptake [367]. The diameter of each liposome was set to the maximum possible synthesized value of ~170 nm to maximize the quantity of drug-cargo being transported per MTB.

The amount of bacteria intended for injection was predetermined prior to the experiments. Since some of the bacteria injected peritumorally might not have ended up inside the tumor, we also estimated an exact percentage of bacteria which actually could be found in the excised tumors. At that point, some of the injected bacteria might have been dead and/or partly cleared from the

tumor tissue, so obtained counts represent only estimates performed for comparative purposes. Some tumors were used for a separate analysis to assess apoptotic and necrotic markers. The remaining tumors were cut in seven fragments and all fragments were paraffin-embedded and sectioned.

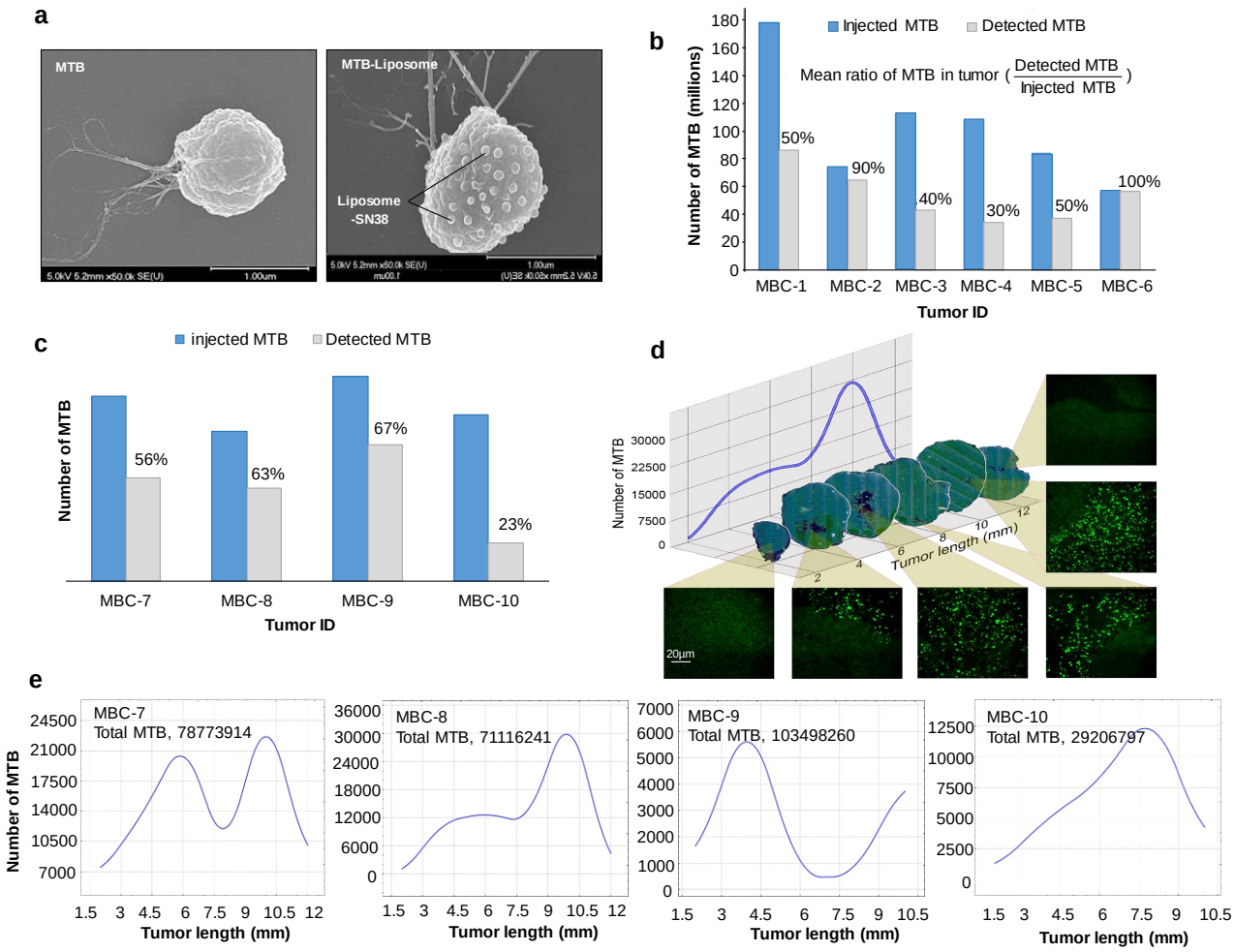

Figure A.3: Targeting ratios of MTB-LP in HCT116 xenografts. (**a**) Unloaded MTB *vs.* MTB-LP (right) with ~70 SN38 loaded liposomes (diam. ~170 nm) attached to the surface of each cell. (**b**) Ratios of MTB-LP in the tumoral tissue obtained by homogenization. (**c**) Estimated mean ratios of MTB-LP (MBC-groups) found in the tumor. (**d**) Transverse tumor sections of group MBC-8 MTB-LP after targeting. (**e**) MTB-LP distribution of the MBC7-10 groups inside the tumor.

Similar to the results achieved with the unloaded MC-1 MTB, high targeting ratios of MTB-LP (Figure A.3b, c) were obtained. Histological sections of the magnetotactic bacterial count (MBC)

samples also revealed that the MTB-LP were distributed throughout the xenografts (Figure A.3d, e) mainly in the neighborhoods of necrotic areas and in large numbers in the center of the tumor where necrosis was more predominant. The mean tumor targeting ratio (~50%) estimated from the MBC samples by image processing techniques allowing to assess the distribution of the MTB-LP complexes in the HCT116 xenografts was coherent with the mean targeting tumor ratio (~59%) obtained by HCT116 xenograft homogenization (Figure A.3b) extracted after experiments performed under similar conditions.

In this initial study, we demonstrated that live MC-1 cells potentially safe for use in humans (see methods: mice and rats cytotoxicity) and acting under magnetotactic directional control can be used as direct targeting systems to enhance the therapeutic index while reducing systemic exposure in currently used passive and active targeting methods [366]. Since magnetotaxis relies on a magnetically-induced directional torque, the magnetic energy required for such self-propelled agents to achieve direct targeting especially in deep tissues is significantly less than the induction of magnetic pulling forces [21, 22] used to displace agents such as magnetic nanoparticles (MNP) where the rapid decay of the magnetic field from the magnetic source generally limits targeting to regions only near the skin. The more recent depth independent direct delivery method known as Magnetic Resonance Navigation (MRN) [20] cannot be effectively applied in the tumoral microenvironments due to the insufficient magnetic induction volume of the agents. Although microscopic artificial swimmers [368] could be envisioned as an alternative to the use of natural microorganisms, embedding an equivalent level of functionality in artificial agents to compete against such natural microorganisms in delivering therapeutics through complex vascular and interstitial networks, may prove to be a far-reaching concept.

Indeed, we showed that harnessing sufficiently small microorganisms exhibiting a magneto-aerotactic behavior such as the MC-1 cells that could be described as an agent with onboard oxygen gradient detectors connected to a low Reynolds hydrodynamic propelling system through some sort of embedded computation or intelligence, all in $< 2\ \mu$m self-powered body capable of being directionally guided from an external source, can represent a suitable alternative to emulate artificial nanorobotic agents that need characteristics and functionalities well beyond actual technological feasibility. Furthermore, such approach could also benefits from the fact that bacteria-mediated delivery of nanoparticles and cargo into cells for various applications has already shown to be feasible [369]. Besides potential future efforts towards genetically modified

transporters [370], these initial findings may influence not only specific engineering concepts and medical interventional methods, but it also opens opportunities for the synthesis of new target therapeutic, imaging, and diagnostic agents while providing further opportunities in enhancing the delivery and therapeutic efficacy of existing nanocarriers.

A.3 METHODS

Magnetotaxis directional control. The animals were placed in the center of a platform consisting of three orthogonal pairs of electric coils positioned in a Maxwell configuration. Two main approaches were investigated, referred to here as spatial targeting and time-based targeting. For spatial targeting, a volumetric targeting zone referred to as the aggregation zone was created using a time varying magnetic field sequence while being positioned at the location of the xenograft. As such, the electrical currents circulating in the coils were adjusted accordingly. Such configuration forced the MTB to accumulate in the aggregation zone since the magnitude of the magnetic field outside the aggregation zone induced a directional torque on the chain of magnetosomes sufficient to force their migration towards the aggregation zone. Once in the aggregation zone, the magnetic directional field was sufficiently low to allow the swimming direction of the MC-1 cells to be influenced by aerotaxis. For time-based targeting, a directional magnetic field was applied toward the xenograft for a predetermined period of time before being switched off to allow aerotaxis to take effect. Both methods proved to be successful. Although spatial targeting has the advantage of being able to constrain the aggregation of the MTB to a specific targeted volume which proves useful in deeply located tumoral lesions, the results presented here were obtained with the time-based targeting method for simplicity since the MTB could not swim passed the outer limit of the external implanted xenograft while providing an adequate distribution profile across the tumoral tissue. During magnetotaxis control, a modulation of the directional field (approx. 4 Gauss) using small angular variations was also applied to enhance the capability of the MC-1 cells to swim around physiological obstacles.

Magnetotactic bacteria count. To visualize and estimate the relative amounts of MTB present in each histological section sampled from each tumor, images of each section were acquired using a fluorescence optical microscope equipped with a 40× magnification objective lens. The acquired images were then processed using an automated software algorithm to evaluate the

number of MTB in each histological section. This algorithm performed graphical enhancements on each image to count the number of MTB. First, a morphological erosion and dilation using a large disk shaped structural element was performed to remove noise resulting from non-uniform lighting in the setup and subtracting the result of this operation from the original image. The contrast of the images was then enhanced and converted to gray scale images by keeping only the green component (since green fluorescence was used to label the MTB) of the RGB image. The number of MTB was then counted by binarizing the resulting images and considering each connected regions as an individual bacterium. The number of MTB counted using this algorithm was then plotted against the depth at which the sample was taken in the tumor. The amount of MTB in each tumor was estimated by adding together the number of MTB corresponding to every sample taken at a certain depth inside the tumor with a step of 2 mm between each value of depth from the first histological section's position to the last position. The curve's data for each 2 mm step were calculated using the equations found by the linear interpolation between each adjacent and actual data points. While the number of MTB counted using this technique represents only an approximate number of MTB located in the tumors, it allows us to visualize the variation in distribution of the injected MTB within the tumor.

Immunohistology staining. Samples were fixed in 10% neutral buffer formalin and embedded in paraffin and cut at 4 μm thickness. Tissue sections were incubated inside an immunostainer (Discovery XT, Ventana Medical Systems, Roche Group) following FISH procedure and manual titrations and by using proprietary reagents. The following antibodies were applied: Polyclonal Rabbit anti-MC1 receptor (GenScript #153335-1, dilution 1/300 for 1 hour at room temperature). Afterwards, the slides were incubated with a FITC-labelled secondary anti-rabbit antibody to visualize MC1 receptor in green, TEXRed-labelled secondary anti-rabbit antibody was used to visualize MC1 receptor in red. The slides were finally washed and mounted using ProLong® Gold Antifade Reagent with DAPI (Invitrogen).

Live/dead mixture preparation. A cell pellet of live MTB was obtained by magnetically concentrate 50 ml of an MTB solution. The pellet was suspended in PBS containing the probe prepared as suggested by the manufacturer for 15 min at room temperature. The MTB was magnetically concentrated to re-form the pellet and incubated for another 30 min at 42 °C at which the MTB becomes inactive, which is assessed by microscope observation. After heat

treatment, the MTB do not recover motility and cell division, also assessed by microscope observation over the duration of the experiment.

Liposome attachment. The attachment relies on direct chemical conjugation of liposomes functionalized with reactive groups (–COOH) which covalently bond to a primary amino groups ($–NH_2$) intrinsic to bacteria cell membrane proteins. Carboxylated liposomes were conjugated to MTB by carbodiimide chemistry. Dehydrated agents such as EDC and Sulfo-NHS were added to 3 ml of 0.5 mM liposomes suspension (EDC: NHS: DSPE-PEG-COOH = 35: 35: 3, molar ratio) in PBS buffer (pH 6.5). The mixture was incubated at room temperature for 20 min. The free activating reagents were removed using Sephadex G-50 column. Then, activated liposomes were added to 4×10^7 MTB ($\sim 10^7$ MTB ml^{-1}) and incubated for 2 h at room temperature, under gentle mixing. Liposomes attached to MTB were separated from non-attached liposomes by applying a 2D magnetic field. The sample was washed three times in PBS and finally resuspended in PBS (pH = 7.4).

Determination of MTB-LP in hypoxic areas. MTB-LP distribution in HCT116 xenografts was predominantly found in regions of the tumors where oxygen concentration was sufficiently low to induce morphological signs of ischemic necrosis. Notably, those areas exhibited a specific immunohistochemical profile consisting of a lack of expression of proliferation markers (Ki-67 and survivin) and a concomitant increased in the expression of the apoptotic marker Caspase-3.

Mice and rats cytotoxicity. Systemic response to MC-1 cells: No significant difference in the expression of inflammatory cytokines between PBS and MTB injections both in A/J and in C57BL6 mice in the blood was observed. *P.aeruginosa* used as a positive control without MTB injection induced inflammatory cytokines, IL-6 induced at the highest level at 6h. Immunogenicity and organ toxicity assessment: Assessment of several immunological parameter of inflammation have been completed -Immunogenicity studies has been completed using various doses of MTB and harvesting blood as well as organs at various time points post *i.v.* infusion of MTB bacteria into two different strains of mice A/J and C57BL/6 strain. Following *i.v.* injection with *P.aeruginosa,* blood plasma displayed the highest levels of inflammatory cytokines compared to liver, spleen, and lungs. MTB did not induced significant increase in inflammatory cytokines levels in the liver, spleen, lungs as well as in the plasma. Rats were injected with 10^8 MTB intravenously and the complete biochemical and hematological assessment was performed

after 6, 24, and 72 h. Our preliminary results demonstrated that the injection of MTB did not lead to inflammation, no hematological distortions were detected and biochemical parameters were within normal range.

Acknowledgements

This project was initially supported in part by the Canada Research Chair (CRC) in Micro/Nanosystem Development, Fabrication and Validation and grants from the National Sciences and Engineering Research Council of Canada (NSERC), and the Province of Québec. This work was supported by the Québec Consortium for Drug Discovery (CQDM) and in part by the Research Chair of École Polytechnique in nanorobotics, and MITACS. The magnetotaxis system was built with the financial help of the Canada Foundation for Innovation (CFI). Preliminary *in vivo* results were obtained with the financial help of the US National Institute of Health (NIH) Grant Number R21EB007506 from the National Institute of Biomedical Imaging and Bioengineering. Judith Caron from CQDM is acknowledged for her involvement in the coordination of the project. Ronald Gladue from Pfizer Inc., Robert M. Garbaccio from Merk & Co., and Corinne Reimer from AstraZeneca R&D, are also acknowledged for their guidance and insights from the pharmaceutical industry. Julie Hinsinger (UdM, IRIC) and the histological team (UdM, IRIC) are acknowledged for tumors histology preparation.

APPENDIX B – THERAPEUTIC EFFECT OF LIPOSOMAL SN38 TRANSPORTED BY MAGNETOTACTIC BACTERIA TO TUMOR HYPOXIC REGIONS: A PROOF OF CONCEPT STUDY

This chapter presents the experimental team works, developed methodologies, and the therapeutic achievements of the proposed MTB-based drug targeted delivery system. The aim was to explore an entirely novel therapeutic modality to demonstrate an incremental therapeutic benefit and the biological efficiency of the SN38 (anti-cancer drug) encapsulated in liposome attached to MTB cellular envelope for therapy of localized cancer. The MTB-LSC as an efficient self-propelled microcarrier exhibits delivery and diffusion of the drug to the inaccessible site of the solid tumors.

B.1 EXPERIMENT PROCEDURE

B.1.1 Tumor model

The experimental procedures were conducted on 72 SCID-beige with HCT116 human colorectal tumor cells implanted in their flank. The tumor size of each experimental group was meticulously assessed and verified statistically not to have any significant difference between the assigned groups at the initiation of the experimental treatment. Once the size of tumor xenografts were reached 80-100 mm^3, each mouse was received the multiple treatments every other day from day 0 to day 18 with the total of ten injections. The experiments were performed peritumorally by injection of therapeutic-loaded MTB into the tumor xenograft. By the peritumoral-based interventions, drug-loaded MTB can be directly injected into regions located adjacent to the tumor mass to take advantage of the directional blood flow towards the tumor and bypass entering the larger vasculature. The tumor growth rate was estimated by a direct measure of the tumor size every second day using an electronic caliper. The tumor volume was then calculated using the following formula [331]: [(length) × (width) ^{2} × 0.5]. The animals were sacrificed 2 days after the 10th injections, which commenced on day 20 after the first treatment. Table B.1 describes the experimental procedure and applied conditions.

B.1.2 MTB-LSC group

For preparation of MTB-LSC, (15 ml of 0.5 mM) functionalized liposome-SN38 was incubated with 50 ml of MTB in culture medium with an initial concentration of ~2×10^6 MTB ml^{-1} in the exponential growth phase. To control the drug dosage delivered to the tumor, the chemical environment and the carbodiimide attachment technique were adjusted to prevent the release of the drug during the attachment and navigation process. After a 2 h incubation period, the MTB-LSC was washed twice using a magnetic field and resuspended in 100 μl PBS with a final concentration of 10^9 MTB ml^{-1}. The magnetic purification helps to remove non-attached liposomes concentrating the MTB-LSC in injectable volume, and replacing bacteria culture media with a physiological solution like PBS. It was adjusted to inject ~500 ng SN38 per each injection with the cumulative dose of ~5 μg at the end of the experiment. Therefore, 60 μl aliquots of the complex were considered for peritumoral injection and 20 μl aliquots were reserved for subsequent analysis using high-performance liquid chromatography (HPLC). Another 20 μl aliquot from each purified batch was used for counting the exact number of bacteria present in the aliquot of injected MTB-LSC, using optical microscopy. Once the injection was performed, the considered mouse that was needed to be magnetically targeted was immediately positioned inside the 3D magnetic field navigation system for a defined period of 30 minutes. The ability to remotely control migration of MTB-LSC as well as their penetration and distribution following multiple injections inside the tumor were evaluated using histopathological analysis. As validated in Appendix A, the magnetically navigated MTB-LSC preferentially selects the low oxygen regions and readily accumulates into the hypoxic and necrotic areas.

B.1.3 LP-SN38 and LP groups

This group of mice received LP-SN38 alone to assess any potential treatment effect. Each 60 μl aliquots of LP-SN38 was contained of 500 ng SN38. The SN38 as an active metabolite form of CPT-11 showed to be ineffective in controlling tumor growth. Empty liposome group was also served as a control to verify the effect of empty liposomes.

B.1.4 MTB alone group

The MTB alone with or without magnetic targeting were examined as a control. Animals were treated with the equivalent dose of bacteria as used in MTB-LSC samples to evaluate for possible contribution of MTB alone to prevent tumor growth. A 50 ml of 2×10^6 MTB ml^{-1} was

concentrated and then resuspended in 100 μl of a PBS solution. 60 μl aliquots of MTB were injected peritumorally in both MTB groups. In the 9 mice, 30 min magnetic navigation was applied to target the tumor.

B.1.5 CPT-11 group

The irinotecan known as CPT-11 was chosen as the pro-drug of SN38 and served as positive control for the treatment modality. The effective dose of CPT-11 in reducing tumor growth was reported 40 and 60 mg/kg/dose for a multiple and single administration, respectively, in SCID mice [371]. Since mice can efficiently convert CPT-11 to SN38, the CPT-11 dosage was adjusted on the basis of SN38 equivalents. Robert *et al*. (2012) reported the SN38 mole equivalents are based on 60% of CPT-11 mass [372]. Each mouse in this group was injected with 50 μl of 16.67 ng μl^{-1} CPT-11 in dextrose per injection, which gives a cumulative dose of CPT-11 8.33 μg per mouse. According to the calculation, the injected cumulative dose of CPT-11 was approximately equivalent to 5 μg of SN38 dose delivered by the MTB-LSC group. Two different routes of injection were examined for CPT-11 including peritumorally (*p.t.*) and systemic intraperitoneal (*i.p*.) every second day. None of the CPT-11 groups were successful in preventing tumor growth.

Table B.1: Description of the treatment groups.

Groups	Composition	Means of injection	Volume of injection (μl)	Magnetic targeting	Number of mice	Number of injections
MTB-LSC	MTB-Liposome-SN38	*p.t.*	60	30 min	9	10
LP-SN38	Liposome-SN38	*p.t.*	60	No	9	10
LP	Empty Liposome	*p.t.*	60	No	9	10
MTB	MTB alone	*p.t.*	60	30 min	9	10
	MTB alone	*p.t.*	60	No	9	10
CPT-S	Irinotecan (CPT-11)	*i.p.*(systemic)	50	No	9	10
CPT-P	Irinotecan (CPT-11)	*p.t.*	50	No	9	10
PBS	PBS	*p.t.*	60	No	9	10

B.2 RESULTS

B.2.1 Analytical assessment of SN38 content

The HPLC was used to precisely determine the quantity of SN38 present in MTB-LSC formulation. The HPLC results demonstrated that the cumulative dose of SN38 delivered by MTB-LSC to each mouse was to be determined ~6.4 μg for a total of 10 injections (Table B.2).

Table B.2: Cumulative dose of SN38 per mouse treated with MTB-LSC.

Individual mice treated with MTB-LSC	M-1	M-2	M-3	M-4	M-5	M-6	M-7	M-8	M-9	**Mean cumulative dose (μg)**
Minimal cumulative dose which shows the significant effect after 7 injections (μg)	4.3	4.9	4.7	4.9	4	4.5	4.4	4.7	3.8	**4.5**
Cumulative dose received by each mouse after 10 injections (μg)	6.1	7.2	6	7.1	6.1	5.9	6.3	6.8	5.9	**6.4**

B.2.2 Tumor growth rate and tumor weight

The comparative kinetic of tumor growth and efficacy of MTB-LSC *versus* all controls during the course of the treatment are presented in Figure B.1a. None of the control injections at different time points induced any significant inhibition of tumor growth ($P > 0.05$). In sharp contrast animals treated with the MTB-LSC groups were demonstrated a statistically significant therapeutic effect and decrease in tumor volume. From day 0 through day 12 no significant differences were observed between groups. Beginning on day 8 a distinct change in the slope of tumor growth was observed for the complex group compared to all controls. Tumor growth is stabilized on day 14 with the cumulative dose of ~4.5 μg (after seven injections) while all other groups were continued to grow at a rapid pace. These differences and reduction in tumor size were statistically significant *versus* all other groups from day 14 to day 20. Tumor growth is eradicated completely to day 20. The change in tumor volume following treatment with MTB-LSC demonstrated that the cumulative dose of delivered SN38 (~6.4 μg per mice) was sufficient

to induce biological effect and make significant impact on tumor volume by multiple dosing with complex. The size of tumors was homogeneous in each group, which producing tight error bars.

Control groups including animals treated with an equivalent dose of CPT-11 and SN38 encapsulated into liposomes without magnetic guidance showed no comparable control of tumor growth. It was observed that the LP-SN38 group presents a slightly slower growth rate than empty liposomes and PBS (negative controls) even the differences are not significant ($P > 0.05$). MTB alone with the equivalent amount as therapeutically effective MTB complexes did not show significant contribution to prevent tumor growth. As shown in Figure B.1b, no significant changes in mice body weights were observed in any treated groups during the course of the treatment.

B.2.3 Tumor volume and weight on day 20th of treatment

As shown in Figure B.2a, b , the results confirmed the statistically significant reduction (*P*-value < 0.001) in tumor size and weight in the group treated with the MTB-LSC compared to tumor-bearing animals treated with the equivalent dose of MTB or SN38 either systemically or peritumorally at day 20th. For the MTB alone compared to PBS, the significant inhibition of tumor growth and the decrease in tumor volume were reached only for the last time point of 10th injections (day 20th). However, the tumor did not disappear as observed in the case of treatment with MTB-LSC containing the same amount of MTB. Figure B.2c presents tumor photographs of all the groups at day 20th. All the control groups appear to develop and maintain large pendulous subcutaneous tumors at the end of the experiment, which their size exceeded 2 cm in diameter. On the contrary, animals that were treated with the MTB-LSC had either a very significant tumor regression with barely visible bumps under the skin at the site of injection or nearly complete tumor lysis. Of note, pendulous tumor masses were never observed in any of the MTB-LSC treated animals.

B.3 STATISTICAL ANALYSIS

Quantitative data are presented as a mean ± standard error. Statistical significance was assessed with the use of a two-way ANOVA followed by a posthoc Bonferroni test to compare individual means using GraphPad Prism software. The level of statistical significance was established at *P*-values less or equal to 0.05. *P*-value more than 0.05 is considered as not significant.

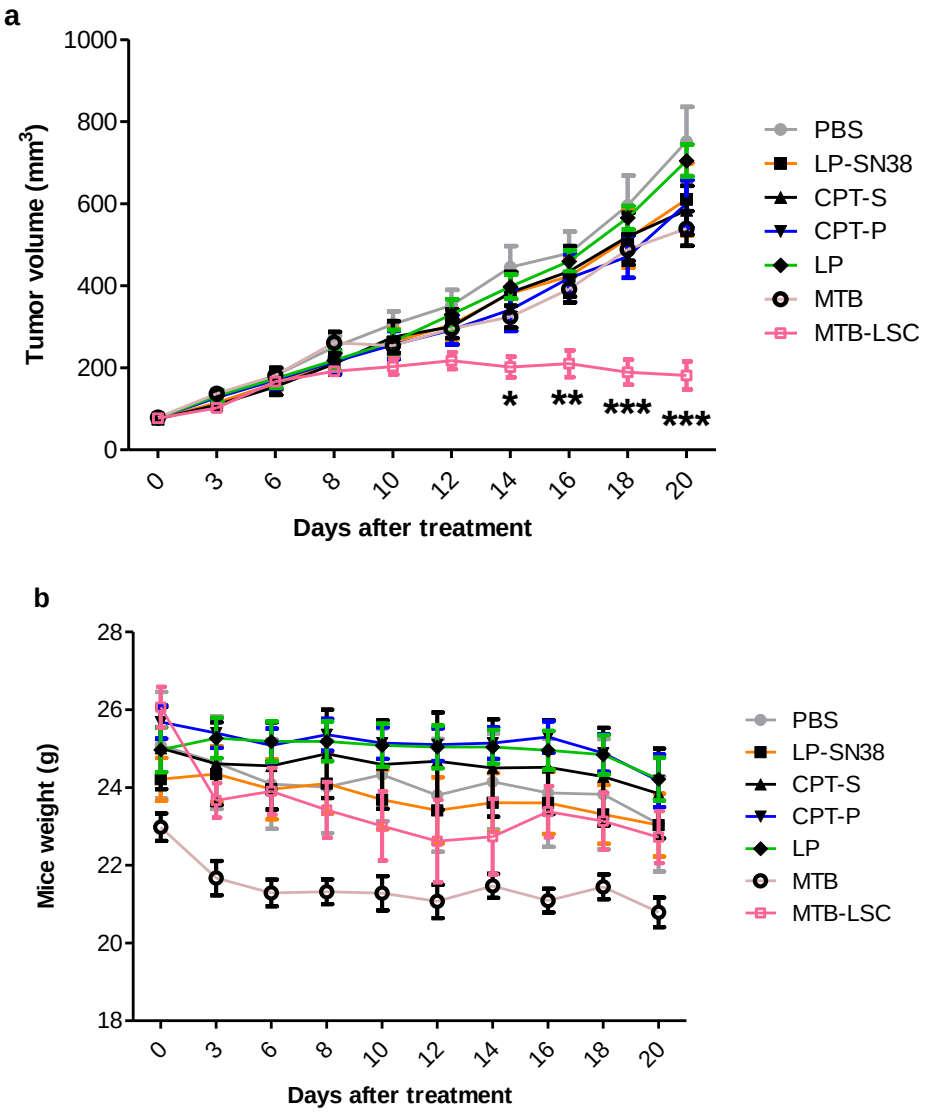

Figure B.1: (**a**) Comparison of therapeutic efficacy of MTB-LSC *vs.* controls during the course of the treatment. Statistically significant tumor inhibition growth was observed for MTB-LSC groups *vs*. controls from day 14 to 20 in which **P*-value < 0.05, ***P* < 0.01, ****P* < 0.001 are considered as significantly different (n = 9). Statistical analysis was performed using two-way ANOVA. (**b**) The weight of treated animals during the course of the experiment. No statistically significant difference was observed between groups (P > 0.005).

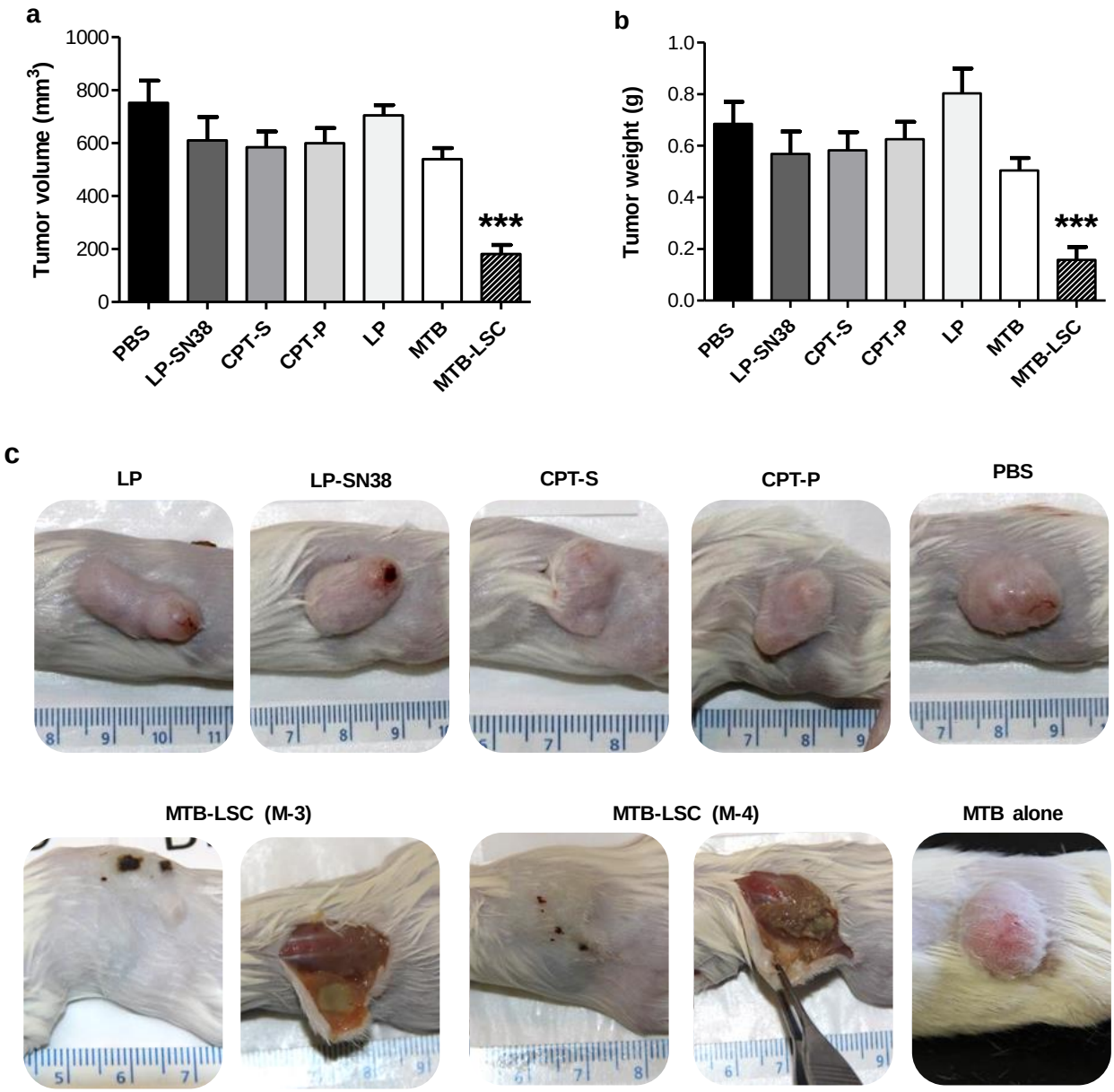

Figure B.2: (**a**) Tumor volume, (**b**) tumor weight, and (**c**) representative tumor photographs of MTB-LSC (M-3 and M-4 as an examples) and the control groups at the end of treatment (day 20th). The results demonstrated that 10 injections of MTB-LSC with a cumulative dose of ~6.4 μg of SN38 significantly impact on tumor growth. $^{***}P$-value < 0.001 is considered as significantly different (n = 9).

B.4 DISCUSSION

Hypoxic environments in solid tumors that are distant from the blood vessels lead to a negative impact on treatments based on radiotherapy and chemotherapy [13, 351, 355]. Current cancer therapies fail to provide all the fundamental capabilities necessary to efficiently target these hypoxic regions within solid tumors. The studies showed that the clinical application of SN38 an anti-cancer drug is not possible to date due to poor solubility and inactivity at physiological condition [111, 119, 371]. The liposomal formulation of SN38 can enhance solubility, and favorably alter the pharmacokinetics [111, 127] but still the liposomal drug cannot passively access to the unattainable hypoxic regions due to increased TIFP and high packing density of extracellular matrix constitute a barrier to transport of therapeutic agents towards these regions [12, 42, 54, 55, 365]. The critical factors for determining the drug dose delivered to the tumor are consist of (i) the trapping efficiency of drug in each liposome, ii) the number of liposomes attached to bacteria, and (iii) targeting ratio (delivered/injected) of MTB-LSC found in the tumor.

The promising obtained *in vivo* results demonstrated that multiple peritumoral dosing of MTB-LSC in the cumulative effective therapeutic dose of ~6.4 μg SN38 delivered deep into the hypoxic and necrotic regions resulted in a dramatic improvement in therapeutic effect and statistically significant inhibition of tumor growth in a HCT116 tumor xenograft. There exists a correlation between better therapeutic efficacy and amount of SN38 in the MTB-LSC treated group. Therapeutic effects of MTB-LSC was significantly different compared to all controls including animals treated with an equivalent dose of CPT-11 and LP-SN38 that showed no control of tumor growth. MTB alone demonstrated a decrease in tumor volume only at the last time point (10th injections).

The previous studies showed that the CPT-11 effective dose for reducing tumor growth was reported 40 and 60 mg/kg/dose for a multiple and single administration, respectively, in SCID mice [371]. Also, tumor-bearing mice multiple dosed *i.v.* for 5 days with liposomal SN38 at 5.5 or 8 mg/kg/day inhibited 98% and 100% tumor growth respectively, in a pancreatic tumor model [373]. Our results demonstrated that the therapeutic effect of multiple-dose *p.t.* injections (10 times, every other day) with MTB-LSC (~0.03 mg/kg/day) in SCID mice to produce a statistically significant reduction in tumor size was found to be ~91.6-fold less than liposomal SN38 and ~133.3-fold lower than *i.v.* injection of CPT-11. Overall, the results translate the

formulated MTB-LSC into a higher therapeutic index for SN38 as a relatively insoluble and physiologically inactive drug compared to conventional chemotherapy.

APPENDIX C – LIST OF MANUSCRIPTS ACCEPTED AND SUBMITTED FOR PUBLICATION, SELECTED CONFERENCE PROCEEDINGS, AND AWARDS

MANUSCRIPTS ACCEPTED, SUBMITTED, AND TO BE SUBMITTED

1. **Samira Taherkhani**, Mahmood Mohammadi, Jamal Daoud, Sylvain Martel, and Maryam Tabrizian, "Covalent Binding of Nanoliposomes to the Surface of Magnetotactic Bacteria for the Synthesis of Self-Propelled Therapeutic Agents", ***ACS Nano***, 8 (5), pp 5049–5060, 2014. (Accepted and available online at: http://pubs.acs.org/doi/abs/10.1021/nn5011304)

2. Martel S., **Taherkhani S**., Tabrizian M., Mohammadi M., de Lanauze D., and Felfoul O, "Computer 3D Controlled Bacterial Transports and Aggregations of Microbial Adhered Nano-components", ***Journal of Micro-Biorobotics,*** 9:23–28, 2014. (Accepted and available online at: http://link.springer.com/article/10.1007%2Fs12213-014-0076-x)

3. Ouajdi Felfoul*****, Mahmood Mohammadi*****, **Samira Taherkhani***, Danuta Radzioch*****, Dominic de Lanauze, Sherief Essa, Nicole Beauchemin, Michel Lafleur, Louis Gaboury, Maryam Tabrizian, Neila Kaou, Michael Atkin, Dumitru Loghin, Té Vuong, Gerald Batist, and Sylvain Martel, "Non-systemic magneto-aerotactic bacteria-mediated delivery of drug-loaded nanoliposomes in tumor hypoxic regions", submitted to the journal of ***Nature Nanotechnology***, 2015.

   ***** *These authors contributed equally to this work.*

4. Sylvain Martel, Ouajdi Felfoul, Danuta Radzioch, Dominic de Lanauze, **Samira Taherkhani**, Sherief Essa, Nicole Beauchemin, Michel Lafleur, Louis Gaboury, Maryam Tabrizian, Neila Kaou, Michael Atkin, Té Vuong, Gerald Batist, and Mahmood Mohammadi,"MC-1 magnetotactic bacteria as nano-structured therapeutic microrobots for targeting tumor hypoxic regions", submitted to ***International Journal of Robotics Research***, 2014.

5. **Samira Taherkhani**, Nina Olamaei, Farida Cheriet, Danuta Radzioch, Mahmood Mohammadi, Gerald Batist, Nicole Beauchemin, Louis Gaboury, Té Vuong, Maryam Tabrizian, and Sylvain Martel, "Magnetic resonance imaging of tumor hypoxia using computer-assisted magneto-aerotactic bacteria-mediated superparamagnetic iron-oxide nanoparticles", to be submitted.

CONFERENCES:

1. **Samira Taherkhani**, Mahmoud Mohammadi, Maryam Tabrizian, Sylvain Martel, “Magnetotactic Bacteria-Liposome Complexes as Navigable Microcarriers for Drug Delivery Applications”, MEDTEQ innovation for health , Quebec, Quebec city, Canada , 2014 (Poster)

2. Martel S., **Taherkhani S**., Tabrizian M., Mohammadi M., de Lanauze D., and Felfoul O, "Computer 3D Controlled Bacterial Transports and Aggregations of Microbial Adhered Nano-components," International Conference on Manipulation, Manufacturing and Measurement on the Nanoscale (3M-NANO), Suzhou, China, August 26-30, 2013

3. **S. Taherkhani,** M. Mohammadi, J. Daoud, S. Essa, S. Martel, and M. Tabrizian," Attachment of liposomes on magnetotactic bacteria acting as self-propelled drug delivery agents ", XX International Conference on Bioencapsulation, Orillia, Ontario, Canada - September 21-24, 2012. (Oral)

4. S. Martel, F. Afkhami Zarreh, **S. Taherkhani**, M. Mohammadi, "Encapsulation of Magnetotactic Bacteria for Targeted and Controlled Delivery of Anticancer Agents for Tumor Therapy", 33rd Annual International IEEE EMBS Conference, Boston, USA, 2011.

PRESS ARTICLE FEATURING RESEARCH:

Letarte, Martine. "Polytechnique - Le cancer a une légion d'ennemis." Le Devoir. 11 January 2011. http://www.ledevoir.com/societe/education/315635/polytechnique-le-cancer-a-une-legion-d-ennemis

AWARDS:

1. Poster award, MEDTEQ (the Quebec Consortium for Industrial Research and Innovation in Medical Technology), 2014.

2. Awarded the Biomedical Science and Technology Research Group (GRSTB) scholarship funded by the Fonds de la recherche en santé du Québec (FRSQ), 2010.